Final Report

DSE 2017-2018

AerGo

Group 03

A. van den Bergh	4154010
K. Beukers	4098668
L. Callens	4391330
M. Garber	4158067
J. Jördens	4191250
S. de Kok	4164520
R. Palings	4283120
M. Reekers	4233905
N. Smith	4161459
M. Taams	4388410

TU Delft

Preface

This is the work of enthusiastic ten students, currently completing the Bachelor program of Aerospace Engineering at Delft University of Technology. The intention of this report is to give a thorough explanation of the process and final result of the design synthesis exercise as executed by this group of students. The project started in November 2017 with a 2 week literature study. The divergent design phase generated 18 aircraft concepts that were analysed by the different technical disciplines and concluded with an initial screening. In the second phase 5 concepts were left which were technically studied in more detail and eventually conducting a final trade-off. After this, detailed design phase begun. This report cover the final design of the *AerGo*. We would like to give our recognition to out project coordinator, Ir. V.P. Brügemann, as well as our project coaches, Dr. ir. M. Karásek, Ir. J.A. Kupski and Ir. W. Terra for their useful feedback on this report and their constant availability to answer our questions. Likewise we would like to express our gratitude to Ir. J.J.A van Kuijk and Ir. T. Sinnege, who have helped expand our knowledge on different design disciplines. Also the support of the system engineering staff for their advice is greatly appreciated. Finally a big thank you to all group members to be so motivated through out the ten project weeks.

Group 03,
Delft, January 2018

Contents

Abbreviations

Abbreviation	Explanation	Abbreviation	Explanation
ac	Aerodynamic Centre	OEM	Operational Empty Mass
A/C	Aircraft	OP	Operations
AC	Alternating current	ET	Polyethylene Terephthalate
AoA	Angle of Attack	POS	Project Objective Statement
AVL	Athena Vortex Lattice	PL	Planning
BLDC	BrushLess direct current	PM	Project Management
BR	Baseline Report	PP	Power and Propulsion
BU	Budget	REQ	Requirement
CoB	Centre of Buoyancy	RM	Risk Management
CFD	Computational fluid dynamics	RAMS	Reliability, Availability, Maintainability and Safety
CFRP	Carbon Fibre Reinforced Polymer	RAND	Research and development
CO_2	Carbon Dioxide	R/C	Rate of Climb
CoG	Center of Gravity	RD	Rate of DescentSE & System Engineering
Conf.	Design Configuration	RPM	Rotations per minute
DAPCA	Development and procurement cost	RHO	Materials used specific
DC	Direct current	RHO	Materials used specific
Dp	Dimensions propulsion system	SM	Structures and Materials
Ds	Dimensions centre frame	SU	Sustainability
D/B	Draught over width	SWOT	Strength Weakness Opportunity Threat
DOT	Design Option Tree	TBD	To Be Determined
DSDS	Delft Systematic Deadrise Series	TUD	Technische Universiteit van Delft
DSE	Design Synthesis Exercise	USAF	United States Air Force
EoM	Equation of motion	WBS	Work Breakdown Structure
EW	Empty Weight	WFD	Work Flow Diagram
EASA	European Aviation Safety Agency	W/S	Wing Loading
FAST	Fast Sea Transportation	W/P	Specific Power
FBS	Functional Breakdown structure		
FFD	Functional Flow Diagram		
GAMA	General aviation manufacturing association		
GPS	Global positioning system		
HD	Hydrodynamics		
HSMV	High speed marine vehicles		
KNMI	Koninklijk Nederlands Meteorologisch Instituut		
L/B	Length over width		
MBF	Maximum buoyancy per float		
MIT	Massachusetts Institute of Technology		
MNS	Mission Need Statement		
MTOW	Maximum Take-Off Weight		
NACA	National Advisory Committee for Aeronautics		
np	Neutral Point		

List of Symbols

Symbol	Unit	Description
a	$[m/s^2]$	Acceleration
A	[-]	Aspect ratio
A_c	$[m^2]$	Frontal area of the component
A_p	$[m^2]$	Projected planing area
A_s	$[m^s]$	Cross-sectional area of the segment
b	$[m]$	Wing span
B	$[N/m]$	Buoyancy force
b_{low}	$[m]$	Span of the lower wing
B_s	$[m]$	Stringer width and height
b_{up}	$[m]$	Span of the upper wing
B_{px}	$[m]$	Width of the planing area
$cg-2$	$[m]$	Centre of gravity without floating system
$cg-f$	$[m]$	Centre of gravity floating system
$cg-p$	$[m]$	Centre of gravity propulsion system
$cg-p$	$[m]$	Centre of gravity frame
$\bar{c}$	$[m]$	Wing chord
$\bar{c}_{up}$	$[m]$	Chord of the upper wing
$\bar{c}_S$	$[m]$	Chord length control surface
C_{ap}	[%]	Centroid of planing area as a percentage of length
C_d	[-]	2D drag coefficient of the airfoil
C_D	[-]	3D drag coefficient of the wing
C_{D_c}	[-]	3D drag coefficient of the component
C_{D_i}	[-]	Induced drag coefficient
C_{D_0}	[-]	3D zero-lift drag coefficient
C_{d_0}	[-]	2D zero-lift drag coefficient
$\bar{c}_{low}$	$[m]$	Chord of the lower wing
C_{ℓ_β}	[-]	Roll moment coefficient with respect to change of side slip
$C_{\ell_{\delta_a}}$	[-]	Roll moment coefficient with respect to change of aileron deflection
$C_{\ell_{\delta_r}}$	[-]	Roll moment coefficient with respect to change of rudder deflection
C_{ℓ_e}	[-]	Roll moment coefficient with respect to change of engine thrust (failure)
C_{ℓ_p}	[-]	Roll moment coefficient with respect to change of pitch rate
C_{ℓ_r}	[-]	Roll moment coefficient with respect to change of yaw rate
C_L	[-]	Lift coefficient
C_{L_α}	[-]	3D lift coefficient with respect to change of angle of attack
$C_{L_{\alpha_{low}}}$	[-]	3D lift slope of the lower wing
$C_{L_{\alpha r}}$	[-]	Required 3D lift coefficient with respect to change of angle of attack
$C_{L_{\alpha_{up}}}$	[-]	3D lift slope of the upper wing
$C_{L_{des}}$	[-]	3D design lift coefficient
$C_{l_{max}}$	[-]	Maximum 2D lift coefficient of the airfoil
$C_{L_{max}}$	[-]	Maximum 3D lift coefficient of the wing
$C_{L_{max,r}}$	[-]	Maximum 3D lift coefficient of the wing (reference)
C_{l_0}	[-]	2D lift coefficient at $\alpha = 0$
C_{L_0}	[-]	3D lift coefficient at $\alpha = 0$
C_m	[-]	Moment coefficient
C_{m_0}	[-]	Moment coefficient at zero lift
C_{m_α}	[-]	Moment coefficient with respect to change of angle of attack

$C_{m_{\dot{\alpha}}}$	[-]	Moment coefficient with respect to change of rate of angle of attack
$C_{m_{ac}}$	[-]	Aerodynamic moment coefficient
$C_{m_{ac,r}}$	[-]	Aerodynamic moment coefficient required
C_{m_q}	[-]	Moment coefficient with respect to change of pitch rate
C_{m_u}	[-]	Moment coefficient with respect to change of horizontal velocity
C_{N_1}	[-]	Normal lift force coefficient for the lower wing
C_{N_2}	[-]	Normal lift force coefficient for the lower wing
C_{N_α}	[-]	Normal lift force coefficient with respect to change in angle of attack
C_{n_β}	[-]	Yaw moment coefficient with respect to change of side slip
$C_{n_{\dot{\beta}}}$	[-]	Yaw moment coefficient with respect to change of rate of side slip
$C_{n_{\delta a}}$	[-]	Yaw moment with respect to change of aileron deflection
$C_{n_{\delta_r}}$	[-]	Yaw moment with respect to change of rudder deflection
C_{n_e}	[-]	Yaw moment coefficient with respect to change of engine thrust (failure)
C_{n_p}	[-]	Yaw moment coefficient with respect to change of roll rate
C_{n_r}	[-]	Yaw moment coefficient with respect to change of yaw rate
C_{X_0}	[-]	Longitudinal force coefficient at intitial contion
C_{X_α}	[-]	Longitudinal force coefficient with respect to change of angle of attack
C_{X_q}	[-]	Longitudinal force coefficient with respect to change of pitch rate
C_{X_u}	[-]	Longitudinal force coefficient with respect to change of horizontal velocity
C_{Y_β}	[-]	Side force coefficient with respect to change of side slip
$C_{Y_{\dot{\beta}}}$	[-]	Side force coefficient with respect to change of rate of side slip
$C_{Y_{\delta a}}$	[-]	Side force coefficient with respect to change of aileron deflection
$C_{Y_{\delta_r}}$	[-]	Side force coefficient with respect to change of rudder deflection
C_{Y_p}	[-]	Side force coefficient with respect to change of pitch rate
C_{Y_r}	[-]	Side force coefficient with respect to change of yaw rate
C_{Z_0}	[-]	Vertical force coefficient at intitial contion
C_{Z_α}	[-]	Vertical force coefficient with respect to change of angle of attack
$C_{Z_{\dot{\alpha}}}$	[-]	Vertical force coefficient with respect to change of rate of angle of attack
C_{Z_q}	[-]	Vertical force coefficient with respect to change of pitch rate
C_{X_u}	[-]	Vertical force coefficient with respect to change of horizontal velocity
D	$[N]$	Drag force
D_0	$[N]$	Profile drag
D_{ae}	$[N]$	Aerodynamic drag force
D_b	[-]	Non dimensional time derivative for asymmetric motion
D_c	[-]	Non dimensional time derivative for symmetric motion
D_{hd}	$[N]$	Hydrodynamic drag force
D_i	$[N]$	Lift-induced drag
D_l	$[N]$	Drag force in landing configuration
e	[-]	Oswald factor
E	$[MPa]$	Young's Modulus
F	$[N]$	Force
F_c	$[N]$	Control force
F_p	$[N]$	Pressure force
F_s	$[N]$	Force in the back strut
F_{side}	$[N]$	Sideforce
G_r	$[m]$	Root gap, or vertical distance between the two wings at the root
G_t	$[m]$	Tip gap, or vertical distance between the two wings at the tip
$\frac{G}{c}$	[-]	Gap to chord ratio
h	$[m]$	Altitude
I	$[m^4]$	Area moment of inertia
$I_{A,xx}$	$[m^4]$	Area moment of inertia around the x axis
$I_{A,xy}$	$[m^4]$	Area moment of inertia in the xy plane
$I_{A,xz}$	$[m^4]$	Area moment of inertia in the xz plane
$I_{A,yy}$	$[m^4]$	Area moment of inertia around the y axis
$I_{A,zz}$	$[m^4]$	Area moment of inertia around the z axis

$I_{m,xx}$	$[kgm^2]$	Mass moment of inertia around the x axis
$I_{m,xy}$	$[kgm^2]$	Mass moment of inertia in the xy plane
$I_{m,xz}$	$[kgm^2]$	Mass moment of inertia in the xz plane
$I_{m,yy}$	$[kgm^2]$	Mass moment of inertia around the y axis
$I_{m,zz}$	$[kgm^2]$	Mass moment of inertia around the z axis
l_r	$[m]$	Lever arm from CoG to rudder aerodynamic centre
K_p	[N]	Thrust vector
L	$[N]$	Lift force
L'	$[N/m]$	Lift distribution
$(L/D)E$	[-]	Lift over drag ratio for maximum endurance
$(L/D)R$	[-]	Lift over drag ratio for maximum range
L_h	$[m]$	Hull length
L_{low}	$[N]$	Lift force on the lower wing
L_s	$[m]$	Length of the section
L_{sp}	$[m]$	Length of the spar
L_{up}	$[N]$	Lift force on the upper wing
LCG	[%]	Longitudinal position of the Centre of Gravity from C_{ap}
L_p	$[m]$	Length of the planing area
m	$[kg]$	Mass
M	$[Nm]$	Moment
M_2	[kg]	Mass aircraft Without foating system
M_c	[kg]	Control system mass
M_f	[kg]	Floating system mass
M_{pr}	[kg]	Propulsion system mass
M_{r_t}	$[Nm]$	Denotes the righting moment corresponding to the current heeling angle
M_s	[kg]	Structural mass
M_t	[kg]	Total mass aircraft
M_{TO}	[kg]	Take-off mass
M_x	$[Nm]$	Moment around the x axis
M_y	$[Nm]$	Moment around the y axis
M_0	$[Nm]$	Moment at $x = 0$
n	[-]	Load factor
n_p	[-]	Load factor present
n_r	[-]	Load factor required
P_a	$[kW]$	Power available
P_{cr}	$[MPa]$	Critical buckling stress
P_{a_C}	$[kW]$	Power available cruise
$P_{a,TO}$	$[kW]$	Power available take-off
P_e	$[kW]$	Excess power
P_r	$[kW]$	Power required
P_{r_C}	$[kW]$	Power required cruise
$P_{r,TO}$	$[kW]$	Power required take-off
P_w	$[MPa]$	Hydrostatic pressure
q	$[Pa/m]$	Shear flow
q_h	$[N/m]$	Aerodynamic force distribution
q_s	$[N/m]$	Control surface aerodynamic force distribution
Q	$[m^2]$	Surface area applicable to shear stress
q_∞	$[MPa]$	Dynamic pressure
R_r	$[km]$	Range required
RD	$[m/s]$	Rate of descent
Re	[-]	Reynolds number
R_t	$[N]$	Reaction force
S	$[m^2]$	Wing area
S_c	$[m^2]$	Control surface area
S_h	$[m^2]$	Stabiliser area
S_{low}	$[m^2]$	Area of the lower wing

S_{side}	$[m^2]$	Area of the sideplates
S_{up}	$[m^2]$	Area of the upper wing
S_x	$[N]$	Shear loads in the x direction
S_y	$[N]$	Shear loads in the y direction
s_{TO}	$[m]$	Take-off length
t	$[s]$	Time
T	$[N]$	Thrust force
T_{a_C}	$[N]$	Thrust available cruise
$T_{a,TO}$	$[N]$	Thrust available take-off
t/c	[-]	Thickness to chord ratip
T_{wb}	$[N]$	Wingbox resisting moment for some angle of twist
t_{lift}	$[m]$	Spar thickness to take up shear loads
T_{r_C}	$[N]$	Thrust required cruise
$T_{r,TO}$	$[N]$	Thrust required take-off
t_s	$[m]$	Stringer thickness
T_s	$[Nm]$	Torsion due to shear
t_{torque}	$[m]$	Spar thickness to take up torsion loads
t_{tot}	$[m]$	Total spar thickness
t_{web}	$[m]$	Web thickness
V	$[m/s]$	Velocity
$\bar{V}$	$[m/s]$	Wind speed vector
V_∞	$[m/s]$	Free flow velocity
V_a	$[m/s]$	Axial velocity
v_b	$[m]$	Deflection
V_c	$[m/s]$	Cruise velocity
$V_{D_{min}}$	$[m/s]$	Airspeed for minimal drag
V_l	$[m/s]$	Landing speed
$V_{P_{r_{min}}}$	$[m/s]$	Airspeed for minimal power required
V_s	$[m/s]$	Stall speed
V_{side}	$[m/s]$	Velocity of the side wind
V_t	$[m/s]$	Tangential velocity
V_{TAS}	$[m/s]$	True Airspeed
V_{TO}	$[m/s]$	Take-off velocity
V_y	$[N]$	Shear force
W	$[N]$	Weight force
W_a	$[N]$	Weight of the aicraft mass
W_p	$[N]$	Weight of the pilot mass
W/S	$[N/m^2]$	Design wing loading
$\tilde{x}$	$[m]$	Distance to the x axis
$\bar{x}$	$[m]$	X-coordinate of the centroid
x_a	$[m]$	Acting point of the aircraft weight along the keel, measured from the stern
x_b	$[m]$	Battery location
x_{cg}	$[m]$	X-coordinate of center of gravity of the aircraft
x_e	$[m]$	Engine location
x_{F_c}	$[m]$	The arm from control force to centre of twist
x_{F_s}	$[m]$	X-coordinate of the back strut
x_p	$[m]$	Acting point of the pilot weight along the keel, measured from the stern
x_{pilot}	$[m]$	X-coordinate of centre of pilot
x_{pr}	$[m]$	Propeller location
x_{st}	$[m]$	Stagger
x_{sc}	$[m]$	Control surface position
x_{tw}	$[m]$	X-coordinate of location of the rotation of twist
$\tilde{y}$	$[m]$	Distance to the y axis
$\bar{y}$	$[m]$	Y-coordinate of the centroid
Y'_{CB}	$[m]$	Y-coordinate of the centre of buoyancy in the rotated system

Z_s	$[m]$	Rib spacing
α	[°]	Angle of attack
α_0	[°]	Angle of attack at zero lift
β	[°]	Angle of sideslip
γ	[°]	Flight path angle
γ	[°]	Buttock angle
Γ	[°]	Dihedral angle
Γ_0	$[m^2/s]$	Vorticity
γ_d	[°]	Descent angle
$Delta$	$[m^3]$	Displacement
ϵ	[°]	Twist angle
λ	[-]	Taper ratio
Λ	$[m]$	Sweep angle
μ_b	[-]	Non dimensional mass in asymmetric motion
μ_c	[-]	non dimensional mass in symmetric motion
φ	[°]	Roll angle
ρ	$[kg/m^3]$	Air density
ρ_w	$[kg/m^3]$	Water density
σ	[-]	Interference factor
σ_{cr}	$[MPa]$	Critical buckling stress
σ_p	$[MPa]$	Stress due to pressure
σ_r	[-]	Interference factor at the tip
σ_t	[-]	Interference factor at the root
σ_y	$[MPa]$	Yield stress
σ_z	$[MPa]$	Compression/tension stress in the z axis due to bending
τ	$[MPa]$	Shear stress
τ_{avg}	$[MPa]$	Average shear stress
τ_{max}	$[MPa]$	Maximum shear stress
θ	[°]	Pitch angle
θ_t	[°]	The heeling angle at the previous step
$\dot{\theta}_t$	$[°/s]$	The angular velocity at, respectively, the current and previous time step

Summary

The ambition of this project is to design a recreational ultralight water-aircraft that is transportable by bike and license free for the recreational user. This report describes the preliminary design of an aircraft called the *AerGo*. A summary is given on the concept configuration, the specific characteristics and the feasibility of the design.

The design is a biwing aircraft with swept wings that are closed with vertical plates at the tips. The wing chord is 0.79 m and is constant over a wing span of 12 m. The aircraft is driven by two six bladed propellers that are placed on the top wing and powered by electric engines. The lower wing is attached in the middle to a main hull that is buoyant on water and stabilised by sidefloats on the tips. A paddle is used for taxiing and docking on the water. The aircraft will take-off and land on water only. The pilot will be seated inside the hull and can control the pitch by shifting his weight forward and backward on a swing. The roll is performed with wing warping while yawing is done by rudders. The total empty mass of the *AerGo* is 44.7 kg. To operate the *AerGo* a multipurpose trailer system will make storing, transporting and deploying the aircraft as easy as possible. The *AerGo* is designed to be operated, assembled and maintained by a single person. The aircraft will be safe to fly on more than 270 days of the year.

A market analysis is conducted on ultralight aircraft where it is found that there are more than 25,000 ultralight and microlight aircraft in Europe of which 500 are registered in the Netherlands. Most ultralights are privately built by flight enthusiasts, therefore the production and sales are limited. However, a number of outstanding designs like the *Woopyfly* and *Lazair* are produced at large scale with production of 2,000 to over 10,000 units. The *AerGo* has a lot of opportunity and would stand out with the competition, for mobility, ease of use, no license and hydrodynamic qualities. Staying conservative it is estimated that at least 20 aircraft can be sold per year during the start-up phase. Of these 20, around 25% is aimed at the Dutch market whereas the other 75% for the rest of Europe. Expanding to America and Canada is considered as an opportunity for the future.

The requirements for the aircraft have been analysed and used as a starting point for the design iteration. The empty weight of the aircraft is constructed for a large part by the battery weight. The biggest contribution to the energy requirement is the cruise flight phase, there the performance of the aircraft is optimised for this phase. The airfoil selection is based on the required lift. A detailed airfoil analysis was done to obtain the required C_l value for 0° angle of attack. A high C_{l_0} was required for optimal performance and this was the main driver for the airfoil selection. The NACA 6415 airfoil was selected, because it has a high C_{L_0} at zero angle of attack such that the drag will be minimum and provide the required C_L value during cruise. The airfoil has a $C_{L_0} = 0.68$ which provides the performance department with a $C_L = 0.57$ during cruise flight at an angle of attack of $\alpha = -0.2°$.

The hydrodynamic model is based on the DSDS database that estimates the drag during take-off, with a take-off speed of 9.9 kg and distance of 170 m respectively. Combining this with the aerodynamic drag computed for the airfoil characteristics, the power required for take-off and cruise is computed. With a climb rate of 1.43 m/s the cruise altitude of 150 m is reached within 105 seconds after lift-off.

The take-off power is the driving factor in the engine design while the power required during cruise is driving for the battery design. 2 electrical engines are chosen to power 2 six blade propellers. The aircraft batteries are sized to reach a minimum flight time of 60 minutes per set of full batteries. With a cruise speed of 15 m/s the aircraft has a minimum range of 40 km.

The most critical parameter for stability, the longitudinal pilot position was found to be optimal at $x_{pilot} = 1.6m$ after several iterations. The aircraft is statically and dynamically stable for both cruise and take-off. A pilot of 100 kg contributes 68 % of the Maximum Take-Off Weight (MTOW) of the aircraft, thus the *AerGo* is designed for weight shifting to perform pitch control. The upper wing has positive stagger. It is shifted 0.45 m forward relative to the lower wing. This creates a balancing seesaw which makes weight shifting control less impulsive and more smooth. The roll control is performed by wing warping and yaw is controlled by the use of two rudders that are placed at the tips of the wing. A sweep of 15° is chosen to increase rudder effectiveness and the size of the rudder was evaluated to be 0.237 m^2. This makes it possible to fly with only one engine operating. If future research were done on the stability it is recommended from experience to use the Aerospace Toolbox given out by Simulink. This produces a very detailed dynamic stability model.

When the pilot shifts his weight slightly right or left it will take about 5 to 15 seconds, depending on the CoG shift for the pontoons to hit the water. Once the aircraft has attained speed it becomes even more stable due a stabilising effect of the wing making it hydrodynamic stable. The hull is designed to allow the aircraft to pitch up freely during take-off.

A skin on frame structure is used to minimise the weight of the hull and wing. With a rib stop nylon skin, carbon fibre rods as spar structure the weight of the wing is estimated to be a lean 11.3 kg. The hull has the same carbon fibre structure and a dacron skin coming down to a structural weight of 4 kg.

The 6 blade propellers are chosen to reduce noise below the 40 dB requirement. It is found that the noise of the gear box has the largest contribution to noise. Combining the noise of the propellers, gear box and electrical engine a total noise of 79.5 dB is estimated at 1m distance. Converting this to a 100m range gives a noise level of 39.5 dB.

It is estimated that around 74% of the weight can be recycled and the carbon footprint is close to 800 kg of CO_2 per aircraft.

When 20 units of the *AerGo* are being sold per year for a price of €20,000 the break even point will be 9.5 years after start of the design and the return on investment after 12 years will be €700,000.

A risk analysis is performed to check the feasibility of the design. It can be concluded that a more detailed analysis of the cost budget must be performed as well as the impact resistance of the structure. Furthermore a proper instruction must be included for the pilot to assemble the aircraft himself.

1 Introduction

On December 17, 1903, the Wright brothers made history by flying their powered aircraft for 12 seconds covering 120 feet. These pioneers in early flight were able to construct a heavier than air, controllable and powered flying device with a bare minimum of resources. The Wright Flyer I entailed a bi-plane with double canard configuration, fully constructed from wood and fabric. Almost 114 years, several technological revolutions and half a century of commercial flights later, this project is performing a homage to the *Wright Flyer I* by designing the next generation Hydroplane. Inspired by the Wright brothers' ability to fly with minimal power, the idea is that a new class of simple and low power aircraft will make flying possible for the average person. This new class of aircraft would have to be so light that no license is required, cheap enough to be available to most people and compact enough to store in the average garage.

The Hydroplane project aims at designing an ultralight water aircraft that can be used without airport or license by the recreational user. Besides that, the aircraft must also be able to be transported by bicycle. The goal is to provide a user friendly aircraft that can be flown with a minimal amount of effort and investment, thereby significantly reducing costs compared to current personal aircraft. Recent improvements in lightweight materials and capacity of energy storage make it possible to apply this technology to achieve previously unfeasible low aircraft masses, thereby opening a market niche. The product is designed for the Netherlands since there are many water runways available, but is likely to expand on to the international market. Previously, a project plan, a baseline report and a midterm report were published. These reports detailed, respectively, defining the project scope [6], generating concepts [4] and selecting the most suitable concept [5].

The purpose of this final report is to further develop the selected concept. This development consists of deciding on the general layout and geometry and choosing/designing subsystems. The design choices made in this report are done in order to comply as much as possible with the Mission Need Statement: *"To provide a recreational hydroplane that is transportable by bike, costs less than €20,000 and can operate from a 20 meter wide body of water"*.

This report starts with short explanation on the organisation of the project in Chapter 2. Next, in Chapter 3, the market is analysed as a basis for the cost budget and business plan, detailed in Chapter 14. Chapter 4 visualises the design and provides a general overview of the major design parameters. Chapter 5 shows the compliance matrix and gives more explanation on requirements that are not met. The general performance of the *AerGo* is detailed in Chapter 6. Those interested in the aerodynamical characteristics of the *AerGo* can turn to Chapter 7. Chapter 8 discusses the stability, both static and dynamic, and control of the design. The design choices regarding structures and materials are shown in Chapter 9, while those regarding the propulsion system are explained in Chapter 10. The hydrodynamic qualities, such as resistance, stability and control, are included in Chapter 11. The last technical part is then Chapter 12, which explains the operational side of this design. Chapter 13 shows the mass breakdown, while sustainability is discussed in Chapter 15, which gives amongst others, the carbon footprint, end of life plans and recyclability. Chapter 16 identifies and mitigates the technical risks, while Chapter 17 analyses the sensitivity of the used methods. Finally, Chapter 18 details future plans.

2 Project Scope

This chapter explains the organisation of the *AerGo* project. It will mainly focus on the changes that have been implemented since the Midterm report [5]. In Section 2.1, a recap of the design process up until the current design phase is given. In Section 2.3, the updated organogram will be discussed. Secondly, in Section 2.4 the N^2 Chart will be explained which serves as an outline of the design process in the detailed design phase.

2.1 The project until mid-term

This report details the last phase of the design project. Earlier phases are described in the project plan[6], baseline report[4] and midterm report[5]. This section reminds the reader of the main steps taken in the phases up to the midterm.

First, the customer needs were translated into a Mission Need Statement (MNS):

"To provide a recreational hydroplane that is transportable by bike, costs less than €20,000 and can operate from a 20 meter wide body of water."

Which was translated into a Project Objective Statement (POS):

To design a lightweight, compact, sustainable hydroplane at minimal cost that adheres to FAR 103, by 10 students in 10 weeks.

From the MNS, a set of user, mission and system requirements was derived in order to define the design space.

Once this design space was defined, the group came up with 18 different concepts, making sure to fill each section of the design space with at least one design. Each of these concepts was then graded on criteria such as: sustainability, flight experience and ease of use. With this grading, an initial trade-off was performed, in which the five highest scoring concepts were selected. However, due to limitations in time and resources only three concepts could be taken to the next phase. For this reason, several concepts were combined into one concept with different configuration possibilities. For example: two of the concepts were tailless, double winged aircraft, where the major difference was the propulsion system. These were combined into the *Flying Biwing*, where a future subsystem trade-off was to define the propulsion system.

These final three concepts, the *Flying Biwing* (Figure 2.1b), the *Surf Glider* (Figure 2.1c) and the *X-Machine* (Figure 2.1a), were analysed more fully, with a focus on the differences between, and the major drawback/benefits of each concept. The results of this analysis were used in a final trade-off,Appendix A, where the best concept was to be selected. This trade-off did however not select a clear winner, with the *Surf Glider* and the *Flying Biwing* sharing the first place. For this reason, a group discussion was held, were it was decided unanimously to select the *Flying Biwing* as the winning concept. The major arguments for this choice were: the group felt that as the *Surf Glider* would result in a sub-optimal adaptation of an existing design, the chances of economical success for this design would be slim to none. Secondly, the *Flying Biwing* was deemed to be a more elegant solution, that fell more in line with the design philosophy and the customers vision.

The major result of the phases up to this report is thus the selection of a final concept that is to be developed more fully in this phase of the design. An artist impression of the chosen design can be seen in Figure 2.1b. As can be seen, this design consists of a tailless box wing, mounted on top of a floating device.

The final design is called the *AerGo*, due to the analogy between the pilot movements and the movements when using an ergometer. Next to that it is a combination of the words 'ergo' (action, labour) and 'aer' (air, wind), which summarises the user experience: it is an intensive sport, performed in the air. A third meaning of this name is the combination of the words 'air' and 'go', denoting the ease of use; 'just go and fly'.

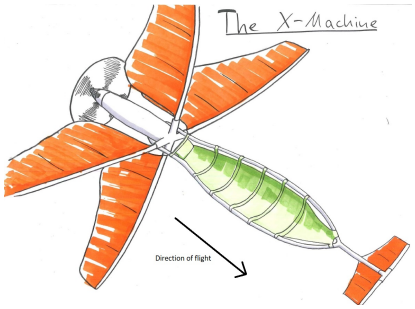

(a) Artist impression of the *X-Machine*.

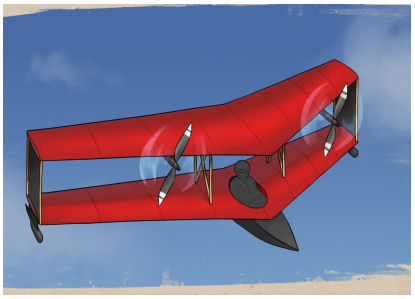

(b) Artist impression of the *Flying Biwing*, the selected design.

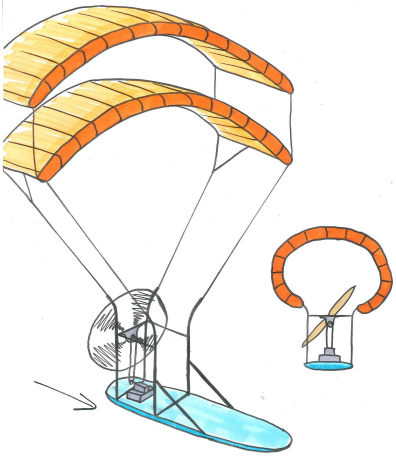

(c) Artist impression of the *Surf Glider*.

2.2 Mission Profile

The mission will consist of a return flight, with taxi, take-off, climb, cruise, descent, approach & landing occurring on both the outbound- and inbound flight. The approach phase is including a little loiter to account for an occupied river for which diversion to waters with less traffic is needed. The docking phase is also not included since this will be done by paddling as will be discussed in Chapter 11 in Section 11.6.3.

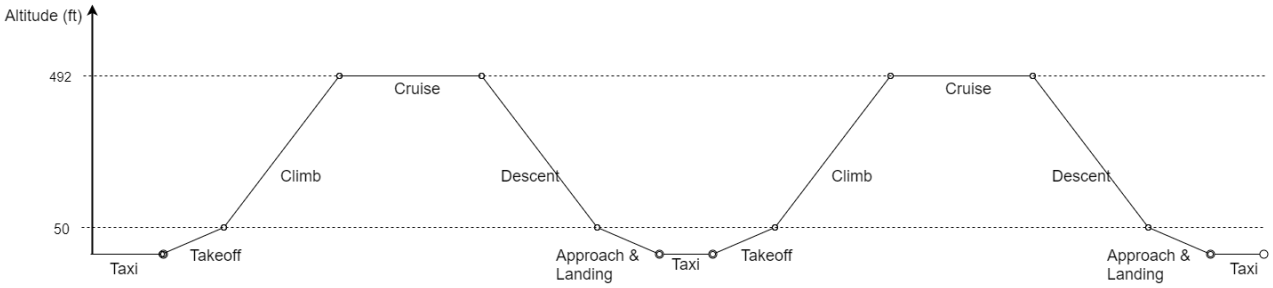

Figure 2.2: Mission Profile

2.3 Team Organisation

Throughout the entire project the team members are assigned specific technical and non-technical (semi-technical) roles in order to be able to work as efficiently as possible. This consists of non-technical roles such as planning, management, etc. and technical roles such as structures, aerodynamics, etc. These roles have changed slightly since the mid-term report [5]. First of all, it was decided to treat aero- and hydrodynamics as two separate departments instead of two closely related subdepartments as the methods and models used by both departments are completely different. Secondly, the group felt that materials and structures has a work load which is much higher than others, while the workload of performance and propulsion was too low. For that reason, one team member was transferred from performance and propulsion to materials and structures. The updated roles for all members are displayed in Figure 2.3. An exact representation of how these technical disciplines work together, is given by the N^2-Chart in Section 2.4.

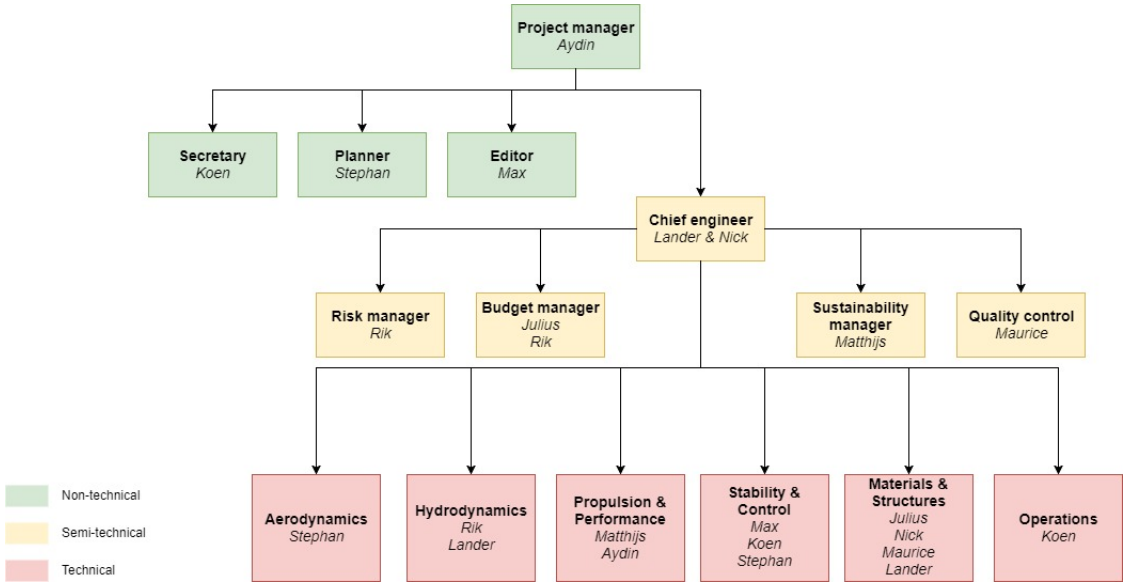

Figure 2.3: Organisational Breakdown Structure

2.4 N2-Chart

In this chart, the green squares along the diagonal represent the different engineering disciplines, while the white squares denote the parameters and information that flows between these disciplines. Each parameter is located in the same row as the discipline that provides it, while the column shows which discipline uses this parameter as input. Referring to Figure 2.4, the outputs from the red box (e.g. OEW, Operational empty weight (constraint)), are parameters distilled from requirements analysis, reference systems and initial estimates. These used to initialise the concept candidate initial sizing and analysis. As can be seen the red box does not have an input flow after providing its output, to ensure its initialising nature. The main technical disciplines present in the design process are depicted on the diagonal in green. As this is a performance driven design, it is decided to start the flow at the performance discipline. Data and parameters flow to and from this discipline to other technical disciplines, forming loops that denote design iterations. For example; the wing loading, W/S, is computed by the performance discipline, using the Operational Empty Eeight constraint (OEW), and acts as input to the aerodynamics discipline. The aerodynamic discipline uses this wing loading to, amongst others, estimate the wing characteristics, e.g. parasitic drag polar ($C_{D_{0_{wing}}}$). With these wing characteristics, the performance discipline starts a second iteration, resulting in an updated value for the wing loading, which in turn is used by the aerodynamics discipline. Several of these loops exist to ensure an iterative and thus optimising design process.

Requirements, constraints & (reference systems, Initial estimates)	• V_s • $C_{L_{max,r}}$ • V_c • $(R)_r$ • OEW • x_{to} • b	• b		• n_r • b	• Conf.		
	Performance	• W/S • $(L/D)_E$ • $(L/D)_R$	• $(T_{to})_r$ • $(T_c)_r$ • $(P_{to})_r$ • $(P_c)_r$	• M_f • n_p • S	• S	• M_2 • V_{to}	
	• e • C_{D_0} • $C_{L_{max}}$ • C_L/C_D	Aerodynamics		• t/c • c • c_h • q • q_h	• CL-alpha • $C_{m_{ac}}$ • c • S_h		
	• $(T_{to})_a$ • M_p • $(T_c)_a$ • $(P_{to})_a$ • $(P_c)_a$	• D_p • V_p • x_p	Propulsion	• x_{pr} • x_e • x_{bt}	• cg_p • K_p		
	• M_s	• D_s		Structures & Materials	• cg_s		• Rho • H_m
	• M_c	• $(C_L\text{-alpha})_r$ • $(C_{m_{ac}})_r$ • $(S_h)_r$		• Z_p • x_h	Stability & control	• cg_2	• $(cg_R)_a$
	• M_h • C_{Dh}	• D_h		• D_h	• cg_h • Z_h	Hydrodynamics	
		• D_{pay}		• Assemb.	• x_{pay}		Operations

Figure 2.4: N^2 Chart illustrating the interconnection between multiple disciplines

3 Market Analysis

In this chapter an analysis of the market is described. The market analysis from the start of this project is narrowed down and the ultralight aircraft segment is more elaborated on. This in order to find market opportunities and determine how many aircraft can be sold to find the feasibility of a business model. In Section 3.1 the market definition as determined in the baseline report [4] is given. Section 3.2 defines the most important customer needs while Section 3.3 summarises the two most important market segments forming the competition of the *AerGo*. The size of the market is described in Section 3.4 and this chapter concludes with defining the sales opportunities in Section 3.5.

3.1 Market Definition

In aerospace engineering there is a wide range of aircraft types. The *AerGo* will be a one manned, lightweight hydroplane which is silent, affordable and suitable for recreational flight with minimal amount of training. Being transportable by bike and the ability to take off from water are special features of the aircraft. From this, the market is defined as follows:

Lightweight aircraft used for recreational flight which are accessible to all flight enthusiasts without the need of a pilot license and with minimal training.

3.2 Customer Identification

The main features of every design are dependant on the target customer. It is important to define the customer needs to be able to design an aircraft satisfying their desires. In this section a behavioural analysis of potential customers has been performed and customer characters are determined. Who will buy this product and how is it appealing to them?

The *AerGo* sales price of €20,000 makes the aircraft accessible to not only the small rich part of the population but allows any flying enthusiast the opportunity to afford an aircraft. The ultralight and slow characteristics of the aircraft is likely to attract people who want to experience flying for the first time but have no or a minimum pilot license.

Next to this group, it will be attractive to several other customer types. Athletes that are fascinated by extreme sports such as kite surfing or wind surfing will be keen to try out the sport of recreational flying if it becomes accessible to them. The ultralight aircraft structure in combination with the ease of use and physical exercise while flying creates an entire new sport they can be attracted to.

In addition to these thrill seeking athletes, all people interested in outdoor sports are considered. The experience of being free in the air and experiencing the nature from above, be able to get to locations which are hardly reached by foot or bike fits in their profile of being in the wild and enjoying nature. Furthermore, since the product will be designed to be able to take off and land from water and will be transportable by bike, it may encourage people who are not necessarily enthusiastic about flight to start building an interest. Boat enthusiast can be affected since they will have the opportunity to fly from the water. To be able to experience boating and flying at the same time.

After the identifying the customer groups, the needs of the customers can be defined. Three main customer needs are given below and guide the design.

- Ease of use: The customer wants to be able to fly whenever they desire if weather permits and spends roughly the same amount of time on assembling the plane as he would on preparing his (For example windsurfing) gear.
- Transportable: The customer can easily transport the aircraft with a bicycle and a trailer to a body of water.
- Affordable: The aircraft must be an affordable price to the general public and should not exceed the price of other ultralight aircraft.
- Exercise: The customer would like to be active while flying this aircraft and wants flying to be an actual sport.

3.3 Market Segmentation

The purpose of this section is to identify key players in the market with a product similar to *AerGo*. Aircraft featuring the the ultralight plane and trike segments have most resemblance with the requirements and are considered as the biggest competitors. For a more thorough analysis of market segmentation can be referred to the baseline report [4].

3.3.1 Lightweight trikes and boat gliders

Lightweight trike aircraft are basically hangliders where the harnass carrying the pilot is replaced by a trike. Trikes are always motorised and the range of these aircraft is longer than for regular gliders. Some trikes accommodate for multiple passengers which is a way to introduce new potential pilots and flight enthusiasts to a gliding flight. Prices for trikes vary tremendously. To illustrate this variation, Table 3.1 shows the cost and production for five types of trikes. For most trike glider types the production has not gone over 1,000 units. The *Weedhopper* however is an exception as over 13,000 units of this aircraft are produced[(1)]. This shows that even though the market seems limited, excellent products can succeed and the market is bigger than just a small group of flight enthusiasts.

In some configuration a boat has been attached to a hang glider. This boat is motorised as well and obviously gives the opportunity to take off and land on water. In Figure 3.1a an example of a boatglider is given. These products typically cost around 15,000 to €20,000. Since there is only a specific customer group for this product, production is on a small scale and prices are relatively high compared to motorised gliders and trikes. Thus this product is quite customer specific. The AerGo will broaden its customer segment compared to these boats by the lighter, more quiet, sporty and easy to use characteristics.

(a) Seair flying boat (b) Weedhopper

Figure 3.1: Two different types of reference aircraft the Seair [(2)] and Weedhopper[(1)]

3.3.2 Ultralight planes

Ultralight planes are fixed wing aircraft which can carry one or two people. They are made in order to experience recreational flying or flying for sport. It is comparable to the concept of hang gliding, but then using a motor in order to have enough power to take off from the ground. These aircraft normally weigh from 100 kg to 500 kg depending on the aircraft. These aircraft vary in propulsion systems and can fly at several cruise velocities depending on the configuration. The prices range greatly from 9,000 to €150,000. For these ultralight planes a pilot license is required.

3.3.3 Competition

Based on that market segmentation, the customer identification and the design requirements, competitors have been identified and are shown in Table 3.1.

[(1)] `http://www.ultralightnews.com/ssulbg/weedhopper-weedhopperaircaft/experimental_amateurbuilt.html`, Retrieved: 22-11-2017

[(2)] `http://www.seair.com/flyingboat.htm`, Retrieved: 22-11-2017

[(3)] `hhttp://lazairinfo.com/electric-lazair/`, Retrieved: 22-11-2017

[(4)] `http://flynano.com/`, Retrieved: 29-01-2018

(a) E-Lazair Ultralight hydro [3] (b) Flynano [4]

Figure 3.2: Two different types of reference ultralight planes

Table 3.1: Different types of competitor aircraft w.r.t cost, units built and empty weight

Aircraft	Cost [€]	Units built	Empty weight [kg]
Pegasus quantum[5]	30,000	600	204
Mosquito NRG[6]	4,180	2,000	45
Weedhopper [7]	6,795	13,000	113
ISON Airbike[8]	10,400	127	136
Zigolo[9]	13,600	20	102
Aerolite 103[10]	13,600	150	120
CGS Hawk Arrow[11]	14,400	1,712	150
Lazair[12]	3,910	2,000	95
E-Lazair [13]	20,000	1,200	95
Belite Superlite[14]	9,520	10	126
FlyNano[15]	25,000	1	70

The main competitor is the Weedhopper which has an exceptional amount of units built (over 13,000 as seen in Table 3.1) and is sold for a relatively low price (€6,795). Although the Weedhopper differs due to the fact that it operates from land, its target customers are very similar.

Another big competitor is the *FlyNano*. The *FlyNano* is a relatively new aircraft and it also functions on water. It has a mass of 70 kg so no pilot licence is needed. This is closely related to the design at hand. However, it is not easily transportable and can only fly for 5 minutes. In addition, it costs €25,000. The *FlyNano* is still a prototype and might improve with time making them competition in the market that is less predictable.

Finally the *E-Lazair* has a hydro configuration and is electrical which greatly resembles the AerGo. Their sales figures are a good reference to determine the units that can be sold in 5 years.

[6] `http://www.pmaviation.co.uk/pegasus.html`, Retrieved: 22-11-2017
[7] `http://www.swedishaerosport.se/products/product/mosquito-nrg/`, Retrieved: 22-11-2017
[8] `http://www.ultralightnews.com/ssulbg/weedhopper-weedhopperaircaft/experimental_amateurbuilt.html`, Retrieved: 22-11-2017
[9] `http://www.jordanlakeaero.com/ultralight.html`, Retrieved: 22-11-2017
[10] `http://aeromarine-lsa.com/zigolo-mg/performance-specs/`, Retrieved: 22-11-2017
[11] `http://www.uflyit.com/aerolite_103_specifications.htm`, Retrieved: 22-11-2017
[12] `http://www.cgsaviation.com/cgs-hawk-arrow-kit-aircraft.html`, Retrieved: 22-11-2017
[13] `http://lazairinfo.com/lazair-series-1/`, Retrieved: 22-11-2017
[14] `http://lazairinfo.com/electric-lazair/`, Retrieved: 29-01-2018
[15] `http://www.beliteaircraft.com/wp-content/uploads/2016/01/Superlite_by_Belite_Ultralight_Review.pdf`, Retrieved: 22-11-2017
[16] `http://flynano.com/`, Retrieved: 22-11-2017

3.4 Market Size

In this section, the market size is evaluated. In order to quantify the market, research on ultralight aircraft in Europe is essential while considering the geographical opportunities of the country with respect to waterways. Looking at which countries with waterrich environments boast in ultralight aircraft help in determining where the product can gain most opportunity. The GAMA, General Aviation Manufacturing Association provides information on the amount of ultralight and microlight aircraft produced and registered since 2008[17]. Table 3.2 shows the amount of ultralight aircraft registered in selected European countries up until now. The selection is made mainly based upon data available. Figure 3.3 shows the relative market size of these countries compared to each other. It can be seen that Italy, France and the UK are large players in the ultralight aircraft market. Expanding to these countries potentially opens up a huge market for the *AerGo*. Zooming in on the rest shows that also in the Netherlands the market is of significant size.

Table 3.2: Amount of ultralights throughout Europe

Country	# of Ultralights
Netherlands	484
France	8778
Czech Republic	5843
Italy	12556
United Kingdom	4033
Belgium	417
Poland	216
Portugal	510
Finland	302
Lithuania	161
Slovenia	108
Total	33415

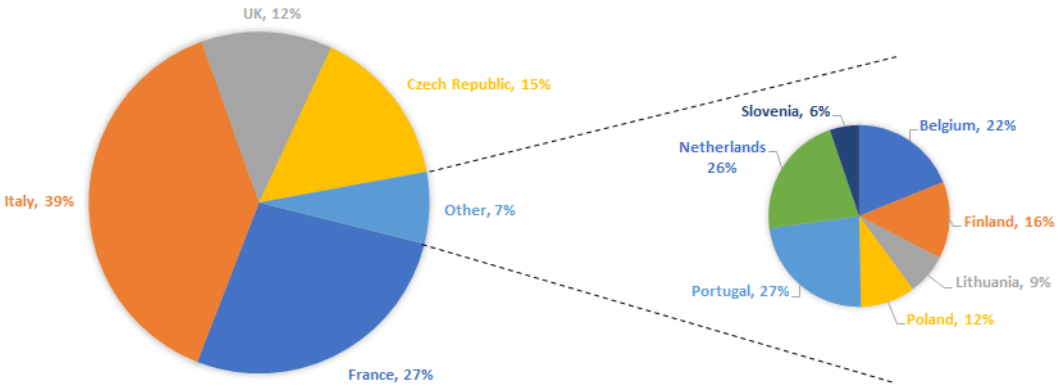

Figure 3.3: Percentage of ultralights in several countries in Europe

3.5 Market Opportunities

In this section the opportunities of the product will be determined and evaluated. Considering the market size there are several open spots in the market. In this chapter it is determined why these spots are open and if there is a opportunity to fill this. Potential spin-off markets are considered as well.

The opportunity the product will have in the market is the ability to launch from any water body and it is transportable by bike. There are other aircraft which are also transportable by bike such as hang gliders but hang gliders require a high point of land to be able to take-off. With the product at hand, it is possible to leave the house, put the aircraft in a trailer, attach it to a bicycle, ride to the nearest river and assemble it. From this point on get ready to take

[17] `https://gama.aero/wp-content/uploads/2016-GAMA-Databook_forWeb.pdf`, Retrieved: 20-01-2018

off and fly. There are little products in the market which can comply to this giving the design an edge and opening windows to new possibilities in flight, especially recreational flying.

Especially in the Netherlands, the opportunity is vast. This country boasts in cycling and water areas. In addition, rural areas are limited, so being able to transport the aircraft to the water and launch from water is ideal. But why limit the market to the Netherlands only? These opportunities hold for waterrich areas throughout all of Europe. Countries which were displayed in Figure 3.3 such as Italy, France, the United Kingdom, etc. have plenty of lakes and rivers where the the AerGo would be able to operate. This means a chance at expanding into the entire European market. Opportunities arise in different industries such as the surfing industry for example where lightweight materials for kites and sails are used. The bicycle industry is also attractive due to the opportunity of transporting the aircraft in a bicycle trailer. Since the *AerGo* is assembled with separate parts and needs different systems for operation, the influence of the surfing technology and bicycle trailers comes in convenient where parts can be bought and sold.

Figure 3.4 shows a SWOT analysis of the AerGo. For a more elaborate explanation on the statements can be referred to the market analysis in the baseline review [4]. It shows the strengths, weaknesses, opportunities and threats of the aircraft as a whole and concludes the market analysis.

INTERNAL FACTORS	
STRENGTHS (+)	**WEAKNESSES (–)**
- The aircraft is lightweight - 74% of the parts are recyclable - The hydroplane is transportable by bike - The aircraft is able to take off from water - The aircraft price is affordable - The aircraft requires minimal license - The design is silent - The design can be assembled and disassembled	- The aircraft can not take off from land - The aircraft is not operable during harsh weather conditions - Low customer awareness - The aircraft is unable to take off from rough water
EXTERNAL FACTORS	
OPPORTUNITIES (+)	**THREATS (–)**
- The Netherlands is a water-rich landscape with many take off opportunities. - Not many aircraft with the same characteristics - Able to use new technologies for water aircraft - Able to benefit from technologies coming from other industries - Large market for recreational flight	- Danger of pilot getting injured ruining the companies reputation - Large supply for recreational aircraft by leading companies - Change in regulations - Large competition by alternative recreational aircraft

Figure 3.4: SWOT analysis of the AerGo on the market

3.6 Conclusion and Recommendations

To conclude the market analysis it is desired to determine an estimation for the amount of aircraft that can be sold within a 5 year time span. Based upon the market size and competition it is easy to be ambitious on the number of units that can be sold. Narrowing it down to the Netherlands however reduces the opportunities. On average in the Netherlands 10 to 15 new ultralight aircraft are registered each year. Considering that in the start-up phase a large part of the production will be sold in the Netherlands it is chosen to be conservative and aimed for a sale of 20 units per year or 150 units within 7.5 years after the first sale. Leaving open the opportunity to expand through Europe very rapidly after the first production batch. Considering the same market growth[18] and with the assumption that 25% of the units will be sold on the Dutch market this would mean that 7.5 years after the product release the *AerGo* would have a market share of 7.5% and 0.6% on the ultralight aircraft market in the Netherlands and Europe respectively.

[18] `https://gama.aero/wp-content/uploads/2016-GAMA-Databook_forWeb.pdf`, Retrieved: 20-01-2018

4 Design Configuration

This chapter presents an overview of the final design of the *AerGo*. Section 4.1 presents the functional flow of the design, while the main design parameters are given in Section 4.2. Section 4.3 visualises the general layout with the help of three drawings: top-, side- and front view. Next, Section 4.4 includes several detailed Catia renderings to show how the *AerGo* will look in action. More details outlining the technical side of the project can be found in the chapters of the respective disciplines. A detailed power system layout can be found in Chapter 10. The layout of the control systems is described in Chapter 8, while the structural layout of the aircraft is explained in Chapter 9.

4.1 Functional Flow

This section bundles all the functions the design has to perform using a Functional Flow Diagram (FFD) and a Functional Breakdown Structure (FBS). The FFD shows the functions chronologically, where arrows indicate the order. The FBS follows a different approach, and shows the functions hierarchically, using an AND tree.

Figure 4.1 shows the top level of the FFD, while a detailed version can be found in Appendix B. These top level functions show the major tasks the user will perform during a regular mission. The mission starts by taking the aircraft out of the garage and transporting it to the take-off location. The next phase is the flight preparation, consisting of amongst others; assembly and putting the aircraft into the water. Once the aircraft has been assembled the user will take-off, which is followed by cruise flight. During the cruise phase, the user has the option to make an intermediate stop and land somewhere. This intermediate stop is represented by the turn-around phase, after which the user will once again be in cruise. After the cruise, the pilot will land the aircraft and go through the post-landing procedures, including disassembly and getting the aircraft out of the water. The mission is concluded with another transport phase, which includes storage and maintenance.

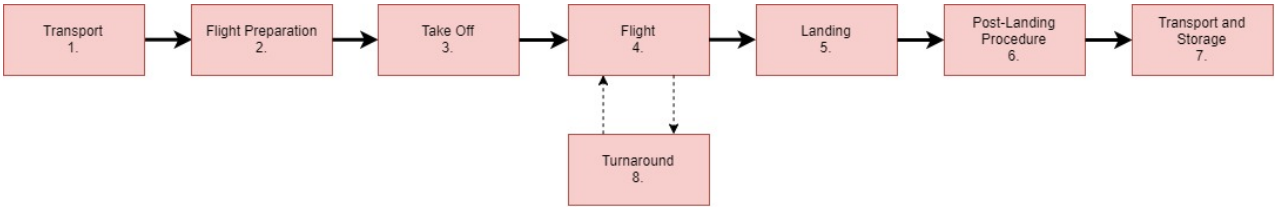

Figure 4.1: The Functional Flow Diagram for the *AerGo*.

The Functional Breakdown Structure is shown in Figure 4.2. This diagram starts with the Mission Need Statement (MNS), from which the four main functions of the aircraft are derived. The first being its ability to perform controlled, powered flight. Next to that, the aircraft has to operate from water. The third main function of the aircraft is that it should allow for personal use, meaning that one person can easily assemble, start and fly the aircraft. Finally, the aircraft should be durable, easy to use, require little maintenance, be compact, ecological and affordable.

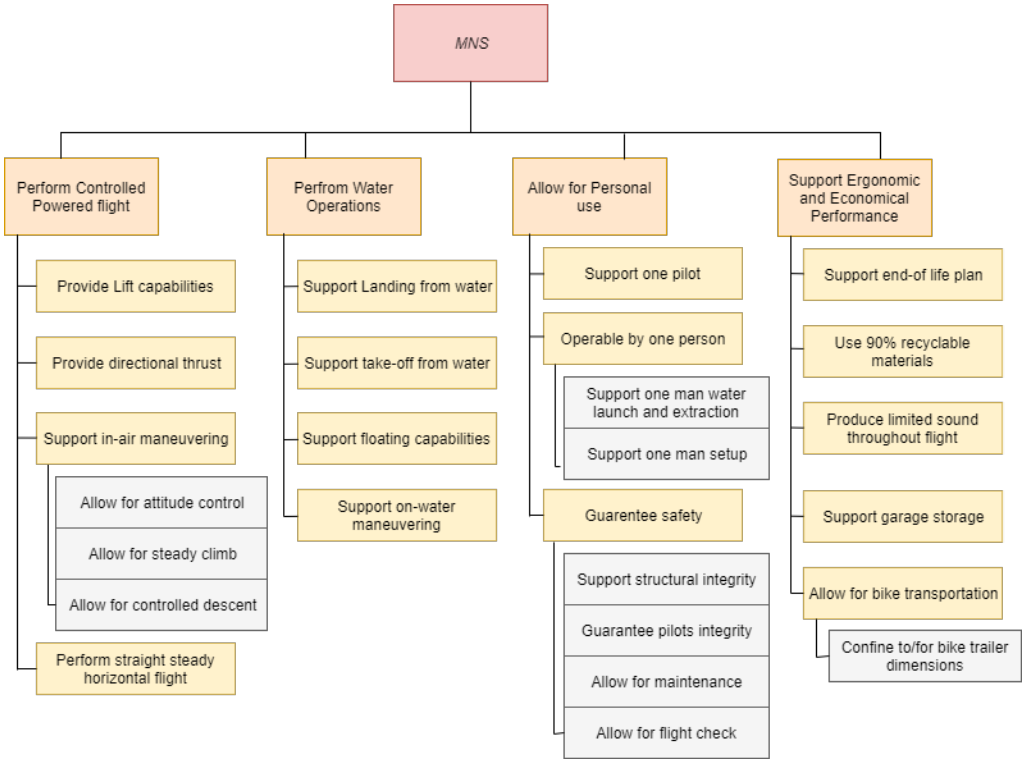

Figure 4.2: The Functional Breakdown Structure for the *AerGo*.

4.2 Design Parameters

Table 4.1 includes the main design parameters that define the performance, geometry and mass of the *AerGo*.

Table 4.1: Main design parameters of the *AerGo*.

Parameter	Value
Take-off speed $[m/s]$	9.9
Cruise speed $[m/s]$	15
Range (no wind) $[km]$	58.7
Range (with 10 kts headwind) $[km]$	40.2
Total cruise time $[hours]$	1
Wingspan $[m]$	12
Chord $[m]$	0.79
Wing area $[m^2]$	18.9
Sweep $[°]$	15
Dihedral $[°]$	5
Stagger $[m]$	0.45
Root gap $[m]$	1.31
Tip gap $[m]$	0.79
Maximum Take-Off Mass (MTOM) $[kg]$	144.66
Operational Empty Mass (OEM) (inc. batteries) $[kg]$	44.66
Battery mass $[kg]$	19.2
Maximum pilot mass $[kg]$	100

4.3 Layout Geometry

In this section the main layout of the design is shown. Figure 4.3 gives a topview of the *AerGo*, together with values for the defining geometrical parameters. The same is done for the sideview, Figure 4.5, and the frontview, Figure 4.4.

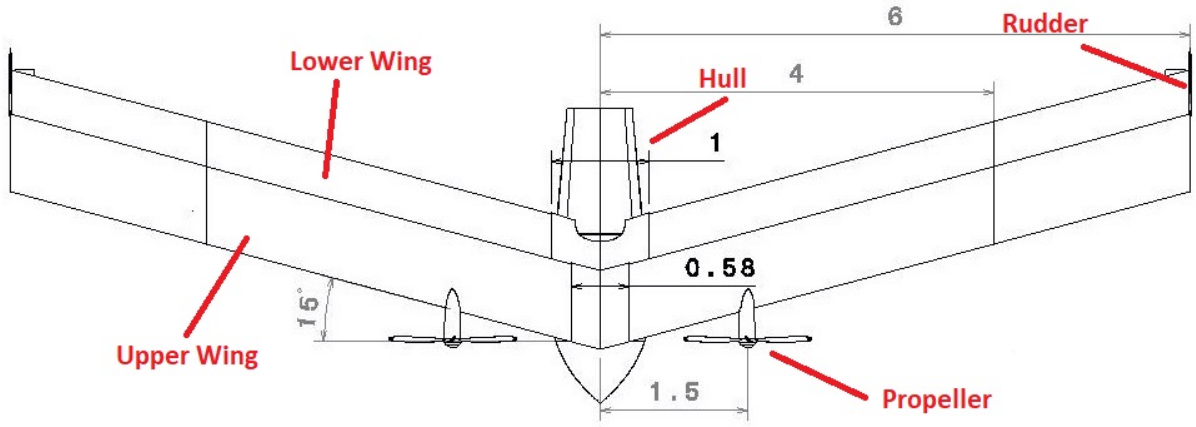

Figure 4.3: Topview of the *AerGo*

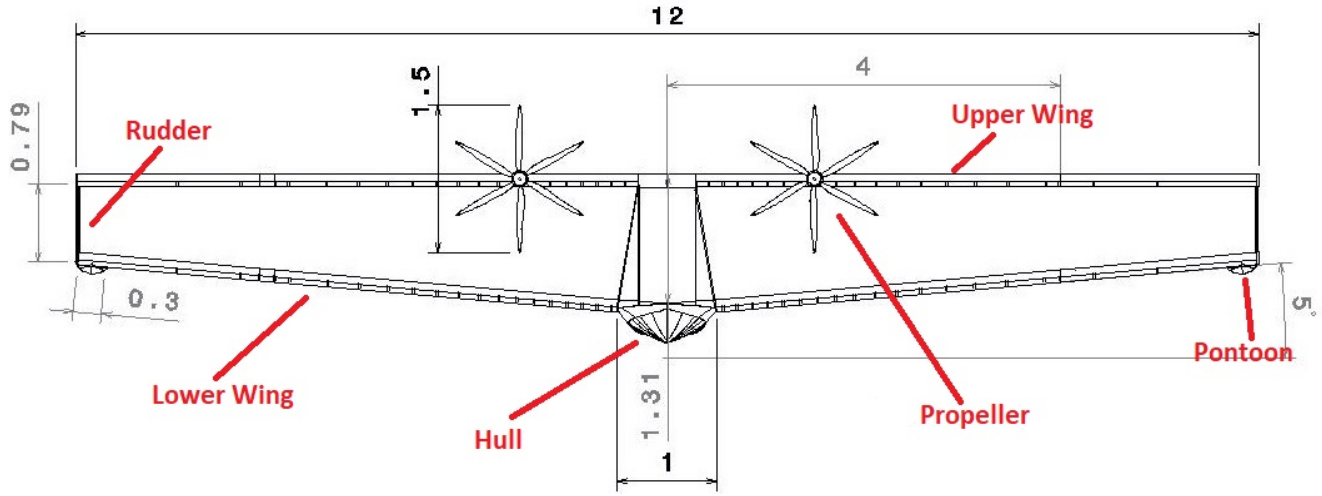

Figure 4.4: Frontview of the *AerGo*

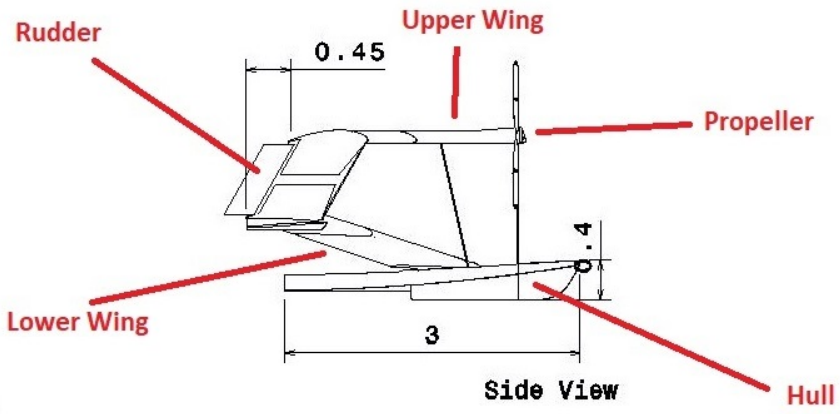

Figure 4.5: Sideview of the *AerGo*

4.4 Catia Renderings

Figure 4.6 shows the *AerGo* in different stages of the assembly, ranging from the bare hull/fuselage (Figure 4.6a) to the fully assembled design (Figure 4.6d).

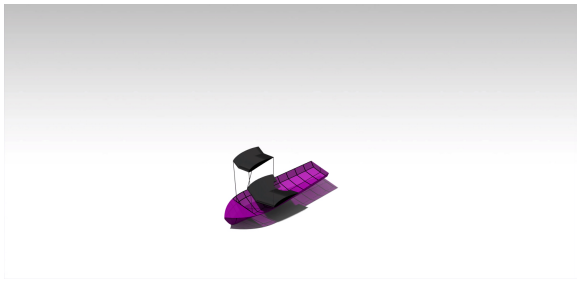

(a) 3D view of the hull and wing connectors.

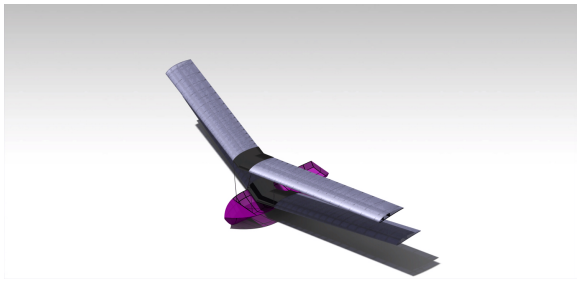

(b) 3D view after the main wing sections are attached.

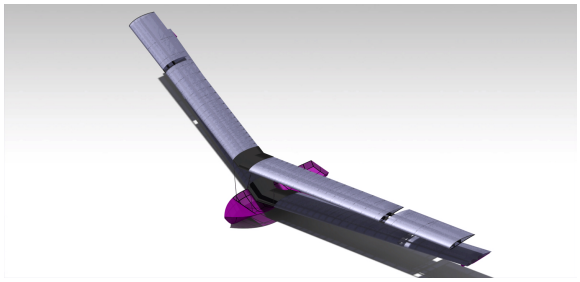

(c) 3D view after all wing sections are attached.

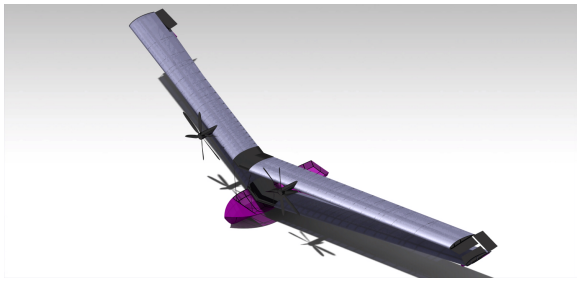

(d) 3D view of the fully assembled *AerGo*.

Figure 4.6: Renderings of the assembly process of the *AerGo*.

Figure 4.7: The *AerGo* in action.

4.5 Hardware Layout

Figure 4.8 gives a schematic overview of what hardware components are present and how they are connected. In order to visualise the flow between the components, two inputs are added although these are no actual hardware obviously, these inputs are given in yellow. First there is the pilot input, which asserts forces on the control sticks and throttle lever, but also the footboard. The second input is aerodynamic force on the wing and airfoils. These

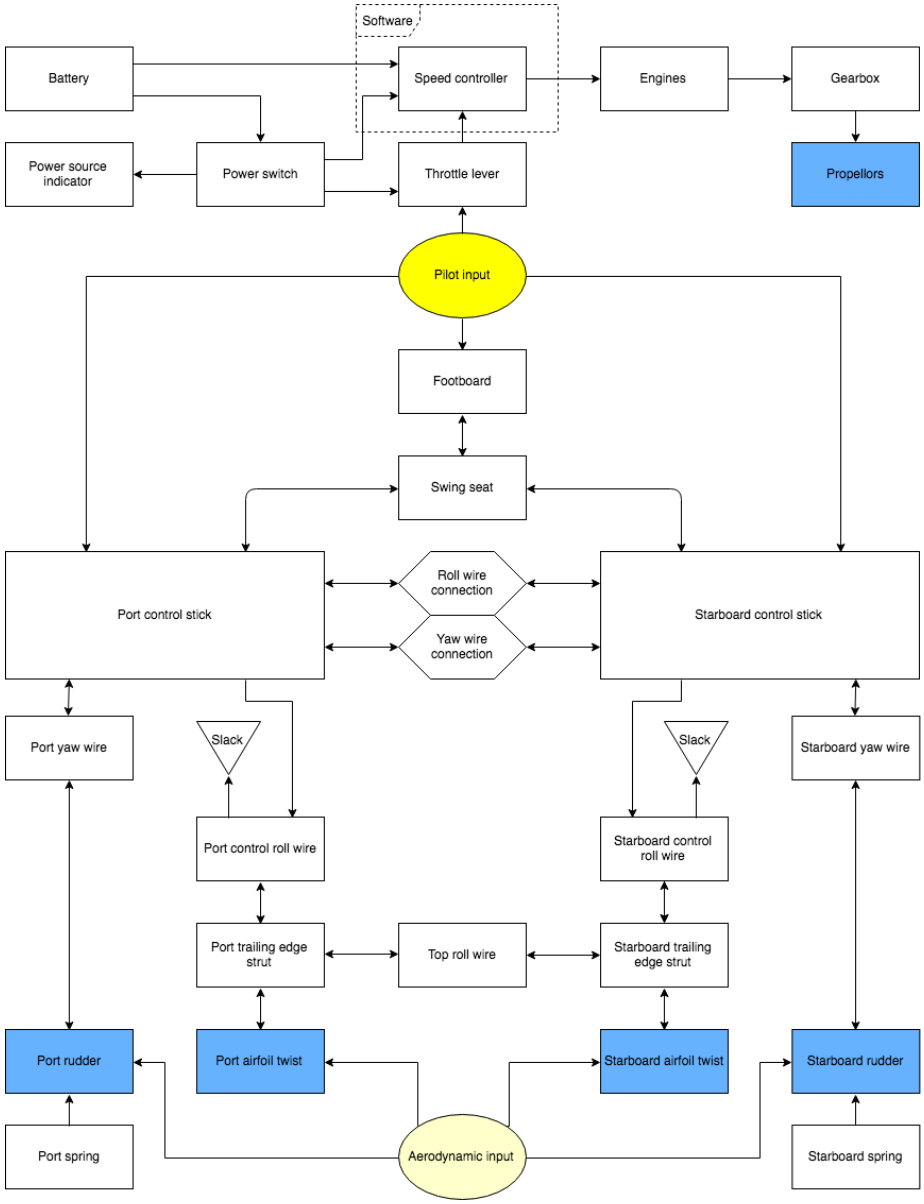

Figure 4.8: System hardware diagram

forces are added because they also work back through the struts and cables to the control sticks. (gust can be felt through the controls) The diagram is structured with the electrical system at the top and the mechanical system at the bottom. Only the speed controller uses some software, which relates the voltage output of the throttle control lever to voltages passed to the engines. A little amount of software was to be expected for this type of aircraft.

5 Requirement Compliance

In the Baseline Report [4], a summarising list of requirements was distilled from the laws, regulations and customer needs/wishes. This section shows the *AerGo*'s compliance with those requirements. In the case the requirement is not, or only partially met, an explanation as to why this is the case will be provided in Section 5.2.

5.1 Compliance Matrix

Table 5.1: The *AerGo*'s compliance with the requirements set.

Requirement	Description	Compliance
WFH-Sys-PP01	The aircraft shall be able to cruise for 30 min, including manoeuvring, climb and take-off.	✓
WFH-Sys-PP02	The aircraft shall have a range of at least 17 km.	✓
WFH-Sys-PP03	The aircraft shall meet the range requirement with a headwind of 10 kts	✓
WFH-Sys-PP04	The aircraft shall have a stall speed (V_s) in the range of 7.5 to 11 m/s.	✓
WFH-Sys-PP05	*The aircraft shall have a cruise speed (V_{cruise}) in the range of 15 to* 20 m/s. *(Note 1)*	✓
WFH-Sys-PP06	The maximum payload (including the pilot) shall not exceed 120 kg.	✓
WFH-Sys-PP07	The aircraft shall have a service ceiling of 1000 ft.	✓
WFH-Sys-PP08	The aircraft shall be able to perform a controlled and stable glide without using the propulsion system.	✓
WFH-Sys-PP09	The aircraft's take-off length shall be less than 200 m.	✓
WFH-Sys-PP10	The aircraft shall be able to perform a dead-stick landing without serious injury to the pilot.	✓
WFH-Sys-PP11	The maximum take-off mass shall not exceed 200 kg.	✓
WFH-Sys-PP12	The empty mass shall be in the range of 20 to 70 kg.	✓
WFH-Sys-PP13	The wing area shall be in the range of 10 to 25 m^2.	✓
WFH-Sys-PP14	The power shall be in the range of 10 to 20 kW.	✓
WFH-Sys-SC01	The aircraft shall be capable of straight, horizontal, steady flight.	✓
WFH-Sys-SC02	The aircraft shall be capable of controlling attitude.	✓
WFH-Sys-SC03	The aircraft shall be capable of a manoeuvring on a body of water.	✓
WFH-Sys-SC04	*The aircraft shall withstand relative gusts of up to 6 m/s. (Note 2)*	✓
WFH-Sys-SM01	The aircraft shall withstand an ultimate load factor of +6g and -3g.	✓
WFH-Sys-SM02	The aircraft shall withstand the landing loads, with a load factor of 2.33 .	✓
WFH-Sys-SM03	The aircraft shall be able to perform an emergency landing without serious injury to the pilot.	✓
WFH-Sys-SM04	The aircraft shall not be damaged by water.	✓
WFH-Sys-OP01	The aircraft shall be transportable by bike to and from the take-off and landing site.	✓
WFH-Sys-OP02	The aircraft shall be operable by one pilot.	✓
WFH-Sys-OP02 01	The aircraft shall be able to be set up by one person.	✓
WFH-Sys-OP02 02	The aircraft shall have an engine which is startable by one person.	✓
WFH-Sys-OP02 03	The aircraft shall be able to be manoeuvred in and out of the water by one person.	✓
WFH-Sys-OP02 04	The aircraft shall have instrumentation to allow a single person to safely operate the aircraft.	✓

WFH-Sys-OP03	The aircraft shall be storable in a garage that is 2.4 m wide, 5.8 m long and 2.1 m high.	✓
WFH-Sys-OP04	The aircraft shall be operable from a 20 m wide body of water.	✓
WFH-Sys-OP05	The aircraft shall have a wingspan below 12 m.	✓
WFH-Sys-BU01	The aircraft shall have a development time of maximum 5 years.	✓
WFH-Sys-BU02	*The maximum selling price of the aircraft shall be €20,000.(Note 3)*	✓
WFH-Sys-BU03	The aircraft shall have maximum operating cost of €50 per hour.	✓
WFH-Sys-LE01 01	The aircraft in transport configuration shall have a maximum weight of 80 kg.	✓
WFH-Sys-LE01 02	The aircraft in transport configuration shall have a maximum width of 1.5 m.	✓
WFH-Sys-LE01 03	The aircraft in transport configuration shall be equipped with 2 red rear reflectors.	✓
WFH-Sys-LE02	The pilot shall be able to operate the aircraft without a pilot license.	✓
WFH-Sys-LE02 01	The aircraft shall have a maximum weight of 70 kg, including power source [1].	✓
WFH-Sys-LE03 01	The aircraft shall comply with ANNEX II of the EASA Basic Regulations.	✓
WFH-Sys-LE03 02	The aircraft shall comply with the Dutch regulations regarding ultra light aircraft.	✓
WFH-Sys-SU01	Up to 90% of the aircraft's weight shall be recyclable.	×
WFH-Sys-SU02	End-of-Life Plans shall be specified for the aircraft.	✓
WFH-Sys-SU03	The noise of the aircraft shall not exceed 40 dB at 100m distance (=80dB @ 1m).	✓
WFH-Sys-SU04	The aircraft shall be designed in such a way that the CO_2 footprint is maximum 100 g/km per passenger.	✓

5.2 Notes on the Compliance Matrix

As can be seen from Table 5.1, two requirements are not met, while others are changed or require more explanation:
Note 1:

- Requirement **WFH-Sys-PP05** was changed on 12-01-2018 after consulting the client.
- Reasoning: Due to performance constraints, it is preferable to keep the cruise velocity as low as possible. However, safety issues due to wind gusts require the cruise speed to be at least 6 m/s above the stall speed. This resulted in an optimal cruise speed of 15 m/s or 29.2 kts, which is only barely outside the original range (30 to 40 kts). More information on the calculation of this optimal cruise speed can be found in Section 6.2.1.

Note 2:

- Requirement **WFH-Sys-SC04** was changed on 16-01-2018 after consulting the client.
- Reasoning: Before the change, absolute gusts of up to 5 Beaufort had to be taken into account. This meant that at an average windspeed of 0 m/s, sudden changes in windspeed of up to 10.7 m/s might occur. This affects several design parameters, but the most important one is the cruise speed. In the worst case scenario, this gust is coming from behind, effectively reducing the airspeed by 10.7 m/s. This means that unless the difference between the cruise speed and the stall speed is larger than this gust, the aircraft will stall and fall out of the air. The absolute gust of 5 Beaufort would drive the cruise speed up to an unreasonable value, making it impossible to meet several other requirements, eg. aircraft mass. Next to that, this requirement implies that at higher windspeeds the difference between the gust and the average windspeed becomes smaller. As this is not an accurate depiction of wind in The Netherlands, it was decided to modify the requirement to use relative gusts. With relative gusts the difference between the average windspeed and the maximum windspeed is meant. For example, with an average windspeed of 5.14 m/s (the maximum headwind for this design) and a sudden gust of 5 Beaufort, the relative gust is around 5.5 m/s. In order to translate the absolute gust of 5 Beaufort to a relative gust, wind statistics of the KNMI are used [(1)]. These statistics consist of measurements of

[(1)] `https://projects.knmi.nl/klimatologie/uurgegevens/selectie.cgi`, Retrieved: 07-12-2017

one hour each. Every measurement consists of the average windspeed and the maximum windspeed during the hour. Only measurements where the average windspeed is equal to or below the headwind specified in **WFH-Sys-PP03** are taken into account. Next, the relative gust for each measurement is calculated. With this data a plot is generated, showing the percentage of hours where the maximum relative gust is below a certain value. As can be seen in Figure 5.1, for more than 97 % of the measurements, the relative gust is 6 m/s or lower. Designing for this value gives a minimum cruise speed of 15 m/s. Although further increasing this value could increase the availability of the aircraft with almost 3 %, the increase in cruise speed would dramatically reduce the performance (more information in Section 6.2.1). Next to that, at an average wind of 10 kts, a relative gust of 6 m/s results in a maximum absolute gust of more than 5 Beaufort.

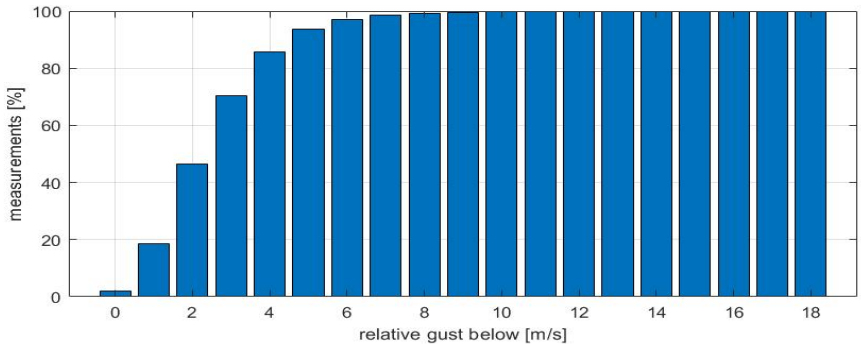

Figure 5.1: Graph showing the percentage of measurements where the maximum relative gust is below a certain value.

Note 3:

- Requirement **WFH-Sys-BU02** is met, however

Furthermore, requirement **WFH-Sys-BU02** is met according to the current cost model as described in Chapter 14. However this cost model could not be accurately verified and is still very sensitive to change. If mayor design changes are made or the market analysis appears to be inaccurate it is likely the cost budget is overshot and the sale price should be increased to €25,000 in order to have a return on investment after 12 years. At this point however, the sale price of €20,000 seems to be a reasonable price. A more thorough analysis on the cost budget must be performed during the next design phase in order to have a descend conclusion on the feasibility of this requirement.

6 Performance

Flight performance of an aircraft is one of the key features of the design, as it sets an outline for other technical disciplines and consequently drives the design. How well does the design perform with respect to it's requirements? This department has been closely in touch with mainly the Hydrodynamics, Aerodynamics and Propulsion department to design for the best performing overall aircraft, while remaining feasible for the Stability & Control and Structures & Materials department. This chapter contains the explanation of the entire performance analysis. The approach of the analysis will be elaborated in Section 6.1, the results in Section 6.2, verification and validation in Section 6.3 and finally conclusions and recommendations in Section 6.4.

6.1 Approach

When initialising the performance characteristics of the design, a desired maximum lift coefficient $C_{L_{max}}$ and the desired stall speed, V_S, were specified to determine the required wing loading. The former was an assumption based on reference data [5] while the latter was limited by the requirements given in Chapter 5. From the required wing loading and the desired maximum take-off weight, W_{to}, the required surface area S is determined. In turn, the aspect ratio of the wing is determined by the wingspan that came also from the requirements given in Chapter 5 and using the area. The values of the above mentioned parameters are listed in Table 6.1. Figure 6.1 contains a flowchart describing this process. Note that this flowchart is initialising the setup only, iteration was not performed in this stage of the design.

Table 6.1: Initial Performance Parameters

Parameter	**Value**
V_{stall} [m/s]	9
$C_{L_{max}}$ [-]	1.74
$\frac{W}{S}$ [N/m^2]	77.89
W_{TO} [N]	1450
S [m^2]	18.9
b [m]	12
A [-]	7.62
h_{scr} [m]	15.24

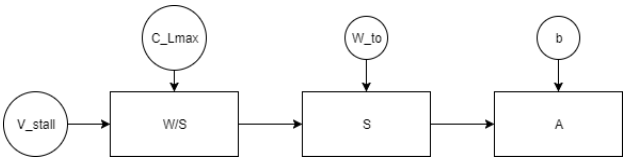

Figure 6.1: Flowchart initial performance setup

The aerodynamics department subsequently provided the lift and drag coefficients, which the performance department used to compute the required thrust, energy and power for all phases in the mission profile.
In order for the aircraft to stay within the noise limits, an electrical propulsion system was decided upon at an early stage of the design phase. In order to comply with all other requirements, a significant amount of energy would need to be carried, which significantly influenced the empty mass of the aircraft. When the aircraft became to look more and more like a flying battery, the required cruise speed was reconsidered. Initially, the cruise speed was brought down to 11 m/s and the stall speed was brought down to 9 m/s, to fly at the lowest power possible. However, this modification brought along a rather dangerous side effect; the cruise and the stall speed would be so close together, that the aircraft would be very prone to instantaneous stall due to wind gusts. In order to make up for this hazard, the cruise speed was increased to 15 m/s. Due to optimisation of other subsystems and finding a more energy efficient propulsion system, the operational empty mass could still be reduced by 10 kg.

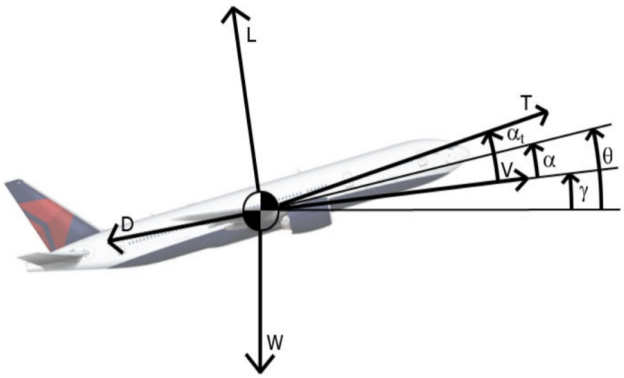

Figure 6.2: Free body diagram aircraft

The performance of the aircraft has been modelled using several different tools. In all of these tools, the performance requirements and constraints stated by the customer and other relevant stakeholders have been included. They will be mentioned in the subsections describing each flight phase if they are introduced in the analysis tools. After the setup of these tools, iteration was performed to aim for the best performance characteristics while staying within the boundaries of the requirements. The most prominent driving factor in this iteration was lowering the take-off mass as much as possible. A lower take-off mass provides a product that is more sustainable and more convenient to operate.
A number of general assumptions have been made during the performance analysis:

- Assumption: The density ρ is assumed to be constant and at sea-level. The reason behind this is that at low cruise altitude (< 200 m), which applies to this design, the density change is less than 1 %.
- Assumption: The power available from the propeller is assumed to be constant with airspeed and altitude [29].

6.2 Performance Analysis Results

During this performance analysis, the different flight phases have been analysed individually. The different flight phases are discussed in the mission profile in Chapter 2. In the next subsections, the analyses of these flight phases are discussed. Note that the taxi phase was not taken into account in this analysis. It is assumed that taxiing will be performed by using a paddle and is therefor not driven by the performance of the aircraft.

6.2.1 Cruise Performance

In this subsection, the performance during the cruise phase is analysed and explained. Referring to Chapter 5, this design should be able to meet the requirements during cruise as restated in Table 6.2.

Table 6.2: Requirements effecting the cruise performance

Requirement	Description
WFH-Sys-PP01	The aircraft shall be able to cruise for 30 min, including manoeuvring, climb and take-off.
WFH-Sys-PP02	The aircraft shall have a range of at least 17 km.
WFH-Sys-PP03	The aircraft shall meet the range requirement with a headwind of 10 kts
WFH-Sys-PP05	The aircraft shall have a cruise speed (V_{cruise}) in the range of 30 to 40 kts.

These requirements are interconnected. The goal of this cruise performance analysis is to have a safe and stable cruise speed with minimal battery mass while still being able to meet the requirements stated above. To understand how the cruise speed affects the aircrafts performance, the governing equations are investigated. This allows to get a understanding of how the cruise speed requirement will affect the design. Referring to Figure 6.2, the equations of motion can be set up for this aircraft. Here, the assumption is made that the thrust angle α_t and the angle of attack α are relatively small to the flight path angle γ. With these two assumptions, the equations of motion can be set up by doing a force analysis parallel and perpendicular to the wind speed vector V:

$$\frac{W}{g}\frac{dV}{dt} = T - D - W\sin(\gamma) \qquad \frac{W}{g}V\frac{d\gamma}{dt} = L - W\cos(\gamma) \tag{6.1}$$

These are the governing equations during the cruise phase of any aircraft. During cruise, the aircraft will usually perform a steady and horizontal flight. The former means that there is no acceleration along the wind speed vector: $\frac{dV}{dt} = 0$. A horizontal flight means that there is no centrifugal acceleration or equivalently, that there is no change in flight path angle (γ) over time: $\frac{d\gamma}{dt} = 0$. Lastly, it is assumed that the flight path angle is very small during the cruise phase. This has the implication that $\cos(\gamma) \approx 1$ and $\sin(\gamma) \approx 0$. Using the two flight conditions and the aforementioned assumption, Equation (6.1) reduces to:

$$T = D \qquad L = W \tag{6.2}$$

Where T is the thrust, D is the drag, L is the lift and W is the weight respectively. Furthermore, the Lift and Drag during cruise can be expressed as:

$$L = \frac{1}{2}\rho {V_c}^2 \cdot S \cdot C_L \qquad D = \frac{1}{2}\rho {V_c}^2 \cdot S \cdot C_D \tag{6.3}$$

Where ρ is the density at cruise altitude, S is the wing area, C_L is the lift coefficient and C_D is the drag coefficient respectively. In turn the latter two coefficient are related through the drag polar:

$$C_D = C_{D0} + \frac{{C_L}^2}{\sqrt{\pi Ae}} \tag{6.4}$$

Where C_{D0} is the zero-lift-drag coefficient, A is the aspect ratio and e is the Oswald factor respectively. Combining Equation (6.2) and Equation (6.3), the lift coefficient can be expressed as:

$$C_L = \frac{W}{S}\frac{2}{\rho}\frac{1}{{V_c}^2} \tag{6.5}$$

In turn, Equation (6.5) can be used in Equation (6.4) to express the drag coefficient as a function of the airspeed. Combining then this equation with Equation (6.3) gives the final relation of the drag as a function of the airspeed:

$$D = \frac{1}{2}\rho S C_{D0} \cdot {V_c}^2 + \frac{W^2}{S}\frac{2}{\rho}\frac{1}{\sqrt{\pi Ae}} \cdot \frac{1}{{V_c}^2} \tag{6.6}$$

This equation can also be written in the form:

$$D = k_1 \cdot {V_c}^2 + k_2 \cdot \frac{1}{{V_c}^2} \tag{6.7}$$

Where $k_1 = \frac{1}{2}\rho S C_{D0}$ and $k_2 = \frac{2W^2}{S\rho\sqrt{\pi Ae}}$. Equation (6.7) holds an important and remarkable result. It shows that for an aircraft, one part of the drag increases with the airspeed squared while the other part decreases with the airspeed squared. The term $k_1 \cdot {V_c}^2$ is also called the profile drag D_0 while the term $k_2 \cdot \frac{1}{{V_c}^2}$ can be denoted by the lift-induced-drag D_i. By setting the parameters as depicted in Table 6.1, the drag vs airspeed curve can be plotted. This curve is showed in Figure 6.3. An important point in this graph is the airspeed for minimal drag. With the design parameters from table, the airspeed for minimal drag $V_{D_{min}}$ is 11.13 m/s.

Evidently, this is well below the lowest limit of the cruise speed requirement given at the beginning of this section. However, as mentioned before, the second requirement also determines the optimal speed during the cruise phase. Referring to Equation (6.2) and multiplying both sides with the airspeed:

$$\begin{aligned} T \cdot v &= D \cdot v \\ P_a &= P_r \end{aligned} \tag{6.8}$$

Where P_a denotes the power available and P_r denotes the power required. Combining Equation (6.7) and Equation (6.8), the power required can be expressed in terms of the cruise speed:

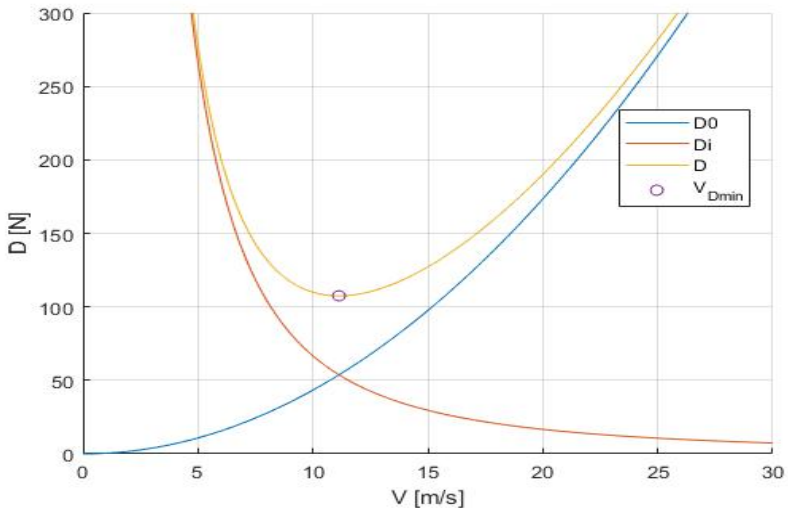

Figure 6.3: Drag vs airspeed curves

$$P_r = k_1 \cdot {V_c}^3 + k_2 \cdot \frac{1}{V_c} \tag{6.9}$$

This relation is shown in Figure 6.4. Equation (6.9) is another important result. The energy required for cruise is directly proportional to the power required. An electrical propulsion system will be used, as explained in Chapter 10. Consequently, for the same type of batteries, the battery mass is in turn proportional to the power required. In conclusion, to minimise the battery mass, the airspeed should be such that the power required is minimum. Referring to Figure 6.4, the airspeed for minimal power required $V_{P_{r_{min}}}$ is 8.46 m/s.

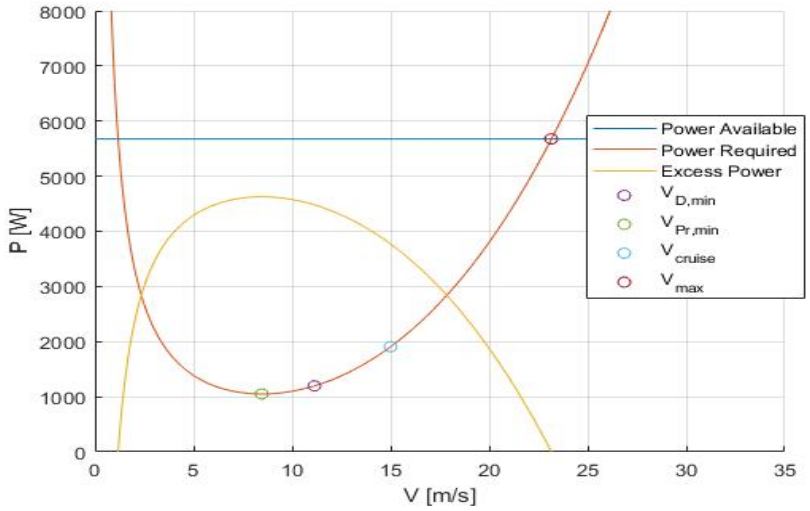

Figure 6.4: Power vs airspeed curves

As stated in the beginning of this subsection, the cruise speed shall provide a safe and stable flight. To protect the aircraft from stalling during cruise when there is a tail wind gust, the cruise speed should be such that the difference with the stall speed is larger than the wind gust speed that is designed for. The requirement on the wind gusts is explained in Table 5.1 in Chapter 5. Section 5.2 states that the wind gust speed for which should be designed is 6 m/s:

$$V_c - V_s \geq 6\,\text{m/s} \tag{6.10}$$

The stall speed was given at the beginning of this chapter and was set at 9 m/s (Table 6.1). Therefore, the minimal value for the cruise speed is given by Equation (6.10) and is thus 15 m/s. This value is outside of the cruise speed range given by the requirement given at the beginning of this subsection. However, to also minimise the battery mass the cruise speed is set at 15 m/s. After a consult with the client, the client agreed with setting the cruise speed to 15 m/s. With the stall speed and the cruise speed, the limits of this aircrafts performance can be determined. These limits will be shown in what is so called a flight envelope. This diagram shows certain limits on the speed and at what load factor these speeds are attained. Requirement **WFH-Sys-SM01** states that the aircraft shall withstand an ultimate load factor of +6 and -3 g. However, this requirement is solely used in the structure design as explained in Chapter 9. In terms of performance, the load factor is used to determine the maximum bank angle that can be achieved while maintaining a steady turn. The bank angle is the angle at which the aircraft is inclined about its longitudinal axis with respect to the horizontal axis (the angle between the wing and the horizontal axis).

The relationship between load factor and bank angle is given by:

$$n = \frac{1}{\cos \mu} \tag{6.11}$$

Where n is the load factor and μ is the bank angle in degrees. This relationship is plotted in Figure 6.5.

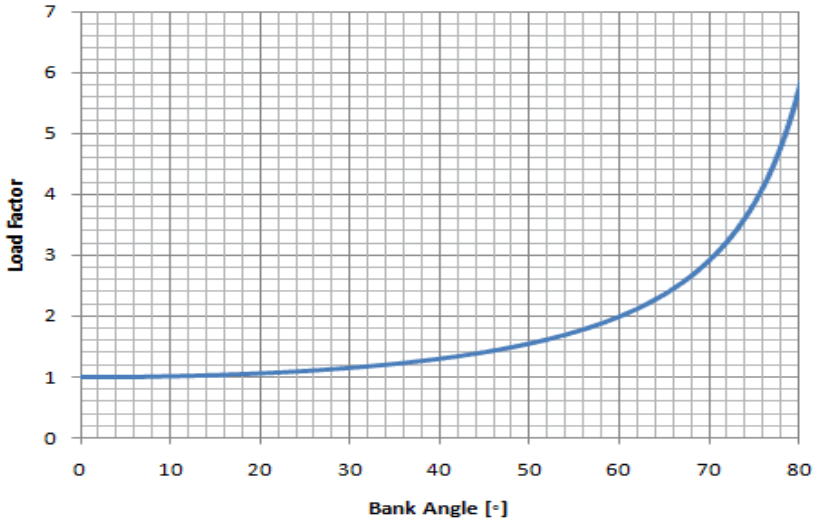

Figure 6.5: Relationship between load factor and bank angle

For a coordinated, constant altitude turn, the approximate maximum bank for the average general aviation airplane is 60° [(1)]. This is a bank angle that will be outside of practical operating bank angles, which is expected to be more in the range of 15–45°. Nevertheless, this bank angle (and the corresponding load factor) should be accounted for in the performance analysis.

The maximum corresponding positive load factor is $n = 2$ for a bank angle of $\mu = 60°$. In turn, a maximum negative load factor of $n = -1$ will be accounted for. This corresponds to an aircraft being inverted [(2)]. Now the flight envelope diagram can be constructed. This is shown in Figure 6.6. The flight envelope indicates the limit on the speed for the range of the load factor n. Several speeds are depicted in the flight envelope. Besides the stall speed V_S there is the maneuver speed V_A for which the limit load factor is reached when flying at C_{Lmax}. The maneuver speed is equal to $V_A = V_S\sqrt{n_{cruise}} = 9 \cdot \sqrt{2} = 12.73$ m/s. Secondly, V_B denotes the high alpha speed which has to be larger than than V_A but lower than the cruise speed V_C. In this case $V_B = 14$ m/s but it can be any value as long as it is between V_A and V_C. Lastly, the dive speed is denoted by V_D. This is the maximum speed at which the aircraft can fly during a dive flight. This speed should be the greater than $V_D = 1.5 \cdot V_A = 19.1$ m/s, according to several ultralight aircraft manufactures [7]. Consequently, the dive speed is set at $V_D = 20$ m/s.

[(1)] `http://www.free-online-private-pilot-ground-school.com/Load_factors.html`,Retrieved: 29-01-2018
[(2)] `http://www.free-online-private-pilot-ground-school.com/Load_factors.html`,Retrieved: 29-01-2018

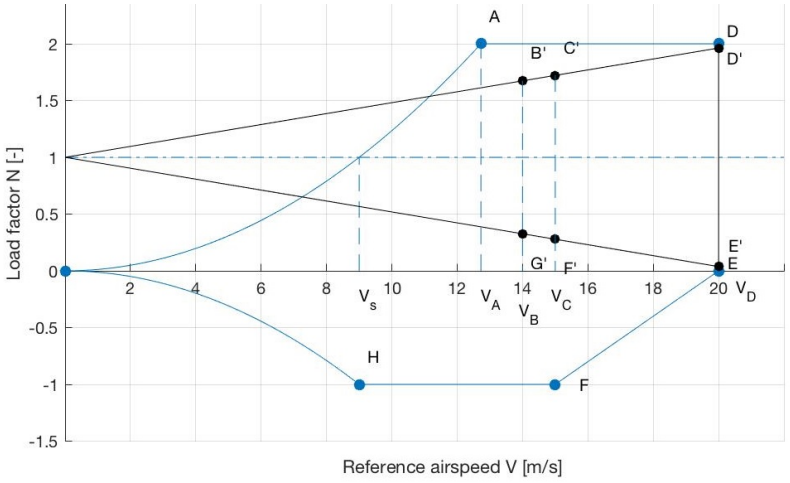

Figure 6.6: Flight envelope

6.2.2 Take-off Performance

The take-off phase only has to answer to three take-off requirements as restated in Table 6.3, where WFH-Sys-OP04 is the one that actually determines that the *AerGo* has to take-of from water.

Requirement	Description
WFH-Sys-PP04	The aircraft shall have a take-off speed (V_{TO}) in the range of 15 to 20 kts.
WFH-Sys-PP09	The aircraft's take-off length shall be less than 200 m.
WFH-Sys-OP04	The aircraft shall be operable from a 20 m wide body of water.

Table 6.3: Requirements effecting the take-off performance

The take-off phase was modelled as a dynamic process. The aircraft is required to accelerate to the take-off speed of 9.9 m/s, which has been decided to be 10 % higher than the stall speed [27]. The acceleration of the aircraft depends on the resultant force acting on the aircraft. The resultant force is the summation of all forces acting on the aircraft; the aerodynamic drag, the hydrodynamic drag and the thrust. The free body diagram and the kinetic diagram describing the forces during the take-off phase are visualised in Figure 6.7a and Figure 6.7b.

(a) Free Body Diagram at Take-off

(b) Kinetic Diagram Take-off

Figure 6.7: Free body and kinetic diagrams during take-off

From these two diagrams, a dynamic equilibrium equation can be set up from Newton's 2nd Law:

$$F = m \cdot a(V) = T(V) - D_{ae}(V) - D_{hd}(V) \tag{6.12}$$

F represents the resultant force acting on the aircraft, while m is the constant mass, a is the acceleration, T is the thrust provided by the propulsion system and D_{ae} and D_{hd} represent the aerodynamic drag and the hydrodynamic drag. The latter 4 parameters are a function of the velocity V.
The aerodynamic drag increases with airspeed and is determined by the following relation:

$$D_{ae} = C_D \frac{1}{2} \rho V^2 S \tag{6.13}$$

C_D is the total drag coefficient during take-off, while ρ is the air density and S is the surface area of the wing.
The hydrodynamic drag follows from the design of the floating system, as described in Chapter 11. The development of the hydrodynamic drag with respect to the velocity is also discussed in this chapter. The thrust provided by the propeller is not constant with airspeed. The propeller thrust decreases as the airspeed picks up if the power of the propeller remains constant. More on the propeller performance is discussed in Chapter 10.

To visualise, the forces have been plotted with respect to the airspeed in Figure 6.8. Note that ground effect is not yet taken into account in this analysis. In general, the ground effect increases the lift and reduces the drag during the take-off phase, implying a better outcome in terms of power required to take-off.

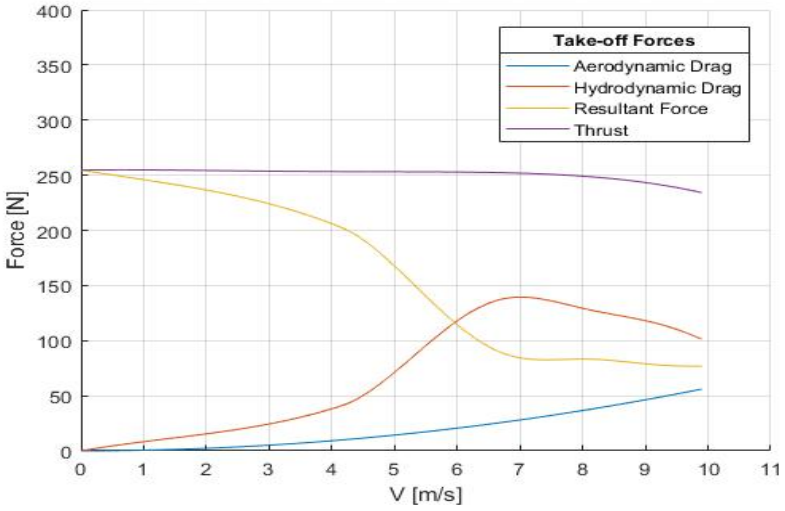

Figure 6.8: Take-off Forces

In order to ensure liftoff, enough resultant force should be provided to accelerate the aircraft up to the take-off speed of 9.9 m/s. The distance needed to accelerate to the take-off speed was found to be 63.5 m. It has been decided that the power for the ground run should be equal to the power of the airborne take-off phase. This way, during the entire take off phase, the pilot does not have to adjust the power settings which ensures an efficient and convenient take-off. In this manner, both hands can be used for control and adjusting the aircraft path during the take-off phase. The rate of climb that can be achieved is found to be 1.43 m/s, which causes the aircraft to reach it's screen height in 170 m. This is well within the maximum allowed take-off distance of 200 m. More about rate of climb is discussed in the next section.

6.2.3 Climb Performance

The aircraft is required to have a service ceiling of 1000 ft or 304.8 m. The service ceiling is defined as the altitude at which an aircraft can still achieve the required climb rate. No requirements on minimum climb performance have been found in regulations for ultralight aircraft, so the service ceiling is considered to be the same as the absolute ceiling of the aircraft, which is the theoretical altitude that an aircraft can reach at a certain airspeed. The climb rate R/C of an aircraft depends on three parameters; the Power Available P_a, Power Required P_r and the maximum takeoff weight W_{TO}. [28].

$$R/C = (P_a - Pr)/W_{to} \tag{6.14}$$

The available power is dependent on the available thrust and the airspeed while the required power is dependent on the drag at a certain airspeed. The 'excess power' P_e is the difference between power available and power required, which is necessary to be able to climb. During climb, the same engine setting will be used as during take-off, the corresponding climb rate is equal to 1.4 m/s.

Figure 6.9 describes how the maximum climb rate of the *AerGo* relates to the altitude. Note that the maximum climb rate is different from the design climb rate. The maximum climb rate is the climb rate that is achieved when using the propulsion system at full power.

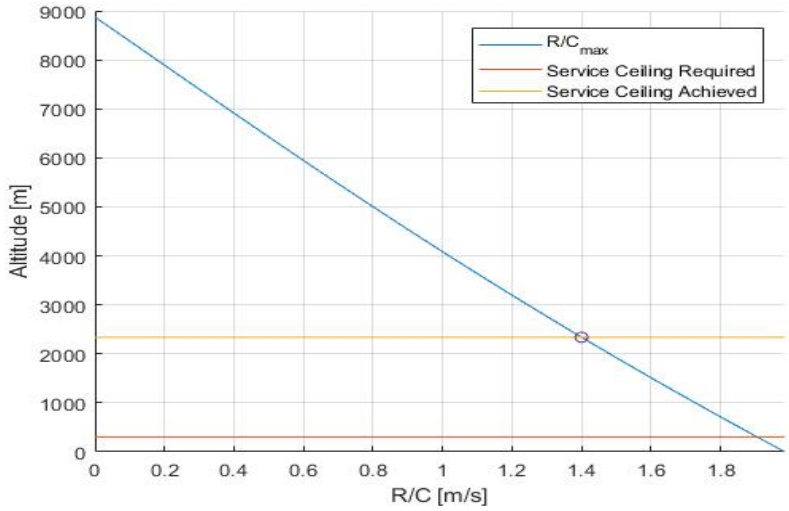

Figure 6.9: Service Ceiling

The rate of climb decreases with altitude because of two contributing factors; the propeller efficiency and the decreased air density. When a higher altitude is reached, the air density decreases, which causes the propeller to produce less thrust at the same airspeed and to perform at a lower efficiency. The decreased thrust at this altitude limits the climb possibilities of the aircraft in such a way that eventually, the aircraft needs to use 100 % of the available thrust to maintain a certain horizontal velocity. The service ceiling is described as the altitude at which the aircraft can still operate at the design rate of climb of 1.4 m/s. The absolute ceiling is generally higher as this is the theoretical maximum altitude an aircraft can achieve. It is clear that the service ceiling of the design is computed at 2338 m (7671 ft), much higher than the required 1000 ft. is rather high with almost 9000 m. It is suspected that this is caused by the fact the design uses an electrical engine. Combustion engines impose an additional decrease in engine efficiency at higher altitudes. For the electrical engines used in this design, it is assumed that the efficiency does not drop with increasing altitude.

6.2.4 Descent Performance

During the descent the equations of motion as given in Equation (6.2) and Equation (6.16) are once again evaluated. The descent phase is assumed to be steady, i.e. there is no acceleration along the speed vector ($\frac{dV}{dt} = 0$). Moreover, there is no change in flight path angle over time ($\frac{d\gamma}{dt} = 0$). However, the flight path angle (γ) is not small enough to assume $\sin(\gamma) = 0$ but it is small enough to assume $\cos(\gamma) = 1$ since the angle will not exceed 10°. Therefore, the equations of motion during the descent phase reduce to:

$$\frac{T-D}{W} = sin(\gamma) \tag{6.15}$$

$$L = W \tag{6.16}$$

Then multiplying Equation (6.15) with the airspeed gives the relation:

$$\frac{TV-DV}{W} = Vsin(\gamma)$$
$$\frac{P_a-P_r}{W} = Vsin(\gamma)$$

For the descent phase it is more convenient to denote the descent angle γ_d. The descent angle is the reciprocal of the flight path angle: $\gamma_d = -\gamma$. Using the descent angle, Equation (6.17) can be written as:

$$\frac{P_r-P_a}{W} = Vsin(\gamma_d) = RD = \frac{dh}{dt} \tag{6.17}$$

Where RD is the rate of descent, h is the height and t is the time. The intended descent phase will be performed by remaining at cruise speed while shifting the weight slightly forward to enter a steady and controlled descent that

is as safe as possible while maintaining the gust margin as given by Equation (6.10). To achieve this, a descent angle of 3° is used which is a considered to be a safe and controlled descent [29]. The corresponding rate of descent is equal to an RD value of 0.8 m/s. It must be noted that this RD is a conservative value and it can be increased according to the pilots wish. However, it must be noted that the descent angle can never exceed 15° [27] since else the pilot would accelerate too much and would not be able to pull the aircraft in order to level again by weight shifting. As can be seen from the flight envelope in Figure 6.6 the maximum dive speed is 20 m/s. Together with a maximum descent angle of 15°, the critical RD would be: $RD = V \sin\gamma_d = 20\sin(15°) = 5.18\,\text{m/s}$. An overview of the aircrafts descent configuration is given in Table 6.4.

Table 6.4: Controlled descent phase of the *AerGo*

Parameter	Value
γ_d [°]	3°
RD [m/s]	0.8
C_L [-]	0.573
C_D [-]	0.045

6.2.5 Landing

The landing phase begins when the screen height is reached. At this point, the power delivered by the engines will be changed such that the power produced by the propeller equals the power required for the take-off and landing speed of 9.9 m/s. The power required by the propeller is given by the following equation:

$$P_r = D_l \cdot V_l = C_D \frac{1}{2} \rho V_l^2 S \tag{6.18}$$

During the landing phase, the pitch will be such that lift coefficient is equal to 1.3. This provides a drag coefficient of 0.0973. Filling in the other parameters provides a required power of 1093 W.

6.3 Verification and Validation

For verification and validation, a comparison was performed between a numerical model in MATLAB and an analytical model in EXCEL used in the performance analysis. The output values of the models were the thrust and the power required for take-off and for cruise. The results are listed in Table 6.5.

Table 6.5: Verification of Performance Model

Parameter	Analytical	Numerical	Error
Pr_{cruise} [W]	1810 W	1810 W	3.4%
$Pr_{takeoff}$ [W]	2597 W	2340 W	11%
T_{cruise} [N]	122 N	122 N	0%
$T_{Takeoff}$ [N]	262 N	240 N	8%

The only differences higher than 1% that have been distinguished were the thrust and power required during take-off. This error is due to different assumptions in both models. The numerical model prescribes a dynamic process in take-off with varying forces with respect to the velocity. It also computes the power required for different airspeeds. The analytical model takes a constant value on the higher end for all of these forces during the entire ground run, and therefor overestimate the required power and required thrust.
Validation of the performance of the aircraft is performed by inserting the specifications of the final design into the design area plot from the midterm report [5]. The design area is visible in Figure 6.10 and it can be concluded that the power loading is rather low compared to reference aircraft. This however can be explained by the fact that it is an intended design choice to aim for the lowest possible power (thus lowest flight speed possible) while staying within acceptable safety margins in terms of wind gusts.

As a second validation method. The performance characteristics were compared to the performance characteristics of the UMF Easy Riser. The results are listed in Table 6.6.

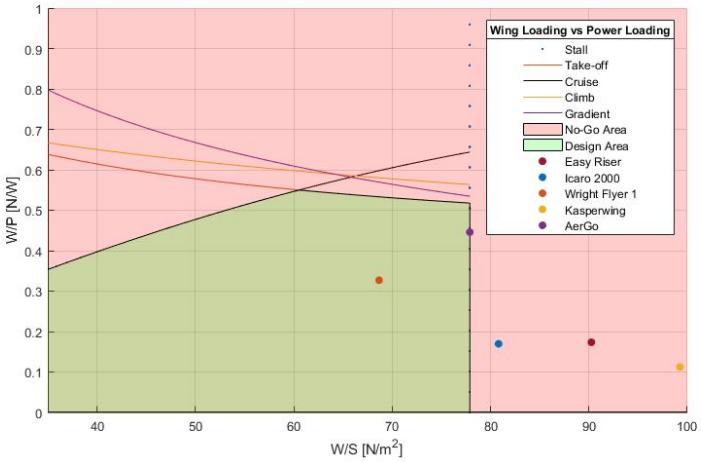

Figure 6.10: Design Area Validation

Table 6.6: Validation comparison Easy Riser

Parameter	AerGo	Easy Riser	Error
Maximum Speed [m/s]	23	18	- 28%
Cruise Speed [m/s]	15	11	- 33%
Stall Speed [m/s]	9.0	8.7	- 3%
Range [km]	20	161	+ 88 %
Service Ceiling [m]	2238	2743	+ 23%
Rate of Climb [m/s]	1.4	1.5	+ 7%

The main differences between the *AerGo* and the *Easy Riser* in terms of performance is the range. This is most likely due to the fact that the Easy Riser makes use of combustion propulsion, which allows a much larger range. The Easy Riser also contains a much smaller offset between the cruise speed and the stall speed. This is probably caused by the fact that the Easy Riser was operated in the United States continental climate conditions where wind gusts are much less common and severe.

6.4 Conclusions and Recommendations

In terms of performance, the aircraft was bound to a number of challenging requirements. The driving factor during the design phase was to aim for an OEW as low as possible. Strict requirements regarding cruise speed, range, endurance, noise and headwinds caused a complicated interference.

A number of modifications can be considered to improve the the performance of the aircraft. The first modification recommended is to further investigate the take-off phase of the aircraft. In the performed analysis, two factors have not been taken into account; the ground effect and stall behaviour after liftoff. Currently, the aircraft experiences lift-off at 99m/s. It is advised to include an additional acceleration after liftoff to the cruise velocity before starting to climb to the screen height. If an aircraft operates close to the water surface, it will encounter increased lift and decreased drag, i.e. the ground effect [(3)], making it less sensitive to stall and more efficient in acceleration. This increase in velocity would increase the safety of the aircraft with respect to wind gusts in flight phases other than cruise. For the additional acceleration, an higher power setting would be required from the propulsion system to meet the required take-off length of 200 m. An initial redesign has been performed to check whether this is feasible. For the current design configuration. Redundancy is present in the propulsion system, so it is expected that with the current design, this would not impose major problems. A higher power setting during take-off would reduce the length of the ground run, reduce the distance to accelerate to cruise speed and increase the climb rate to decrease the distance required to make the screen height.

Also, it is advised to look into combustion engine as a propulsion system in favour of electrical. This is expected to increase the range and endurance of the aircraft, if this is required for future purposes. Combustion is however

[(3)] `https://en.wikipedia.org/wiki/Ground_effect_(aerodynamics)`

expected to increase the total noise of the aircraft, a proper estimation on combustion engine noise levels should be conducted. Otherwise, the design could be optimised for more lightweight pilots. The payload range diagram in Figure 6.11, shows the increase of range with respect to a decrease of payload (mostly pilot) mass. However, the decrease of units sold due to a smaller target audience should be considered before deciding on a different payload mass. The current range of the aircraft in worst case conditions (10 kts headwind outbound and inbound would be equal to 18.85 km. In this analysis, the distance over ground travelled in other flight phases than cruise have also been taken into account.

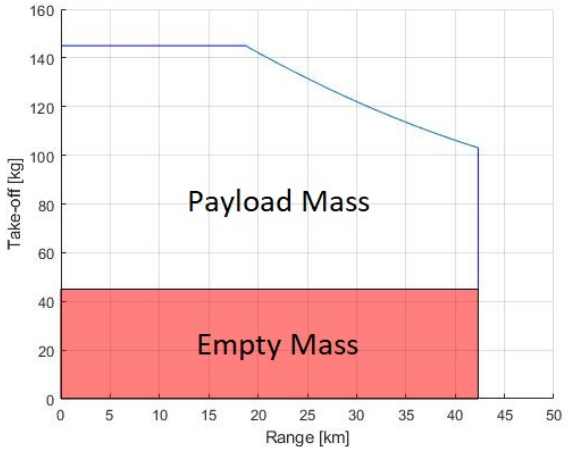

Figure 6.11: Payload-Range Diagram

Another feature that is improved by a reduction of mass is the endurance of the aircraft. Currently, the *AerGo* is designed for an endurance is to 60 minutes of cruise time, on a single charge of batteries. The theoretical endurance could be much higher when flying at lower speed and lower power. But because of hazardous gusts, flying at a lower speed than the cruise speed is not recommended. Furthermore, the pilot should not exceed a descent angle of 15°, as this is potentially not recoverable by weight shifting. Finally, the user of the aircraft should be cautious before flight and during flight. Checking weather conditions is a necessity before taking the aircraft out for a flight.

Finally, a performance analysis on the taxi phase could be considered as the use of differential thrust could be convenient in during taxi and docking of the aircraft.

Table 6.7: Initial Performance Parameters

Parameter	**Value**
$T_{r,TO}$ [m/s]	9.9
T_{r_c} [-]	1.74
$P_{r,TO}$ [m/s]	9.9
P_{r_c} [-]	1.74
S [m^2]	18.9
A [-]	7.62

7 Aerodynamics

In this chapter an analysis of the aerodynamics of the *AerGo* is conducted. An insight to the steps taken to complete this process is elaborated. Section 7.1 explains the approach used to begin the analyis, Section 7.2 gives a detailed overview of the analysis on the lift and drag capabilities of the aircraft. Furthermore Section 7.3 shows the verification and validation (V&V) of the methods used. Finally, Section 7.4 provides a conclusion to the analysis along with recommendations.

7.1 Approach

To begin the aerodynamic analysis, the wing configuration must be decided upon. Once this is established the wing loading is provided by the performance group and it is possible to set a design lift coefficient $C_{L_{des}}$ that drives the choices in this section. With this, an airfoil selection will be made which then provides all the 2D drag and lift elements. After the airfoil is selected, it is possible to analyse the lifting and drag characteristics of the *AerGo* design. The relationship between lift coefficient C_L and angle of attack α is examined to produce the lift distribution along the upper and lower wings. After the lift characteristics are known, the drag can be evaluated by determining the induced drag coefficient C_{D_i} of the two wings after which the zero lift drag coefficient C_{D_0} is determined by taking all the components of the aircraft into account. Once these are determined, relationships between C_D and α as well as C_L and C_D can be generated. These parameters will be put through several iterations after input from the other subsystems until a common ground is found. The following assumptions are used to analyse the aerodynamics.

- Assumption: The flow is considered to be inviscid. This will can lead to slight over estimations.
- Assumption: Ncrit value of 9 for turbulent flow is used. This can also lead to over estimations of coefficients.

7.2 Aerodynamic Analysis

In this section, an elaboration of the wing planform and airfoil selection is given. Furthermore, the lift and drag characteristics of the wing and airfoil are discussed.

7.2.1 Wing Planform

A detailed overview of the wing planform is given in Chapter 4. This wing planform is chosen due to several different reasons. The configuration is mainly influenced by the other technical departments. In terms of lift and drag it is more ideal to have straight wings with no sweep or dihedral [2]. The sweep angle is needed in order to provide stability in the longitudinal direction which is further described in Chapter 8. Furthermore, the dihedral is added to the bottom wing because a ground offset is needed to get clearance from the water. The pontoons at the ends of the wing should not be touching the water. The top wing is kept straight because a straight wing produces more lift. A positive stagger - which means the upper wing with respect to the lower wing is shifted forward - is used because it provides more lift on the upper wing as well as giving the pilot a better view [8]. Additionally, it makes the aircraft more stable in the longitudinal direction which is further explained in Chapter 8. A biwing provides more structural integrity since it can disperse the load among two wings. The wings keep a constant chord along the span to ensure the most beneficial lift distribution [3]. A large wing area is beneficial to achieve take-off at a low airspeed. Table 7.1 shows the specifics of the wing.

Table 7.1: Wing configuration of the AerGo

Parameter	Value	Parameter	Value
b [m]	12	x_{st} [m]	0.45
S [m^2]	18.90	Γ [°]	5
S_{up} [m^2]	9.45	Λ [°]	15
S_{low} [m^2]	9.45	λ [-]	1
$\bar{c}_{up}$ [m]	0.79	G_r [m]	1.31
$\bar{c}_{low}$ [m]	0.79	G_t [m]	0.79

7.2.2 Airfoil Selection

In order to decide on an airfoil, the wing loading during cruise flight must be be extracted from the performance group. With this the design lift coefficient can be determined by [2]:

$$C_{L_{des}} = \frac{1}{q_\infty}\left(\frac{W}{S}\right)_{cruise} \tag{7.1}$$

With a wing loading of 77.89 N/m, a $C_{L_{des}}$ of 0.574 is found. To have an effective airfoil it is preferable to have a high $C_{l_{max}}$ with a C_{l_0} that is close to the $C_{L_{des}}$. One that has a low C_{d_0} is favourable. Furthermore, it is good to have a shape that complies well with the structure. In order to examine airfoils, designs are constructed in XFLR5 which has access to the XFOIL database. Several airfoils have been examined such as the NACA4212, NACA6615 and NACA6415. These airfoils became candidates due to their high camber and the thickness ratios. Increase in camber results in a higher $C_{l_{max}}$ as well as moving the curve relating C_l and α more towards the left thus increasing C_{l_0}. Moving the position of the camber changes the steepness of the curve. After several iterations it is decided that it is ideal to have an airfoil that, when put under the 3D case, provided a C_{L0} of nearly the $C_{L_{des}}$ so that the aircraft can fly at nearly 0 °angle of attack resulting in minimal drag during cruise as well as helping the aircraft plane on the water faster during take off from the added lift being produced. The NACA6615 had too high of a C_{L_0} and had the same $C_{L_{max}}$ as the 6415 and the 4212 fell short on both aspects. Each airfoil produced nearly the same amount of minimum drag. Additionally, the 6415 had the best capabilities in terms of the aerodynamic moment. For stability, a less steep C_m-α is preferred which can be better understood in Chapter 8. Table 7.2 and Figure 7.1 display the shape and specifics of the chosen airfoil. These airfoils are all examined under a Reynolds number Re of 791,530 and a Mach number M of 0.044 which are the cruise conditions.

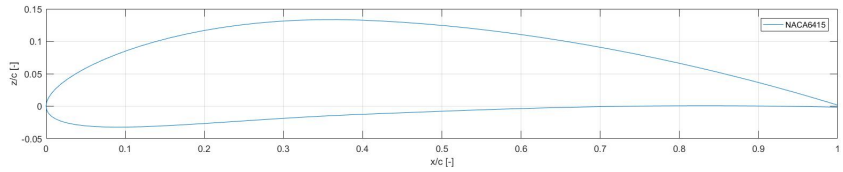

Figure 7.1: Airfoil of the AerGo upper and lower wing

Table 7.2: Characteristics of the NACA6415

Parameter	Value
$C_{l_{max}}$ [-]	1.75
C_{l_α} [-]	6.18
C_{l_0} [-]	0.68
α_0 [deg]	-6.33
C_{d_0} [-]	0.012
C_{m_0} [-]	-0.16

7.2.3 Lift

Now that the airfoil is selected, it is possible to analyse the lifting capabilities of the wing. The first step is to determine the relationship of C_{L_α} for each wing. The wing is swept aftwards therefore it can be written as [3]:

$$C_{L_\alpha} = \frac{C_{l_\alpha} cos(\Lambda)}{\sqrt{1+\left(\frac{C_{l_\alpha} cos(\Lambda)}{\pi A}\right)^2} + \frac{C_{l_\alpha} cos(\Lambda)}{\pi A}} \tag{7.2}$$

Where Λ is the sweep angle and A is the aspect ratio. Equation (7.2) can be used for the upper and lower wing individually with their respective aspect ratios. Both wings have nearly completely identical planforms except that the lower wing has a dihedral angle Γ of 5 °. Since it is a box wing the two wings will act as one total wing while carrying different lifting loads therefore the curves of the upper and lower wing relate to each other as [9]:

$$C_{L_\alpha} = C_{L_{\alpha_{up}}} s1 + C_{L_{\alpha_{low}}} s2 cos(\Gamma); \tag{7.3}$$

Where $s1 = \frac{S_{up}}{S_{up}+S_{low}}$ and $s2 = \frac{S_{low}}{S_{up}+S_{low}}$. Since the upper and lower wing have the same wing area, s1 and s2 will have the same value [9]. Now that the combined C_{L_α} is determined, the lift coefficient of the entire wing as a whole can be expressed as [2]:

$$C_L = C_{L_\alpha}\alpha + C_{L_0} \tag{7.4}$$

Using Equation (7.4), Figure 7.2 is generated. This displays the transformation from the airfoil in 2D to the wing in 3D (C_l-α to C_L-α) as well as the relationship between lift and α. It can be seen that at $C_{L_{des}}$ of 0.57 it has an α of -0.2°.

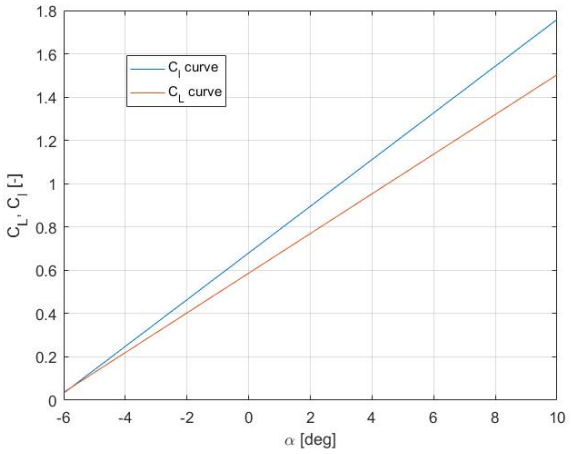

Figure 7.2: 2D and 3D lift curves with respect to α

Once the C_L of the entire wing of the aircraft is found, the next step is to evaluate the relative loading between the upper lower wing due to the positive stagger x_{st} of 0.45 m. This is represented as the following [8]:

$$C_{L_{up}} = C_L + \Delta C_L \qquad C_{L_{low}} = C_L - \Delta C_L \frac{S_{up}}{S_{low}} \tag{7.5}$$

Where ΔC_L = K1 + K2C_L. The coefficient K1 and K2 are determined through graphs from a report by *Walter S. Diehl* who created curves relating stagger, gap and thickness through statistical data [8]. Adding positive stagger on the upper wing will result in a higher relative loading on the upper wing. This is due to the fact that if the wing is more forward then there is less interference underneath the upper wing. The pressure distribution of the upper wing comes into less contact with the lower wing if moved further forward [3]. By determining the thickness to gap ratio $\frac{t}{G}$ as well as gap to chord ratio $\frac{G}{c}$ Figure 7.3a, Figure 7.3b and Figure 7.3c can be used to solve for K1 and K2 where [8]:

$$K1 = K1 + \frac{\Delta K1}{x_{st}} \qquad K2 = 0.05 + 0.17F \tag{7.6}$$

After obtaining K1 and K1 and using Equation (7.5) it is possible to determine $C_{L_{up}}$ and $C_{L_{low}}$. However it must be taken into account that the lower wing has dihedral therefore there is a varying gap from root to tip along the span of the two wings. The wing is more efficient at the root because the gap is larger and this results in less aerodynamic interference. Ultimately, the C_L values under design condition of the upper and lower wing are shown in Table 7.3.

Table 7.3: Relative C_L on upper and lower wing

Parameter	Value
$C_{L_{up}}$ [-]	0.61
$C_{L_{low}}$ [-]	0.54

Next, with the C_L values obtained for top and bottom, the lift distribution along each wing can be analysed. It is assumed that the lift distribution shall be elliptical since both wings have a constant chord length along the span. This implies that the circulation Γ_0 will be constant throughout [3]. The local lift distribution L' is represented as:

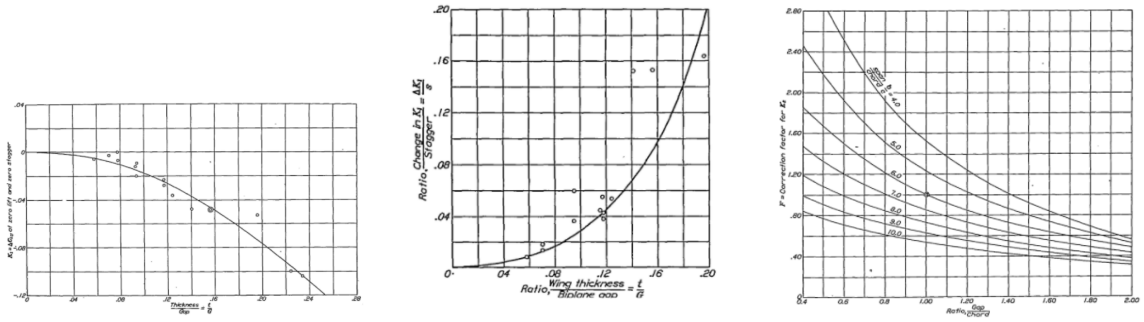

(a) K1 vs. $\frac{t}{G}$ (b) $\frac{\Delta K1}{x_{st}}$ vs $\frac{t}{G}$ (c) F vs $\frac{G}{c}$

Figure 7.3: Stagger coefficients relating to $\frac{t}{G}$ and $\frac{G}{c}$ [8]

.

$$L'(y) = \rho_\infty V_\infty \Gamma_0 \sqrt{1 - \left(\frac{2y}{b}\right)^2} \qquad \Gamma_0 = \frac{2V_\infty S C_L}{b\pi} \tag{7.7}$$

Where y = $\frac{y}{cos(\Lambda)}$ because of the sweep. By inputting, the C_L values of upper and lower wings respectively, the distribution can be plotted. However one more factor needs to be taken into account. The propellers are mounted in front of the leading edge of the upper wing. Each at 1.5 m from the centre. They will cause aerodynamic interference with the wing. The propellers will cause a slipstream creating an upwash and downwash on the top and bottom of the wing in that region which will cause the distribution to deform at these points. This results in an increase of q_∞ in these regions and changes the upper wing local α. As the blades rotate the tangential Velocity V_t will mostly vary due to changes in α where the axial velocity V_a will under go the larger portion of changes in dynamic pressure [32]. XROTOR has a module which takes the propeller design into account under different cases and output the V_a and V_t along the radius of the blade.Figure 7.4a, Figure 7.4b show the behaviour of these speeds along the blade at spanwise position.

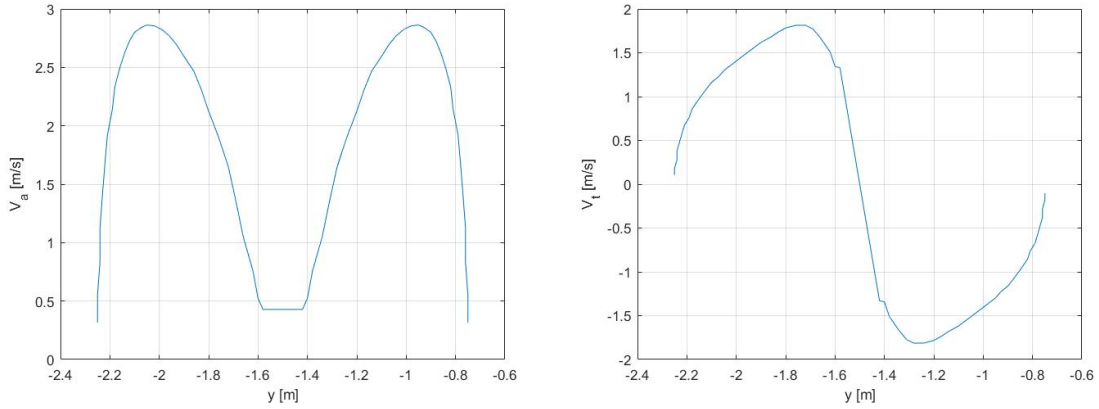

(a) V_a along propeller (b) V_t along propeller

Figure 7.4: V_a and V_t of slipstream at left spanwise position

Now implementing these velocities into Equation (7.7) the complete lift distribution can be generated. Figure 7.5 depicts said distribution. Furthermore, the lower wing will experience a downwash created from the propellers. Since the propellers create an increase in dynamic pressure there will be a larger pressure distribution created underneath the upper wing which counters the pressure on the upper side of the lower wing. In turn, the net difference in pressure on on the lower wing which will ultimately reduce the lift on the lower wing [3]. Further modelling this is beyond the scope of this project.

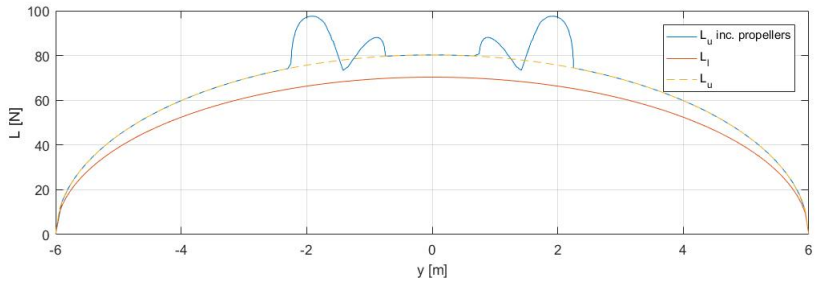

Figure 7.5: Lift distribution in spanwise direction of upper and lower wing

It can be seen from the lift distribution that the upper wing has the humps which ultimately create a larger total lift on the upper wing. Integrating the lift distribution of the upper wing with and without the propellers and finding the difference between the two showed that with the propellers there is a 3.8 % increase in lift on the upper wing. After finding these distributions, the lift characteristics for take off and cruise are determined and are shown in Table 7.4. The hull structure is not taken into account for the lift distribution but at higher angles of attack is is expected to provide an increase in lift due the its rather wide surface area. The pressure can build up and provide a lifting vector upwards [14].

Table 7.4: Lift characteristics of the *AerGo*

C_{L_α} [1/°]	0.092
$C_{L_{max}}$ [−]	1.57
C_{L_0} [−]	0.59
α_{stall} [°]	10.67
α_0 [°]	-6.38

Parameter	**Take off**	**Cruise**
C_L [-]	1.30	0.57
$C_{L_{up}}$ [-]	1.44	0.63
$C_{L_{low}}$ [-]	1.21	0.54
α [°]	7.70	0.21

The values achieved are purely theoretical and putting the aircraft and will be different from actual numbers. Since these numbers are generated through a combination of MATLAB and XFLR5. These estimations do not take into account all the interference between the components of the aircraft. If further design continues, these interference factors will be elaborated on. More on interference will be discussed in the next section. In addition, the effects of wing warping during roll will have an effect on the lift distribution on the wings. Since the warping occurs around the tips of the wing the elliptical shape at those points will straighten out due to the more lift be produced at the warped section [3]. This is left for further analysis.

7.2.4 Drag

After completing the analysis for lift, the drag can be evaluated. The influence of upper wing on the lower wing must be examined. Having this configuration has effects on the induced drag of the wing as whole. The downwash and upwash of the upper and lower wing respectively will interact with each other. Since there is positive x_{st} on the upper wing the lower wing experience more downwash . Prandlt came up with a method to find the total induced drag D_i with the interaction between the upper and lower wing which is described as [26]:

$$D_i = \frac{1}{\pi q_\infty}\left(\frac{L_{up}^2}{b_{up}^2} + 2\sigma\frac{L_{up}L_{low}}{b_{up}b_{low}} + \frac{L_{low}^2}{b_{low}^2}\right) \tag{7.8}$$

Where L_{up} and L_{low} are the lift of upper and lower wing respectively, b_{up} and b_{low} the wing span respectively and σ is the interference factor between the wings. L_{up} and L_{low} have been determined in the previous subsection and b_{up} and b_{low} are known. The only step at this point is to determine σ. This can be done by finding the ratio of b_{up} and b_{low} as well as the average of the two then dividing the gap by the average span [28]. Once this is done using Figure 7.6, σ can be found.

The gap is varying along the span thus σ will vary simultaneously. This is taken into account to find the general D_i that wing as a whole. After D_i is determined, the induced drag coefficient C_{D_i} and the Oswald factor e can be found with [3]:

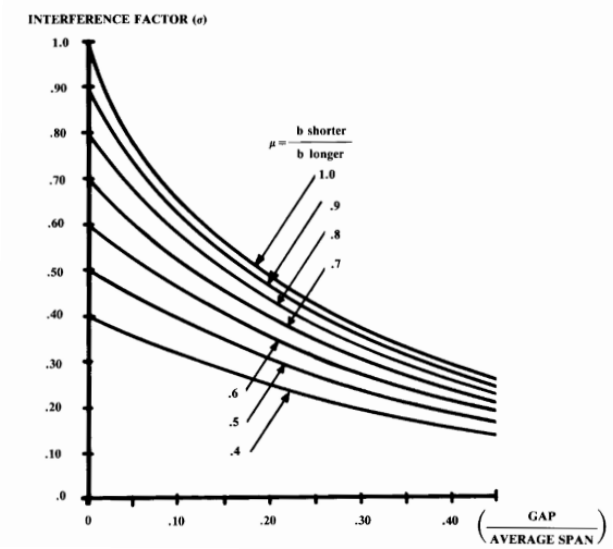

Figure 7.6: Prandtl's interference factor curves [28]

.

$$C_{D_i} = \frac{D_i}{q_\infty S} \qquad C_{D_i} = \frac{C_L^2}{\pi A e} \tag{7.9}$$

Where A and S is the aspect ratio and wing area of the entire wing respectively. Next, the profile (or parasitic drag) C_{D_0} is evaluated which is the sum skin friction and pressure drag of every component of the aircraft with respect to S [28].

$$C_{D_0} = \Sigma \frac{C_{D_c} A_c}{S} \tag{7.10}$$

Where C_{D_c} and A_c are the drag coefficient and frontal area of each component of the aircraft respectively. The C_D values must separately be determined.

First the drag produced by the pilot is evaluated. Only his/her head and neck is exposed therefore a manner to model this needs to be determined. It is decided to model the head as a cylinder of radius 7.5 cm and height of 30 cm. Under cruise conditions, the Reynolds number Re is 150,290 [23].

Next the hull and pontoon are examined. These are specifically designed to be able to take off and land in water which is further explained in Chapter 11. Hoehner explains that the sharp chines which are used for planing on the water increase the drag quite a bit. Also it has a step which is needed to decrease the wetted area and allow for take off rotation [16], but this causes the flow to separate at that point. In all, to have a hydrodynamic efficient hull or pontoon it loses aerodynamic efficiency.

Moving on to the rudder, they are shaped as a symmetric NACA0011 airfoil and are evaluated under a Re of 197,882. symmetric airfoil are preferred in terms of drag since the flow stays more attached because it can follow the streamline [3]. The rudder is examined in the direction of the flow. The behaviour of the rudder changes angle of attack is discussed in Chapter 8. Since these are placed vertically they will produce no induced drag. The airfoil is examined in XFLR5 and has a C_{d_0} value of 0.005 which is then also the C_D of this component. These are attached to sideplates. These side plates are very thin and are evaluated at a Re of 791,530 [(1)].

Finally the rods are most simple, they are 1 cm in thickness and are smooth and cylindrical in shape. They are evaluated with a Re of 10,019 just as with the model for the pilots head. Using these ideas, the estimates for C_{D_c} are given in Table 7.5.

From Table 7.5, it displays that the pilot and the hull produce the most drag of all the components. With this it is possible to generate drag plots relating to C_L and α using Equation (6.4) from Chapter 6 and with Equation (7.4). Figure 7.7a and Figure 7.7b depict these plots and Table 7.6 gives values of the drag. These figures show the relationship between drag and lift (right) and the drag and α (left). It can be seen that when C_L is 0 that C_D is 0.038 and when

[(1)] `https://www.engineeringtoolbox.com/drag-coefficient-d_627.html`, Retrieved: 13-12-2017

Table 7.5: Drag coefficients of different components

Component	C_{D_c} [-]	A_c [m^2]	D [N]
Pilot (2)	1.11	0.071	10.00
Hull [16]	0.22	0.302	9.02
Pontoon [16]	0.080	0.070	0.76
Rod (3)	1.21	0.0084	1.38
Rudder	0.0050	-	0.42
Sideplate (4)	1.17	0.0027	0.43

α is 0, C_D is 0.05 which is the cruise case. To conclude the interference between the components were not evaluated. It is to be expected that these values can increase if this is taken into account. To further optimise the design in the future, this will be considered. At the connection where the hull is attached to the wing, it is expected that the flow will be disturbed. Also flying at higher angles of attack the hull will cause the flow to separate around its nose.

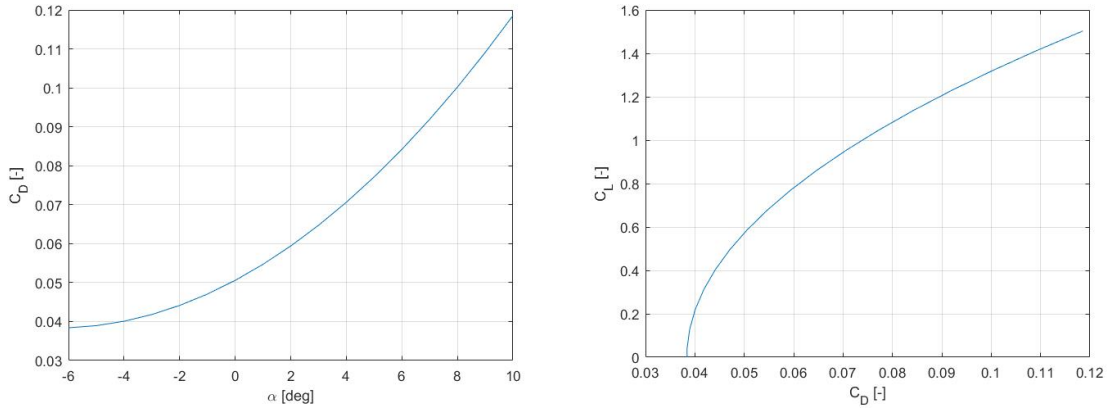

(a) C_D-α curve (b) $C_L - C_D$ curve

Figure 7.7: The behaviour of drag with respect to α and lift

Table 7.6: Drag characteristics

Parameter	Value
C_{D_0} [−]	0.038
C_{D_i} [−]	0.012
e [-]	1.19

7.3 Verification and Validation

To verify XFLR5 and the XFOIL database, they are compared to airfoil database from *Airfoil Tools* as well as a NACA airfoil database provided by *TUDelft* (5). Furthermore the airfoils were also put into JavaFoil (6). The data being produced by XFLR5 for the airfoil was comparable to both Javafoil as well as the numbers provided in the other NACA databases which made it reasonable to use XFLR5 to analyse the airfoil. The coefficients used for each component are estimated through numbers provided by literature written by the likes of Prandtl, Hoerner, Gudmundsson, Diehl and several scholarly articles [23] [14]. In this literature values can be found which are provided from experimental data and derived through statistical models. The methods used previously are a combination of multiple literature sources. For example, determining the C_D values for the hull was done using literature of Hoehner which had done experimental and statistical analysis on float and hull structures in wind tunnels [16]. The shape is largely similar to the shape of the hull of the *AerGo*. This validated the numbers. In order to further validate the numbers in the current model of the *AerGo*, comparisons to graphical models in Athena Vortex Lattice (AVL) and XFLR5 for the

(5) `http://airfoiltools.com/airfoil/details?airfoil=n0012-il`, Retrieved: 10-12-2017
(6) `https://www.mh-aerotools.de/airfoils/javafoil.htm`, Retrieved: 22-01-2018

3D cases are done. Table 7.7 shows the comparison between the parameters of the models. A 15 % margin is the maximum difference that is allowable since the graphical model is only an estimation. The shapes made in AVL and XFLR5 are not to perfect scale thus a difference in value between the current model and that of AVL and XFLR5 is to be expected.

Table 7.7: Comparison of models

Parameter	**Current model**	**AVL**	Δ%	**XFLR5**	Δ%
$C_L[-]$	0.57	0.57	0	0.51	13.5
$C_{L_\alpha}[1/°]$	0.0920	0.0782	15	0.0855	7.1
$C_D[-]$	0.049	0.0474	4.7	0.0441	10
$C_{D_i}[-]$	0.0117	0.0117	0	0.0105	10.3

Both of these cases are run under the cruise case which is not the most pessimistic case but the case in which the aircraft flies most. This is done just to compare the differences between the software and the values obtained theoretically. In AVL the C_L is set which in turn also gave no difference in C_{D_i} but then it was possible to see the differences with XFLR5. For the future, several other cases will be examined beyond this project. After comparing the numbers for C_L and C_D. The numbers fall within the 15 % margin. To this point the numbers have come up as expected.

7.4 Conclusion and Recommendations

In conclusion, the aerodynamics group takes in all the changes and values provided by the other groups and determines the efficiency in terms of lift and drag. A NACA6415 airfoil was chosen because it allows the aircraft to fly close to 0° during cruise and provides a C_L value of 1.57. At these speeds, the performance of the aircraft drives the design. The values produced in the analysis are reasonable but can be further iterated for more accuracy. A key finding is that with positive stagger more relative lift is produced on the upper wing. Another key finding is that due to the propeller wash on the upper wing gains a 3.8 % increase in lift. The finding of the C_{D_0} of 0.038 is still on the higher side compared to reference aircraft found in the previously mentioned literature. If the project continues, it is desirable to decrease the value. To do so, the following recommendations will help in further optimising the *AerGo*. A recommendation is to examine the surface of the materials because the smoothness or roughness of the material has effects on the transition point from laminar flow to turbulent flow. Another recommendation is to perform Computation Fluid Dynamics (CFD) analysis with tools such as OpenFOAM or simFLOW. These software have much greater solver database and will allow for more realistic situations to be modelled. The computational power of the simulators will help in getting more accurate estimations. The possibility to analyse von Kármán Vortex shedding is possible to evaluate induced vibrations around the rods through CFD. Another recommendation is to closely research the interference between the hull and wing structure since it is believed that this will disturb the flow.

8 Stability and Control

The *AerGo* aircraft is a flying biwing. Flying wings in general are unstable in longitudinal motion when the Centre of Gravity (CoG) is not located in front of the neutral point. The hull is also destabilising in the lateral motion. The purpose of this chapter is to discuss how to analyse the stability of the *AerGo* and how statically and dynamically stable, to ensure a safe and enjoyable flying experience. It will elaborate how the pilot will control the aircraft, not by just holding a control stick but by moving his body weight to experience a full workout. The chapter starts with the approach and the method that is applied to the technical discipline. Then it goes into estimating the centre of gravity (CoG) and mass moment of inertia of the aircraft by positioning the components. These results are used in a static and dynamic stability analysis to design a stable aircraft. The positioning of the components has a major influence on this and will be referred back to. Through out the whole chapter the pilot positioning will be mentioned more than once and be the leading subject. After the stability part, the controls and their design will be explained in Section 8.5. At the end of the chapter, the verification and validation will be discussed. It concludes by the final stability results for the *AerGo* and recommendations are given.

8.1 Approach

The method and assumptions of the design procedure for stability and control subsystem will be explained here. The first iteration round starts by setting up a complete geometry of the *AerGo* with an intuitive feel since fixed values of other subsystem do not exist yet. The stability of the aircraft is analysed with several programs, qualitative and quantitative results are obtained from this and communicated to the other subsystem departments. This gives the other subsystem departments a soft constraint that leads over time to converging values. The converging parameters are then iterated through the stability model again to check their sensitivity. The geometry is then changed again and checked until the desired result is obtained. The main geometry parameters on which stability decides are pilot position, stagger, lower wing position, sweep and dihedral. At the same time of the design the control are identified and fed back into the model to see their effect on stability. Finally the design converges to an optimised configuration that favours stability and also takes the other subsystems into account. Cross-checking and small verification's are done simultaneously during the whole design process. This helps to understand the results before an irreversible decision is made. There are a few assumptions done for the stability analysis. The assumptions and their effect on the results are given in the list below.

- Assumption: The pilot weight shifting has no affect on X and Z forces, only on moment. The step input into the linearised system will then only effect moment.
- Assumption: The individual items mass are taken as point masses. This will decrease the total value of the moment of inertia for some objects.
- Assumption: Pilot mass is the human body mass itself, no gear included.

It is noted that the reference frame used throughout this chapter for the x and z coordinates is always taken from the nose of the hull, with the x axis pointing against the direction of flight and z pointing upwards.

assumption: pilot mass includes gear such as helmet, jacket

8.2 Center of Gravity

When all the masses of the components are determined and their positions are known, the CoG can be located. In this subsection the CoG for a standard pilot position is approximated. It should be noted that the CoG will move along the longitudinal axis during flight since the pilot shifts his/her weight for pitch control, this is covered later in Section 8.5.1. To approximate the CoG of the entire aircraft during Operational Empty Weight (OEW) the following formula is used.

$$x_{cg} = \frac{\sum_{i=1}^{n} m_i x_i}{\sum_{i=1}^{n} m_i} \tag{8.1}$$

$$z_{cg} = \frac{\sum_{i=1}^{n} m_i z_i}{\sum_{i=1}^{n} m_i} \tag{8.2}$$

Here m_i is the mass of each individual component, x_i is the location of the components centroid along the longitudinal axis and z_i is the location of the components centroid along the vertical axis. The location of each compentent and the aircaft's CoG is shown in Table 8.1. The control wire and pulleys are not included due to the uncertainty of their location and their almost negligible mass.

Table 8.1: Mass and centre of gravities of all components.

Components	**Mass** $[kg]$	**Position of centroid on X-axis,** x_i $[m]$	**Position of centroid on Z-axis,** z_i $[m]$
Pilot	100.00	1.60	-0.30
Battery	19.24	1.00	-0.35
Hull	3.92	1.48	-0.11
Lower wing	5.50	2.15	0.26
Upper wing	5.50	1.75	1.31
Control sticks/seat	2.80	1.45	-0.10
Propeller (2x)	2.55	0.56	1.28
Motor (2x)	2.16	0.66	1.28
Pantoon (2x)	0.35	2.75	0.46
Instruments	0.20	1.30	0.10
Control wire (40m)	0.10	-	-
Pulleys (9x)	0.07	-	-
Total	**144.66**	**1.51**	**-0.03**

The aircraft is designed to carry a pilot with a mass of 100 kg which is 67% of the entire aircraft mass. Looking at Table 8.1 it is obvious that the main contribution that influence the CoG are the pilot and the battery. The positioning of pilot and the battery are thus critical to longitudinal stability and control, also different pilot masses have to be accounted. Section 8.5.1 covers the former aspects in detail. The main components and their position are shown in Figure 8.2

8.2.1 Mass Moment of Inertia

The mass moment of inertia is calculated using two different methods. First, Class I calculations are used from Roskam V [29]. This method uses a radius of gyration based on reference aircraft. Once more details are known about the individual subsystems, the standard moment of inertia equations are used for the estimation. The mass moments of inertia are needed in Section 8.4 and are calculated with the following formula:

$$I_{m,xx} = \sum_{i=1}^{n} \left(I_{ox,i} + m_i \left(y_i^2 + z_i^2 \right) \right) \tag{8.3}$$

$$I_{m,yy} = \sum_{i=1}^{n} \left(I_{oy,i} + m_i \left(x_i^2 + z_i^2 \right) \right) \tag{8.4}$$

$$I_{m,zz} = \sum_{i=1}^{n} \left(I_{oz,i} + m_i \left(x_i^2 + z_i^2 \right) \right) \tag{8.5}$$

Where $I_{o,i}$ is the moment of inertia of the individual items and x_i, y_i, z_i are the Cartesian distances to the item. The results of moment of inertia for operational weight are shown in Table 8.2.

Table 8.2: Results for the moment of inertia obtained with the given equations

Moment of inertia	**Estimates** $[kgm^2]$
$I_{m,xx}$	213.4
$I_{m,yy}$	97.0
$I_{m,zz}$	243.1

8.3 Aircraft Geometry for Static Longitudinal and Lateral Stability

An aircraft is statically stable when the CoG is in front of the neutral point. It is desired that the natural tendency of the aircraft is such that when a gust hits the plane, it will return to equilibrium position. This is achieved by having a $C_{m_\alpha} < 0$. On the *Aergo* the CoG will move since the pilot controls the entire aircraft by shifting his weight. This will alter the static longitudinal stability of the aircraft during flight and also change the C_{m_α} value. The moment coefficient, C_m is defined by the following equation:

$$C_m = 2 \cdot C_{m_{ac}} + C_{N_1}\left(\frac{x_{cg} - x_{ac_1}}{\bar{c}}\right) + C_{N_2}\left(\frac{x_{cg} - x_{ac_2}}{\bar{c}}\right) - T_c\left(\frac{z_{prop} - z_{cg}}{\bar{c}}\right) \tag{8.6}$$

Here C_{N_1} and C_{N_2} are the normal force coefficients of the upper and lower wing, x_{ac_1} and x_{ac_2} is the aerodynamic centre of the swept lower wing and upper wing and $\bar{c}$ is the mean chord length. This equation can be differentiated with respect to the angle of attack to find that $C_{m_\alpha} = -3.3$. The $C_m - \alpha$ curve for the *AerGo* can be contracted with Equation (8.6) and is shown in Figure 8.1. This plot is based on the cruise and take-off conditions. However it is assumed that the relaxed cruise position for the pilot is at 1.6 m, measured from the nose of the hull. It can be seen that during take-off the C_m line shifts down by -0.25. This is because the thrust of the engines is then larger than during cruise, inducing an increased pitching down moment. This means that the pilot will have to shift his weight back to overcome this negative pitch moment and in order to make the aircraft pitch up. How much the pilot has to displace his body to overcome this moment will be dicussed in Section 8.5.1.

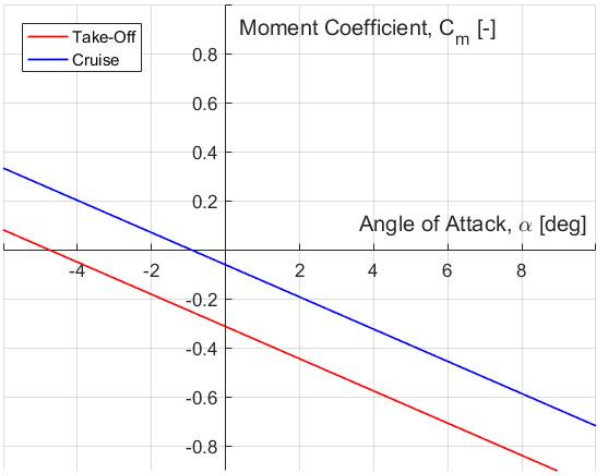

Figure 8.1: The moment coefficient plotted against angle of attack for the *AerGo* for cruise and take-off condition

8.3.1 Lower Wing, stagger and Pilot Positioning

The wing is attached to the hull at a longitudinal distance of $x_{LE} = 0.95$ m taken from the nose point of the hull to the leading edge of the airfoil. The reason for this position is mainly related to the pilot placement. The pilot will be sitting in the hull and extending his legs to control the aircraft, hence he needs enough leg room in front of him. Also since he affects the CoG location the most, he should be sitting in between the two aerodynamic centres of the wings to create a balanced seesaw effect. The upper wing has a positive stagger of 0.45 m at $x_{LE} = 0.5$ m, where positive stagger moves the upper wing forward with respect to the lower wing. It increases controllability because the change in moment due to a shift in CoG will be less abrupt. Placing the wings too close will make the aircraft more sensible to weight shifting whereas placing the wings too far apart will make an under reactive aircraft due the fact that the ratio of CoG shift is small compared to the stagger arm. Think of a very long seesaw arm compared to a short one. The longer one will rotate when introducing a small CoG offset. Also if the stagger gap is too large the pilot weight shifting will not be effective enough in moving the CoG to create a pitch up during take-off. More information on pilot shifting is given in Section 8.5.1. To have $C_{m_\alpha} < 0$ the CoG range is set a bit forward to keep the aircraft stable against gusts at all times but close enough to the neutral point during a take-off to enable the pilot to have pitch control through weight shifting. There will be a physical limits to how far the pilot can be placed forward due to the wing spar in front of him. For this reason the stagger is kept small. The hull having a length of 3 m adds another

limitation to the pilot position. The pilot can not be placed further back than 1.65 m because that will interfere with the hydrodynamic stability during take-off. The stability of the hull is explained later in Section 11.4. The relaxed position of the pilot is chosen to be at x_{pilot} = 1.6 m. The exact position of the pilot is found by doing an iterated trade off between dynamic stability, control and take-off procedure. It will be further elaborated on in the coming sections. The final positions of the major aircraft components are shown in Figure 8.2.

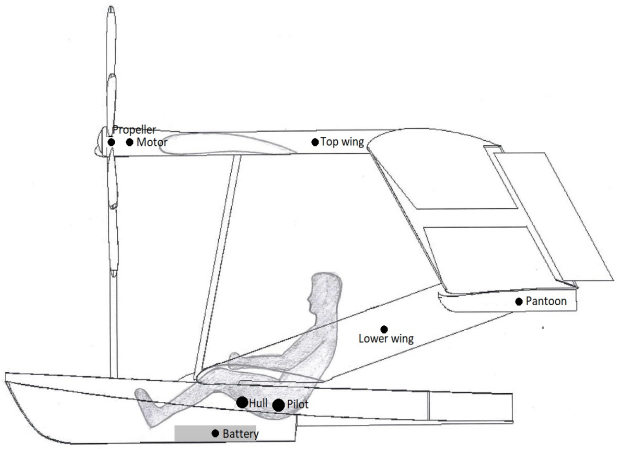

Figure 8.2: The position of the major components on the *AerGo*

Since pilots with different weights will fly the aircraft, the CoG shifting for will have a varying effect on pitch control. The specific pilot position chosen here has also taken the former criteria into account. This is explained in full detail in Section 8.5.1.

8.3.2 Sweep

To obtain lateral stability it is desirable to have a positive C_{n_β}. This is also known as the weather cocking derivative. This means that the aircraft has the tendency to point its nose into the direction of an encountered side gust. The vertical plates at the tip of the *AerGo* have to be offset rearwards in order to generate a positive C_{n_β}. The hull is the destabilising unit to the aircraft and creates a negative yawing moment during sideslip. To counteract this, a minimum sweep of 7° is needed to overcome this. *AerGo* has a sweep of 15° to offset the vertical plates even further and increase the weather cocking characteristics. This sweep is also chosen to increase the rudder effectiveness which is explained further in Section 8.5.3.

8.3.3 Dihedral

Dihedral is added to an aircraft to make it more resistant against side gusts so that it rolls away from a gust to decrease the sideslip angle. The dihedral angle for the *AerGo* is 5°. A dihedral angle of 3° would sufficient to make it aerodynamically lateral stable since the vertical side plates also introduce a Y-force and add to the contribution to move away from the free stream of a side gust. For hydrodynamic reasons an angle of 5° is preferred, this is discussed in Chapter 11.

8.4 Dynamic Stability

The dynamic stability of the *AerGo* is analysed by implementing the methods taught in the 3rd year course Simulation, Verification and Validation (AE3212-II) given at the TU Delft (TUD). A dynamic model is constructed in MATLAB for both symmetric and asymmetric case using the non dimensional linearised Equation of Motion (EoM) of an aircraft. To construct the model for the system, stability and control derivatives are needed. The model is only valid for the cruise case because all derivatives are found based on a steady state velocity and angle of attack. The EoM's are then studied over a time domain by inputting a step input at time t =0s and identifying the eigenmotion of the *AerGo* in terms of time response. Some stability derivatives are more difficult to evaluate than others so two different software are used for that which are discussed in more detail in the following subsection and in Section 8.6, Verification and Validation. Once the motion of the aircraft is known, the stability derivatives that cause undesired behaviour are identified and changed with an iterative process. Some variables are constrained by other subsystems more than others and can not be changed. These had to be discussed with the other subsystem departments to

ensure that no unacceptable choice is made that would affect the design in any negative way. The key parameters that had the most influence are: the wing, pilot and battery position since they have a major impact on the mass moments of inertia that affects the moment equations. The design is optimised for those three parameters through an iterative process [17].

8.4.1 Stability Derivatives and Control Derivatives

Stability and control derivatives are used to linearise the equations of motion (EoM's) so that the stability of the *AerGo* can be more readily analysed. The EoM used for the symmetric case is defined as follows:

$$\begin{bmatrix} C_{X_u} - 2\mu_c D_c & C_{X_\alpha} & C_{Z_0} & C_{X_q} \\ C_{Z_u} & C_{Z_\alpha} + (C_{Z_{\dot{\alpha}}} - 2\mu_c)D_c & -C_{X_0} & C_{Z_q} + 2\mu_c \\ 0 & 0 & -D_c & 1 \\ C_{m_u} & C_{m_\alpha} + C_{m_{\dot{\alpha}}} D_c & 0 & C_{m_q} - 2\mu_c K_Y^2 D_c \end{bmatrix} \cdot \begin{bmatrix} \hat{u} \\ \alpha \\ \theta \\ \frac{q\bar{c}}{V} \end{bmatrix} = \begin{bmatrix} 0 \\ 0 \\ 0 \\ -C_{m_{\Delta x_c g}} \end{bmatrix} \cdot \Delta_{x_c g} \tag{8.7}$$

For the asymmetric flight the linear model for aircraft motion given as:

$$\begin{bmatrix} C_{Y_\beta} + (C_{Y_{\dot{\beta}}} - 2\mu_b)D_b & C_L & C_{Y_p} & C_{Y_r} - 4\mu_b \\ 0 & -\frac{1}{2}D_b & 1 & 0 \\ C_{\ell_\beta} & 0 & C_{\ell_p} - 4\mu_b K_X^2 D_b & C_{\ell_r} + 4\mu_b K_{XZ} D_b \\ C_{n_\beta} + C_{n_{\dot{\beta}}} D_b & 0 & C_{n_p} + 4\mu_b K_{XZ} D_b & C_{n_r} - 4\mu_b K_Z^2 D_b \end{bmatrix} \cdot \begin{bmatrix} \beta \\ \varphi \\ \frac{pb}{2V} \\ \frac{rb}{2V} \end{bmatrix} = \begin{bmatrix} -C_{Y_{\delta_a}} & -C_{Y_{\delta_r}} \\ 0 & 0 \\ -C_{\ell_{\delta_a}} & -C_{\ell_{\delta_r}} \\ -C_{n_{\delta_a}} & -C_{n_{\delta_r}} \end{bmatrix} \begin{bmatrix} \delta_a \\ \delta_r \end{bmatrix} \tag{8.8}$$

For simplicity all the variables are given and explained in the List of Symbols. It is important to note that for the symmetric case the input matrix state variable is not δ_e as in a conventional aircraft that has horizontal tail with elevators but it is Δx_{cg}; the change in in CoG location of the aircraft. This input is directly related to, and depends only on the pilot weight shifting. The equations of motion for the eigenvalues rely on various specific stability and control derivatives. Using these stability derivatives the response to an input to one of the control derivatives can be computed for the aircraft and dynamic stability can be determined. Hence these derivatives need to be determined for the *AerGo*. Some can be found using the DATCOM method and others are found analytically with methods from the Flight Dynamics course, AE3212-I given at the TUD. DATCOM is software designed by the United States Air Force (USAF) that allows you to input the aircraft geometry and returns the aerodynamic characteristics in terms of coefficients based on the inputs. These coefficients are then implemented into the dynamic model. The geometry of the *AerGo* and the graphical output from DATCOM is shown in Figure 8.3.

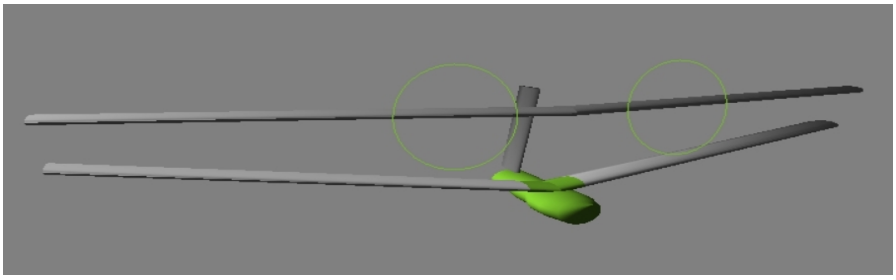

Figure 8.3: The *AerGo* geometry as graphical output from DATCOM

The disadvantage of the DATCOM software is that it can not incorporate vertical plates at the wing tips, like the *AerGo* has. For this reason the vertical plates and their area are modelled as one large fin placed on the hull. This places the fin at the exact same x location as the vertical plates would have due to the wing sweep. This will of course have slight different aerodynamic characteristic behaviour than the real design would. To check that the results returned from the DATCOM program can be deemed suitable another program called Athena Vortex Lattice (AVL) is used. AVL is a program developed by the Massachusetts Institute of Technology (MIT), it uses the vortex lattice method to compute aerodynamic characteristics. The program AVL is explained further in the section Verification and Validation at the end of this chapter. In AVL vertical plates can be incorporate, see Figure 8.4.

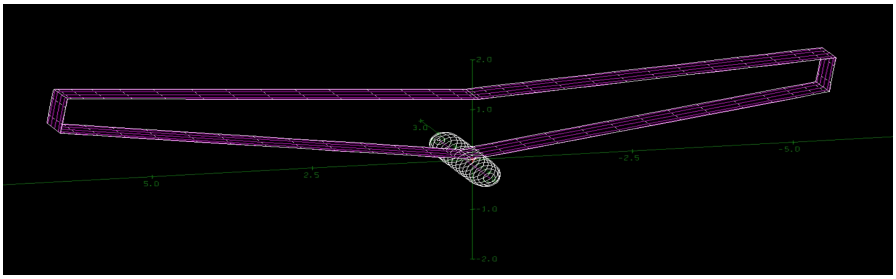

Figure 8.4: The *AerGo* geometry as graphical output from AVL

When running both programs they produce the following aerodynamic coefficient, see Table 8.3. It can be seen that C_{l_β} is larger in the DATCOM than in AVL. The reason for this might be due to the fact that the vertical fin in the DATCOM model is two times the height of the side plates of the model in AVL and thus introduces a larger offset in the z-direction to the Y force on the fin, hence increasing the roll moment, L. The values of C_{Y_p} and C_{n_β} have opposite signs from both programs. This could be because the hull is modelled different in both programs. The other values do not show such a large discrepancy. For the dynamic simulation performed in MATLAB, the AVL parameters will be used further for the investigation of eigenvalues.

Table 8.3: Stability coefficients found using the DATCOM and AVL program

Coefficient	**DATCOM**	**AVL**
C_{l_β}	-0.1391	-0.1520
C_{l_p}	-0.749	-0.566
C_{l_r}	0.183	0.182
C_{n_β}	0.0922	-0.0116
C_{n_p}	-0.0298	-0.0329
C_{n_r}	-0.00332	-0.00382
C_{Y_β}	-0.182	-0.155
C_{Y_p}	-0.00931	0.0491

The remaining stability derivatives are found analytically by using the method given in the Flight Dynamics Lecture Notes [17]. The specific equations and assumptions that determine the stability derivatives can be found on p.187 in the former reference. The results of the calculations are presented in Table 8.4.

Table 8.4: Stability coefficients found analytically

Coefficient	**Calculations**
C_{X_u}	-0.0097
C_{X_α}	0.419
C_{Z_u}	-1.326
C_{Z_α}	-5.25
C_{Z_q}	1.50
C_{m_α}	-4.13
$C_{m_{\Delta x_{cg}}}$	1.662
C_{m_q}	-0.118

The moment of inertia are also used to determine the stability of the *AerGo*, they can be found in Section 8.2.1. The control derivative with respect to a CoG shift is assumed to only have effect on the moment of the aircraft since the X and Z force are barely affected by a weight shift since it does not deflect any aerodynamic surfaces and does not change the lift or a drag force. The moment coefficient with respect to the a shift in CoG, $C_{m_{\Delta x_{cg}}}$, is found by the gradient of the $C_m - x_{cg}$ curve in Figure 8.9b.

8.4.2 Symmetric Motion

Inputting the evaluated stability and control derivatives into the model made in MATLAB and introducing a step input to the control state variable creates a simulation of the dynamic response of the aircraft in the time domain. The step input is made by shifting the pilots position 20 cm to the back. The dynamics of *AerGo* are best analysed by looking at the eigenvalues of the motion. These are stated in Table 8.5.

Table 8.5: Eigenvalues for the symmetric analysis for cruise and take-off

Eigenmotion	Cruise	Take-off
Short period	-0.0317 ± 1.01i	-0.0157 ± 1.06i
Phugoid	-3.27 ± 1.07i	-3.15 ± 8.60i

The *AerGo* has two modes in the symmetric case. All symmetric modes for the *AerGo* are stable. The eigenvalue in the first row of Table 8.5 belongs to the *Short Period* mode that is a highly damped motion. The motions in the time domain is shown in Figure 8.5 and 8.6. Note the bottom graph, it is a zoomed in region of the first 10 s for the pitch rate. The main contribution that causes the high damping is C_{m_q}, the pitch damping coefficient. The motion is damped if $C_{m_q} < 0$. In the second row of Table 8.5 the eigenvalue of the long period mode is shown. The eigenvalue has a real and imaginary part, thus also contains oscillatory features. The real part is negative and very small meaning that the motion is stable but damped out very slowly. This mode is known as the *Phugoid*. It has a period of roughly 6.3 s, these are fast oscillation but very small over a long period. When comparing the cruise and take-off eigenvalues and the time domain figures it is clear that the *AerGo* is more damped out during cruise. The higher velocity and lower engine thrust in cruise are preferred for dynamic stability. The period of *Phugoid* is nearly independent of vehicle parameters and inversely proportional to the flight velocity. Due to the large vertical offset of the engines the *AerGo* always has a tendency to pitch down if the pilot is positioned in front of the trimmed flight condition. If the engines were placed closer to the CoG the negative moment becomes smaller.

The amplitude of the oscillations decreases faster for the cruise condition than for take-off. This means that during cruise the aircraft is more damped than during take-off. So when the velocity is higher the aircraft has a more damped motion than in at lower velocity. The pilot position here also plays a major role. It is found that when the pilot moves the CoG over 1.75 m the aircraft is still stable, but only very lightly damped. However it is necessary that the pilot moves over this point in order to pitch up during take-off. The motion in the time domain is depicted in Figure 8.5 for the cruise case and in Figure 8.6 for the take-off case.

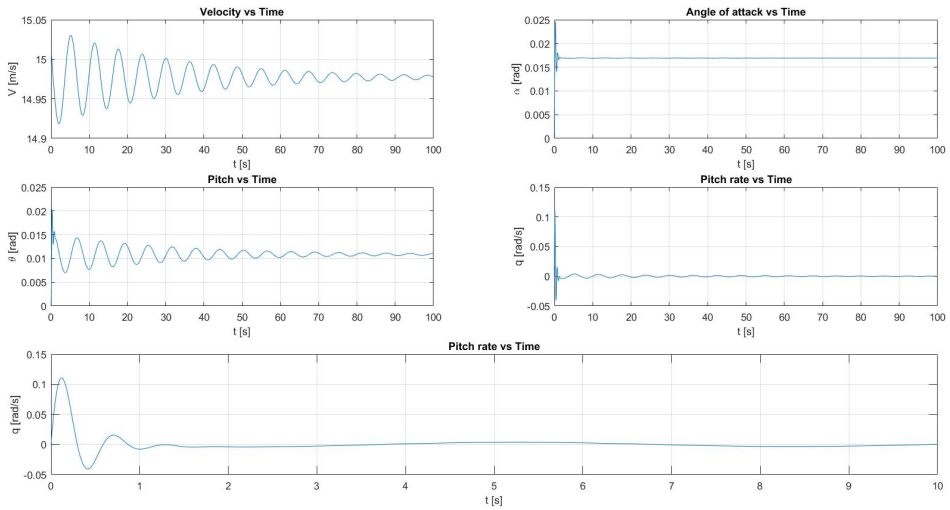

Figure 8.5: The symmetric dynamic stability of the *AerGo* during cruise

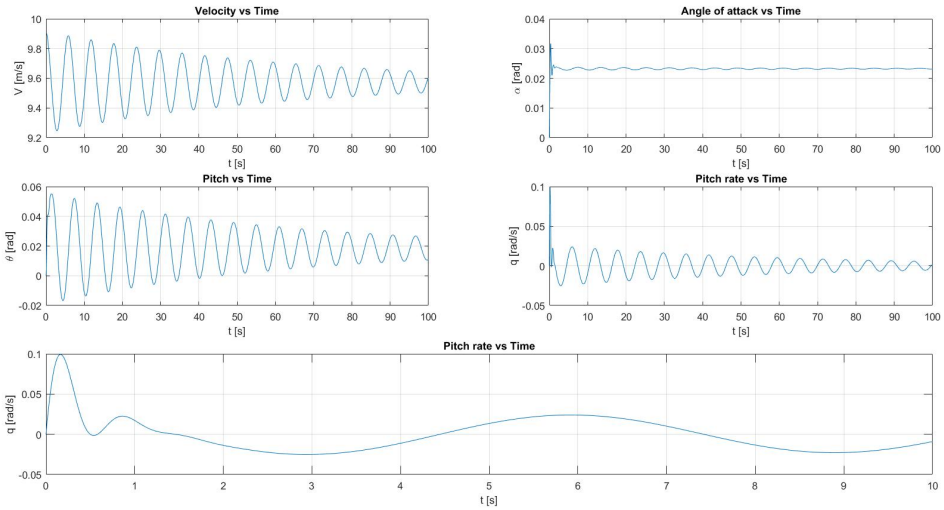

Figure 8.6: The symmetric dynamic stability of the *AerGo* during take-off

8.4.3 Asymmetric Motion

The same method used in the symmetric case is used to analyse the asymmetric motion. A step input is inserted into the model by deflecting the control surfaces by 5°. This will simulate a gust hitting the aircraft from the side.

Table 8.6: Eigenvalues for the asymmetric analysis for cruise and take-off

Eigenmotion	Cruise and Take-Off
Aperiodic Roll	-3.14
Spiral Mode	-0.585
Dutch Roll	-0.488 ± 0.886i

In the asymmetric case the *AerGo* has dynamic stability. The step input simulates a sudden gust hitting the aircraft from the side. The motion for the *AerGo* is damped out in a very short period for all motions at cruise and take-off. The motion in the time domain is depicted in Figure 8.7 for the cruise and take-off case. The eigenvalues for the asymmetric motion are shown in Table 8.6. All the real parts of the eigenvalues are negative meaning the amplitude of the input damps out in about 12 s. The eigenvalue in the first row of Table 8.6 belongs to the eigenmotion known as the *Aperiodic Roll*. The roll rate, p and the roll angle ϕ are damped out very fast after the input is applied. The largest contribution that damps out the *Aperiodic Roll* comes from C_{ℓ_p}, the roll damping coefficient. The eigenvalue in the second row is also real and negative, meaning that it is a stable motion but damped out much slower than the *Aperiodic Roll*. It is presumed that this motion is the *Spiral Mode*. This motion happens when the aircraft is in a roll initially and slowly spirals in if unstable and out to return to a zero roll angle when stable. Many conventional aircraft are slightly unstable in this motion [17]. The *AerGo* shows a stable motion here. In the third row, the eigenvalue has two parts, one real and one imaginary. This is the oscillatory contribution seen in the figures. This motion is know as the *Dutch Roll* and is also a stable motion for the *AerGo*. Sweep can increase the oscillatory motion and decrease damping ratio because the relative velocity that the wing encounters during a yaw rate is less than on a non swept wing, so less lift is created on a swept wing during yaw hence having less induced drag. Drag tends to damp aerodynamic oscillations. The real part is here again negative meaning this mode is stable. To conclude the *AerGo* has good roll and yaw damping capabilities. Different than in the symmetric motion, all three modes have the same eigenvalues for cruise and take-off. The reason for this is that the thrust is not incorporated in the asymmetric motion. It makes sense that thrust will have less effect in lateral motion if the thrust produced by both motors is assumed constant. However when one takes into account the gyroscopic effects that the propellers produce, it will affect the roll and yaw motions. This could be an error in the model that has to be looked at and changed in future.

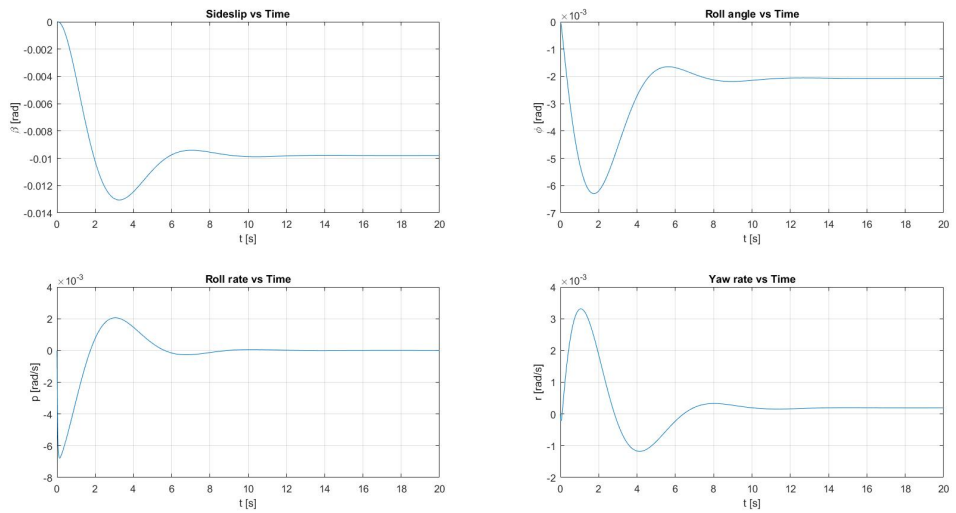

Figure 8.7: The asymmetric dynamic stability of the *AerGo* during cruise and take-off.

8.5 Control

The aircraft will be controlled about three axis. The importance that the pilot will have a sporty and active feeling during flight is a guideline for the design. The control mechanism shall stay lightweight and simple to make the assembly easy. The pitch, roll and yaw control will be explained in the following subsections. Their mechanisms with pros and cons will be elaborated in detail. A few assumptions are done for the control analysis. The assumptions and their effect on the results are given in the list below.

- Assumption: The lift distribution is taken to be square to easier calculate the reaction forces on the struts and wires. The calculated forces will be an overestimation.
- Assumption: The rotational stiffness is assumed to be constant over the span so the angle of twist varies linear over span.
- Assumption: The centre of twist is assumed to be located at 0.3797 cord length and the pulleys are located at this point. Since the thickness of the spars varies over span, this point is difficult to calculate and therefore approximated to be at 3/4 of the distance between the spars.

8.5.1 Pitch Control

The *AerGo* is an ultralight aircraft and designed for recreational sportive flight. Since the mass of the pilot is so large compared to the entire aircraft mass he can control the aircraft by shifting his body weight along the longitudinal axis to alter the total CoG relative to the neutral point on a swing seat Figure 8.8. Also the anatomy of the human body is such that it can shift its own CoG from 0.50–0.75 m in a seated rowing motion [24]. When the pilots position is at 1.6 m the CoG of the aircraft is at X_{cg} = 1.51 m. A good position for the pilot is when he is ergonomically sitting relaxed in front of the neutral point during cruise to maintain static stability..

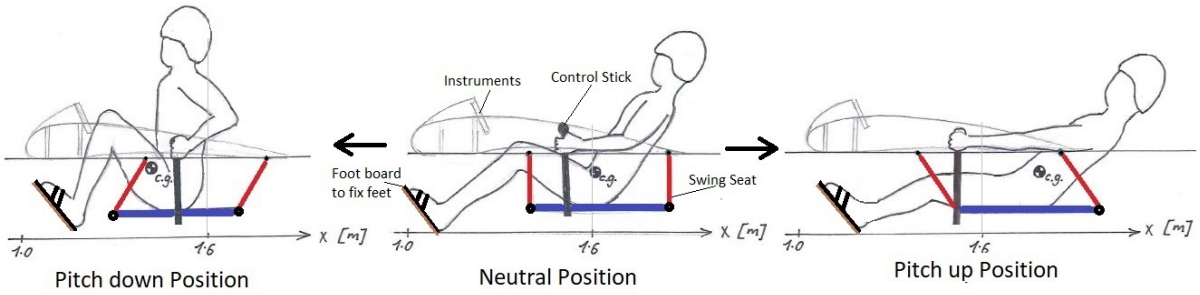

Figure 8.8: The pilot position on the swing seat to achieve different pitch attitudes

There are two flight conditions for which the pilot position is designed for; take off and cruise. In Figure 8.9b the CoG is very close to the trimmed cruise condition, when $C_m = 0$. This point is found by iterating through the dynamic model at different lower wing configurations for different stagger and different pilot positions. This section can be linked back to Section 8.3.1 where lower wing, stagger and pilot position are decided.

During the take-off phase the thrust is at maximum introducing a negative pitching moment due to the vertical offset of the propellers. The pilot has to shift his weight rearwards over the neutral point to create a positive pitching moment in order to introduce a pitch acceleration. The difference of CoG between a trimmed cruise flight and to achieve a pitch acceleration at take-off of 3 °/s^2 is 0.2 m. A pilot of 60 kg has a contribution of 51% of the total aircraft mass and will be less effective in displacing the aircraft CoG than a pilot of 100 kg so he should be moved closer to the neutral point in order to be able to introduce a positive pitching moment during a take-off. See the linear relation of pilot position and CoG location of the aircraft in Figure 8.9a.

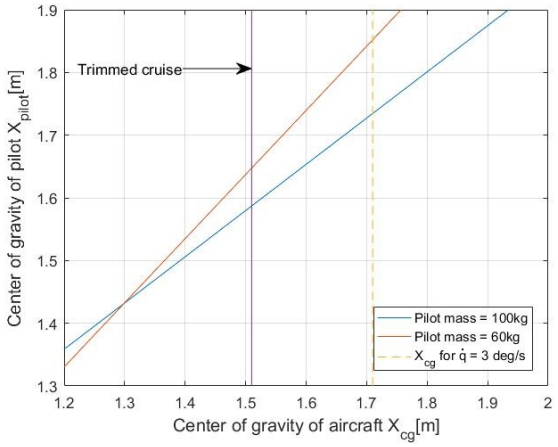

(a) The relation of pilot position versus the CoG position of the aircraft, for a 60 kg and 100 kg pilot

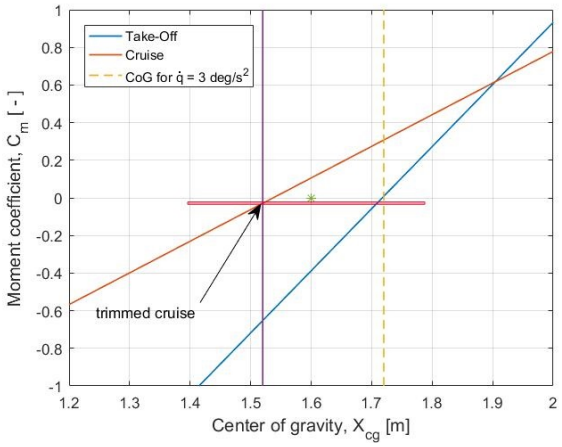

(b) The moment coefficient variation with CoG position for cruise and take-off case

Figure 8.9: Pilot position with different mass and the effect on the aircraft pitching motion

The range between trim points at take-off is such that a 60 kg pilot needs to displace his body centre 22 cm rearwards to create a positive pitch moment whereas a 100 kg pilot has to only move 16 cm to do this. A heavier pilot thus has a much larger range to displace the aircraft's CoG and therefore also has a greater range in possible pitch acceleration. To be sure that a lightweight and short pilot can exceed this critical point the whole swing-seat can be moved back with the foot board where the feet are fixed to. An adjustable swing will add a little more complexity to the design than a fixed swing but ensures that heavy pilots have a stable aircraft during cruise and light pilots can shift the CoG enough during a take-off to create a pitch up motion. The seat can be adjusted before going airborne. The battery is 40% of the empty weight and thus also has a large contribution to the location of the CoG. It is placed near the pilot position to keep the negative pitching to a minimum.

The swing seat has several advantages that outweigh the disadvantages. The first advantage is that a swing-like seat will always try to restore to a equilibrium position. Although this is with respect to the earth reference frame, not necessarily the body frame. In a pitch up manoeuvre, the pilot therefore has to push his weight back behind the neutral point. This will cause the aircraft to pitch up, but as long as the angle the seat makes at 0 degrees of pitch is not exceeded by the pitch angle, the swing want to return the pilot forward decreasing the pitch rate. The downside of this system is that pilot has to fight gravity since the swing seat is not only displacing in 2 direction but also in z direction. Despite the explained downside, the swing seat has a big advantage over for instance a rolling seat. The weight and complexity is very minimum.

8.5.2 Roll Control

Conventionally ailerons are used to control an aircrafts roll orientation. These surfaces require a hinge and therefore the inner wing structure should support this. By leaving out the hinge and just warp the wings, some weight can be saved. The flexibility of the wings will make rotating the airfoil at the tips with respect to the root possible. The bi-wing configuration is excellent for creating the arm required to exert enough force to warp, that is why it was also used in the *wright flyer* [25]. Warping has also the benefit of decreasing the adverse yaw tendency, because a rotation

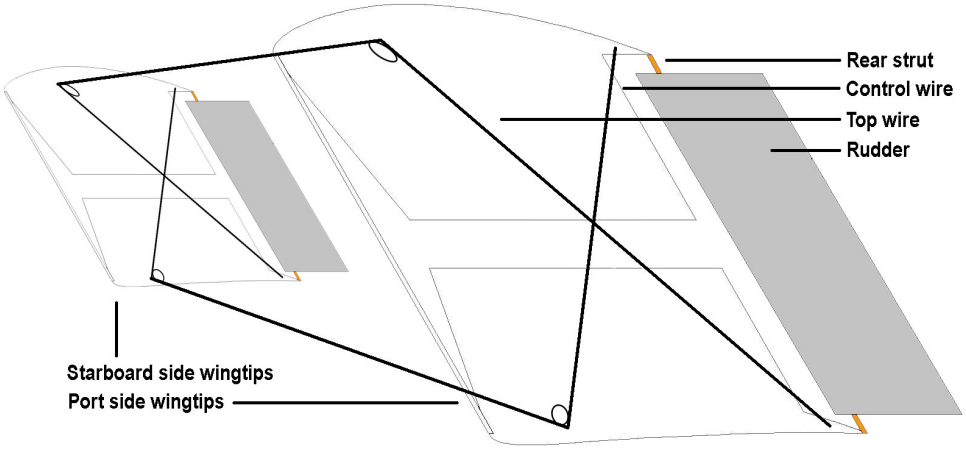

Figure 8.10: Wingtip connection and rudder placement

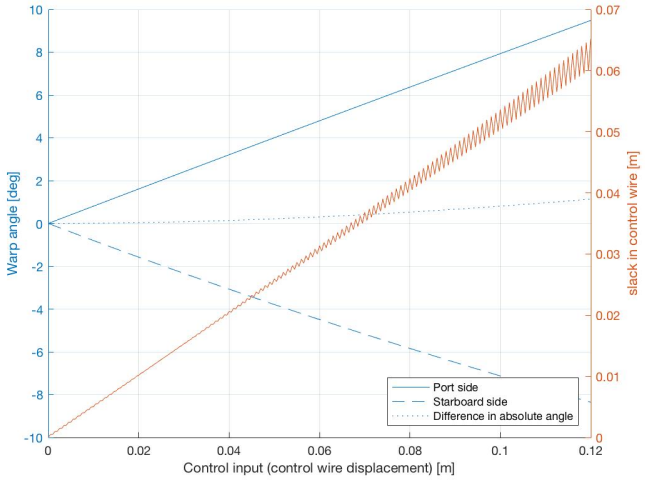

Figure 8.11: Warp angle geometry

at the tip will cause a slight inward movement creating a yaw moment.

The top and bottom are connected at the wingtips with 2 struts and 2 diagonal wires as shown in Figure 8.10. One of the wires is running through the top wing, hence top wire. The other is along the bottom wing and this is the one that will be displaced by the pilot, therefore it is named the control wire. The struts connections are hinged so that the airfoils can still be rotated. By changing the length of the wires, the angle of the airfoils can be controlled while keeping them parallel. The wires of both sides are connected to make a positive deflection at one tip will have a negative deflection at the other. However because of the stagger both deflections are not equal. The difference in angle is not large for small deflections, but this phenomena also causes slack in the bottom wire as shown in Figure 8.11. The length of wires are calculated by numerically approximating the angles, hence the oscillation in the result.

Because warping will be resisted by the torsional stiffness of the wing structure, only the outer two meters of each wing will be warped. This is a logical length since the wings are sectioned there for transportation and storage reasons. These last two meters can be made less stiff to allow for a lower control force.

The moments about the centre of twist are given by:

$$0 = T_{wb} + q_{\infty} \cdot C_{N_\alpha} \cdot (x_{tw} - x_{ac}) + F_c \cdot x_{F_c} - F_s \cdot x_{F_s} \tag{8.9}$$

Where T_{wb} is the wingbox resisting moment for some angle of twist. q the dynamic free stream pressure. C_{N_α} is the aerodynamic normal force for the angle of attack. x_{tw} and x_{ac} are the x location of the rotation of twist and aerody-

namic centre respectively. F_c the control wire force with the arm x_{F_c} to the centre of twist. Similarly F_s is the force in the back strut with x_{F_s} the arm to the centre of twist. Using this equation for all wing ends with adding a relation between port side twist to starboard twist will give a system of 5 equations and 5 unknowns. From Equation (8.9) it can be seen that the forces will depend initial flight conditions. The most common will be at cruise so Figure 8.12 gives the forces in the wires and struts for different angles of warp at cruise.

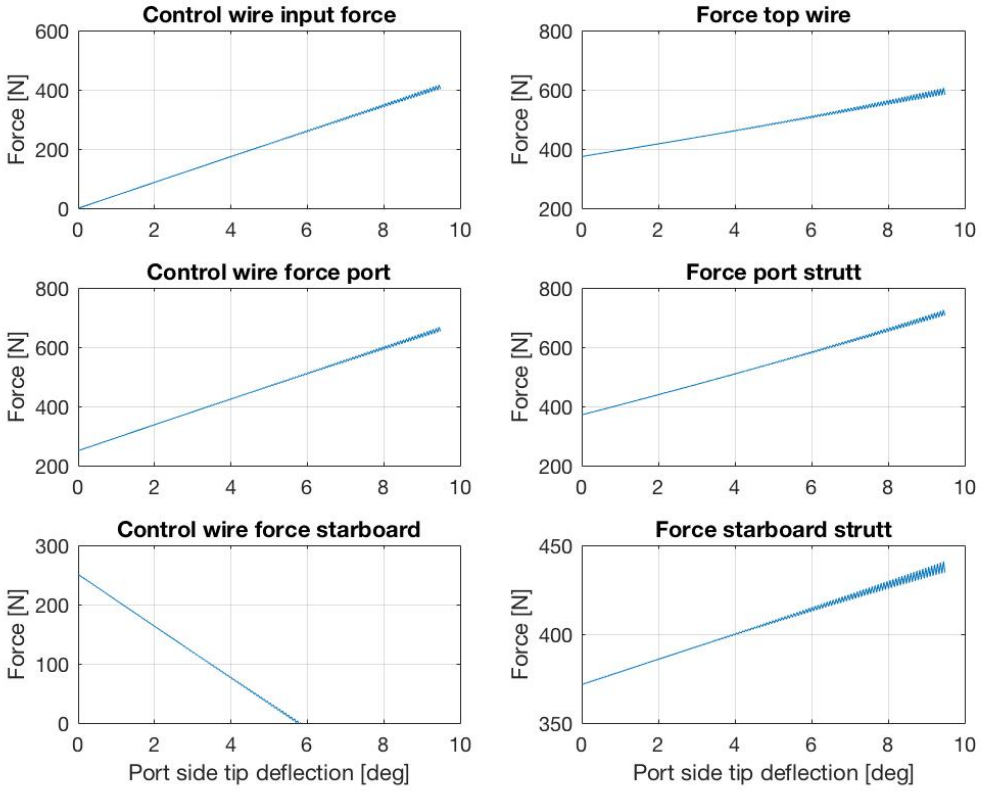

Figure 8.12: Roll system control forces at cruise speed

The related roll acceleration can now be calculated by the following formula:

$$\dot{p} = \frac{M_x}{I_{xx}} \tag{8.10}$$

Where ṗ is roll acceleration, M_x is the moment about the x axis and I_{xx} is the moment of inertia about x. The acceleration is plotted over wingtwist in Figure 8.13, which can then be related to the control force in Figure 8.12.

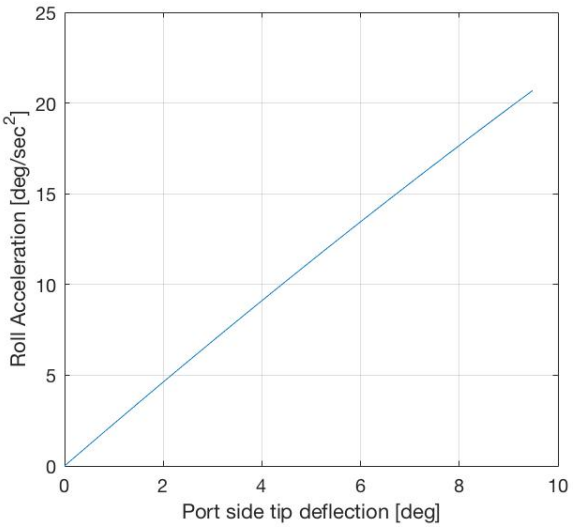

Figure 8.13: Roll acceleration

8.5.3 Yaw Control

Yaw control on conventional aircraft is normally performed by a vertical rudder positioned behind the CoG on the vertical fin. Due to the fact that the *AerGo* has no fuselage where a vertical stabiliser with a large offset can be placed on it is difficult to find a yaw control concept. At the start of the detailed design phase thrust vectoring control was taken as an option. Since two propeller engines exist at an offset to the line of aircraft symmetry it seemed to be the most effective way to yaw. However the scenario when one engines fails has to be taken into account. When one engine fails there is no way to control the yawing motion anymore since no control surfaces exist nor can straight flight be continued with one engine on. The pilot would have to turn the working engine of and immediately decline to land. He can then only land with head wind because any side gust or side wind would cause a side slipping motion therefore becoming more difficult to land in a safe way. It is thus decided that thrust vectoring is not suitable for yaw control for the *AerGo* because of redundancy and safety issues. Herefore the *AerGo* final design will have rudders located at the tips of the wings. As mention before in Section 8.3.2 a 7° sweep angle to offset the vertical plates back is not sufficient to obtain effective yaw control if these were rudders. A positive sweep angle of 15° increases the rudder effectiveness. Since wing warping is used for roll control it is difficult to place a fixed rudder in between the upper and lower wing because it will create shear loads on the rudder that would rip the thin skin. The rudder is placed on the trailing edge of the wings with a hinge. See Figure 8.10, a sideview of the *AerGo* for the position of the rudder. Because of the tilted hinge line due to stagger, deflecting the rudder will also cause a moment about the y axis. So yaw and pitch are coupled, however analysis of this is considered to be outside of the scope of the project.

The rudder is sized for an engine breakdown and has a surface area of 0.237 m^2. The set requirement is that after one engine breaks down, the *AerGo* has to be able to continue straight, level and side slipping flight with a rudder deflection of 6°. The rudder has a standard symmetric NACA0011 airfoil which has a $C_{Y_{\delta_r}} = 1.13$, this can be seen as the lift coefficient with respect to angle of attack the rudder encounters. The data of this foil is obtained from resource [(1)]. The stall angle is 12° so in case one rudder fails, straight flight can still be maintained using only the functional rudder. Using this a relation for yawing moment coefficient with respect to rudder deflection can be estimated as follows:

$$C_{n_{\delta_r}} = 4C_{Y_{\delta_r}} \frac{l_r}{b} \tag{8.11}$$

Where l_r is the arm from CoG to the rudder (1.8 m) and b is the wing span. The equations of lateral motion for an engine failure can be found on p.439 in Lecture Notes Flight Dynamics [17] and is defined as:

$$\begin{bmatrix} C_L & C_{Y_\beta} & 0 & C_{Y_{\delta_r}} \\ 0 & C_{\ell_\beta} & C_{\ell_{\delta_a}} & 0 \\ 0 & C_{n_\beta} & 0 & C_{n_{\delta_r}} \end{bmatrix} \cdot \begin{bmatrix} \varphi \\ \beta \\ \frac{pb}{2V} \\ \frac{rb}{2V} \end{bmatrix} = - \begin{bmatrix} 0 \\ C_{\ell_e} \\ C_{n_e} \end{bmatrix} \tag{8.12}$$

[(1)] `http://airfoiltools.com/airfoil/details?airfoil=naca0011-il`, Retrieved: 22-01-2018

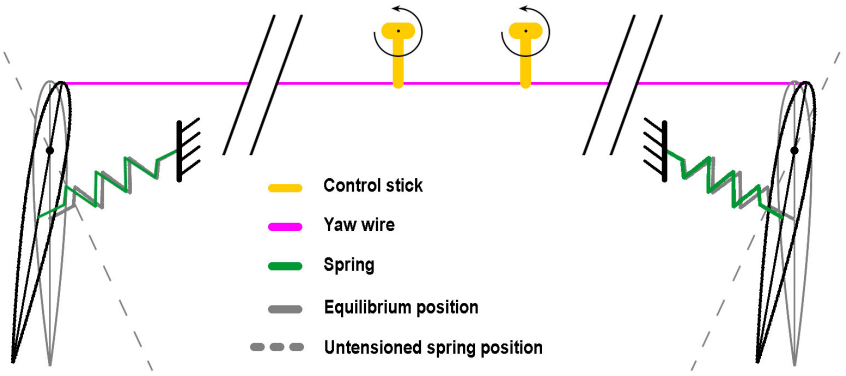

Figure 8.14: The rudder mechanism for yaw control

Where C_{n_e} is the yaw moment coefficient with respect to change in thrust due to one engine out and C_{ℓ_e} is the roll moment coefficient with respect to change in thrust due to one engine out by the only one engine active. These are found using the method given in reference [17] to be $C_{n_e} = 0.0675$ and $C_{\ell_e} = 0.0004$. To keep level flight, $\varphi = 0$ and for straight flight $\beta = 0$. When these are substituted into Equation (8.12) the system reduces to the rudder deflection need as:

$$\delta_r = -\frac{C_{n_e}}{C_{n_{\delta r}}} \tag{8.13}$$

and the wing warp deflection as,

$$\delta_a = \frac{C_{\ell_e}}{C_{\ell_{\delta a}}} \tag{8.14}$$

The rudder deflection needed when one engine fails is $\delta_r = 5.7°$. At this deflection one rudder will generate a side force of 35.8 N. The rudder mechanism is illustrated in Figure 8.14. The concept contains a pre tensioned spring that will be attached to the trailing edge of main wing at a rib location and connected to the trailing edge of the rudder surface. When the pilot rotates the control stick, the wire will pull one spring further into tension and deflect the rudder. The other side of the wire is loosened so that the pre tensioned spring will pull this sides rudder to deflect in the same angle as the other side. When the pilot releases the control sticks the rudders will return back to the neutral position due to the springs seeking equilibrium and helped by the aerodynamic forces. The exact location to where the hinge of the rudder is placed is not decided yet. Also the angle of spring relative to rudder is not optimised due to lack of time. In future work the hinge moment can be found when the hinge and spring location are identified.

8.5.4 Control sticks

Both roll and yaw control make use of cables to actuate or twist the control surface. These cables are connected to two control stick which are designed such that they give the pilot a intuitive and sporty way to control the *AerGo*. A wire system is used for its simplicity over electronic or hydraulic systems and the input forces required can be managed by properly designing the control stick. It is known from Figure 8.12 and Figure 8.13 that for a 10 deg/s^2 roll acceleration 200 N needs to be exerted on the control wire. This force is reduced by having the wire attached at half the distance to the control stick hinge as the handle. However the travel required is now increased. From Figure 8.11 it is found the the displacement of the control wire for the discussed situation is 60 mm. Doubling this is still easily manageable by the pilot. The two sticks are connected to each other by the continuing control cables as seen in Figure 8.15b. This is because then the forces are distributed over the two sticks making the required stick force for a roll acceleration of 10 deg/s^2, 50 N. The linking of the control sticks also allows the controls to be held in place by one hand so the other can be used to adjust the throttle. Finally this will make sure the sticks can not be moved back or forward simultaneously which will make it more comfortable to control the pitch by weight shifting.

The yaw wire is connected to the same control sticks, but at the height of the hinge so that roll input will minimise the yaw wire displacement. The exact stick forces for yaw are considered outside the scope of the project, but very rudimentary analysis showed that the magnitude will be in the order of 20–40 N. Figure 8.15a shown the basic layout of one of the control sticks, where also a knob can be seen to make creating a turning moment easier.

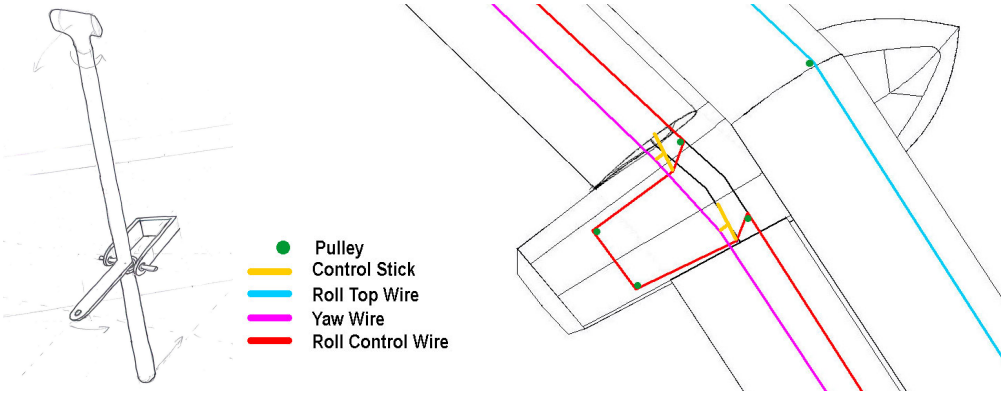

(a) Control stick (b) Control wire connection to sticks

Figure 8.15: The control stick and the cable of the control mechanism

8.5.5 Mass of control system

The control system consists of cables, pulleys and 2 control sticks. Their weights are listed in Table 8.1. Here it can also be seen that the total wire is 44 m, 2 times the span for roll and once for yaw. Adding 4.6 meter for the diagonal lengths at the end plates and 1.2 meter for the swing seat. *Dyneema* kite lines are chosen as control cables, because they have enough strength, small elongation, are lightweight and abrasion resistant. Existing lines of 4.8 mm have a breaking load of 2200 N [(2)]. Also the pulleys will be sources from the kiting industry. Pulleys with breaking loads of 3000 N weight only 6 gram [(3)]. The control sticks are harder to estimate the weight for as they are not designed in detailed yet. Their length has to be approximately 30 cm to provide enough travel in the control cable while keeping the travel on the pilot side ergonomically sensible. The approximated weight for the two control sticks and seat is 2.8 kg, setting the total control system weight at 3.8 kg.

8.6 Verification and Validation

The verification for the stability analysis starts by comparing the two programs used to find the stability derivatives. Looking at the results obtained using DATCOM and comparing that to the output of the AVL program (see Table 8.3 it can be said that they compare well. DATCOM as mentioned before is made by the USAF, this can be taken as a reliable source since it is based on 60 years of experimental data and experience. This indicates that the stability coefficients that are used in the dynamic model are suitable and can be taken as reliable. The analytical stability coefficients are verified by first evaluating them on paper, later inserting them into MATLAB and comparing results. There should be minor difference between these two results. If an error is identified the function used for this specific value is checked in MATLAB and on paper once again. The procedure is repeated until results overlap each other.

The dynamic model that is written into MATLAB contains many variables and functions, it could easily contain a typo in the code. Verifying this by hand can be a tedious and time consuming job. The choice of descent stability coefficients already eliminates the accumulation of some errors in the calculation. To be very sure that the simulation performed with the self written code is functioning right, the program AVL is used for a dynamic stability analysis with visualisation. All the eigenvalues can be obtained in AVL as well as the eigenmotion can be studied visually in real time. The AVL model analysis are are also stable except for one, the spiral mode which has a slightly positive real part, see Figure 8.16. The eigenmotion for the lateral stability case were not evaluated in such detail in the self written model as AVL does, however this can be used as additional information. It is also profitable to know that in the lateral motion the *AerGo* shows stable behaviour in AVL as it does in the MATLAB model.

[(2)] `https://www.teufelberger.com/pub/media/contentmanager/content/downloads/15-08-13_TEUFELBERGER-Kitelines-2015-2016_web.pdf`, Retrieved: 22-01-2017

[(3)] `https://www.jonnieeisler.com/sspage-repair_pictures-bladder_repair_pictures-kite_pulley_blocks_and_bridle.html`, Retrieved: 22-01-2018

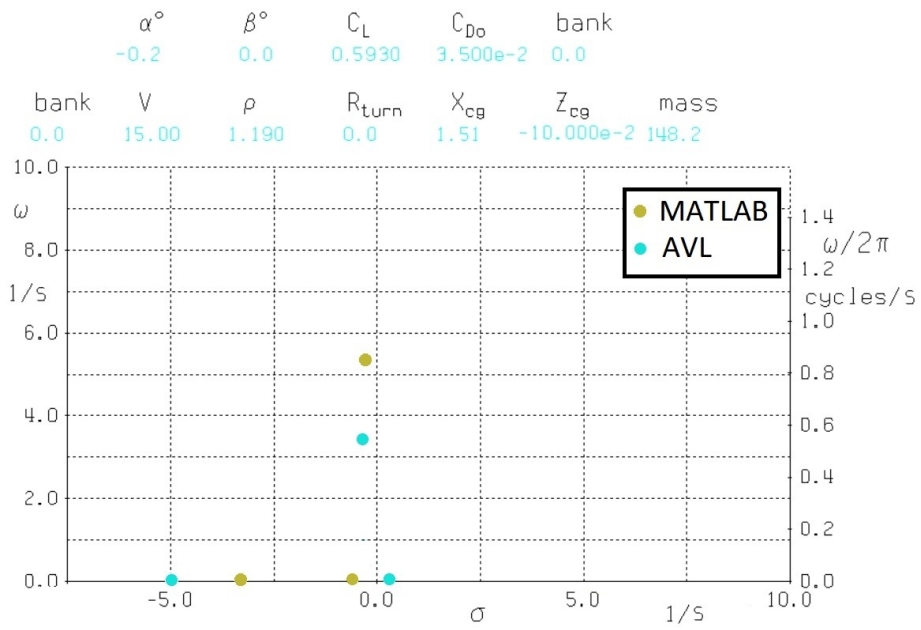

Figure 8.16: The eigenvalues found in the self written code in MATLAB compared to the eigenvalues from AVL plot for the symmetric case, condition are stated on top

To back up these the obtained results even more, another program (XFLR5) that can perform stability analysis and is partially used as a sanity check. This program is also used in the midterm report to model different configurations and compare their aerodynamic characters [5]. This time it also is used to verify the mass moment of inertia. XFLR5 calculates the moment of inertia of the upper and lower wing automatically, it is also possible to insert extra point masses to the aircraft that model subsystems as point masses. Verification for mass moment of inertia is done by comparing the calculated inertias from MATLAB with the ones from XFLR5. The validation is done by using a NACA report that compares existing reference aircraft to their ratio of gyration to empty mass [13]. The ratio of gyration are then rewritten into mass moment of inertia and compared to the MATLAB model. The results for moment of inertia are represented in Table 8.7. The disadvantages for using the NACA report is that it does not contain any aircraft with similar mass to the *AerGo* and that dates back to 1940. To get an estimate of the radius of gyration interpolation is done on the linear regression line given in the report. This of course introduces a certain uncertainty, however the intention here is to get a guideline.

Table 8.7: Results for the moment of inertia estimated with different methods

Moment of inertia	**Calculated**	**XFLR5**	**NACA report**
I_{xx} $[kgm^2]$	213.4	352.5	194.2
I_{yy} $[kgm^2]$	97.0	78.3	98.1
I_{zz} $[kgm^2]$	243.1	347.2	236.4

The control system has different procedure for verification, it is more practical than for the stability. Since a variety of control mechanism can be very complex, the intuitive sense of the engineer is not always enough to be sure that it works like it should. For this reason the control mechanism is build with LEGO™ Technics™ to backup the intuitive sense and see if the design on paper also behaves as expected. Once build, the control engineer studies the mechanism by applying physical inputs to it. Often the mechanism behaves different than expected, so readjustments are done until the desired mechanism is obtained. Also a glider pilot is approached to evaluate the feasibility of the overall control system. Unfortunately a glider pilot is not familiar with weight shifting as a control. However the total system was evaluated to be plausible. The most critical flight phase for the control system will be the approach, here the pilot has to input many small corrections to counter the near ground turbulence. The roll and yaw control are assumed to be sufficiently sensitive with low enough stick forces. However the consulted pilot could not evaluate this for the pitch control. [(4)]

[(4)] Interview with glider pilot: Bart Hermans, 29-01-2018

8.7 Conclusion and Recommendations

The aim of this chapter was to go into detail of the stability analysis and come up with a suitable control mechanism for the *AerGo*. The most important variable that determines stability of the *AerGo* is the centre of gravity which is designed to be at 1.51 m from the reference frame, the nose of the hull, for a trimmed cruise flight. A 100 kg pilot has a 67% contribution to the total aircraft mass and influences the CoG position the most since pilot weight shifting has been decided for pitch control. The relaxed pilot position during cruise is 1.6 m. This position can be varied by adjusting the swing seat forward and rearward for different pilot masses. Since the pilot position is as crucial to the CoG location for stability it is recommended that further research and simulation is done on this. Physical experiments for pilot weight shifting with additional *g* forces should be performed to understand how it will feel and how difficult it actually is to move the body during flight. The wing geometry of the *AerGo* has stagger and sweep to shift the aerodynamic centre apart to create a balanced seesaw for longitudinal stability. The sweep of both wings is 15° to offset the rudder rearward to have enough rudder effectiveness during an engine breakdown. A 7° sweep angle is the minimum angle needed to obtain weather cocking behaviour. A positive stagger is chosen, the upper wing shifts forward with 0.45 m. To obtain lateral stability a dihedral angle of 5° is chosen, an angle of 3° would suffice for aerodynamic stability. Dynamically the *AerGo* is more stable during cruise than during take-off, both regimes are deemed stable. The decrease in stability during take-off comes due to the lower velocities flown. The simulation results with the self written model compared well with the ones obtained from AVL model. Both show that in the symmetric case the *AerGo* has a highly damped short period motions and a low damped Phugoid long period motion.

A recommendation for future is to make use of the Aerospace Toolbox of Simulink (MATLAB) which contains everything for a dynamic stability analysis. This software has a more elaborate existing model already incorporated that is verified. It is easy to use since it visualises the variables in little boxes of a flow chart and the user can drag and drop them in the wanted location. The Aerospace Toolbox in Simulink is also compatible with the DATCOM software where the data can be imported directly into the model which could saves analysis time.

To control the aircraft a 3 axis control system is chosen. The pitch is controlled by weight shifting. This is made possible by positioning the pilot on a swing seat where forces can be exerted to move the CoG. For roll control wing warping is selected. This uses the biwing geometry to twist the wingtips compared to the wing root. A force of 264 N is needed on the control cable to twist the port side wing tips with 6° resulting in a roll acceleration of 13.5 $°/s^2$. Because the pilot has to shift his weight it is desired to combine the other 2 control axis into a single easy to use control mechanism. Two side control sticks are chosen. They move opposite forward and backwards for roll control while twisting them identically will control the yaw. The cables and pulleys used are from the kiting industry and the entire system weight is estimated to be 3.8 kg. Since it is not entirely sure how easy the weight shifting will work in all different flight regimes, it is recommended that other possibilities are also explored further. The idea of adjusting the roll wire loop and its controls to also be able to handle warping of both sides to the same direction is attractive. However the wire system will have to be adjusted to cope with the shortening of one wire while the other needs to extend. Also the control force calculations can be done more accurate by reducing the number of assumptions. For instance connecting the cross wires to the leading edge instead of the centre of twist. The swing seat can also be reevaluated. A rolling seat with springs to centre it can be beneficial because then the springs can be changed to account for the weight of the pilot. This might not be too much more weight as well.

9 Structures and Materials

The aircraft structure is a key component in providing a safe and efficient design. Specifically for this design, a large wing area at low wing loading together with a structure that can be disassembled had to be provided. First, in Section 9.1 the approach of the problem is defined and the assumptions made are listed. Section 9.2 describes the results of the wing analysis, starting with a material selection, followed by the spar, stringer and rib design and ending with a description of the connecting mechanisms. Section 9.3 describes the analysis of the hull structure, including results for the stringers and ribs. Finally, in Section 9.4 other relevant members that need sizing are discussed. The models used are verified and validated in Section 9.6 and the chapter is concluded in Section 9.7.

9.1 Approach

In this section the problem for the wingbox, ribs and hull is defined, presenting the load cases, assumptions and relevant theory.

9.1.1 Wingbox problem statement

During flight the aircraft experiences an ultimate load factor of 4 g and −2 g. Using a safety factor of 1.5, as specified by the requirements, this leads to ultimate load factors of 6 g and −3 g. These instances are treated as a static problem of which the forces on the aircraft include the weight of the aircraft as point load in the centre, the lift of the wings and the forces exerted by the engines. The plates at the wing tip are hinged, meaning the two wings are modelled as two beams where the tips are constrained to remain at equal distance to each other.

For this problem a number of assumptions have to be made in order to solve it. The assumptions and their effect on the results are given in a list below.

- Assumption: The weight of the wing is assumed constant along the wingspan.
  Effect: The wing weight is larger at the root which means the bending relief in the calculations is more than it actually is.
- Assumption: The lift force can be modelled as a $c\sqrt{x}$ function. The force due to drag is a fraction of the lift force, given by the lift- to drag ratio.
  Effect: The forces experienced during flight might be different to the lift distribution designed for. For example, the increased lift due to the propeller air flow was not taken into account.
- Assumption: The elongation of the vertical stiffener at the tip of the wings is considered negligible compared to the deflection of the wing tips.
  Effect: Since in reality the deflection of the tips is multiple orders of magnitude higher this will not affect the design.
- Assumption: For the wing box stress analysis, only the stringers contribute to the area moment of inertia.
  Effect: The inertia is lower meaning that the stress accounted for is higher than what is actually present.
- Assumption: All shear stresses are carried by the shear plates of the wing box, loaded through the shear centre.
  Effect: Small imperfections or changes in geometry might lead to premature failure.
- Assumption: The ribs located in the wing structure have been sized using the Von Mises failure critia
  Effect: As the material used is of anisotropic nature the dimensions of the ribs might need some adjusting in order to prevent failure at maximum applied loads.
- Assumption: The effects of deflections and rotations were not taken into account.
  Effect: Loadings might be different in practice.

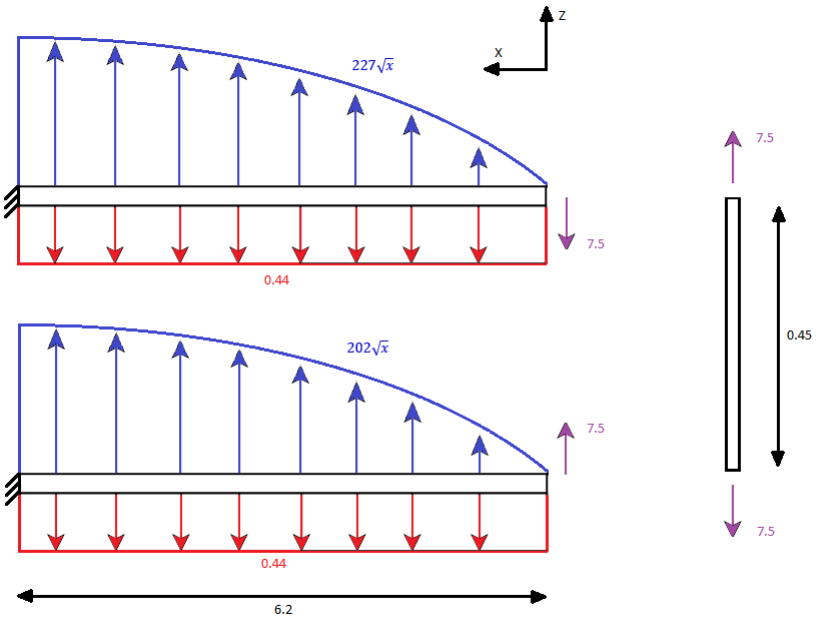

Figure 9.1: Loading diagram

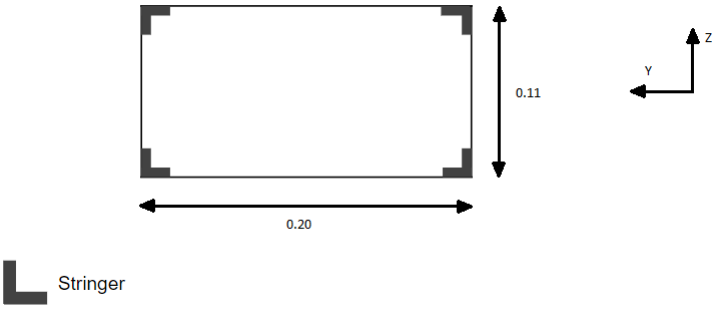

Figure 9.2: Wingbox cross section

The wing is modelled as a cantilever beam clamped at the root with a length equal to half the span ($b/2$) plus the extra component due to the sweep, resulting in a total spar length of $L_{sp} = 6.2$m. Figure 9.1 shows the lift distribution as function of x along the span, from tip to root. It is assumed to be:

$$EI_{A,xx}\left(\frac{d^4v}{dx^4}\right)_L = c \cdot \sqrt{x} \tag{9.1}$$

which is a close representation of an ideal lift distribution as shown in Figure 9.1. The constant c is different for the top and bottom wing, as the top wing produces around 12.7% more lift. It was determined that $c_{Top} = 227$ and $c_{Bot} = 202$. Using the method of integration [15] the shear force, rotation and deflection can be determined. For the shear force it is equal to:

$$EI_{A,xx}\left(\frac{d^3v}{dx^3}\right)_L = \frac{2}{3}cx^{\frac{3}{2}} + D \tag{9.2}$$

where $D = 0$ since no shear force acts at the wing tip. Integrating again yields the moment distribution:

$$EI_{A,xx}\left(\frac{d^2v}{dx^2}\right)_L = \frac{4}{15}cx^{\frac{5}{2}} + E \tag{9.3}$$

where $E = 0$ as no moment acts at the wing tip. Another integration leads to the rotation:

$$EI_{A,xx}\left(\frac{dv}{dx}\right)_L = \frac{8}{105}cx^{\frac{7}{2}} + F \tag{9.4}$$

which is assumed to be zero when $x = L_{sp}$ and hence leads to $F = -\frac{8}{105}cL_{sp}^{\frac{7}{2}}$. Finally, the deflection can be found by integrating one more time:

$$EI_{A,xx}v_L = \frac{16}{945}cx^{\frac{9}{2}} - \frac{8}{105}cL_{sp}^{\frac{7}{2}}x + G \tag{9.5}$$

and inserting $v = 0$ when $x = L_{sp}$ to find $G = \frac{8}{135}L_{sp}^{\frac{9}{2}}$. This results in:

$$EI_{A,xx}v_L = \frac{16}{945}cx^{\frac{9}{2}} - \frac{8}{105}cL_{sp}^{\frac{7}{2}}x + \frac{8}{135}cL_{sp}^{\frac{9}{2}} \tag{9.6}$$

For the weight as a uniformly distributed load and the force P_y the worked out equations can be taken straight from [15], where the deflection equation for the weight is given by:

$$EI_{A,xx}v_w = -\frac{wx^2}{24}\left(x^2 - 4L_{sp}x + 6L_{sp}^2\right) \tag{9.7}$$

And the deflection equation for the force P_y results in:

$$EI_{A,xx}v_{P_y} = -\frac{Px^2}{6}\left(3L_{sp} - x\right) \tag{9.8}$$

By using superposition, all deflections can be added resulting in a total deflection of:

$$EI_{A,xx}v_{total} = EI_{A,xx}\left(v_L + v_w + v_{P_y}\right) = \frac{16}{945}cx^{\frac{9}{2}} - \frac{8}{105}cL_{sp}^{\frac{7}{2}}x + \frac{8}{135}cL_{sp}^{\frac{9}{2}} - \frac{wx^2}{24}\left(x^2 - 4L_{sp}x + 6L_{sp}^2\right) - \frac{Px^2}{6}\left(3L_{sp} - x\right) \tag{9.9}$$

9.1.2 Rib problem statement

For the design of the load carrying structure the span wise lift distribution is considered. This structure is carrying the stresses that arise from the span wise loading. As there is a distribution in the span wise direction, so is there in chord wise direction. A load carrying structure is to be designed for this. A rigid skin connected to the span wise structure is a conventional solution to this problem. However, as the design is striving to be lightweight, a rigid skin will bring too much weight to the structure. Using lightweight fabrics as skin material is more in line with the design philosophy, but this means that a chord wise structure should be implemented to carry the chord wise loading. The chord wise loading is split into two structural problems. First, the structure is to transfer the distributed lift force to the span wise structure, which transfers it to the center of gravity, which is used to counter act the weight. Second is to withstand the compression introduced by upper and lower surface pressure. This compressing force tries to flatten the shape of the airfoil, hence the chord wise structure should maintain the shape of the airfoil.

To uphold the design philosophy, ribs are placed on an interval in span wise direction. Ribs are chord wise structures which are shaped to the airfoils profile. Each rib has an effective load carrying area of one interval, half an interval on each side, to account for the entire wingspan. This implies that the forces used for the rib design are multiplied by this effective area, but also requirement **WFH-Sys-SM01** (found in Chapter 5) is taken into account. The forces acting on a rib are that of the pressure distribution, of the span wise location, multiplied by the effective area. The pressure distribution of the span wise location is assumed to be constant over the effective area and equal to the span wise rib location. When the force distribution is known, Euler-Bernoulli beam theory (used in Equation (9.1) through Equation (9.3)) is used to analyse both the structural problems.

For the first case the rib is modelled as a beam vertically constraint at the connections with the span wise structure, R_{conI} & R_{conII}, and submitted to a lifting distribution, visualised in Section 9.1.2. The deflection of the span wise structure is assumed to be zero between two consecutive ribs. This causes the stress near the points of constraint to be relatively higher than reality. Where in reality the span wise structure has a small deflection, it stores part of the energy that causes the stress near the points of constraint. Thus in reality the stresses will be lower near these points. Another assumption is that the span wise structure does allow for rotation around points of application, as the span wise structure is not directly connected to chord line. The effect of this assumption is that the problem is now statically determinate. By using force and moment equilibrium, one can deduce an internal shear and moment distribution, from which the internal stresses are obtained.

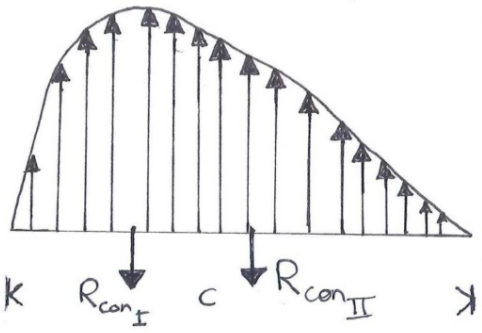

(a) Chord wise lift distribution constraint to span wise structure, indicated by two point forces R_{con_I} & $R_{con_{II}}$

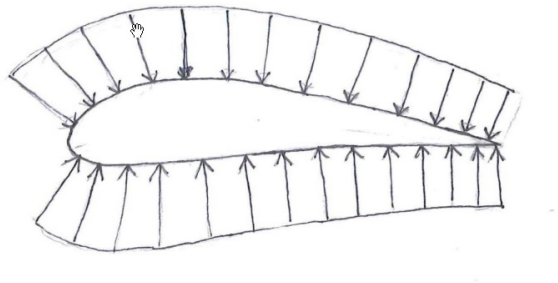

(b) Distributed compression force load case for wing rib

Figure 9.3: Load cases of the rib

For the second loading case, visualised in Figure 9.3, the rib structure endures a compression force the size of the upper surface pressure times the effective loading area of the rib. This force counteracts an equally sized fraction of the relative higher force on lower surface of the airfoil, the resultant is considered the lift force of the airfoil, used in the first load case. The pressure distribution is obtained from the aerodynamics of the airfoil. In the case a thin walled structure is to be designed for the wall members will be of circular nature, thus stress through bending is then obtained from:

$$\sigma = \frac{My}{Ae(r-y)} \tag{9.10}$$

where M is the bending moment acting on the segment with area A, r the radius of neutral axis, e the distance from the centroidal axis to the neutral axis and y the location of the element the stress is calculated for measured from the centroid.

Through discretisation of the chord wise structure, the internal stress on each unit segment can be calculated. These finding are used to find the 2D Von Mises stress in each unit segment:

$$\sigma_v = \sqrt{\sigma_x^2 + \sigma_y^2 - \sigma_1\sigma_2 + 3\tau_{xy}^2} \tag{9.11}$$

where τ_{xy} is the in-plane shear stress and $\sigma_{x,y}$ are the resultant stresses acting on the segment in x & y-direction, respectively. When σ_v is found to be higher than the materials yield stress σ_y, the structure is considered to fail. In the same analogy this is true for the ultimate stress of the material.

The overall governing approach for the design of chord-wise structures is to find a layout that complies with the span wise structure, as this is the main load carrying structure of the entire aircraft. The structure was discretised and the stresses acting in each segment were calculated to obtain dimensions of the layout such that the Von Mises for every segment does not exceed the yield stress of the material used.

9.1.3 Hull problem statement

The aircraft is descending and it hits the water at a flight path angle of zero degrees with a vertical deceleration of 2.33g [31]. At that point the forces are modelled and treated as a static problem, as visualised in Figure 9.4. For simplicity the cross section of the hull is drawn as constant in the loading diagram. However, in stress calculations the actual cross section along the length is used. The cross section of the hull is shown in (Figure 9.5), where dimensions have been left out intentionally, because they change over the length of the hull.

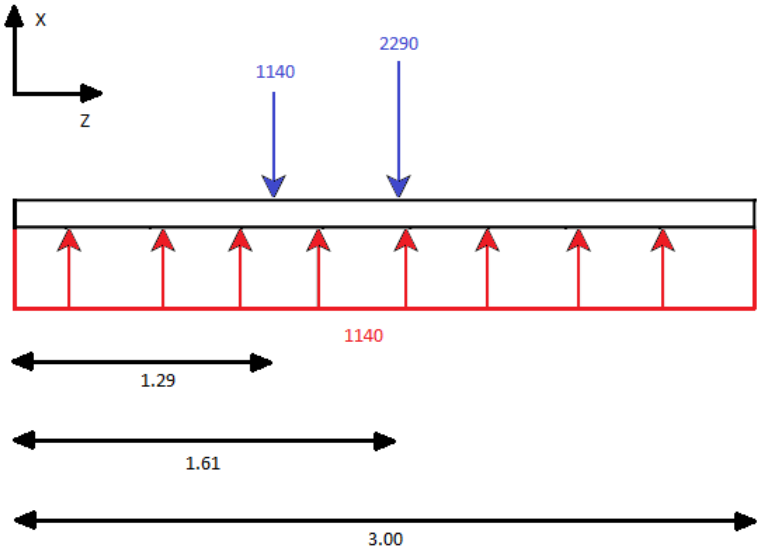

Figure 9.4: Hull loading diagram

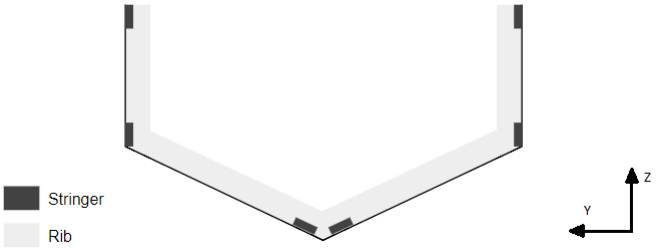

Figure 9.5: Hull cross section

The forces on the hull include the weight of the aircraft, W_a, the weight of the pilot, W_p, and the uniformly distributed load, B, caused by the Buoyancy. The corresponding distances x_a and L_h are fixed and used to determine x_p by equating the moment about x equal to 0:

$$M_0(cc+) = BL_h \frac{L_h}{2} - W_a x_a - W_p x_p = 0 \tag{9.12}$$

which leads to:

$$x_p = \frac{BL_h \frac{L_h}{2} - W_a x_a}{W_p} \tag{9.13}$$

Similar as for the wingbox problem a few assumptions are made to simplify the analysis. The assumptions and their effect on the design are stated in the list below:

- Assumption: The buoyancy is constant over the length of the hull.
  Effect: In reality the peak values of the shear force and moment are slightly higher and on a different location.
- Assumption: The weight of the pilot can be modelled as a point force on the hull.
  Effect: Modelling the pilot weight as a distributed load would result in a lower peak moment, meaning that the system might be slightly over designed when only considering this assumption.
- Assumption: The rotation and deflection at the centre of gravity is zero.
  Effect: This will not effect the design directly at this stage but the way deflection and rotation is visualised. In a later stage one might look at the effect of deflection on e.g. hydrodynamics.

9.1.4 Load distributions

Using the outcome of the problem analysis, load distributions can be made. The load distributions for the top wing are show in Figure 9.6. Each force is created either by external forces or internal forces. In Table 9.1 the force and its dependencies are given. Since the forces on the top wing are larger, the wing structure is designed for the top wing.

Table 9.1: Force dependencies

Force	**Influence**
Shear force in y	Thrust force, drag force
Shear force in z	Wing weight, wing loading distribution
Moment in x	Wing weight, wing loading distribution, sweep angle
Moment in y	Wing weight, wing loading distribution
Moment in z	Thrust force, drag force

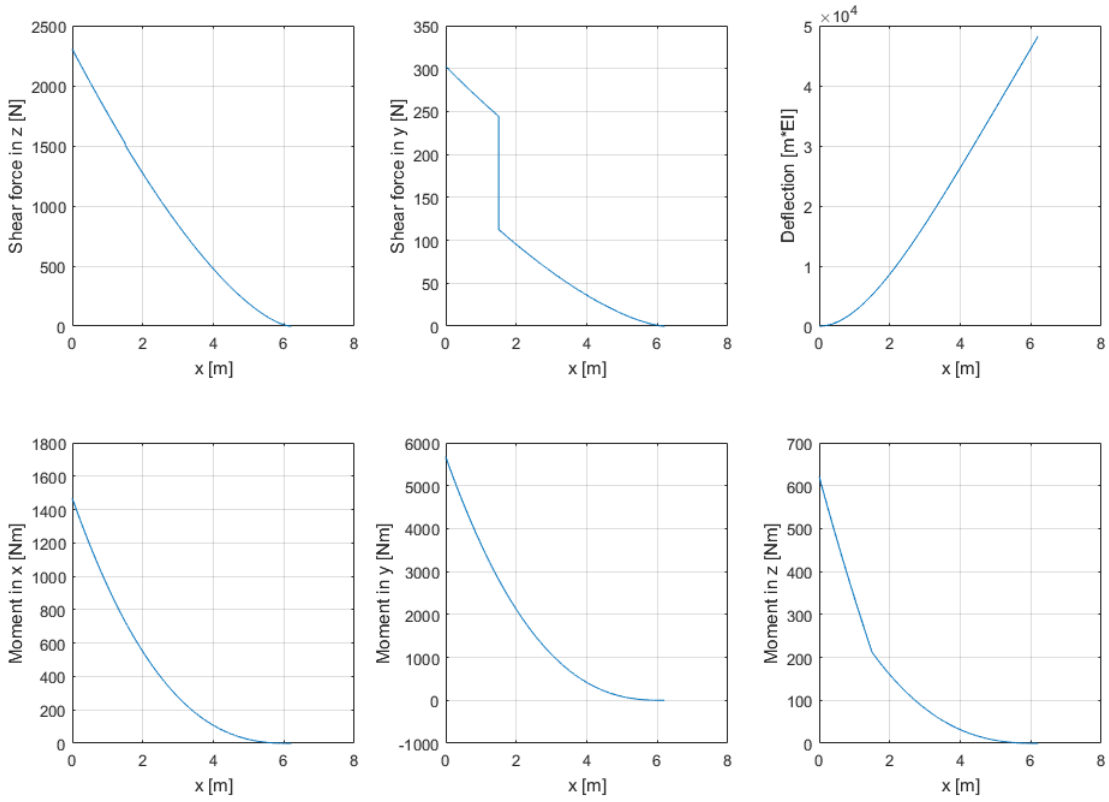

Figure 9.6: Load distributions of the top wing: Shear force in z direction(top-left), shear force in y direction(top-middle), deflection in x direction(top-right), torsion of the wingbox(bottom-left), moment in y direction(bottom-middle) and moment in z direction(bottom-right).

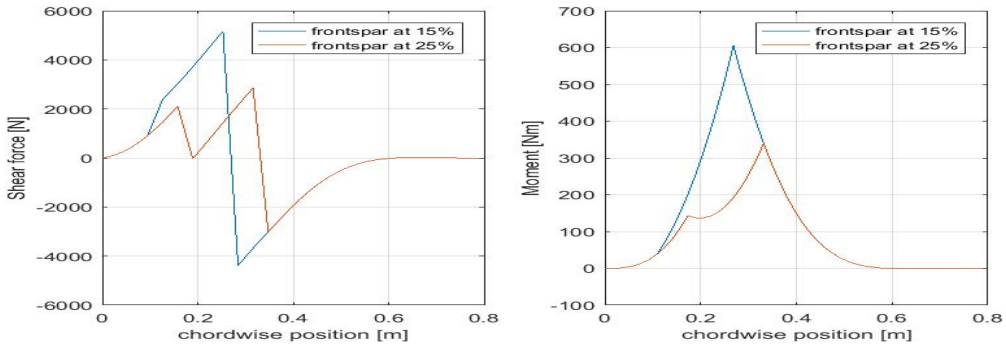

Figure 9.8: Shear(left) and moment diagram(right) constructed for two spar placements

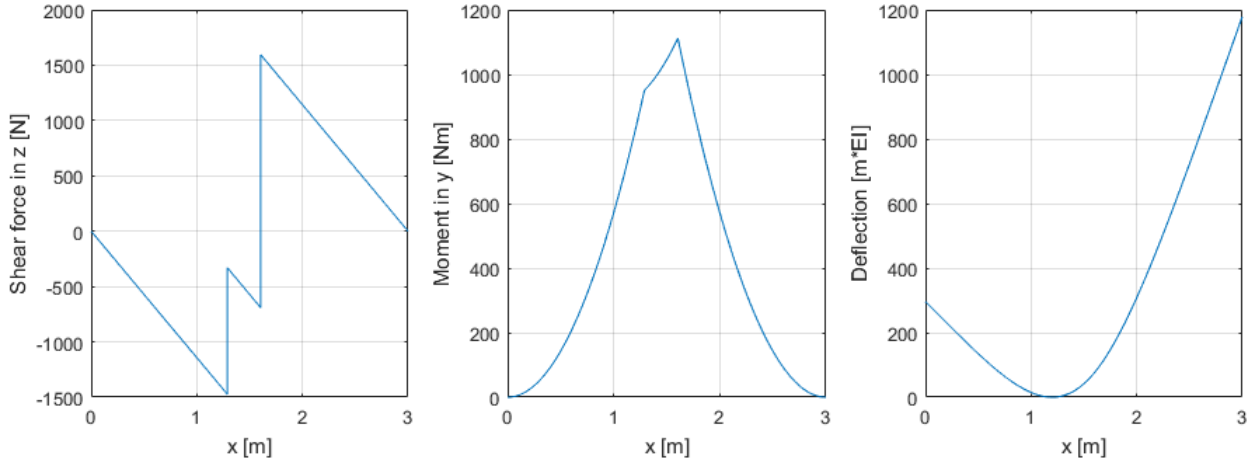

Figure 9.7: Load distributions of the hull: Shear force in z (left), moment in y (middle) and deflection (right).

Combining these variables with initial structural dimensions the first step in calculating stresses can be made.

The load distribution for the chord wise loading is highly dependent on the position of the constraints, being the connection with the span wise structure. A 20.% difference between front and aft constraint position is considered. This is to provide a large enough offset for the span wise structure in coping with the moment around the y-axis, introduced by drag and thrust. The magnitude of the lift distribution varies along the span but also with angle of attack. As the lift is always perpendicular to freestream, the force perpendicular to the chord is found by projecting the force vectors to the chord axis system using the angle of attack. Since the angle of attack is relatively small, the highest chord-wise lifting force are found during the $C_{L_{max}}$ configuration, 11°, located near the root of the wing. The shear and moment distribution for two different constraint positions are shown in Figure 9.8

Both diagrams consider the lift force during a 6 g flight phase. Having the constraints more aft results in a relatively flatter load diagram, which is more beneficial for the rib design problem in section 9.1.2. However, the rib design problem depicted in section 9.1.2 desires a support near the leading edge as the compression force is considered the highest there, reasoned from the location of the highest lift force.

9.2 Wing design

The design process of the wing is discussed in this chapter, including a material selection, spar and rib sizing as well as connecting mechanisms to disassemble the wing structure.

9.2.1 Material selection

A wide range of materials were initially considered for the main structure of this aircraft, especially since 90% of its weight need to be recyclable. The most promising options that were considered are aluminium, carbon fibre epoxy, glass fibre epoxy, balsa wood and bamboo. The mechanical properties of each are shown in Table 9.2.

Balsa and bamboo would be ideal in terms of sustainability, however, have a very low specific strength and stiffness compared to the other materials, making them unsuitable for main load carrying structures. Since it's a seaplane, rot and corrosion are also an issue, unless when used in a sandwich together with epoxy for example.

Aluminium is probably the most common material used in aviation and can also be fully recycled. The main downside is that it has a relatively low specific strength and stiffness compared to CFRP. One of the most relevant reference aircraft, the Easy Riser, uses aluminium and has an empty mass of 54 kg. This is with a combustion engine and without floats to take off from water, meaning it is unlikely aluminium will fulfil the weight requirement.

Composites such as carbon or glass fibre epoxy were considered to be superior to the other materials. Efficient use of the fibre properties allows for very light weight structures to be made. On top of that, epoxy is almost completely resistant to rot, making it a safer option for a seaplane. CFRP outperforms nearly every material there is, making it the ideal choice for light and stiff structures. The major downside of epoxy based composites is that they are very difficult to recycle and more expensive during production.

Table 9.2: Overview of material properties [30] [19] [34]

Material	**Density [g/cm^3]**	**Young's modulus [GPa]**	**Specific stiffness [MPa/kg]**	**Specific strength [kNm/kg]**	**Yield strength [MPa]**	**Tensile strength [MPa]**
Balsa wood	0.27	10.4	38.5	237	-	64
Bamboo	0.90	20.6	22.9	214	-	193
Aluminium 7075 T6	2.8	71.0	25.4	204	505	572
Carbon epoxy[1] (fibre direction)	1.7	135	129	447	-	1,500
E-Glass epoxy (fibre direction)	2.1	40.0	21.4	486	-	1,000

The skin does not carry any loads, but is a key part of the wing structure nonetheless. The main requirements for the skin were to be light, cheap, safe, and wind and water proof. Safe in this case means that a small puncture will not lead to a huge rip in the skin and that it does not buckle when the wing is bent, leading to potentially catastrophic turbulence on the airfoil. The material that best fulfils these requirements is rip-stop nylon such as Porcher's Skytex 27, weighing only 29 g/m^2 and costing 9.40 €/m^2.[2] It is a water repelling, windproof material that is common in kites and paragliders. Anything lighter would have been significantly more expensive and was therefore neglected. Stronger and more expensive material such as Dyneema or Dacron may be applied locally to reinforce prone areas. Around 38.5 m^2 of skin are required resulting in a skin weight of 1116.5 kg.

For the hull, a light material as is used for the wing is not suitable, as a small puncture will lead to the hull filling with water. A more durable fabric like Dacron is therefore preferred. Dacron is still relatively cheap at 13.90€ and weighing 170 g/m^2.[3] Since only a relatively small area is required to cover the hull the weight gain compared to ripstop nylon is only small.

9.2.2 Spar design

The spar not only makes up a significant portion of the wing weight but also carries most, or in this case all of the loads. Therefore it was the main focus of the structures department during the design phase.

Two main spar configurations were considered, namely rods and wing boxes. Rods have the advantage of being readily available on the market and are therefore cheaper. Assembly would also be easier with rods, as they can simply be stuck into each other and secured with a bolt or pin. Rods closely resemble the bones of birds and are the most common choice on human powered aircraft. Nonetheless, they were neglected for this design for multiple reasons, the first one being the resistance to torsion, which is not desired for wing warping (unless the entire wing rotates around the rod). Secondly, an optimised wing box can be significantly lighter and as weight is a driving factor it was decided to be worth the extra costs in production. Thirdly, rods are usually offered with constant thickness and are therefore not tailored effectively to the lift distribution along the wing.

In the end a custom designed spar was deemed necessary to meet the weight requirements. Instead of a wing box with closed cross-section, two separate C-shaped spars were chosen as this makes production and assembly easier.

[2] https://www.extremtextil.de/ripstop-nylon-gleitschirm-nylon-skytex-27-pu-beschichtet-29g-qm.html, Retrieved: 10-01-2018

[3] https://www.extremtextil.de/dacron-gewebtes-polyester-segeltuch-170-ll-mt-mit-kennfaden-170g-qm-2-wahl.html?number=71607.HLLBL, Retrieved: 19-01-2017

The two identical spars could be manufactured relatively easily on a flat surface while a closed wing box would require custom moulds. The C-shaped design also allows for the mechanical properties of composite materials to be exploited fully. The spar is comprised of stringers at the top and bottom and a flat plate connecting the two stringers, discussed in Sections 9.2.3 and 9.2.4 respectively. The stringers consist of unidirectional carbon fiber reinforced polymer (CFRP) that carry the tensile and compression forces that arise due to bending of the wing while the plate is designed to carry all the shear loads and is made up of glass fibre at ±45 degrees. Glass was chosen because the stiffness of CFRP was not really needed and glass offers a comparable specific strength at a much lower cost.

9.2.3 Stringer design

Several different stringer configurations were considered and are shown in Figure 9.9. Here the stringer dimensions are as shown in stringer number 4: a width and height of size B_s and a thickness of t_s. An L-configuration was chosen, because it is easier to produce than a T or I configuration but still offers a higher moment of inertia to achieve a higher buckling load. Also, an L-shape fits better into the ribs and will provide a larger adhesive bond area.

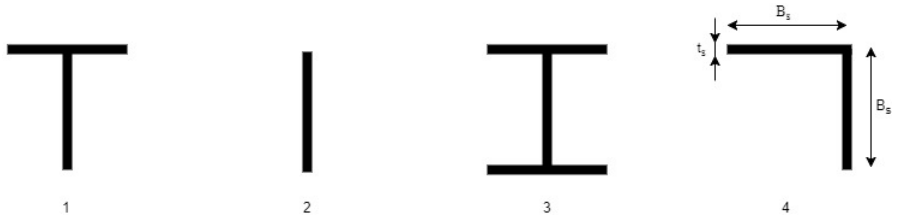

Figure 9.9: Stringer options

It is important that the stringers contribute to the inertia around the x- and y-axis in order to resist bending in both directions. The centroid location for the stringer is given by:

$$\begin{aligned} \bar{x} &= \frac{\sum A_s \ \tilde{x}}{\sum A_s} \\ \bar{y} &= \frac{\sum A_S \ \tilde{y}}{\sum A_s} \end{aligned} \tag{9.14}$$

where A_s is the area of an element and $\tilde{x}$ and $\tilde{y}$ are the distances to the respective reference axis. Now the area moments of inertia of one stringer can be found using:

$$\begin{aligned} I_{A,xx} &= \sum_{n=1}^{2} (A_s d_{yn}^2) + \frac{t_s {B_s}^3}{12} + \frac{B_s {t_s}^3}{12}) \\ I_{A,yy} &= \sum_{n=1}^{2} (A_s d_{xn}^2) + \frac{t_s {B_s}^3}{12} + \frac{B_s {t_s}^3}{12}) \end{aligned} \tag{9.15}$$

For the area moment of inertia of the complete wing box, where only the four stringers contribute, the equation changes to:

$$\begin{aligned} I_{A,xx} &= \sum_{n=1}^{4} (A_s d_{yn}^2) + \frac{t_s {B_s}^3}{12} + \frac{B_s {t_s}^3}{12}) \\ I_{A,yy} &= \sum_{n=1}^{4} (A_s d_{xn}^2) + \frac{t_s {B_s}^3}{12} + \frac{B_s {t_s}^3}{12}) \end{aligned} \tag{9.16}$$

where d_{yn} and d_{xn} are again the distances to the respective reference axis. The total bending stress is given by:

$$\sigma_z = \frac{I_{A,xx} M_y - I_{A,xy} M_x}{I_{A,xx} I_{A,yy} - I_{A,xy}^2} x + \frac{I_{A,yy} M_x - I_{A,xy} M_y}{I_{A,xx} I_{A,yy} - I_{A,xy}^2} y \tag{9.17}$$

where M_x and M_y are the moments about the x and y axis, respectively. Since the cross-section is said to be symmetrical, the area moment of inertia about the x and y-axis, $I_{A,xy}$, is equal to zero and it simplifies to:

$$\sigma_z = \frac{M_y x}{I_{A,yy}} + \frac{M_x y}{I_{A,xx}} \tag{9.18}$$

where $I_{A,yy}$ is the moment of inertia about the y-axis and $I_{A,xx}$ is the moment of inertia about the x-axis.

Next to failure from exceeding the maximum stress, failure due to buckling of the stringers was the driving failure mode during the design phase. The critical buckling stress is calculated by combining:

$$P_{cr} = \frac{\pi^2 E I_{A,xx}}{L_s^2} \tag{9.19}$$

and:

$$\sigma_p = \frac{F_p}{A_s} \tag{9.20}$$

and rewrite this into:

$$\sigma_{cr} = \frac{\pi^2 E I_{A,xx}}{A_s L_s^2} \tag{9.21}$$

where E is the Young's Modulus, I is the Inertia, A_s the area and L_s the length of the section of the stringer, which is determined by the rib spacing. Using equation Equation (9.21) the ribs can be placed in a way such that the stringers do not buckle under the perceived loads. For a given wingbox height, width and stringer dimensions the bending stress distribution is shown in Figure 9.10.

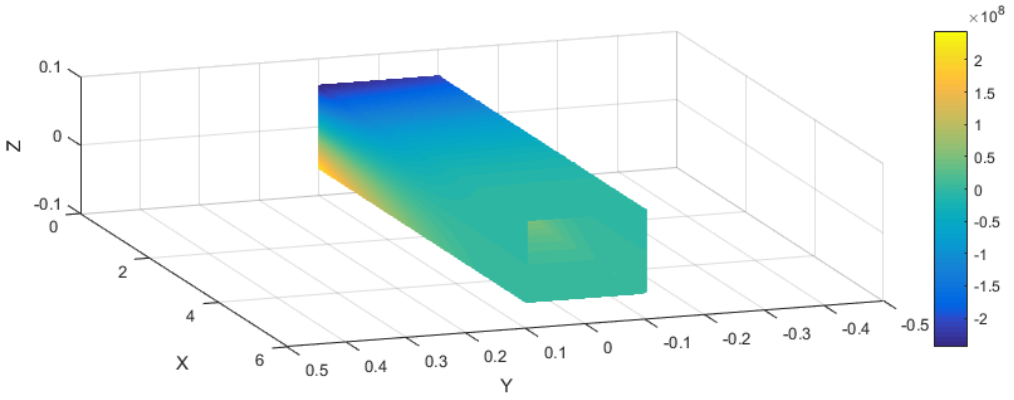

Figure 9.10: Bending stress in the top wing [Pa]

9.2.4 Spar web design

The shear forces are carried entirely by the vertical plates of the C-spars. There are two main contributions, the force created by the lift as described by 9.2 and the shear arising from the torque applied to the wing. Since the aerodynamic moment acts in opposite direction to the torque caused by the sweep and is much smaller in magnitude, it was neglected to simplify the analysis. The centroid of an elliptic distribution was determined to be at $\frac{3}{5}L_{sp}$ from the wing tip or $\frac{2}{5}L_{sp}$ from the root. A moment is calculated by multiplying a force by its arm, together with 9.2 this leads to:

$$M(x) = \frac{2}{3}cx^{\frac{3}{2}} \cdot \frac{2}{5}L_{sp}\sin 15$$

$$M(x) = \frac{4}{15}cx^{\frac{3}{2}}L_{sp}\sin 15 \tag{9.22}$$

where the sine component accounts for the sweep. A closed cross-section was assumed, leading to the relation:

$$M(x) = 2A_{cross}q \tag{9.23}$$

where A_{cross} is the area of the cross-section of the wing box and q is the shear flow, equal to the shear stress times the thickness:

$$q = \tau t \tag{9.24}$$

Using 9.23 and 9.24 and rearranging gives:

$$t_{torque} = \frac{M(x)}{2A_{cross}\tau_{max}} \tag{9.25}$$

which is the required thickness to withstand the given torque. The variable τ is the maximum shear stress of the material, in this case glass fibre epoxy with $\tau_{max} = 150$ MPa [(4)].

The shear force due to lift was assumed to be distributed evenly between the two spars in each wing. The required thickness can be found using:

$$\tau_{avg} = \frac{V_y}{A_s} \tag{9.26}$$

and

$$\tau_{max} = 1.5\frac{V_y}{A_s} \tag{9.27}$$

where V_y is half of the shear force given by 9.2 and A_s is the area carrying the load. The factor of 1.5 is included to account for the maximum shear stress in the middle of a rectangular cross-section [15]. Inserting $A = ht$ and rearranging gives:

$$t_{lift} = \frac{1.5V_y}{h\tau_{max}} \tag{9.28}$$

where $h = 110$ mm, the height of the spar. The subscripts "torque" and "lift" are added to avoid confusion of the two contributions. Finally, the thickness of the vertical members can be found using:

$$t_{tot} = t_{torque} \pm t_{lift} \tag{9.29}$$

Due to the direction of the torque the shear forces are in the same direction for the rear spar and opposite in the front spar, hence the plus-minus in Equation (9.29). Since the shear force varies along the span of the wing the thickness given in Equation (9.29) is a function of x and can be seen in Figure 9.11.

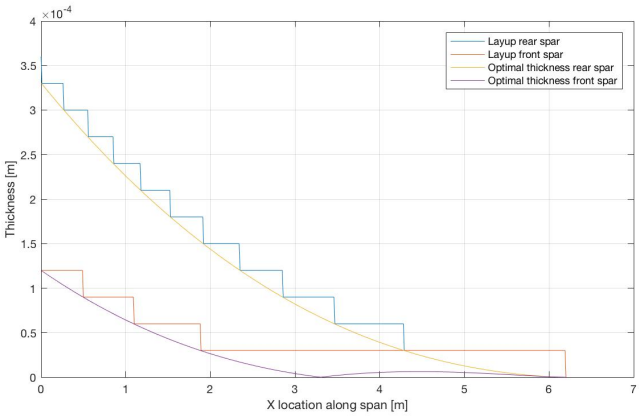

Figure 9.11: Thickness distribution of the shear plates from root to tip

Ideally, the thickness of the shear plates would vary as shown in Figure 9.11, however, that is not feasible from a manufacturing standpoint. Therefore, the curve was discretised into steps, where each bump represents one layer of glass fibre fabric. For this case, a minimum material thickness of 0.03 mm was assumed leading to 11 layers at the root for the rear spar and four in the front spar. The assumed minimum thickness is definitely on the lower end of the spectrum, but still within what can be bought on the market [(5)]. Using thicker material will give fewer steps and therefore drastically increase the overall weight. Applying the above layup to all four wing sections leads to a total weight of 1.95 kg of glass fabric, not including the unidirectional fibres in the stringer.

As a closed cross-section was assumed, shear also needs to be transferred in horizontal direction. During the analysis, the wing box was assumed to have horizontal plates on top and bottom, giving it a closed rectangular cross-section. The plate will be replaced by braced wires for the final design though, to allow for wing warping. While not

[(4)] `http://www.performance-composites.com/carbonfibre/mechanicalproperties_2.asp`, Retrieved: 14-01-2018
[(5)] `https://shop1.r-g.de/en/art/190100`, Retrieved: 17-01-2018

part of the structural analysis, the forces required for steering can be carefully controlled and kept within reason by varying the thickness and type of wire used.

For a more complete analysis on the wingbox webs the following equation was used [22]:

$$q(s) = -\frac{I_{A,xx}S_x - I_{A,xy}S_y}{I_{A,xx}I_{A,yy} - I_{A,xy}^2}\int_0^s txds - \frac{I_{A,yy}S_y - I_{A,xy}S_x}{I_{A,xx}I_{A,yy} - I_{A,xy}^2}\int_0^s t_{web}yds \tag{9.30}$$

Where S_y is the vertical shear force and t_{web} is the thickness of the web. Since the cross section is symmetric and only a vertical force is considered this changes to:

$$q(s) = -\frac{S_y}{I_{A,xx}}\int_0^s tyds \tag{9.31}$$

Making a cut at the bottom and moving from 0 to 1 and from 1 to 2 as shown in Figure 9.12 the shear flow can be computed. These shear flows can be mirrored to find the shear flow in the entire box.

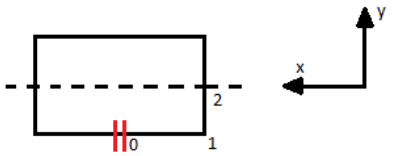

Figure 9.12: Shear flow in wingbox

The shear flow from 0 to 1 equals:

$$q_{01}(s) = -\frac{S_y}{I_{A,xx}}\int_0^s t_{web}yds = \frac{S_y}{I_{A,xx}}t\frac{h}{2}s \tag{9.32}$$

and the shear flow from 1 to 2 equals:

$$q_{12}(s) = q_{01} - \frac{S_y}{I_{A,xx}}\int_0^s t_{web}yds = \frac{S_y}{I_{A,xx}}(\frac{hw}{4} + \frac{h}{2}s - \frac{1}{2}s^2) \tag{9.33}$$

In the same manner the shear flow due to a horizontal force can be found. Using Equation (9.23) the shear flow due to a torque can be calculated. Adding all shear flows and dividing by the thickness gives the shear stress (Equation (9.24)). The shear stress distribution for a given wingbox height, width and stringer dimensions is shown in Figure 9.13.

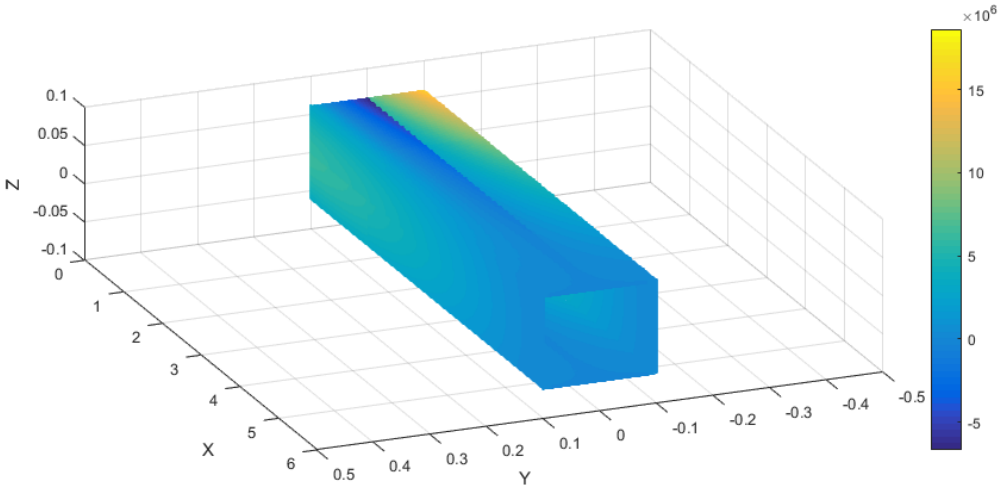

Figure 9.13: Shear stress in the top wing [Pa]

9.2.5 Rib design

Since there is a plurality of ribs in the wing structure, it is key to reduce the mass of the ribs as much as possible, whilst conserving functional tasks, prescribed in Section 9.1.2. A material or configuration should be chosen such that the structure does not deform under the loads present. An additional requirement is that the rib should be relatively easy to manufacture in bulk, at minimum costs. Now that the span wise structure is determined, the ribs are designed such that they comply with it. Two C-shaped spars run at constant offset to each other from root to tip. The spars allow for various connection options, as the C-shapes have a large continuous surface area on the back side of the C's.

With the aformentioned requirements in mind, the rib is chosen to consist out of one continuous piece of material, shaped to the airfoils profile. Since CFRP is a relatively stiff and lightweight material and the spars mostly consist of it, it is decided to be used for the ribs as well. The reason to use materials with similar specifics in a structure is that deformations are going to be of same order of magnitude. Also failure is relatively more predictable, reasoned by the saying that *you are as strong as your weakest link*. Two vertical members are placed at the same offset as the spars are wide, creating a box-like structure that hulls the C-shaped spars. The layout for the rib design is shown in fig. 9.14a.

(a) Wing rib layout consisting of one piece

(b) Manufactering mould for the rib, present is the sheared lower surface to account for the sweep of the wing

Figure 9.14: Wing rib layout(left) and its manufacturing mould(right)

The methodology of the analysis is elaborated on firstly, to be followed by the results. The results provide a Von Mises stress distribution for the most straining and relatively least straining load case. Deduced from this are the dimensions for the rib near the root and the rib near the tip of the wing.

The moment and shear diagram for the first loading case, section 9.1.2, are seen in Figure 9.8. Now that the layout is known, the internal bending stress, per cross-section of the rib, is calculated using Equation (9.18) as:

$$\sigma = \frac{M_c y}{I_c} \tag{9.34}$$

here, I_c is the moment of inertia for each cross-sectional plane and M_c is the moment distribution found in Figure 9.8. As the airfoils profile has an organic shape the moment of inertia varies along the chord.

As a first design step the cross-sectional shape of each surface is simply taken to be a rectangle with dimensions: rib width as width and skin thickness as height. Since the dimensions and thickness of the layout determine the moment of inertia of the cross-section, these are used as input for the analyses. As the rib is constraint to the spars in a box like structure, the neutral axis, where each cross-section will bend around, is assumed to run through the center of this aforementioned box, parallel to the chord line. This is reasoned by mentioning that the centroid of this rib-spar configuration is inside this box, accompanied by the shear center and thus the center of twist. This is mainly due to the relatively higher stiffness of the span-wise structure with respect to the locally attached rib. The Steiner-terms in the moment of inertia calculations for each cross-section are determined with respect to this neutral line. Using the chord-wise shear distribution from Figure 9.8, the internal shear stress is calculated in the same fashion using:

$$\tau = \frac{V_y Q}{I t} \tag{9.35}$$

where V_y is chord wise shear force and Q is the product of the area of the surface the shear stress is calculated for, A_s, and its centroid measured from the neutral axis of the airfoil.

The internal stresses for the compression load case are determined by dividing the airfoil into three sections. Section I is modelled as two quarter circles clamped at both ends submitted to a constant distributed pressure. Section II has the shape of a square box also loaded by a constant distributed pressure. Here the vertical members are assumed to take up the resultant of the distributed compression force acting on section II. Since the vertical members are attached to the spars, the compression load carrying capacity of the vertical members is allowed to be taken higher than it prescribes from its dimensions. Section III consist of, similar to section I, two doubly clamped

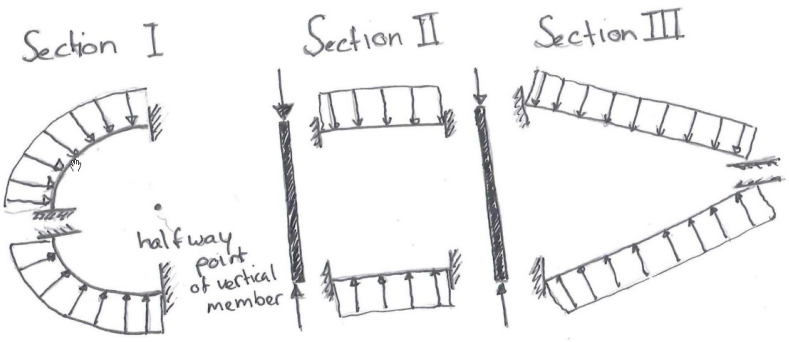

Figure 9.15: Decomposition of the compression load case for the rib into section I (front), section II (center) and section III(aft).

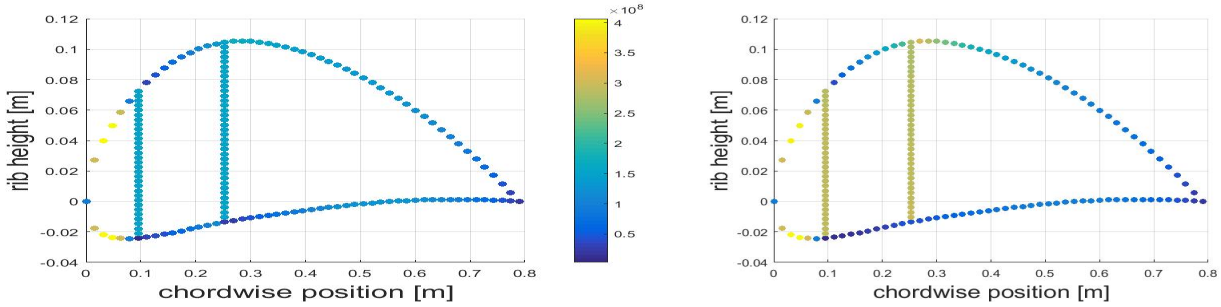

(a) rib located near root

(b) rib located near tip

Figure 9.16: Von Mises stress distribution for ribs near root (a) and tip (b) with dimensions such that the material yield stress is not exceeded

beams submitted to constant distributed pressure. The three sections with their loading case are depicted in Figure fig. 9.15.

The compression load case is converted into four statically indeterminate beam problems, two from section I and two from section III. The load diagrams (shear and moment) for these are obtained using Euler-Bernoulli classical beam theory by using symmetry and implying boundary conditions. Implying zero angle of rotation, $\frac{dv}{dx}$ at $x = 0$ & $x = \frac{L}{2}$, one obtains a value for the moment at the root. Implying zero deflection, $v = 0$, at $x = 0$ provides an equation for the moment distribution, which upon differentiating, gives the shear force distribution of the beam. For the load diagram of the curved beams in section I, the beams are at first considered straight with size the length of the curvature, and solved with the technique as stated above. With the moment and shear force distribution from the load diagrams, Equation (9.10) is used to determine the stress for a curved member. The radius of curvature is taken from the halfway point on the front spar(vertical member). The stress in the straight beams from section III are determined using Equation (9.34) applied to the beams cross-section. Shear stresses are computed in an orderly fashion using Equation (9.35). The compression force in section II acting on the vertical members is computed using Equation (9.20). The doubly clamped beam in section II is solved in same analogy as the beams in section III.

Now for each section the internal stresses for each discretised unit segment are obtained. Finding the resultant in x & y-direction, together with the shear stress, for each unit segment, provides the necessary input to determine the Von Mises stress, σ_v (Equation (9.11)), in each unit segment.

As was mentioned in Section 9.1.2 the effective area of the rib comes from the rib spacing. The rib spacing is determined from the buckling criteria for the stringers, which depends on the average weight of the ribs in one wing. This *chicken and the egg*-problem is solved by assuming an average rib weight and then iterate to the converging point. The results are shown and elaborated on below.

Figure 9.16 depicts the Von Mises stress distribution for both the rib near the root (most straining load case) and near the tip (least straining load case). Obtained from the stringer design, the rib spacing near the wing root was set on 150mm, whereas the maximum spacing towards the wingtip is found to be 1060mm. The thickness at the root for which the Von Mises stress does not exceed the compressive yield stress of CFRP (1200 MPa)[6] is shown in Figure 9.22. The compressive yield stress has been chosen over the tensile yield stress because CFRP yields due to compression at an earlier stage. The average thickness of the rib is given, where for the optimised case the

[6] `http://www.performance-composites.com/carbonfibre/mechanicalproperties_2.asp`, Retrieved: 14-01-2018

thicknesses per section (I through III) are not equal. Also In the table is the average of all the ribs present in the wing.

Also visible in Figure 9.16 is the Von Mises distribution for both the vertical members. One can see that the vertical members for the rib near the tip are experiencing a relatively higher stress than the vertical members for the ones near the root. This seems counter intuitive as the load case is considered less straining. But since the effective area for near the tip is almost eight times higher than for the root, it does not come as a surprise. One would argue that the lift at the tip is a fraction of the lift near the root. This is true however only by a factor of approximately 0.4 This critical feature of the tip rib can be prevented my either decreasing the rib spacing near the tip, or increasing the surface area of the vertical member. For both cases the vertical members have been checked on buckling by using Equation (9.21). For a rib width of 10 mm it was found that the vertical members require a thickness of 13 mm to prevent buckling in the vertical member located aft in the airfoil. In same analogy to the findings for an optimised thickness distribution (in sections I through III in the rib itself), the necessary width for the vertical members to prevent buckling varies along the span. As mentioned, the rib near the tip endures relatively the highest compression force due to the larger effective area. Therefore, to provide consistency, the vertical members for every rib are sized accordingly.

Since the ribs are connected to the spars, it is beneficial to have a large as possible connecting surface area. This is already suggested by the C-shape it has, however the width of the rib provides the size of the connecting surface. Therefore it is chosen to take a rib width of $10mm$ for every rib. Using a constant rib width eases the manufacturing process.

Manufacturing of the rib is done using three moulds which have the shape of the airfoil, shown in fig. 9.14b. Uni-directional CFRP strips are wrapped around the each mould separately until the desired thickness (with some margin) is achieved. Then the moulds are aligned such that the shape of the airfoil arises. Strips are wrapped around the entire out surface to create a smooth airfoil shape. The reason for the moulds to have a sheared deformed shape is that every rib has an parallel orientation to the freestream. And since the wing has a sweep angle and the stringers are aligned with this sweep, the connection of rib and stringer has an angle. 'Shearing' the moulds over an angle equal to the sweep provides a rib that is orientated as desired.

9.2.6 Connecting mechanisms

One important function of the structure is to allow for the aircraft to be disassembled into a compact format. This means the wings need to be broken down into smaller sections. It was decided to break each wing into two sections, giving a total of eight pieces. The first section, starting from the root, is four metres in length while the second section goes to the tip and is 2.2 m long. This is done to reduce loads on the joints and to provide a slightly more flexible wing tip section that allows for easy wing warping.

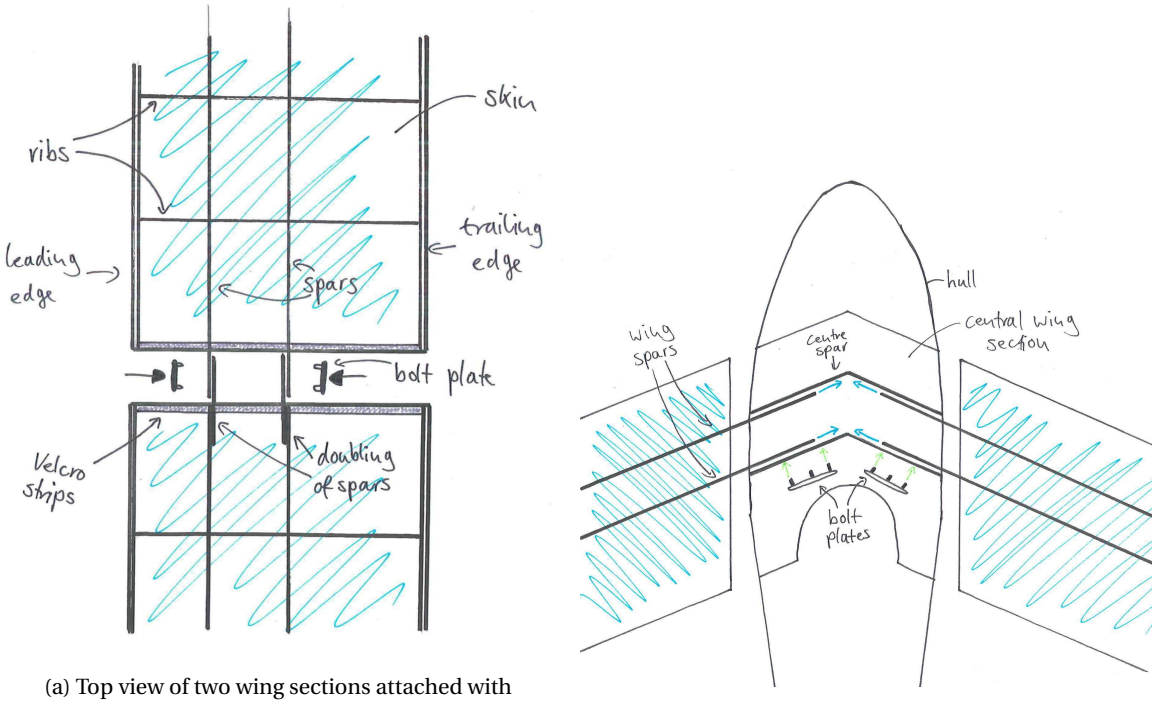

(a) Top view of two wing sections attached with overlapping spars

(b) Top view of the centre connection of both wings

Figure 9.17: Connecting mechanisms for assembly of the wings

As all loads are carried by the spar, it makes sense to extend it and connect the separate wing sections by overlapping the two spars, as is shown in Figure 9.17a. This way, the loads on the stringers will be transferred directly to the stringers of the next wing section. One of the spars needs to be doubled in thickness for both sides to fit into each other nicely. The gap between the wing sections and hence the overlap of the spars should be as short as possible while still allowing for the loads to be transferred efficiently. Also, the customer should be able to fit his or her hand in the gap to allow for easy assembly.

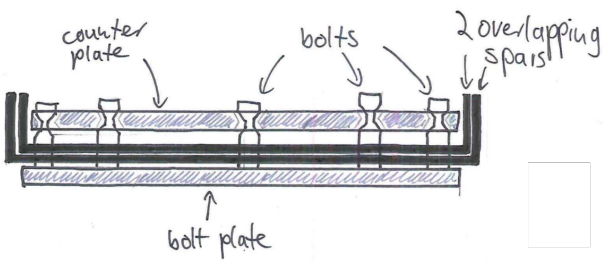

Figure 9.18: Cross-sectional view of the bold plate with a counter plate to secure the bolts in place

With multiple bolts that go through both spars the loads can be well distributed. To save the customer from having to do too much screwing, the bolts could be glued onto a plate so that only the plate needs to be attached and secured with a safety pin, see Figure 9.18. To maintain good aerodynamics, the connecting gap needs to be covered with skin material, attached on each side with Velcro for example.

The same connecting mechanism is used for the central hull section, only with longer overlaps to account for the increased bending moment. On top of that, the wing spars are slid into the central wing section to avoid having spar ends that stick out when the aircraft is disassembled. As a result there is no gap between the two wing sections making the addition of extra skin with Velcro obsolete.

9.3 Hull design

In this sections the first steps in designing the hull structure are made. As for the wingbox design, the hull consists of ribs and stringers, covered with a skin. Stringers and ribs are sized according to the forces that are present.

9.3.1 Stringers

Since the shape of the hull is varying over the length an important factor in selection a stringer shape is the cost and difficulty of the production of the stringers. The stresses on the hull are considered low and for these reasons a simple shaped stringer, the |-shape (#2) is selected as stringer for the hull.

Since the stringer has a symmetrical shape the centroid is located at the exact centre. The area moment of inertia for one stringer is given by:

$$\begin{aligned} I_{A,xx} &= \frac{t_s {B_s}^3}{12} + \frac{B_s {t_s}^3}{12} \\ I_{A,yy} &= \frac{t_s {B_s}^3}{12} + \frac{B_s {t_s}^3}{12} \end{aligned} \tag{9.36}$$

From this the area moment of inertia of the cross section of the hull becomes:

$$\begin{aligned} I_{A,xx} &= \sum_{n=1}^{5} (A_s d_{yn}^2 + \frac{t_s {B_s}^3}{12} + \frac{B_s {t_s}^3}{12}) \\ I_{A,yy} &= \sum_{n=1}^{5} (A_s d_{xn}^2 + \frac{t_s {B_s}^3}{12} + \frac{B_s {t_s}^3}{12}) \end{aligned} \tag{9.37}$$

After calculating the area moment of inertia the normal stresses are computed using Equation (9.18) and for buckling again Equation (9.21) is used. Figure 9.19 shows the stress distributions along the span of the hull for given dimensions of the stringers.

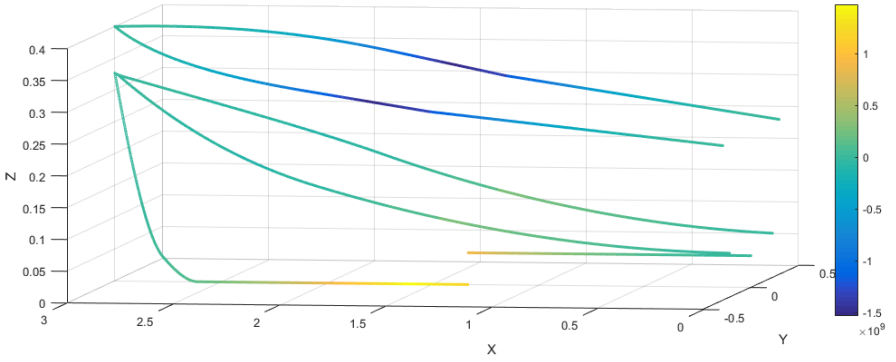

Figure 9.19: Bending stress in the hull [Pa]

9.3.2 Pontoons

The pontoons at the wing tips of the aircraft were designed in a very simple manner. The volume and surface area were determined to be 0.01 m^3 and 0.37 m^2 respectively, see Section 11.4.1. Using EPS foam with a density of 25 kg/m^3 the total foam weight is 250 g.[7] The outside surface is then covered with three layers of 49 g/m^2 glass fibre, leading to a total weight of 350 g per pontoon.[8] The structure could be optimised by hollowing out part of the foam and thereby decreasing the total foam weight.

9.3.3 Ribs

The function of the ribs, located in the hull, is to cope with the compression force introduced by the water pressure. The ribs prevent the hull from collapsing around the axis of symmetry. The load case is depicted in fig. 9.20.

[7] `http://www.thermalps.com.au/imagesDB/wysiwyg/TDS_Expanded_Polystyrene.pdf`, Retrieved: 24-01-2018
[8] `https://shop1.r-g.de/en/art/190105`, Retrieved: 24-01-2018

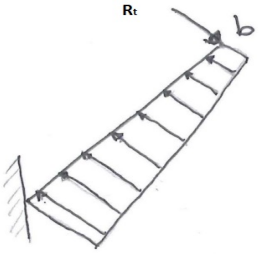

Figure 9.20: Free body diagram of the hull rib load case, containing constraint force R_t

The strategy of this rib design has similarities to the compression loading case for the ribs in the wing, found in section 9.1.2. As the ribs for the hull have an axis of symmetry around the bottom stringer, keel, the rib is considered clamped at that point. The water pressure varies linearly with depth and is calculated through:

$$P_w = \rho_w g \Delta h, \tag{9.38}$$

where ρ_w is the density of water, g the gravitational acceleration and h the water depth. Similar to the wing rib design the distributed due this water pressure is found by multiplying it by the effective loading area. As the hull structure has a skin on truss design, the rib has to carry the pressure loads of the skin around it. The effective area is taken to be the length of the rib member multiplied by the hull rib spacing, Z_s. The stringer, running perpendicular to the plane, is assumed to constraint at the rib perpendicularly. This implies that the stringer is connected to under the same angle as the rib is orientated in fig. 9.20. This statically indeterminate loading problem is solved by stating that members have the same deflection size in opposite direction:

$$v_b' = -v_b \tag{9.39}$$

in which,

$$v_b = v_{b_I} + v_{b_{II}} + v_{b_{III}}, \tag{9.40}$$

where $v_{b'}$ is the deflection of the stinger and v_b the ribs tip deflection, consisting out of deflection due to the point force, v_{b_I} and the square and triangular distributed load, $v_{b_{II}}$ and $v_{b_{III}}$, respectively. The deflections are found by applying the standard clamped cantilever beam deflections, from [22], for both the point load as for the distributed force as:

$$v_b' = \frac{R_t Z_s^3}{3EI_s} \tag{9.41}$$

and,

$$v_b = \frac{w_0 L_r^4}{8EI_r} + \frac{w_2 L_r^4}{30EI_r} - \frac{R_t L_r^3}{3EI_r} \tag{9.42}$$

where Z_s is the rib spacing, R_t is the force implying the tip constraint, L_r is the rib length spanning from clamped root to stringer connection, I_s & I_r are the moment of inertia about their axis of rotation for the stringer and rib, respectively. Here, a deflection towards the axis of symmetry is considered positive. Using the expressions above provides a relation for the point force R_t, dependent on I_r and Z_s. I_r is determined for a rectangular cross-section of the rib computed through:

$$I_r = \frac{1}{12} w_{rib} t_{rib}^3 \tag{9.43}$$

where w_{rib} and t_{rib} are the rib width and thickness, respectively. Here is it assumed that the stringer and the rib are made from the same material, CFRP. Using the expression for R_t, an internal moment and shear force distribution along the rib can be obtained. These distribution are used to determine the stress acting on each cross-section along the length of the rib. This is done using Equation (9.34) and Equation (9.35). The distilled expressions are used to obtain an expression for the Von Mises stress, using Equation (9.11). As This expression is dependent on I_r and Z_s, it is chosen to find the necessary I_r for a fixed Z_s of 25 mm. The rib spacing is fixed on said value because of the relatively low strain capacity of the usage of a non load carrying skin. Striving for a minimum mass and a rib which does not yield under the loads present, the rib dimensions used for I_r are varied until an optimal point is found. One obtains the lowest possible value for which the ribs yield. Incorporating a safety factor of 1.5 gives the design

weight of the rib. As the shape of the hull varies along the longitudinal axis, so does the length of the rib and thus the necessary moment inertia.

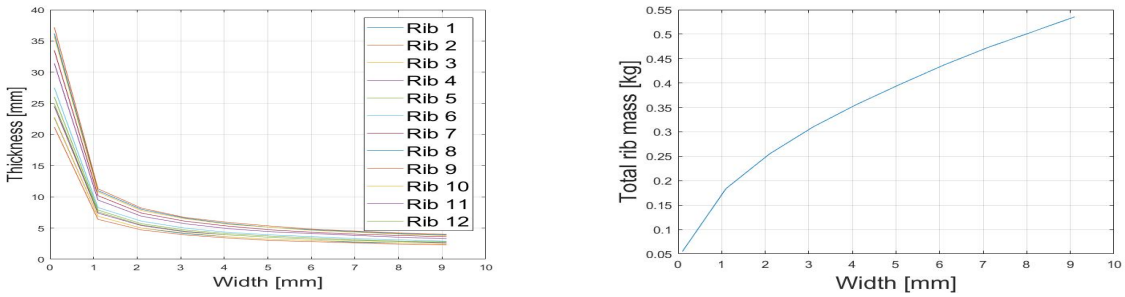

(a) Relation between rib width and thickness for necessary moment of inertia

(b) Total rib mass for chosen constant rib width

Figure 9.21: Visualisation of rib mass optimisation, with the area relation on the left and related optimised total mass of the ribs

Figure 9.21a displays possible options for the areal dimensions of each rib placed from back of the hull (rib 1) to the back (rib 12). Figure 9.21b displays the total rib mass (of the entire hull) for a certain constant, for all, rib width chosen in Figure 9.21a.

From a lightweight structure point of view a constant rib width of 2 mm gives a total rib mass of 0.25 kg. From a manufacturing point of view this rib width is problematic, as the width of the rib is the connecting surface with the stringer. Therefore it is chosen to set a minimum rib width of 5 mm to comply with manufacturing preferences. These entail that an adhesive bonding requires a certain minimum surface area to be effective. As can be seen in Figure 9.22 this gives a total rib mass of 0.4 kg.

9.4 Other Relevant Structures

Other members used for the aircraft structure include leading and trailing edge beams, multiple rods to connect the top and bottom wing and a structure to support the propeller.

To size the leading edge beam, the dynamic pressure at a velocity slightly higher than the maximum speed was used, hence $V = 27\ m/s$. Using the atmospheric density at sea level, ρ, this leads to:

$$q_{max} = \frac{1}{2}\rho V^2 = 446.5\text{N}$$

The beam was designed to withstand this maximum pressure to ensure the leading edge maintains its profile. The largest rib spacing was taken to be 300 mm and the dynamic pressure was assumed to act on an area 100 mm high. The total force is then found:

$$F_{LE} = \frac{q_{max}}{0.3 \cdot 0.1} = 17.9\text{N}$$

while the distributed load is:

$$w_{LE} = \frac{F_{LE}}{0.3} = 44.7\text{N/m}$$

To simplify the geometry, a half tube with a radius of 15 mm was used, which was the measured radius of the leading edge of the airfoil. The problem was then treated as a beam hinged at both ends with a distributed load acting on it. Using Equation (9.18) for only one axis resulted in a thickness for CFRP of $1.6 \cdot 10^{-5}$m. This is assumed to be beyond what is practical to manufacture, therefore the thickness was increased to 0.06 mm, which is equivalent to two layers of 0.03 mm CFRP. While this is still very thin, it is within what can be bought on the market.

For simplicity the trailing edge beam was assumed to have the same cross-sectional area, resulting in a weight for both beams of 60 g per wing section or 240 g for both wings from tip to tip.

The truss members connecting the two wings in the centre section were designed to each carry the load of the aircraft for safety. Assuming rods and using Equation (9.20) the required cross-sectional area of each rod was determined. The diameter of the tubes was chosen to be 10 mm, leading to a required thickness of just under 0.5 mm. All four rods combined amounted to less than 120 g [(9)].

[(9)] `http://www.exelcomposites.com/Portals/154/documents/Brochures/Exelite%20Technical%20Data%20Sheet%202014.pdf`, Retrieved: 22-01-2018

To support the propeller, engine nacelles are required, going from the front spar to the propeller. With a safety margin of 100 mm for the propeller tip from the leading edge, the length was determined to be 450 mm. The hub of the propeller has a radius of 75 mm. The geometry of the nacelle was then assumed to be a thin walled tube with the same radius as the propeller hub. The engine nacelle is designed to carry the forces exerted by the weight and thrust of the propeller, but the torque is transferred through the shaft directly to the gear box. With a propeller weight of 1.2 kg and an acceleration of 6 g this leads to a maximum moment of 31.8 Nm. The maximum thrust multiplied by a safety factor of 1.5 was rounded up to 400 N. Combining the two load cases and using Equations (9.18) and (9.20) leads to a thickness to the power of -6. Therefore it was decided to increase it to two layers of 0.1 mm plain weave CFRP [10]. This resulted in a weight of 160 g per wing or 320 g in total. CFRP was preferred over other materials in this case to ensure the propeller has a stiff support that does not deflect or vibrate during flight.

For the rudder beams a similar procedure was used. The maximum rudder force is 75 N and the maximum thickness of the airfoil is 33 mm. Using half of that as radius for a rod and applying the same procedure as for the leading edge beam led to impractical thicknesses. Therefore a thickness of 1 mm was assumed allowing for rods available on the market to be used. The rod then weighed just under 70 g meaning 140 g in total. A rod with equal thickness but diameter of 10 mm was assumed as front member at the wing tip, adding a total of 42 g.

The total overlapping area between the wing beams and each rib were determined to give an initial estimate on the adhesive required. Assuming a bond thickness of 0.3 mm resulted in a total weight of 126 g for Spabond 345 adhesive [11].

9.5 Results

Table 9.3 includes the masses of all structural components that have been determined in this chapter. Stress relieving truss members or wires were not deemed necessary, as the tip deflection during cruise was determined to be less than 300 mm.

Table 9.3: Compilation of all structural components and their respective weight

Component	**Weight [g]**	**Material**	**Thickness [mm]**	
			Root	Average
Stringers (width = 11 mm)	3340	CFRP	1.5	1.0
Spar web (front)	268	±45 GFRP	0.12	0.047
Spar web (rear)	706	±45 GFRP	0.360	0.123
Horizontal spar webs	974	Braced wires (in the future)		
Ribs	2200	CFRP	1.5	1.3
Skin	1116	Ripstop Nylon		
Hull stringers (width = 24 mm)	1500	CFRP	2.0	2.0
Component	**Weight [g]**	**Material**	**Thickness [mm]**	
Hull ribs	390	CFRP	4.0	
Hull skin	622	Dacron	-	
Pontoons	700	Foam + GFRP	0.16	
Leading edge beam	238	CFRP	0.06	
Trailing edge beam	238	CFRP	0.06	
Central truss members	119	CFRP	0.5	
Rudder beam	160	CFRP	1.0	
Connecting mechanisms	500	Local reinforcements + bolts	-	
Adhesive	126	Spabond 345	0.3	
Propeller mounting	320	CFRP	0.2	
Reinforced centre stringers	653	UD CFRP	3.0	
Reinforced centre spar web (front)	89	±45 GFRP	0.24	
Reinforced centre spar web (rear)	266	±45 GFRP	0.72	
Total	**14,525**			

[10] `http://www.easycomposites.co.uk/#!/fabric-and-reinforcement/carbon-fibre-reinforcement/woven-carbon-cloth-under-150gsm/Plain-weave-90gsm-1k.html`, Retrieved: 22-01-2018

[11] `www.gurit.com/-/media/Gurit/Datasheets/spabond-345.ashx`, Retrieved: 17-01-2018

9.6 Verification and Validation

The main tool that is used for the structural analysis is MATLAB. The code that is written is verified in several ways. As a first example the calculation for the centroid and area moment of inertia of a stringer is compared with those properties of that same stringer with known dimensions which can be found in [15]. In a similar manner the code that produces loading diagrams can generate loading diagrams for a case that is identical to a case that is worked out in the book. An example of this type of verification is shown in Figure 9.22, where w is equal to 981 and L is equal to 3.

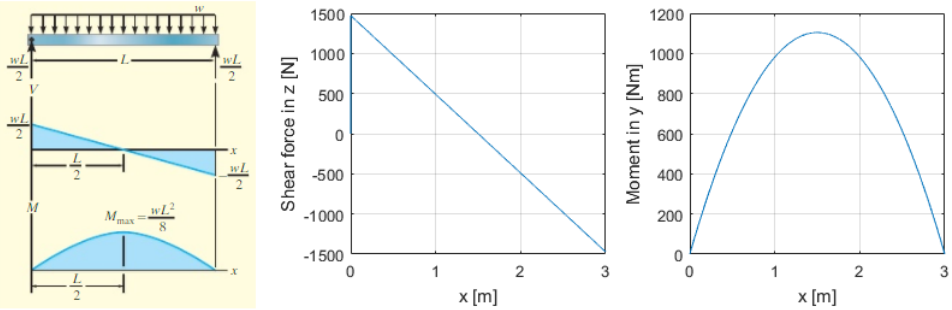

Figure 9.22: Loading diagram verification [15]

Secondly, if a problem is solved numerically it is verified by comparing the results to an analytical solution. For the deflection of the wing, the displacement by integration method is used. When considering only the elliptical lift distribution the analytical solution of this problem is described in Section 9.1.1, Equation (9.6). The numerical solution is found by integrating numerically. In Figure 9.23 the difference in solutions is visualised.

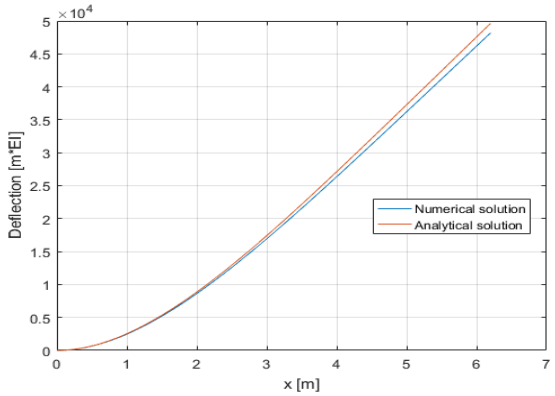

Figure 9.23: Verification of deflection

A more straightforward way to verify is to do the same calculation by hand and compute the error. Still considering the deflection, when looking at the difference in deflection at the tip one can fill in the equation with x equal to 0, L equal to 6.2 and c equal to 227. This gives

$$EI\upsilon(0)_{ana} = 49551 m^3 N$$

Using the same variable, the numerical tool spits out a deflection of:

$$EI\upsilon(0)_{num} = 48794 m^2 N$$

which gives the fraction for the numerical value of:

$$EI\upsilon(0) = \frac{48794}{49551} * 100\% = 98.5\%$$

Meaning there is a 1.5% difference between the numerical and analytical value. Since discretisation is used for the numerical model an error of this magnitude is expected.

Validation is important to see whether the final results are realistic. Steps for validation include demonstration, analysis, inspection and testing. Due to the limited time and resources for this project, inspection is the most suitable method of validation.

A good measure to compare is the weight per metre of span. Using the total wing span of both wings for the *AerGo* leads to a value of 0.462. The *Easy Riser* without motor in comparison has a value of 1.368, which is significantly higher [(12)]. This is to be expected though because of the use of aluminium for spars and ribs. Also, the *Easy Riser* was designed in the 1970s whereas the *AerGo* uses the lightest modern materials.

Another aircraft of interest is the human powered *Gossamer Albatross*, since it uses a similar wing configuration with CFRP tube spars and soft skin. The ratio of weight over span for this aircraft is 1.112 [(13)]. The weight used here is the total weight of the aircraft, including the cockpit, cycling mechanisms and the tail. Nevertheless, it is surprising how much lower the ratio is for the *AerGo* compared to the *Gossamer Albatross*. This could be partially due to the choice of spar, since a wing box is generally said to be lighter than tube spars. The *AerGo* uses stringers with unidirectional CFRP, fully exploiting the thickness of the airfoil as well as the mechanical properties of CFRP.

Further methods of validation that should be done in the future include a thorough analysis and load testing. The analysis might include use of the finite element method to see if all loads are accounted for and whether the structure will fail due to local stress concentrations. Since the wing is relatively easy to produce, a full scale stress test can be done without using too many resources.

9.7 Conclusion and Recommendations

The goal of the structural design phase was to provide a light weight wing structure that can be disassembled. This goal was certainly achieved, with a final weight of almost half the initial budget of 19.9 kg. On top of that, the structure includes connecting mechanisms that do not require much time to set up and therefore make it highly likely that the aircraft can be assembled in under an hour. The choice of the C-spar was effective in making good use of the directional properties of composites, leading to very low spar weights, 5.29 kg.

Nevertheless, the question remains of whether the structure presented in this chapter is suitable for many cycles of assembly/disassembly. Many of the determined thicknesses were extremely small, making the part prone to damage, either during transportation or during handling by the customer. In the end this is also a safety concern, as the customer will most likely not have engineering knowledge and might therefore not realise he or she is flying with a slightly damaged wing. The downside of composites is that they are very brittle and small out of plane impacts can drastically reduce the mechanical performance of the material. Therefore it is advised to review the structural design to ensure it remains safe to use throughout its life cycle. To reduce the risk of damaging the structure by the customer, it is advised to handle each wing section by touching the skin instead of the ribs and spars. This will distribute the applied forces more evenly and should keep the load carrying components unharmed.

The two aircraft used for validation indicate that the wing structure is certainly on the lighter side. It is likely that after more detailed design the weight will increase due to local reinforcements and safety margins for imperfections during production. Throughout the structural sizing it was assumed that all components are loaded the way they are meant to, which might not be the case in practice. Small initial imperfections could lead to buckling occurring earlier than predicted for example. The shear plates are extremely thin and are likely to fail if damaged during assembly or bad production.

One area that needs attention are the horizontal shear plates of the wing box, or rather the braced wires that are meant to replace them. Diagonal rods could be used too, but the idea was that using wires or strings of different materials and diameter allows for the stick forces to be tailored to desired magnitudes. Another area that requires more investigation is the vibration characteristics of the wing. The natural frequency has to be computed in order to be able to analyse flutter for example.

The skin of the hull is another potential risk for the design. Small holes will be enough to fill the entire hull with water, making flight impossible. A more durable skin was chosen to prevent this, but at some point damage should be expected to occur. Apart from the obvious fact that a hole in the skin should not lead to sinking of the aircraft, the customer should be able to repair or replace the skin by him or herself. The mechanical properties of the wing skin were not taken into account during the structural analysis. Therefore it should be verified that the ripstop nylon does not tear or buckle due to the forces experienced during flight.

Finally, the choice of materials should be reviewed to investigate whether more sustainable or affordable materials could meet the mass budget.

[(12)] `https://www.delta-club-82.com/bible/637-hang-glider-icarus-2.html`, Retrieved: 22-01-2018

[(13)] urlhttps://airandspace.si.edu/collection-objects/maccready-gossamer-albatross, Retrieved: 22-01-2018

10 Propulsion

This chapter elaborates on the design of the propulsion subsystem. The approach will be discussed in Section 10.1. The power system design, electrical system design and the propeller design will be discussed in Sections 10.2 to 10.4 respectively. The tools that have been used for these designs are verified and validated in Section 10.5. Finally, in Section 10.6, the conclusions and recommendations will be given for the propulsion subsystem.

10.1 Approach

The design of the propulsion system is initialised after the required propulsive performance is determined by the Performance department. The required propulsive performance parameters are the Power Required (for take-off and cruise), the required amount of energy and the allowed mass for the entire propulsion system. Since the design is required to produce no more than 40dB of noise at a 100m distance, an electrical propulsive system has been chosen in the subsystem trade-off. The electrical system consists of an energy and power source connected to two propellers. The efficiencies of the propeller, the engine and the gear system in between are assumed to be able to start designing the different components of the propulsion system to to provide the required performance. The designing of the propulsion system is performed in parallel; the energy and power system should be compliant with the propeller. Reducing the total weight to a minimum but also keep the efficiency of the entire system as high as possible is desired. In the design process of the propeller, it was assumed that the slipstream of the propeller maintains it's path downstream. In reality, this slipstream vortex would propagate into a larger radius with lower speeds when moving downstream of the propeller.

10.2 Power System Design

This section covers the design of the power system. Section 10.2.1 covers the selection of the engines, while Section 10.2.2 describes the analysis of the selected engine and Section 10.2.3 elaborates on the gear system between the engines and the propellers.

10.2.1 Engine selection

In this section, the power system design is reasoned and explained. The intention is to get as much detail in this subsystem as possible while also coming up with a design that has a TRL of 9 and is thus directly available on the market. The required power for the different flight phases, as determined by the performance department, served as basis for the power system design. The power required is the power that the propeller has to deliver, which was highest during the take-off phase. Assuming certain values for the propeller, cabling and engine efficiency, a first estimate of the required power was made. Based on the values given in Table 6.1, the required power needed from the propeller during take-off is equal to P_{prop} = 3000Watt. Based on literature, the propeller, cable and engine efficiency (a gear system was in this stage not accounted for) were set at 0.8, 0.95 and 0,8 respectively [33]. Then, the initial power that has to be delivered by the engine is equal to: $P_{eng} = \frac{3000}{0.8 \cdot 0.95 \cdot 0.8}$ = 4930Watt. Furthermore, to increase the life span of electrical systems in general, the *80%-rule-of-thumb* is used. This rule states that one should aim to operate electrical systems at 80% of their rated power and current (or charge for batteries). This increases the lifespan by a factor of around 18 compared to the lifespan at 100% power usage. This is illustrated below in Figure 10.1, where the x-axis denotes the operating setting (with 1.0 being at 100%) and the y-axis denotes the average lifespan factor compared to a factor of 1.0 at 100% of the operating setting. As mentioned before, at an operating setting of 0.8, the average lifespan increases by a factor 18. Therefore the required maximum continuous power is: $P_{eng} = \frac{4930}{0.8} = 6170$Watt.

Several engines were investigated on the website *hobbyking*[(1)]. There are more suppliers for electrical engines but based on customer experience and reviews, *hobbyking* offers the highest quality products and is most widely used in Europe [(2)]. At this point in the design, multi-propeller configurations were still an option. The engine candidates from *hobbyking* are listed in Table 10.1. Besides the rated power, the mass and power density were interesting characteristics for the engine selection. The number of propellers was chosen to be two, in order to have smaller

[(1)] `https://hobbyking.com/nl_nl/?___store=nl_nl`,Retrieved: 19-12-2017

[(2)] `https://nl.trustpilot.com/review/www.hobbyking.com`,Retrieved: 15-01-2017

propellers. This is beneficial for noise reduction while it still keeps the power system as simple as possible, as will be further explained in Section 10.4. In turn, this had the consequence that the power available has to be delivered by two separate engines driving two separate propellers. For a dual propeller system, it was investigated whether single engine operation would still be feasible and it was found that only one engine would be sufficient for this emergency case. The result is that two *Turnigy RotoMax 50cc*[3] electrical engines are chosen as power units.

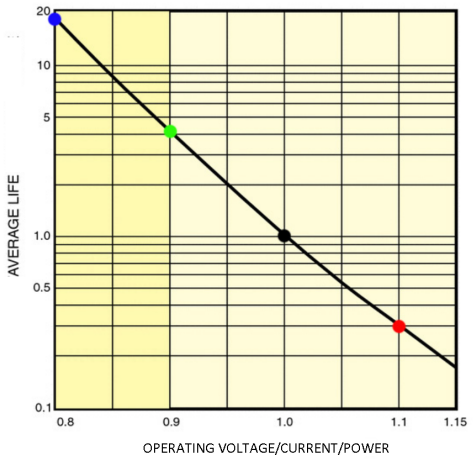

Figure 10.1: Lifespan electrical system

Table 10.1: Candidates of Turnigy electrical engines for the power system

Engines	P [W]	KV [rpm/V]	I_{max} [A]	U_{max} [V]	m [kg]	Power density [W/kg]
Aerodrive SK3 74	2250	149	70	44	0.84	2679
Aerodrive SK3 54	2360	260	70	37	0.49	4816
Aerodrive SK3 64	2450	190	65	37	0.70	3500
Aerodrive SK3 74-9	2750	192	80	44	0.86	3198
RotoMax 50cc	**5300**	**172**	**120**	**44**	**1.08**	**4907**
RotoMax 100cc	7992	167	170	44	2.08	3842
RotoMax 150cc	9800	150	190	52	2.53	3874

10.2.2 Engine analysis

Now that the engine is chosen, a specific analysis of this engine is conducted. The *Turnigy RotoMax 50cc* is what is called a BrushLess DC (BLDC) outrunner engine. Firstly, without going into too much detail, a brushless engine has an electronic servo system to replace the brushes of a mechanical commutator. The reversion in current through the windings (and thus a reversion in magnetic field) is electronically controlled in a BLDC and not mechanically as in a brushed motor. Secondly, DC denotes "direct current" which means that the BLDC can be indirectly driven by DC power supply. Although, a BLDC actually requires alternating current (AC) to drive the separate phases of the motor, an inverter or switching power supply is used to convert the DC to AC [33]. Finally, an outrunner type engine is a type of engine where the 'outside' armature (or rotor) spins around the 'inside' stator. On the contrary, for an inrunner engine, the 'outside' armature is the stator in which the 'inside' rotor spins. To start the specific analysis of this engine, some basic understanding of the input voltage and current and their respective losses is given. In general, an electrical engine converts voltage into rotational speed and current into mechanical torque. The conversion from voltage to rotational speed is denoted by the constant k_v, which has units rpm/volts and indicates how much rpm is produced per volt. In turn, the conversion from current to torque is denoted by the constant k_t, which has units Nm/A and indicates how much torque is produced per ampere (the torque constant is related to the speed constant through: $k_t = \frac{60}{2\pi k_v}$). However, the effective voltage and current can only be used to create speed and torque respectively. The engine has a certain internal resistance R due to copper and iron losses. This creates a voltage drop

[3] `https://hobbyking.com/en_us/turnigy-rotomax-50cc-size-brushless-outrunner-motor.html`,Retrieved: 19-12-2017

along the engine[4]:

$$U_{eff} = U_{in} - I_{in}R = \frac{n}{k_v} \tag{10.1}$$

Where U_{eff} is the effective voltage that can be used for rotational speed, U_{in} is the input voltage from an electrical source, I_{in} is the input current and n is the rotational speed in rpm that can be generated by the effective voltage. The input current however has to overcome a certain rotational friction to get the engine 'moving'. The effective current is thus lower than the actual input current:

$$I_{eff} = I_{in} - I_0 = \frac{T_c}{k_t} \tag{10.2}$$

Where I_{eff} is the effective current, I_0 is the zero-load-current to overcome the rotational friction and T_c is the torque that can be generated by the effective current. These basic effective voltage and current relations are used to construct the engine characteristic equation. This is an equation that relates the rotational speed of an electrical engine to the generated torque and is a decreasing linear relation. Using Equation (10.1) and Equation (10.2), this relation can be constructed:

$$n = k_v \cdot U_{eff} = k_v(U_{in} - I_{in}R) = k_v(U_{in} - R(T_c/kt + I0)) \tag{10.3}$$

Where U_{in} is the input voltage, T_c is the torque in Nm and n is the rotational speed in rpm. Important to note is that this curve shifts upward for increasing voltage and downward for decreasing voltage. Two characteristic values are of importance for the visualisation of Equation (10.3). These are the stall torque (T_{c_s}) and the zero-load-speed (n_0). The former is the torque when there is a load applied that causes the rotational speed to become zero, i.e. the engine stalls. Inserting $n = 0$ into Equation (10.3) and manipulating to find for T_{c_s}:

$$T_{c_s} = \frac{k_t \cdot U_{in}}{R_{in}} - I_0 \tag{10.4}$$

The latter is the speed when there is no load applied. By inserting $T = 0$ in Equation (10.3) the zero-load-speed is found:

$$n_0 = k_v(U_{in} - R \cdot I0) \tag{10.5}$$

Besides the relation given by Equation (10.3), the engine output power can also be related to the torque. From rotational mechanics it is known that the mechanical power is the product between torque and rotational speed, which must be equal to the effective electrical power:

$$P_{mech} = \omega \cdot T_c = n \cdot T_c \cdot \frac{2\pi}{60} = U_{eff} \cdot I_{eff} = (U_{in} - I_{in}R) \cdot (I_{in} - I_0) \tag{10.6}$$

Where ω is the rotational speed in rad/s. One of the last engine characteristic that is of interest is the engines efficiency. The efficiency is equal to the ratio of output and input power:

$$\eta_{eng} = \frac{P_{out}}{P_{in}} = \frac{P_{mech}}{P_{elec,in}} = \frac{n \cdot T_c \cdot \frac{2\pi}{60}}{U_{in} \cdot I_{in}} = \frac{U_{eff} \cdot I_{eff}}{U_{in} \cdot I_{in}} \tag{10.7}$$

Lastly, the current for maximum power, the current for maximum efficiency and the corresponding maximum efficiency are of interest. These last characteristics are given by [5]:

$$I_{P_{max}} = \frac{U_{in} + RI_0}{2R} \tag{10.8}$$

$$I_{\eta_{max}} = \sqrt{\frac{I_0 U_{in}}{R}} \tag{10.9}$$

$$\eta_{eng_{max}} = \left(1 - \sqrt{\frac{RI_0}{U_{in}}}\right)^2 \tag{10.10}$$

[4] https://www.rcgroups.com/forums/showthread.php?185271-Inside-Story-February-2003&highlight=bergmeyer,Retrieved: 15-01-2018

[5] https://www.rcgroups.com/forums/showthread.php?185271-Inside-Story-February-2003&highlight=bergmeyer,Retrieved: 15-01-2018

Where the maximum power can be calculated by using the value from Equation (10.8) in Equation (10.6) for the input current. The specifications of the *Turnigy RotoMax 50cc* are given in Table 10.2 among with the characteristics when a 12 cell Lithium Polymer battery, i.e. an input voltage of 44.4 volts is attached. It must be noted that the maximum current I_{max} is limited to 120 A as given by the manufacturer. Exceeding this current will cause overheating and probably damage to the electrical engines.

Table 10.2: Turnigy RotoMax 50cc parameters

Specifications	
Parameter	**Value**
k_v $[rpm/V]$	172
k_t $[Nm/A]$	0.0555
R $[\Omega]$	0.021
I_0 $[A]$	1.65
I_{max} $[A]$	150

Characteristics	
Parameter	**Value**
U_{in} $[V]$	44.4
T_s $[Nm]$	117.3
n_0 $[rpm]$	7631
$I_{P_{max}}$ $[A]$	1058
P_{max} $[W]$	23420
$I_{\eta_{max}}$ $[A]$	59
$\eta_{eng_{max}}$ [-]	0.945

To finalise this section on the engine, several plots will be shown. Firstly, the speed against torque is plotted according to the relation given by Equation (10.3). In the same plot, the power against torque is also plotted according to the relation Equation (10.6). In the second plot, the current is plotted against torque according to Equation (10.2). Lastly, the efficiency is plotted against the torque according to Equation (10.7). These plots are shown in Figure 10.2 and it should be noted that these plots are based on an input voltage of 44.4 V while the current should be limited to 120 A.

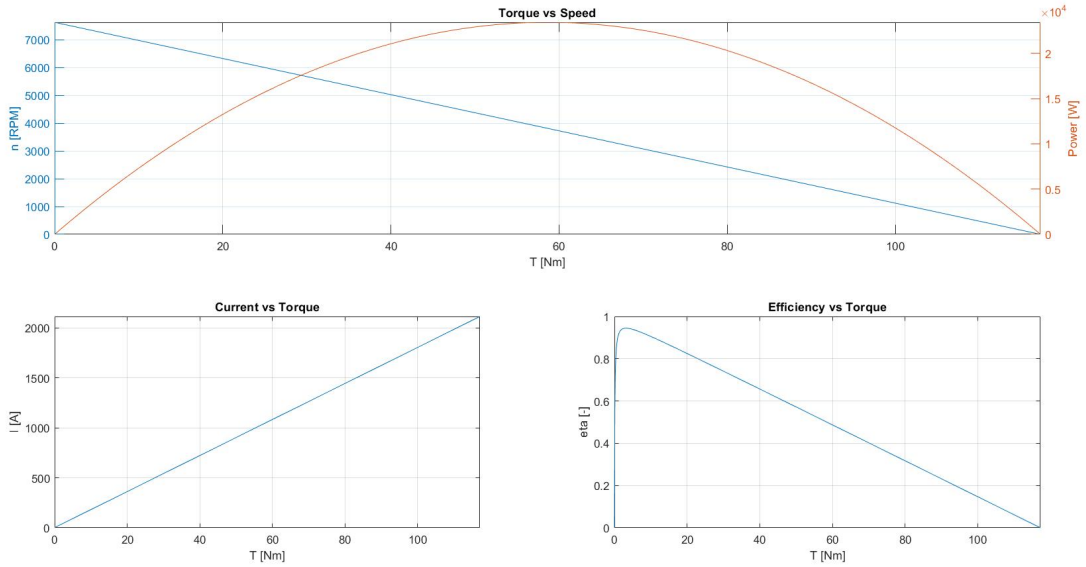

Figure 10.2: Turnigy RotoMax 50cc characteristics plots, $U_{in} = 44.4V$

10.2.3 Gear system

The last part of the power system design is the gear system. As will be explained later in Section 10.4, the noise that the propeller will generate has a certain limit. For noise reduction it is beneficial to have a very large propeller that spins at a very low speed compared to a smaller propeller that turns at a higher speed. However, the engine has a certain rotational speed of its axis as output which is much higher than the rotational speed of the propeller. To solve this problem, a gear reduction unit is used to connect the output axis of the engine to the driving axis of the propeller. The working principle is that the output speed can be reduced by a certain gear ratio GR, while consequently the output torque will increase by the gear ratio:

$$T_{c_{out}} = GR \cdot T_{c_{in}} \eta_{gear} \tag{10.11}$$

$$n_{out} = \frac{1}{GR} \cdot n_{in} \tag{10.12}$$

Where $T_{c_{in}}$ and n_{in} are the torque and speed of the input axis to the gearbox respectively, while $T_{c_{out}}$ and n_{out} are the torque and speed of the output axis of the gearbox respectively and η_{gear} denotes the gears efficiency. A continuous iteration process between engine setting and propeller sizing is needed to get the most efficient and suitable gear ratio. After this continuous iteration process, it was concluded that for the current design, the gear ratio is set at six ($GR = 6$). For now, this ratio allows a reduction of the rotational speed of the propeller which would be sufficient to comply with the noise requirement. At the same time this ratio allows the engine and propeller to also operate at an efficient level. However, it is concluded that a detailed design of this gear system is needed within the integration of selecting the best engine and propeller design. Currently, this detailed design is considered to be beyond the scope of this report and project but some recommendations for a gearbox design will be given at the end of this chapter in Section 10.6. An overview of a single propulsion power layout system is also given in Figure 10.10 in Section 10.6 for the take-off and cruise phase respectively.

10.3 Electrical System Design

This section covers the design of the electrical system, with the battery selection and connection in in Section 10.3.1 and Section 10.3.2, the speed controllers in Section 10.3.3 and the electrical system layout in section 10.3.

10.3.1 Battery selection

In this section, the electrical system design will be reasoned and explained. Just as with the engine selection, the intention is to get as much detail in this subsystem as possible while also coming up with a design that has a TRL of 9 and is thus directly available on the market.

The electrical system design will compose of a selection of battery and electronic speed controller (ESC) and overall integration of all the electrical parts in an electrical block diagram. The battery is a very crucial component of this aircraft. The aircraft is designed to have a mass of around 50 kg and first estimates in the midterm report showed that the battery mass will comprise of 30% to 40% of the total empty mass. Therefore, the batteries should be selected such that there is enough energy for the single inbound trip (see Figure 2.2) but at the same time have a low mass as possible. This concludes to finding batteries that have a high specific energy while taking into account their costs and availability. As an initial step the total trip energy needed to cruise for 30 minutes was examined from the performance department. Performance analysis showed that to comply with a cruise speed of 15 m/s for 30 minutes, a total energy of $E_{trip} = 1.36$ kWh is needed. Furthermore, to increase the life span of electrical systems in general, the *80%-rule-of-thumb* is used as explained in Section 10.2. Referring to Figure 10.1, to increase the lifespan of the batteries, they will be used up to 80% of their charge. This means that the energy that a battery should carry is: $E_{batt} = \frac{1.36}{0.8} = 1.7$ kWh. As mentioned before, there will be two propulsive units (one unit is one propeller plus one engine). This means that the carried energy will be divided evenly over the two propulsive units: $E_{batt_{unit}} = \frac{E_{batt}}{2} = \frac{1.7}{2} = 0.85$ kWh.

Several batteries were investigated on the website *hobbyking*.[6] The battery candidates from *hobbyking* are listed in Table 10.3. In combination with the engine that was selected, a possible series and/or parallel circuitry was investigated. It quickly became apparent that to have the possibility of using the engines at full power, a battery with around 44 V would be needed. For Lithium Polymer (LiPo) batteries, this means that a 12 cell battery is required since a LiPo battery has an average potential of around 3.7 V per cell. Another option is to have two separate 6 cell batteries in a series circuit, which adds up their potential (but not their charge!). It was concluded that any possible battery from the candidates would require at least a series circuitry. Finally, it was decided to select the battery that has the highest charge to meet the required battery energy per propulsive unit ($E_{batt_{unit}}$). The result is that for a single trip, two *Multistar 20Ah 6S*[7] batteries per propulsive unit are selected, or four *Multistar 20Ah 6S* batteries in total for a single trip.

[6] `https://hobbyking.com/nl_nl/?___store=nl_nl`,Retrieved: 19-12-2017

[7] `https://hobbyking.com/en_us/multistar-high-charge-6s-20000mah-multi-rotor-lipo-pack.html`,Retrieved: 08-01-2018

Table 10.3: Candidate batteries for the electrical system

Batteries	charge (Ah)	U [V]	E [Wh]	m [kg]	Energy density [Wh/kg]
Multistar 16Ah 4S	16	14.8	236.3	1.29	184
MultiStar 12Ah 6S	12	22.2	266.4	1.61	165
Multistar 20Ah 4S	20	14.8	296.0	1.61	184
Multistar 16Ah 6S	16	22.2	355.2	1.92	185
Multistar 20Ah 6S	**20**	**22.2**	**444.0**	**2.41**	**185**
Tattu 22Ah 6S	22	22.2	488.4	2.51	195

10.3.2 Battery connection

The batteries were initially designed to land at a certain location and take off with a turnaround time of one hour. An investigation was done to see if it was possible to take chargers on board and use them to charge the four batteries within one hour. The conclusion was that in order to achieve this turn around time, two chargers would be required which would have a combined mass of more than 6.2 kg. Therefore the decision was made to double the amount of batteries without incorporating a turnaround phase (or charging phase) in the mission profile. Referring to Figure 2.2 in Chapter 7, the aircraft must perform an inbound and outbound flight on a single charge of the batteries. However, an alternative mission can also be performed. This alternative mission would not have a landing phase between the inbound and outbound flight but would be a single cruise phase with take off and landing at the same location as shown in Figure 10.3.

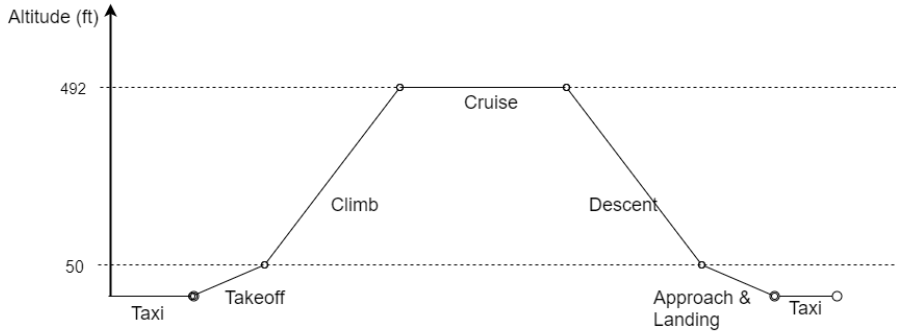

Figure 10.3: Alternative mission profiel

Concluding, the amount of batteries needed to perform this mission is set at double the amount that was initially set for a single inbound flight resulting in a total of two times four batteries, eight batteries in total. To double the charge as well, the initial two batteries in series will be put in a parallel connection together with two other batteries in a series connection. In Figure 10.4, an overview is given of this series/parallel connection.

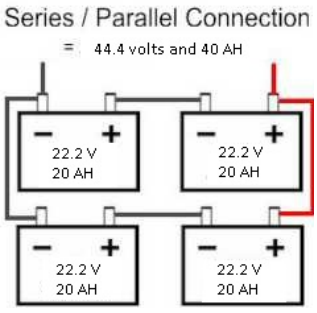

Figure 10.4: Batteries in a series/parallel combination circuit

In a series connection, the potential is summed while the charge remains the same:

$$U_{tot} = \sum U_i \tag{10.13}$$

where U_i denotes the potential of each separate battery in a series connection. In this case $U_{tot} = 22.2 + 22.2 = 44.4\,\text{V}$. The charge in a series connection remains the same as in a single battery. In analogy, in a parallel connection the charge is summed:

$$Q_{tot} = \sum Q_i \tag{10.14}$$

where Q_i denotes the charge of each separate battery in the parallel connection. In this case $C_{tot} = 20 + 20 = 40\,\text{Ah}$. The potential and charge of the series/parallel connection are also shown in Figure 10.4. This concludes the discussion on battery selection.

10.3.3 Speed controller

Next step in the electrical system design is the selection of an electronic speed controller (ESC). An ESC is an electronic circuit that controls and regulates the speed of an electronic motor. An ESC achieves this by following a speed reference signal that is for instance derived from a throttle lever. For a brushless motor this is achieved by adjusting the timing of pulses of current delivered to the different windings of the motor. Since there are two propulsive units, two ESC are needed. For the ESC the *80%-rule-of-thumb* also applies. The ESC that is selected is the *AeroStar Advance 150A* from the *hobbyking* website.

10.3.4 Electrical system layout

An overview of the electrical block diagram is given in Figure 10.5. This is the electrical system layout for the *AerGo*. The throttle control and the instruments that are present in the *AerGo* will be explained in Chapter 12. This layout shows that the two battery units are physically not connected. This is to make sure that when one battery fails, it would only affect one propulsion unit and not both. The instruments would require a smaller separate battery but the whole electrical system should be designed in such a way that the system can be turned on and off with the switch given in the grey block This is an example of how the electrical system layout could be. For a more detailed design phase it is advised to check whether the battery units can all be connected in parallel and how the main switch operates these batteries and the battery for the instruments.

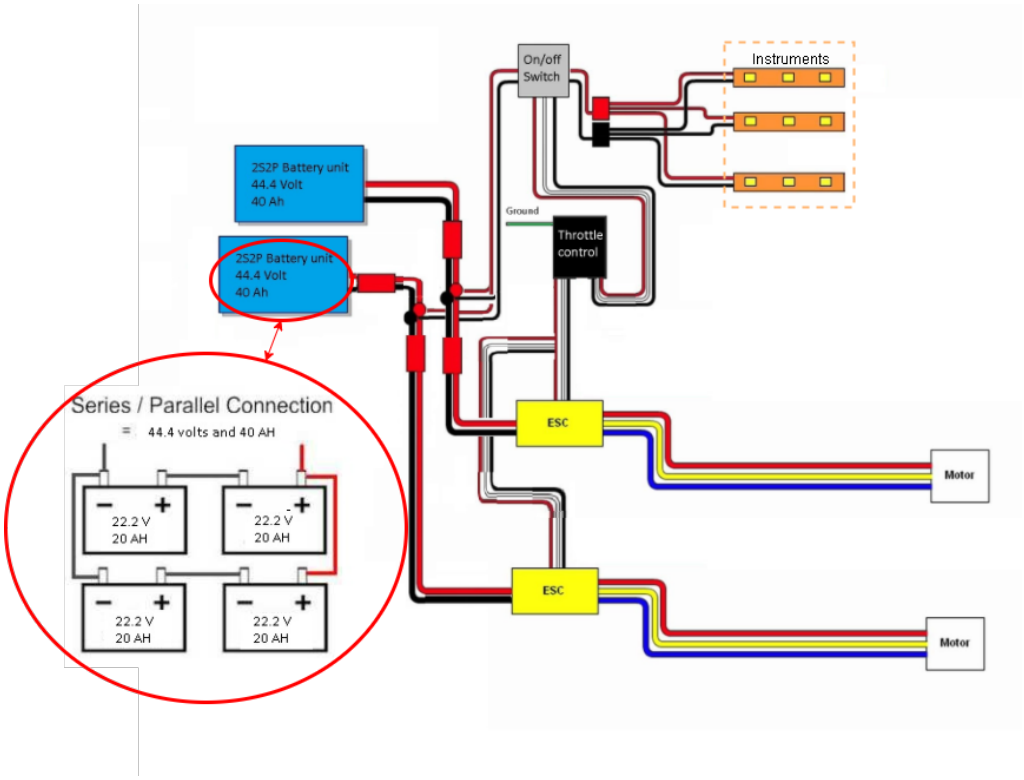

Figure 10.5: Electrical block diagram for the *AerGo*

10.4 Propeller design

This section contains the design stage of the propeller. The trade-off between every feasible option is discussed in Section 10.4.1, the propeller geometry is discussed in Section 10.4.2 and the noise characteristics are discussed in Section 10.4.3.

10.4.1 Propeller considerations

When it comes to the trade-off of the propeller design, three criteria were taken into account; mass, cost and noise. The most critical flight phases to design for were the cruise and take-off. The propeller was required to provide 61 N of thrust during cruise and 120 N at the end of the ground run, just before liftoff.

The trade-off between fixed pitch and variable pitch propellers was made relatively quickly and based on common sense. When the required performance of the propeller does not differ much for different fight phases, fixed pitch is feasible. [(8)] The take-off and cruise speeds are relatively close together and so is the required thrust for both phases. Finally, the cruise altitude of 150 m does not impose a noticeable effect with respect to the take-off altitude at sea level. On top of that, fixed pitch propellers are generally cheaper and more lightweight than variable pitch propellers. Fixed pitch propellers require a simpler manufacturing method and do not need heavy hydraulics to adjust the pitch of the propeller blades.

In the midterm report of this project [5], the noise production of propellers was investigated extensively. A number of ways to reduce propeller noise were identified; reducing the blade loading and reducing the tip speed of the propeller. The blade loading could be reduced by increasing the number of blades and increasing the overall number of propellers used, while the tip speed could mostly be reduced by flying at a low rpm. At the start of the propeller design, the overall design of the aircraft allowed a maximum propeller radius of 0.75 m. A smaller propeller radius generally implies a larger rpm to produce the same amount of thrust, so it was decided to fix this maximum propeller radius to aim for the lowest rpm possible. Following the investigation in the midterm report [5], increasing the number of propellers from one to two and increasing the number of blades to six would provide the propellers with the least amount of noise produced.

The investigation in the midterm report [5], also concluded that a push propeller produces more noise than a tractor propeller, especially at low speeds. On top of that, placing the propellers in front of the wing creates a slipstream over the sections of the wing downstream of the propeller. This slipstream creates increased dynamic pressure, which increases the overall aerodynamic performance of the wing.

With the required thrust, number of propellers, number of blades and maximum tip radius in mind, the remaining decision for the propeller design was to decide for which flight phase it would be optimised. Efficiency during cruise was considered to be the most important phase as this would be beneficial to the range and endurance of the aircraft. Either the operational empty weight (OEW) would be lower because of a smaller battery mass, or the energy provided by the batteries could be used to fly longer or further.

Finally, it was decided that the propellers rotate outboard up to maintain a symmetrical lift distribution. The slipstream created by the propellers would have the same effect on both wings in this configuration. Further explanation on this phenomenon is discussed in Chapter 7.

10.4.2 Propeller Geometry

An external tool called XROTOR was used to design the resulting propellers. XROTOR was developed by MIT and can be used to obtain an optimal propeller design for a given thrust, airspeed, rpm and linear lift coefficient. As mentioned, the cruise phase was selected to design the propeller for. The design parameters are listed in Table 10.4. The Hub Radius (RH) and the Body Radius (RW) are set at 10% and 5% of the Tip Radius (RT), which impose typical hub-to-tip ratio's for low-speed aircraft propellers [(9)]. The linear lift coefficient CC is set at 0.5 which is achievable by selecting a conventional airfoil such as NACA0012 for this design.The overall layout of the propellers is visible in Figure 10.6a and Figure 10.6b.

[(8)] `http://okigihan.blogspot.nl/p/types-of-propellers.html`, Retrieved: 22-01-2018
[(9)] `http://web.mit.edu/drela/Public/web/xrotor/xrotor_doc.txt`, Retrieved: 22-01-2018

Table 10.4: Propeller Design Parameters

Parameter	Value
# of Blades	6
RT $[m]$	0.75
RH $[m]$	0.075
RW $[m]$	0.0365
T $[N]$	60
CC [-]	0.5

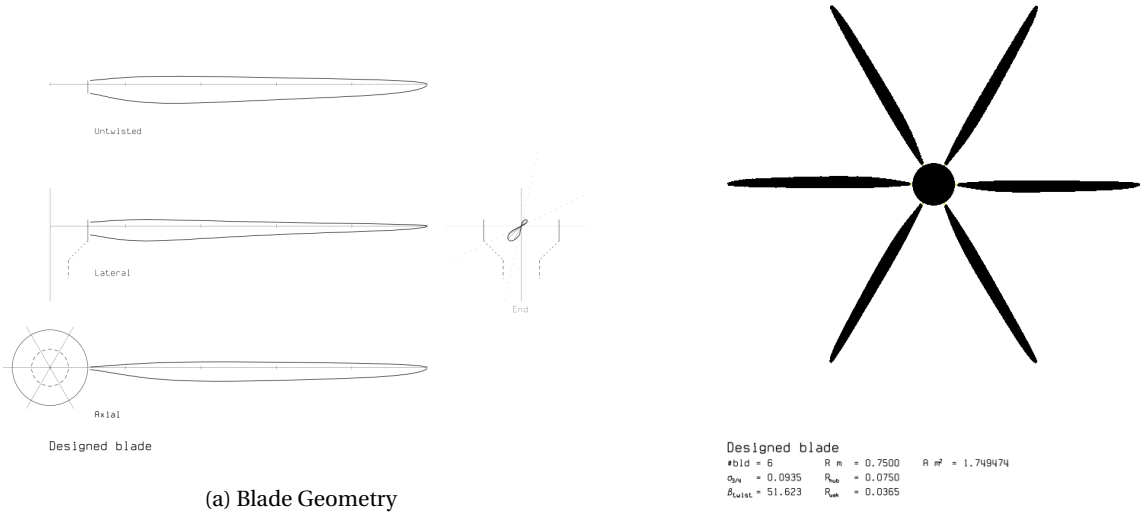

(a) Blade Geometry

(b) Propeller Geometry

Figure 10.6: The design of the propeller and its geometry

As mentioned, the propeller was designed for efficiency in cruise. In Figures 10.7a and 10.7b the blade distribution and corresponding efficiency are evaluated for the cruise case and at the end of the ground run just before liftoff. The x-axis in these plots represent the relative position with respect to the total blade length.

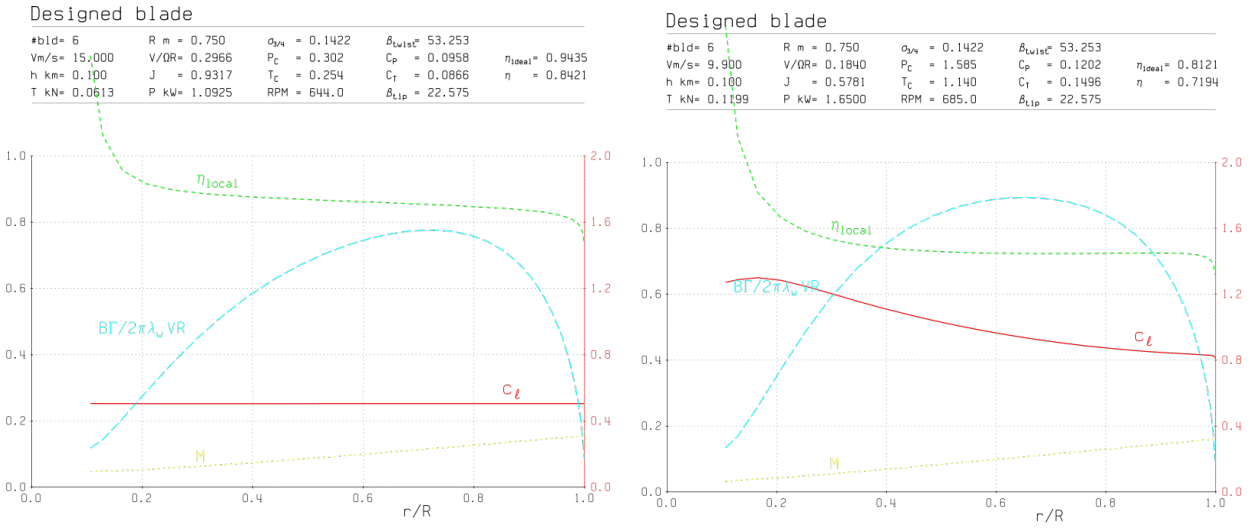

(a) Blade Distribution Cruise

(b) Blade Distribution Take-off

Figure 10.7: Blade Distribution for different conditions

The efficiency during cruise is 0.84 and the efficiency at the end of the ground run is 0.72. For both of these cases, an appropriate tuning of the power and energy system was proposed to achieve the required power for these flight phases. This exact propeller has not been found on the market. The combination of a propeller with such a low thrust required and six blades is rather rare. All propellers found on the market were either twin-bladed or heavily over designed, so the propellers will have to be manufactured. This imposes en estimated manufacturing cost of 5000 euros per propeller. The average total cost of the propellers will decrease depending on the amount of aircraft to be in production.

10.4.3 Propeller Noise

Regarding the noise requirement, XROTOR contains a convenient feature, a module to plot the noise footprint of a designed propeller for a certain area around and below the aircraft. Because the noise of the design performs such an important role in the design, this noise footprint was checked regularly during the iterations of the propeller design. The resulting noise footprints are visible in Section 10.4.3, Figure 10.8b and Section 10.4.3. These figures describe three cases; the static case before takeoff when the velocity of the aircraft is close to zero, the liftoff case where the pitch angle is applied to climb to the screen height and the cruise case. The cruise case was evaluated at 1 m altitude instead of the 150 m cruise altitude because no noise footprint could be distinguished on the ground when flying at the cruise altitude. The noise footprint is plotted at an area two meters in front, 2 meters behind and 1 meter left and right of the aircraft. The critical value to evaluate is the maximum noise level at 1 m distance from the aircraft. Chapter 15 evaluates the noise results of the propeller compared to the requirements.

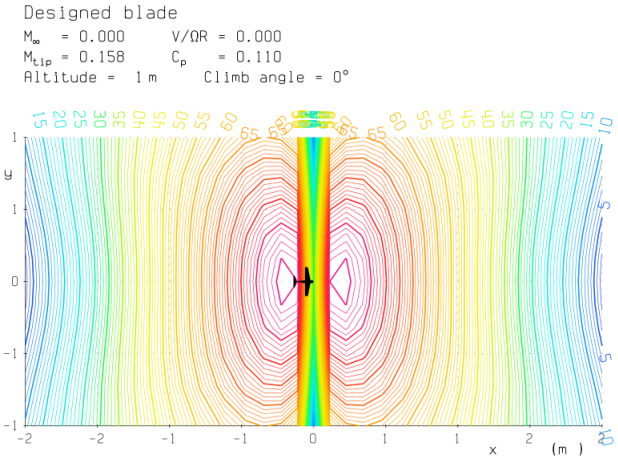

(a) Noise footprint static case

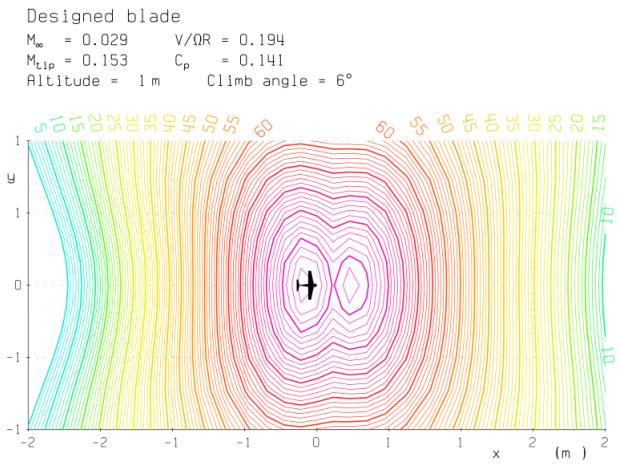

(b) Noise footprint liftoff case

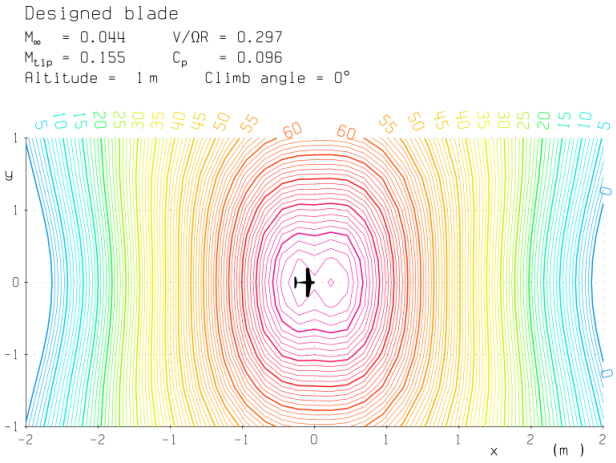

(c) Noise footprint cruise case

Figure 10.8: Noise footprint for different cases

10.5 Verification and Validation

10.5.1 Engine

The analysis of the electrical engine was performed by constructing a tool in MATLAB. To verify this tool an analytic analysis is made to see if the tool is correctly build. Referring to Table 10.2, the *Turnigy RotoMax 50cc* is analysed 'by hand' to see what the error is with the values that were calculated with the tool that was constructed in MATLAB. An overview of the verification process is shown in Table 10.5.

Table 10.5: Verification engine MATLAB tool

Parameter	MATLAB Value	Analytic Value	Error
U_{in} [V]	44.4	44.4	-
T_s [Nm]	117.25	118.3	0.9%
n_0 [rpm]	7631	7675	0.6%
$I_{P_{max}}$ [A]	1058	1057	0.1%
P_{max} [W]	23420	23432	0.05 %
$I_{\eta_{max}}$ [A]	59	57.7	2.2 %
$\eta_{eng_{max}}$ [-]	0.945	0.943	0.2 %

The maximum error is found to be 2.2%. This is considered to be acceptable. To validate this tool, experimental data is used from existing engines to see if this tool generates comparable results. In this manner, it can be checked whether the correct tool has been built. Experimental data from the *Maxon 6W* engine is used[10]. An overview of the *Maxon 6W* engine specifications is given in Table 10.6.

Table 10.6: Maxon 6W specifications

Parameter	Value
k_v [rpm/V]	173
k_t [Nm/A]	0.0552
$R[\Omega]$	41.5
I_0 [A]	0.0146

These values are then used as inputs in the MatLab tool and the outputs are compared to the existing data. An overview of the validation process is shown in Table 10.7.

Table 10.7: Validation of engine MATLAB tool using experimental data from the Maxon 6W

Parameter	MATLAB output	Experimental data	Error
U_{in} [V]	24	24	-
T_s [Nm]	0.0311	0.0319	2.5%
n_0 [rpm]	4047	3990	1.4%
$\eta_{eng_{max}}$ [-]	0.70	0.71	1.4 %

Compared to experimental data, the maximum error in the MATLAB model is 2.5%. The MATLAB tool is therefore considered to be validated as an accurate tool to be used for electrical engine analysis.

10.5.2 Propeller

The design of the propeller was performed in XROTOR. A simple analytical solution was obtained from static and dynamic thrust theory [11]:

$$T = 1.225\frac{\pi(0.0254d)^2}{4}\left[\left(0.0254\text{RPM}\cdot\text{pitch}\frac{1}{60}^2\right) - \left(0.0254\text{RPM}\cdot\text{pitch}\frac{1}{60}\right)V\right]\left(\frac{d}{3.29546 * \text{pitch}}\right)^{1.5} \tag{10.15}$$

[10] `http://hades.mech.northwestern.edu/index.php/Brushed_DC_Motor_Theory`, Retrieved: 17-01-2018

[11] `http://electricrcaircraftguy.blogspot.com/2013/09/propeller-static-dynamic-thrust-equation.html`, Retrieved: 22-01-2018

d is the propeller diameter in inches, RPM is the propeller rotational speed in revolutions per minute and the pitch is the relative distance travelled by the propeller in one revolution. The behaviour of the thrust with increasing airspeed could then be compared. The analytic model behaves in a linear manner, while the numerical model is based on polynomial regression. Because these lines are relatively far apart, it is useful to integrate the thrust for the analytic and numerical functions over airspeed. The error that pops up is used to verify if thrust provided by the propeller in the model is reflective to the provided thrust by the analytic relation. This error is found to be 1.6 %, so it is considered acceptable.

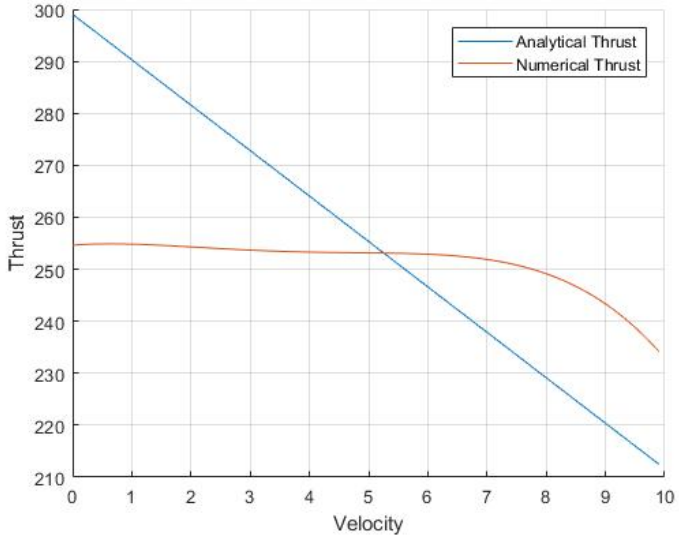

Figure 10.9: Verification Designed Propeller

Insufficient resources have been available to perform a proper validation for this tool, so validation was performed by doing a literature study on the tool. T. Sinnige et al. conducted validation of XROTOR in an paper published by the American Institute of Aeronautics and Astronautics in 2014 [12]. Verification and validation of the noise module has been performed at an earlier stage by George P. Succi et al [12].

10.6 Conclusions and Recommendations

To conclude the propulsion subsystem, a general layout of all the components of this subsystem is given during the take-off phase and during the cruise phase. During these phases, the engines requires a certain power setting. The power settings for the take-off and the cruise phase respectively are given below in Table 10.8. An overview of the power system layout is given in Figure 10.10.

Table 10.8: Engine setting during take-off and cruise

Parameter	**Take-off**	**Cruise**
U_{in} [V]	25.5	23.7
I_{in} [A]	70.8	50.2

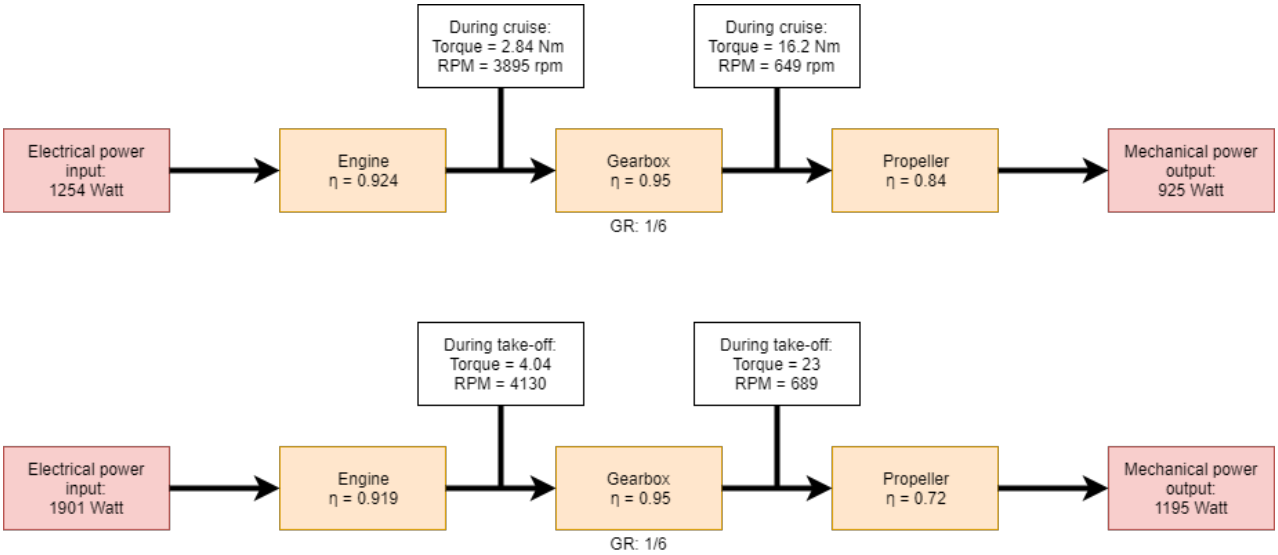

Figure 10.10: Power system layout during cruise & take-off

A number of recommendations exist for further design and use of the propulsion subsystem. For instance, the propellers are somewhat slender when they reach the root of the blades. This is potentially a fragile section. Structural failure should be investigated to make sure the blades are strong enough to perform under the given circumstances. Reinforcements at the root of the blades is recommended, as this is an area that produces the least amount of thrust. Also, the propellers are recommended to turn inboard up instead of the current outboard up configuration. Inboard, the generated lift is generally higher than outboard, making the effects of induced thrust on the upwash side of the propeller more significant. For the gear system, there exist several design options. Example gear systems are belt drive systems, conventional gear drive systems and planetary gear systems. Belt drive systems are the most inexpensive and most simple of the given options. Belt drive systems also have the benefit of being very silent which would comply with the requirement on a low noise level. However, as mentioned in Section 10.2.3 the current gear ratio is set at six and belt drive systems are usually limited to gear ratios of around four. A possible solution is to use a compound belt drive gear system. In this system a dual belt gear is used to get the desired gear ratio. It is advised to investigate this gear system for the *AerGo*. To get an idea of this system, an illustration of a compound drive gear system is given in fig. 10.11.

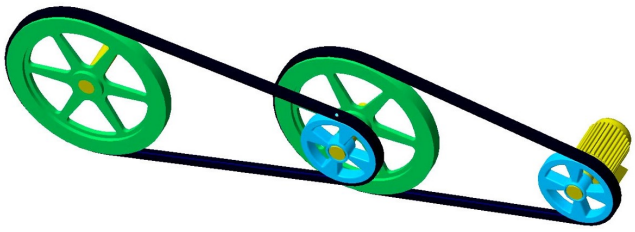

Figure 10.11: Compound belt drive gear system

11 Hydrodynamics

In this chapter the hydrodynamic qualities of the aircraft will be described. It starts with a trade-off on the float configuration, explained in Section 11.2. Once this configuration is known, the hull can be optimised. This optimisation is based on hydrodynamic resistance (Section 11.3) and the stability characteristics of the hull; the stability characteristics are analysed both for static cases (Section 11.4) and for dynamical cases (Section 11.5). Next, the steering system is discussed in Section 11.6.1, after which the chapter is concluded by Verification and Validation in Section 11.8.

11.1 Approach

After a trade-off between different float configurations, an initial sizing is done. Based on reference aircraft and simple rules of thumb, a general hull size is found. To reduce the hydrodynamic drag as much as possible is desired to limit the power needed at take-off. To perform this optimisation, a drag model is constructed which shows the effect of geometrical variations of the hull on the drag. As the required stability limits this optimisation, it is important to find this limit. This is done with a static stability analysis in both the lateral and longitudinal direction, and a dynamic stability analysis in the lateral direction. Once the hull shape and stability characteristics are known, the control system can be chosen and sized.

- Assumption: The effect of the step on the hydrodynamic resistance is not taken into account due to its analysis being outside of the scope of this project. The effects of this step are not entirely straightforward, but in general it reduces the resistance.
- Assumption: Hydrodynamic roll damping of the hull is not taken into account, resulting in very conservative stability estimations. As the hull has hard chines, this damping will be fairly significant.
- Assumption: The loading factor is assumed to be 8.5 . Although the actual loading factor is 9.9, the model only gives accurate results up to 8.5 . A higher loading factor will only reduce the resistance further, meaning that calculations where 8.5 is used are more conservative.

11.2 Float Configuration

With the final concept in mind it is important to make a trade-off for the float configuration. There are two configurations left due to the concept choice. A hull (with pontoons) and a two float configuration. This trade-off will be based on five criteria, The aerodynamic and hydrodynamic drag, the structural weight, hydrodynamic stability and operations. criteria are compared with each other and graded with a + if favourable, a - if unfavourable and 0 if the options do not differ.

As found in the previous report [4], the weight of both the two float and hull configuration does not differ much because their volumes will be the same. Therefore the same amount of material will be needed. In order to choose the best design configuration the entire weight contribution is considered.

The hull needs extra support to withstand high stress forces at the wing assembly points and also to support the pilot seating position. However the two float configuration also needs a pilot seating structure and wing structure at assembly points. Incorporating the hull in the wing structure would decrease the overall weight and is therefore preferred over the two float configuration.

Integrating the hull in the wing reduces the aerodynamic drag compared to one or multiple floats attached underneath. Especially at high speeds, a two float configuration is undesirable. The difference at low speeds however is much lower. Furthermore, seating the pilot in the hull reduces the drag a lot and therefore the hull configuration is again the most favourable.

For operational purposes it is better to use the hull configuration. Building a trailer which can get the aircraft out of the water would be easy because the float and the basic wing structure fits right on it. For a two float configuration this trailer should be at least 1.6 m wide which is not allowed due to regulations and thus other options to get it out of the water should be determined. For example sliding, entering and exiting the water would be possible at shallow coastlike shores.

The two float configuration has problems with operational stability. It is impossible to step on the float because the buoyancy is not large enough. The size should be increased by at least 25% to make sure it does not sink. Therefore entering the aircraft should be done by swimming between the floats.

For the hydrodynamic stability, a two float configuration is much more stable. The spacing of the floats ensure lateral stability. The hull will roll due to small inputs or center of gravity changes and needs to be wide enough to ensure lateral stability. When increasing the speed, the hull gets more stable due to the compensating lift forces of the hydrodynamic lift on the hull and aerodynamic lift on the wings respectively.

The hydrodynamic drag does not effect the float configuration much since it is dependant on the wet surface. This is mainly determined by the weight of the aircraft. The length over width does affect the hydro drag a little, this makes the two floats a little less draggy than the single float. However most hydrodynamic drag is generated by the hull shape which will be quite similar in both configurations.

Considering the results in Table 11.1 it is seen that the hull configurations has no real downsides and thus it is decided that the hull configuration will be designed for.

Table 11.1: Trade-off summary of the float configuration

Subsystem	hull	two floats
Aerodynamics	+	-
Structural weight	+	-
Stability	0	+
Operations	+	-
Hydrodynamics	0	0

11.3 Hydrodynamic Analysis

11.3.1 Initial sizing

Before optimising calculations on the hull shape can be performed an initial sizing is done. This section is a short summary of the initial sizing. For a more thorough insight on the initial sizing can be referred to the midterm report [5].

The main purpose of the hull is to ensure that the aircraft floats while on water. This means the volume of the hull must be enough to keep the MTOW of the aircraft afloat. Because of the under 70kg empty weight of the design, regulations on buoyancy capacity for floatplanes are not directly applicable to the *AerGo*. In order to still build in enough safety margin and not over design the hull at the same time buoyancy safety factors are determined based on sailing industries. It is determined that a buoyancy safety factor of 1.33 is sufficient for total hull volume [(1)]. In case the unfortunate event of the hull being pierced would occur the pilot must still be able to retrieve his *AerGo*. The hull is required to have two separate watertight compartments with both enough floating capacity for the OEW plus an additional10 kg [(2)]. It will then be possible for the pilot to, in case of emergency, get out of the *AerGo* quickly and swim to shore.

The volume of the hull is determined by multiplying the MTOW of the hull with the freshwater density of 1.000 kg/m^2 and taking into account the safety factor of 1.33. A first estimation on the width of the hull, further referred to in this chapter as beam, is based on the relation from the book *Seaplane Float & Hull Design* [20] given by:

$$B_x = 0.36 \cdot W_0^{1/3} \tag{11.1}$$

With B_x in feet and the weight being the *MTOW* in pounds. Statistical data is gathered on the *Searay*, *IconA5*, *SR/A1* and *Catalina* in order to estimate the step location of the hull and the total hull length. The height of the hull is determined using the volume needed to acquire the minimum buoyancy.

The step in the hull provides the ability to pitch during take-off without pushing the rear of the hull in the water. Furthermore it reduces the wetted area significantly while planing and thereby reducing the hydrodynamic drag. The step height will be determined so that there will be significant distance between the water surface and the aft of the hull at take-off pitch. Based on a step geometry approximation by Gudmundsson the step height is estimated to be 0.07 times the beam[14].

A higher deadrise produces less hydrodynamic lift at low speeds but relates to a lower impact load at landing and provides better seaworthiness. Since the take-off speed is relatively low compared to conventional seaplanes it is

[(1)] `https://www.glen-l.com/weblettr/webletters-7/wl55-flotation.html`, Retrieved: 8-12-2017

[(2)] urlhttp://moth-sailing.org/wp-content/uploads/2015/02/Att-10-141228-Moth-Class-Rules-2015-DRAFT.pdf, Retrieved: 8-12-2017

desired that the aircraft is planing at an early stage. Furthermore the aircraft will be operating on quiet waters only and therefore a low deadrise of 15 °is first considered [20].

The initial sizing of the hull is summarised in Table 11.2. These values are the starting point of the hull optimisation.

Table 11.2: Results of the initial sizing of the hull used for further optimisation of the hydrodynamic performance

Parameter	**Value**
MTOW [N]	1470
Total buoyancy [m^3]	0.2
Beam [m]	0.75
Height [m]	0.16
Forebody length [m]	1.95
Length [m]	3.4
Step height [m]	0.05
Deadrise angle [°]	15

11.3.2 Hull optimisation

In order to estimate the hydrodynamic resistance of the design, the Delft Systematic Deadrise Series (DSDS) database is used. This is a database with shapes and their respective hydrodynamic behaviour for a wide variety of planing hulls. Research by Keuning and Hillege [18] using this database suggests two different methods to calculate the hydrodynamic resistance, the FAST method and the HSMV method. Although both methods are applicable to this design, the HSMV method is longer and more difficult to implement in an optimisation script. The calculations are done with the FAST method and the HSMV method is be used later on for model verification (see 11.8).

The FAST method for drag calculation consists of two formulae. The first formula gives the specific resistance of the prismatic hull:

$$\begin{aligned}\frac{R_t}{\Delta} =& a_0 + a_1 LCG + a_2 LCG^2 + a_3\left(\frac{L_p}{B_{px}}\right) + a_4\left(\frac{L_p}{B_{px}}\right)^2 + a_5\left(\frac{L_p}{B_{px}}\right)^3 + a_6\left(\frac{A_p}{\nabla^{\frac{2}{3}}}\right) + a_7\left(\frac{A_p}{\nabla^{\frac{2}{3}}}\right)^2 + a_8\left(\frac{A_p}{\nabla^{\frac{2}{3}}}\right)^3 \\ &+ a_9\left(LCG\cdot\frac{L_p}{B_{px}}\right) + a_{10}\left(LCG\cdot\frac{A_p}{\nabla^{\frac{2}{3}}}\right) + a_{11}\left(\frac{L_p}{B_{px}}\cdot\frac{A_p}{\nabla^{\frac{2}{3}}}\right)\end{aligned} \tag{11.2}$$

Where a_0 to a_{11} are coefficients that depend on the velocity, the deadrise angle and the displacement which are taken from the DSDS database. The deadrise angle, or β is the average angle between the bottom of the hull and the horizontal plane. LCG denotes the longitudinal distance between the centre of gravity and the centroid of the planing area. A_p or the planing area is the projection of the entire wetted area onto the horizontal plane. $\frac{L_p}{B_{px}}$ is the fraction between the length and the width of the planing area. $\frac{A_p}{\Delta^{2/3}}$ is the loading coefficient, or the fraction between the planing area and the displaced volume, which is raised to the power of $\frac{2}{3}$ to make the coefficient dimensionless. $\frac{R_t}{\nabla}$ is the specific resistance, or the ratio between the total hydrodynamic resistance and the weight of the displaced mass (in Newton).

The second formula gives the additional specific resistance caused by the twist and the buttock angle:

$$\begin{aligned}\frac{dR_t}{\Delta} =& b_0\gamma + b_1\epsilon + b_2\left(\gamma\cdot\frac{A_p}{\nabla^{\frac{2}{3}}}\right) + b_3(\gamma\cdot LCG) + b_4\left(\gamma\cdot\frac{L_p}{B_{Px}}\right) + b_5\left(\epsilon\cdot\frac{A_p}{\nabla^{\frac{2}{3}}}\right) + b_6(\epsilon\cdot LCG) + b_7\left(\epsilon\cdot\frac{L_p}{B_{px}}\right) + b_8\left(\gamma\cdot\left(\frac{A_p}{\nabla^{\frac{2}{3}}}\right)^2\right) \\ &+ b_9(\gamma\cdot LCG^2) + b_{10}\left(\gamma\cdot\frac{A_p}{\nabla^{\frac{2}{3}}}\cdot\frac{L_p}{B_{px}}\right) + b_{11}\left(\gamma\cdot\frac{A_p}{\nabla^{\frac{2}{3}}}\cdot LCG\right) + b_{12}\left(\gamma\cdot LCG\cdot\frac{L_p}{B_{px}}\right)\end{aligned} \tag{11.3}$$

Where γ is the buttock angle, or the average angle between the keel line from the middle to the stern and the horizontal axis. ϵ stands for the twist, or the difference in deadrise angle between the middle and the stern.

From these formulae, the total specific resistance is calculated. However, for clarity and simplicity, the total resistance (R_t) is preferred. The relation between the two is as follows:

$$R_t = \frac{R_t}{\Delta}\cdot\Delta \tag{11.4}$$

Usually, the weight of the displacement (Δ) is equal to the weight of the ship. In seaplanes however, the wings produce a certain amount of lift, which gives the following equation for the weight of the displacement:

$$\Delta = m \cdot g - C_l \frac{1}{2} \rho V^2 S \tag{11.5}$$

Where m is the total aircraft mass, g is the gravitational acceleration, S is the wing surface, V is the groundspeed and C_l is the lift coefficient. To simplify the calculations, the angle of attack is assumed to be zero during the entire take-off run. Combining this with Equation (11.4) and Equation (11.5) gives:

$$R_t = \frac{R_t}{\Delta} \cdot \left(m \cdot g - C_l \frac{1}{2} \rho V^2 S \right) \tag{11.6}$$

The a and b coefficients depend on the displacement, deadrise angle and Froude number. To give the hydrodynamic resistance as a function of velocity, it is preferable to fix the displacement and deadrise, while varying the Froude number. The Froude number is related to the velocity as follows:

$$F_n = \frac{V}{\sqrt{g \cdot LWL}} \tag{11.7}$$

Where F_n is the Froude number and LWL is the waterline length. The coefficients are determined by fitting a cubic interpolation through the coefficients corresponding to a certain displacement and deadrise value. For an example, see Section 11.3.2.

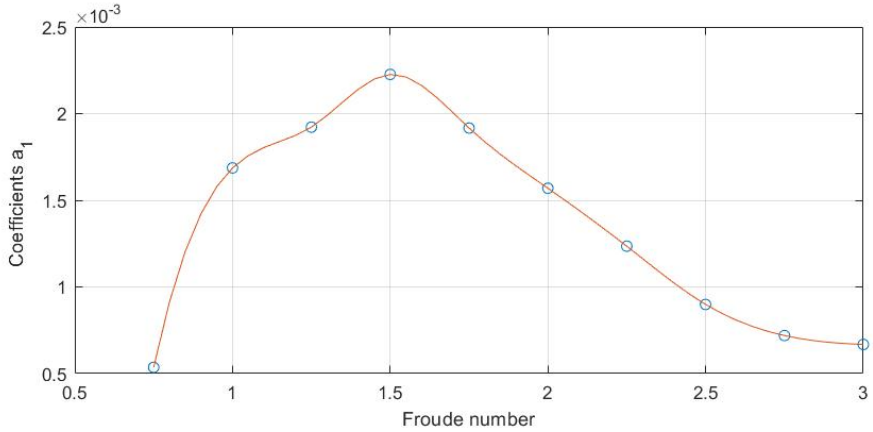

Figure 11.1: Interpolation for a_1 as in function of F_n

Once interpolations for all coefficients is done, all equations are combined into a Matlab script to create drag vs velocity plots. By repeating these calculations for different hull shapes, the effect of the geometry on the drag can be analysed. Clarifying examples of these variations are shown in Figure 11.2.

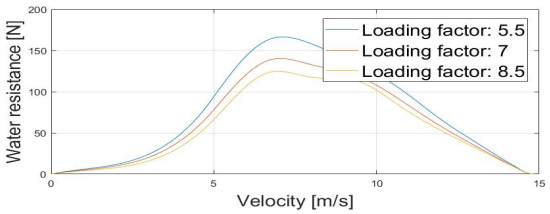

(a) The effect of varying the Loading factor on the water resistance

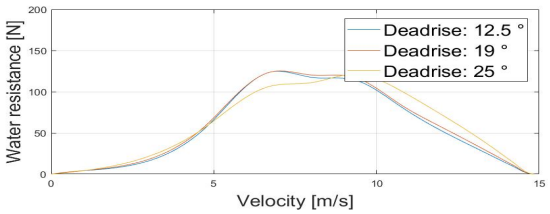

(b) The effect of varying the Deadrise angle on the water resistance

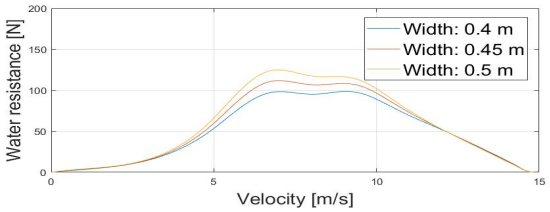

(c) The effect of varying the Width on the water resistance

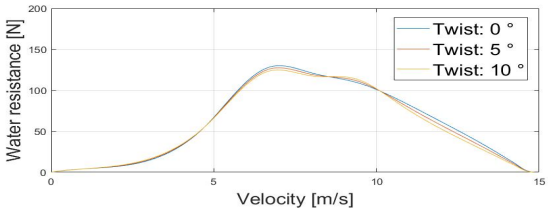

(d) The effect of varying the Twist angle on the water resistance

Figure 11.2: Graphs demonstrating the effect of varying several parameters on the hydrodynamic drag

From these graphs it can be seen that there is still some room for improvement. For example, increasing the length to width ratio would greatly reduce the drag. However, stability and operational concerns limit this change; and only a 10 % increase is possible. Increasing the twist angle to 10° reduces the drag at higher speeds slightly. As this is the phase where the engine thrust is lowest and the aerodynamical drag is highest, this improves the take-off performance. An added benefit is that this increases the loading factor, which once again reduces the resistance. The addition of a buttock angle has a more complex result: the maximum drag increases, but the drag at higher speeds reduces. As slightly higher drag at low speeds does not affect the engine or battery sizing, but lower drag at higher speeds (the more critical phase for accelerating) increases take-off performance and is therefore preferred. For these reasons, it is decided to add a small buttock angle. A comparison of the drag characteristics of both the original and the optimised design can be seen in Section 11.3.2, while their hull parameters can be found in Table 11.3.

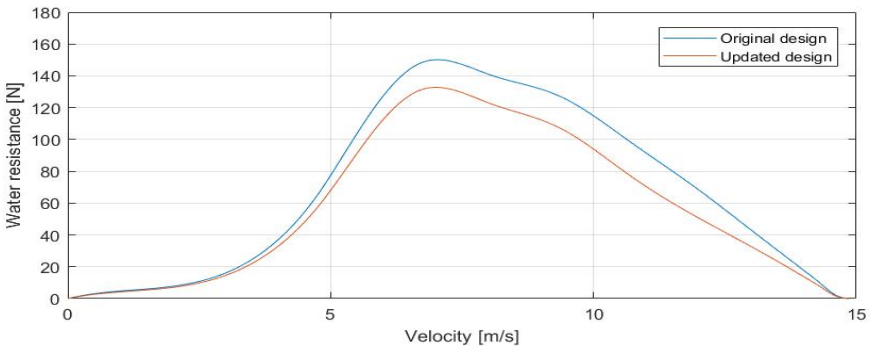

Figure 11.3: Drag characteristics for the original and the optimised hull design

Table 11.3: Geometrical parameters of the hull design

Parameter	**Original design**	**Optimised design**
Overall length [m]	3.0	3.0
Maximum width [m]	1.0	1.0
Deadrise angle [°]	15.0	12.5
Twist angle [°]	0	10
Buttock angle [°]	0	-1
Loading Factor [-]	7.0	8.5*

**: Actual value is 9.9, but model-input is 8.5 .*

11.4 Static Stability

11.4.1 Pontoon Sizing

Pontoons on the wingtip are necessary for providing extra safety to the aircraft in extreme situations. They are attached to protect the wingtips from hitting the water directly and provide a righting moment. The main function of the pontoons is to counteract the moment created by the pilot when entering the aircraft due to the difference in centre of gravity and centre of buoyancy causing it to roll. The assumptions made in order to perform an estimation of the pontoon size are stated below:

- The worst case scenario is considered where the pilot will be standing on the outer edge of the hull at the widest point of the hull.
- The righting moment due to the hull is so low it will not make a significant difference in the pontoon volume and is therefore neglected.
- Following this it is considered that the centre of buoyancy of the hull is at the same position.
- The pontoons are sized based on buoyancy only. The pilot must roll the aircraft to the point where one pontoon is already in the water before entering so impact loads are minimal. Impact is therefore neglected in the sizing of the pontoons.
- the centre of the pontoons will be attached at a distance of 10cm measured from the wing tip.

A simple analysis has been done on the forces and moments acting on the aircraft in this position. A schematic overview of the forces is shown in Section 11.4.1. Considering the aircraft to be at rest at this point, the minimal required force for the righting moment of the pontoon can be found by solving the moment equation around the centre of gravity of the aircraft and the sum of the forces

$$F_{R_{Pontoon}} \cdot ((0.5b - 0.5B)cos(\Gamma) - 0.1) = F_{Pilot} \cdot 0.5B \tag{11.8}$$

and

$$F_{R_{Pontoon}} + F_{Hull} = F_{Pilot} + F_z \tag{11.9}$$

This results in a required righting force $F_{R_{Pontoon}}$ of 91.5 N. Taking into account a small safety factor it is estimated for each wingtip float to have a minimum volume of 0.01 m^3.

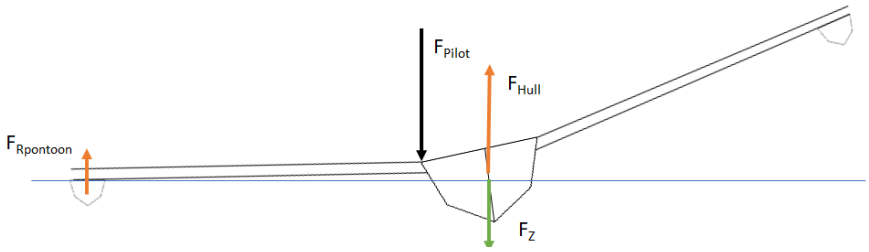

Figure 11.4: Disturbed position of the aircraft with pontoons hitting the water due to the pilot position

In the book "Design for flying" it is stated that the pontoon volume must fall between: $\frac{0.75W}{y}$ to $\frac{1.25W}{y}$ [31]. This would result in a volume between 0.006–0.0106 m^2. The estimated float value is on the high end of this range and at this point in the design it is determined to be detailed enough.

Adding pontoons to the wing will add weight. As the pontoons only need to withstand a buoyancy load it is decided to use a lightweight foam material covered by two layers of carbon fibre skin. To reduces weight, 25 % of the foam material in the centre of the float is taken away. For further explanation of the material selection of the floats can be referred to Section 9.3.2.

When having an impact, worst case scenario is that the skin gets damaged and the foam slowly starts to absorb water and therefore losing its buoyancy. This is considered to be a small risk, and will not damage the aircraft much. In this situation the floats can be replaced at relatively low costs. Foam material that would not absorb water are considered to mitigate this risk. However these are more expensive and more heavy which is not worth the benefit.

11.4.2 Centre of buoyancy location

Although a fully detailed hydrodynamic stability analysis is outside of the scope of this design, a static stability analysis already gives a good indication of the hydrodynamic behaviour of the *AerGo*. As the general shape of the hull is based on the DSDS, which consists of hull shapes that have been used extensively since 1962, it can be assumed that the hull is at least adequately stable. However, due to the abnormal loading case (ultra light hull compared to payload and wings) which leads to a centre of gravity that is located exceptionally high, this is not automatically the case. For this reason, the effect of this loading on longitudinal and lateral stability are analysed and the validity of the aforementioned assumption is checked.

Although the centre of gravity is located above the waterline, the Z-distance between the centre of gravity and the centre of buoyancy is small when compared to the total length of the hull, which is at least 10 times larger. This means that at relatively small pitch angles, the centre of buoyancy will shift further than the centre of gravity, which has a stabilising effect. As can be seen in Figure 11.5b, a positive pitch angle affects which part of the hull provides the buoyancy, therefore changing the longitudinal CoB position backwards. It also shifts the CoG forward, however this shift is neglible. Due to this offset between CoG and CoB, a restoring moment occurs, and the hull will pitch down until CoB and CoG are aligned again. This position is the neutral position, shown in Figure 11.5a. When the CoG shifts forwards, the opposite happens; the hull pitches down, causing CoB to move forward, until CoG and CoB are aligned. This results in a new neutral position, as shown in Figure 11.5d.

It is thus safe to assume that at low pitch angles (10° or less), the hull is stable in the longitudinal direction. However, once the aircarft has reached the V_{TO}, the pilot should be able to reach a pitch angle of at least 7.7° in order to take off, which is a difficult operation in a stable hull. In order to solve this problem, the aft part of the hull is made to be less deep than the forward part. This means that once the hull is planing and the draft reduces, the aft part of the hull is raised out of the water completely. As can be seen in Figure 11.5e and Figure 11.5f, the effect of a positive pitch angle on the CoB location is greatly reduced, resulting in an easier pitch-up motion.

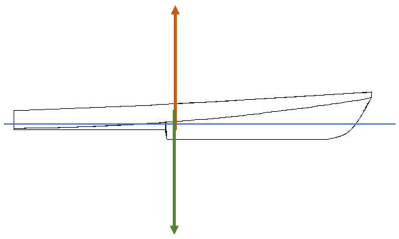

(a) The neutral position at speeds below V_p.

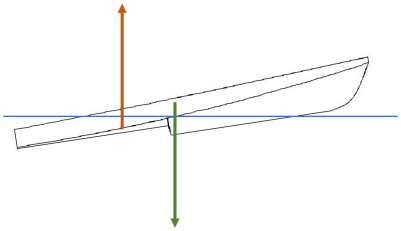

(b) Disturbed position at speeds below V_p.

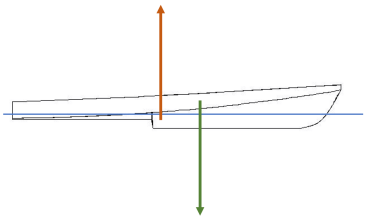

(c) Forward shift in the centre of gravity at speeds below V_p.

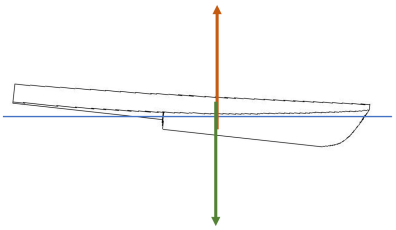

(d) Neutral position for a forward shift in the centre of gravity at speeds below V_p.

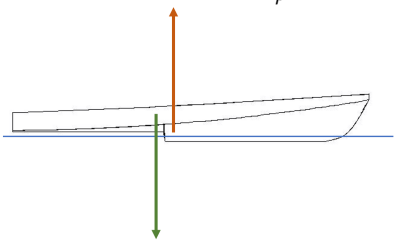

(e) Backward shift in the centre of gravity at speeds near V_{TO}.

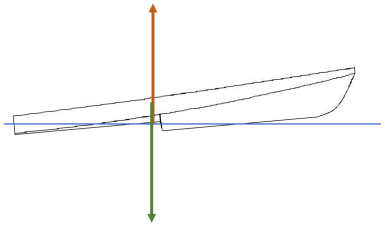

(f) Neutral position for a backward shift in the centre of gravity at speeds near V_{TO}.

Figure 11.5: Longitudinal positions of the weight and buoyancy forces for different situations.

11.5 Dynamic lateral stability

11.5.1 Effect of CoG-location and width

When it comes to lateral stability, the vertical distance between CoB and CoG has a much larger effect. Since the ratio between this distance and the width of the hull is a lot larger, the shift in the Y-direction of the CoG is comparable with that of the CoB. Figure 11.6f and Figure 11.6c shows how the position of the CoG influences the lateral stability. If the CoG is located very low a small disturbance angle causes a restoring moment. However if the CoG is located higher a small disturbance angle causes a destabilising hull, even though the hull shape has not changed. As the CoG is located fairly high (only 3 cm) below the highest point of the hull, one cannot simply assume that the lateral stability is adequate. This means that further analysis is required.

Figure 11.6 shows how the width of the hull affects the lateral stability. It can be seen that when a disturbance angle is added to the thin hull, the CoG shifts more than the CoB, which results in a destabilising moment. When the same is done for a wide hull, the opposite occurs, leading to a restoring moment.

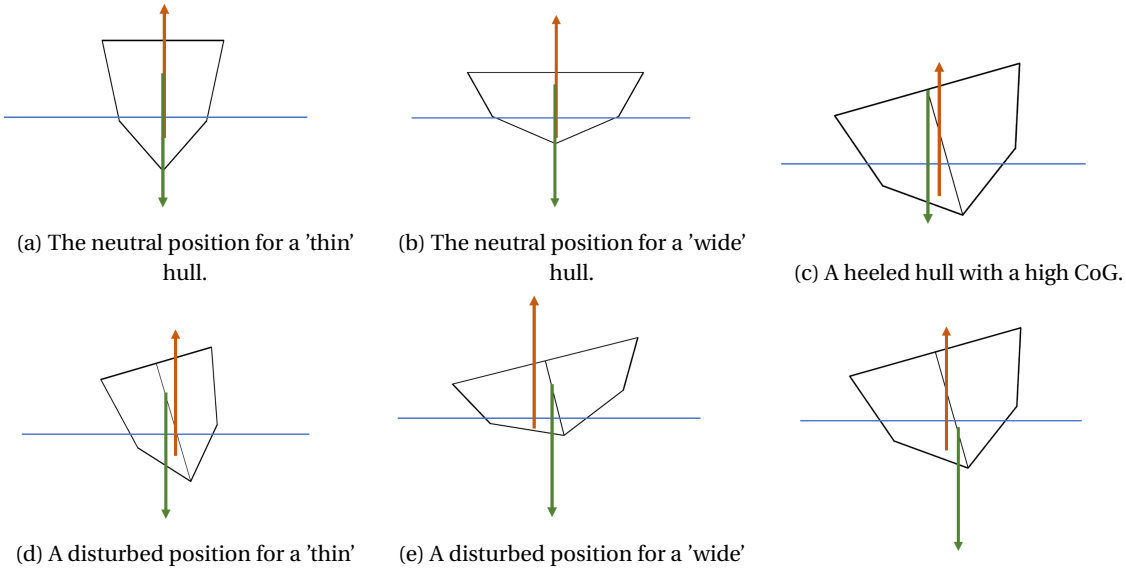

(a) The neutral position for a 'thin' hull.

(b) The neutral position for a 'wide' hull.

(c) A heeled hull with a high CoG.

(d) A disturbed position for a 'thin' hull.

(e) A disturbed position for a 'wide' hull.

(f) A heeled hull with a low CoG.

Figure 11.6: Stability for different .

11.5.2 Righting moment

The method used in this subsection is based on the method proposed by Fossati [11], used to analyse the heeling characteristics of sailing yachts.The first step in this dynamical lateral analysis of the hull is calculating the righting moment. This righting moment depends on a multitude of other parameters and equations, which are explained in this section.

The first step is calculating the moment arm of the heeling moment. This moment arm (ΔY_{heel}, which is the lateral distance between the keel and the centre of gravity, is calculated as follows:

$$\Delta Y_{heel} = Y_{CG} + Z_{CG} \cdot sin(\theta) \tag{11.10}$$

Where Y_{CG} and Z_{CG} are, respectively, the Y- and Z-coordinate of the centre of gravity, and θ is the heel angle. Once the moment arm is found, the heeling moment (M_h) can be calculated:

$$M_h = W \cdot \Delta Y_{heel} \tag{11.11}$$

Where W is the total weight of the aircraft.

The centre of buoyancy is equal to the centroid of the part of the hull below the waterline. Therefore, the first step is to find the location of the waterline. This is done by first discretising the hull into approximately 20,000 elements, and then rotating the entire hull by $theta$, as the part of the hull that is underwater changes with the heel angle. The rotation is done with the following formula:

$$\begin{aligned} Y_i' &= Y_i cos(\theta) - Z_i sin(\theta) \\ Z_i' &= Z_i cos(\theta) + Y_i sin(\theta) \end{aligned} \tag{11.12}$$

Where Y_i' and Z_i' are, respectively, the Y- and Z-coordinates of element i in the rotated system. Y_i and Z_i are the Y- and Z-coordinates of element i in the original system. Now the hull is modelled at the desired heeling angle, the waterline location can be calculated. This is done by iteration, which is started with an educated guess regarding the draft (the Z-distance between the waterline and the deepest part of the hull). The volume of all elements below the waterline is summed and compared to the required displacement. Based on the difference, a smaller or larger draft value is taken, until the difference between the calculated and required displacement is less than 0.1 % of the displacement.

Now the exact volume and location of each element below the waterline is known, and the location of the centre of buoyancy can be calculated as follows:

$$Y'_{CB} = \frac{\sum V_i Y'_i}{\sum V_i} \tag{11.13}$$

Where Y'_{CB} is the Y-coordinate of the centre of buoyancy in the rotated system, while V_i is the volume of element i. This is also the moment arm of the buoyancy force, resulting in a total righting moment (M_r) that can be calculated as follows:

$$M_r = M_h - \Delta \cdot Y'_{CB} + M_{aero} \tag{11.14}$$

Where Δ is the weight of the displaced volume and M_{aero} is the aerodynamical restoring moment caused by the wings. This moment is defined as follows:

$$M_{aero} = C_{l_p} \bar{q} S c \theta \frac{b}{2V_{TAS}}; \tag{11.15}$$

Where C_{ℓ_p} is the roll damping coefficient, $\bar{q}$ is the dynamical pressure, S is the wing surface, $\bar{c}$ is the chord length, b is the wing span and V_{TAS} is the true airspeed.

These righting moments already give an indication as to whether the aircraft is hydrodynamicly stable: a negative $\frac{dM_r}{d\theta}$ means that the hull tries to counteract the heeling angle, resulting in a statically stable design. On the other hand, a positive $\frac{dM_r}{d\theta}$ means that the hull will increase the heeling angle, resulting in a statically unstable design.

11.5.3 Dynamic heeling behaviour

In order to perform a dynamic lateral stability analysis, the variation of the heel angle with time is calculated for different starting conditions, over an interval of 100 s with a timestep dt of 0.001 s. This angle is calculated as follows:

$$\begin{aligned} \dot{\theta}_t &= \dot{\theta}_{t-1} + \frac{M_{r_t}}{I_{xx}} \\ \theta_t &= \theta_{t-1} + \dot{\theta}_t \cdot dt \end{aligned} \tag{11.16}$$

Where $\dot{\theta}_t$ and $\dot{\theta}_{t-1}$ are the angular velocity at, respectively, the current and previous step. M_{r_t} denotes the righting moment corresponding to the current heeling angle, θ_t, while θ_{t-1} is the heeling angle at the previous step.

For the hull dimensions given in Section 11.3.1, the aircraft will not have stable heeling characteristics, as can be seen in Figure 11.7a. As explained earlier, there are two major options when it comes to improving the lateral stability; the first being lowering the CoG. As this is not possible, due to operational restrictions and the impact on flight dynamics, the only option is to increase the width of the hull. However, the hydrodynamic analysis shows that this has a negative impact on the water resistance. Therefore, the width of the hull has to remain as low as possible, while still providing adequate stability.

11.5.4 Effect of pilot movements

The width at which the hull becomes stable is 95 cm, as can be seen from Figure 11.7b. However at this width the hull is barely stable, and if the pilot were to shift his CoG less than 1 cm to the side, the hull would become unstable again. As these lateral CoG shifts are likely to occur, it is decided that the stability corresponding to a width of 95 cm might not be adequate. In order to analyse the effects of these shifts, a conservative estimation for lateral CoG shifts is made. Although the biomechanics of rowers is closely related to the movements of the pilot in this design, no accurate data is readily available. Therefore, movement data of cyclists during a moderate training[3]. is used. As cyclist going in a

[3] `https://bioracermotion.com/#bioracer-motion-3d-system`, Retrieved: 20-01-2018

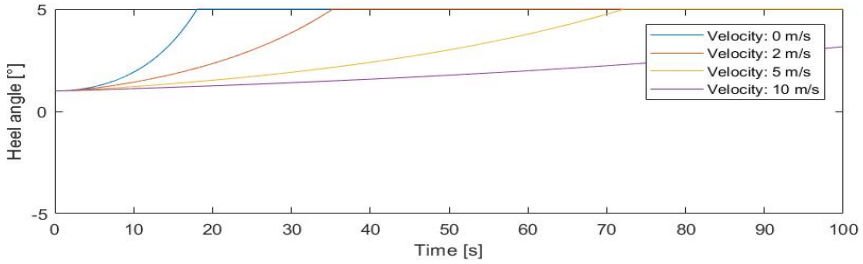

(a) Heeling motion for a hull width of 75 cm.

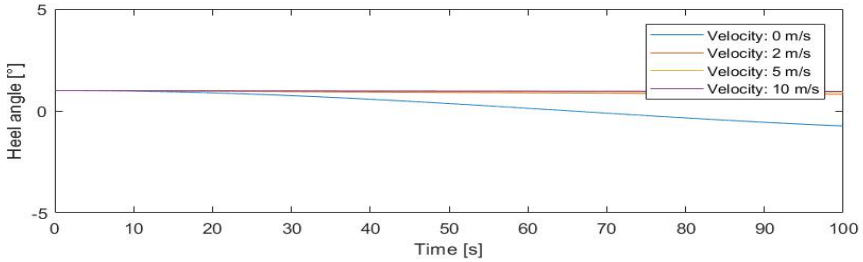

(b) Heeling motion for a hull width of 95 cm.

Figure 11.7: Heeling behaviour a different hulls, with a disturbance angle of 1°, for varying velocities.

straight line try to keep their CoG from shifting sideways, any sidewards movements they do make are involuntary. The data shows that when doing this, the shoulders of cyclists move up to 3 cm left and right. Assuming the CoG of the body being halfway between the hips and the shoulders, this results in lateral shifts in the CoG of the body of no more than 1.5 cm. With this conservative estimate for lateral CoG shifts for the pilot's mass, lateral CoG shifts for the total aircraft mass are calculated. These shifts are then included into Equation (11.10) and new heeling behaviour is found.

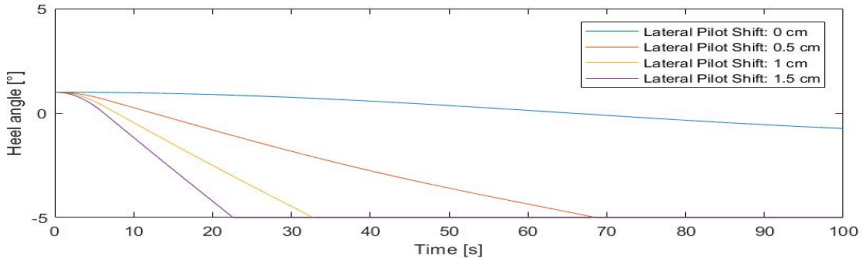

(a) Heeling motion for a hull width of 95 cm, for different pilot positions.

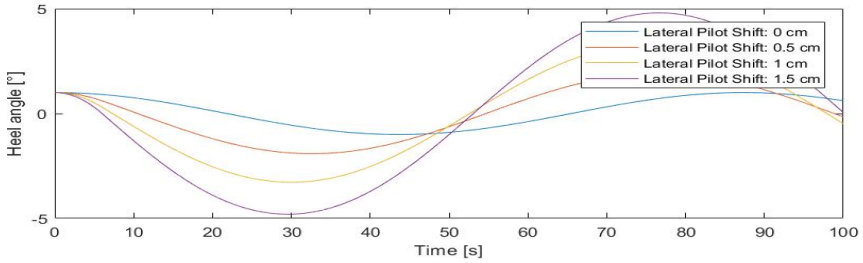

(b) Heeling motion for a hull width of 100 cm, for different pilot positions.

Figure 11.8: Heeling behaviour a different hulls, with a disturbance angle of 1°, at a velocity of 0 m/s.

Figure 11.8b shows that for the involuntary pilot movements discussed earlier, the pontoons will not touch the water if the hull is at least 100 cm wide. This means that even if the pilot is not sitting perfectly upright, he will still be able to perform a straight and safe take-off run.

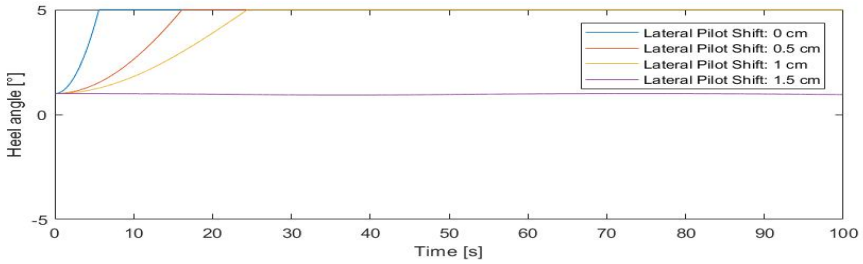

(a) Heeling motion due to sidewind at a aircraft velocity of 0 m/s, for different pilot positions.

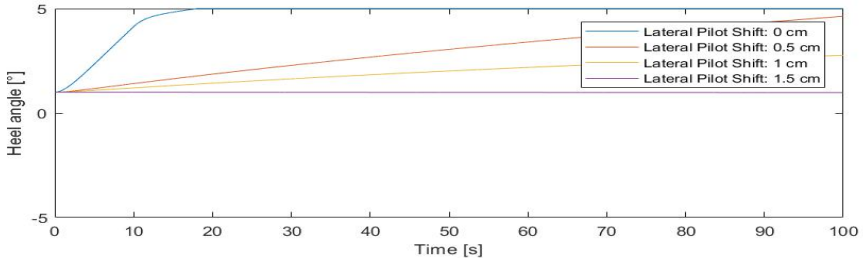

(b) Heeling motion due to sidewind at a aircraft velocity of 5 m/s, for different pilot positions.

Figure 11.9: Heeling behaviour a different hulls, with a disturbance angle of 1°, with a sidewind of 5.14 m/s and a sidegust of 6 m/s for 10 s.

11.5.5 Effect of sidewind

In order to find the effect of sidewind on the heeling behaviour of the aircraft, the heeling moment caused by this sidewinds has to be calculated. In order to do this, several assumptions are made. First of all, the sideforce due to this wind is assumed to act mainly on the sideplates, given that during take-off, the aircraft will not have any roll angle. These plates are modelled as rectangular plates perpendicular to the wind. This results in a drag coefficient of 1.5[10]. With this drag coefficient the sideforce can be calculated as follows:

$$F_{side} = \frac{1}{2}\rho {V_{side}}^2 S_{side} C_d \tag{11.17}$$

Where F_side is the sideforce, V_{side} is the velocity of the sidewind, S_{side} is the area of the sideplates perpendicular to the wind and C_d is the drag coefficient. Secondly, the sideforce is assumed to act in the middle of the sideplates, resulting in the moment arm:

$$Z_{Side} = \frac{Z_{gap}}{2} + b \cdot tan(\Lambda) \tag{11.18}$$

Where Z_{side} is the moment arm of the sideforce, Z_gap is the height of the sideplates, equal to the gap at the tip and Λ is the dihedral angle.

The analysis is done for the worst case scenario, where the aircraft is already heeling over to one side, there is a constant sidewind of 10 kts (WFH-Sys-PP03) and a gust of 6 m/s (WFH-Sys-SC04) takes place for 10 s, resulting in a temporary total windspeed of 11.14 m/s. As can be seen in Figure 11.9a, unless the pilot's CoG shifts 1.5 cm into the wind, the pontoon hits the water fairly fast. However, the pontoons hitting the water is only dangerous when the aircraft is going at speeds of 5 m/s or more. This is because at those speeds, the pontoon hitting the water causes a moment large enough to yaw the aircraft, which can have catastrophic results. For this reason, the analysis is repeated for an aircraft velocity of 5 m/s, shown in Figure 11.9b. Here one can see that unless the pilot does not lean into the wind at all, the pontoon hits the water after more than a minute. Keeping in mind that one automatically leans into the wind (eg. when cycling with crosswind) it can be assumed that for speeds of 5 m/s and more, even the worst possible sidewind does not cause the pontoon to hit the water.

11.6 hydrodynamic control

11.6.1 Steering requirements

Several control possibility's that allow for controllability when the aircraft floats on water are examined. At high speeds the normal control mechanisms will be effective. At lower speeds however, these are less effective and thus a different control mechanism is needed. For this reason it is important to investigate hydrodynamic control. Conventional flying boats use a water rudder to control the aircraft at low speeds. Boats furthermore use inboard jet

engines. This has multiple benefits for the hydrodynamic performance. It reduces noise during take-off, the power required during take-off is reduced because those engines are much more efficient on water and the required skill for docking is less. An extra inboard jet engine will however increase the weight and complexity of the system and will also be more expensive with respect to the rudder alternative. Given the ultra-light design philosophy the idea of adding an additional engine for water control purposes is off the table.

As there are many different choices in order to determine the right control devices it is important to determine how much controllability is needed and when. For the design, there are 3 important mission phases in which hydrodynamic controllability is needed. During taxi, during take-off and when docking. By examining these phases more thorough the required controllability is defined.

At take-off the aircraft will accelerate in a straight line for about 100m. Since the river is only 20m wide and rivers are never completely straight, it should be possible to correct for small deficiencies in direction and the aircraft must be able to maintain the take-off run while following small bends of the river. There is no need for manoeuvring during take-off.

When taxiing, the same controllability requirement holds since it also follows the river. However when boats approach the aircraft is to wide to allow smooth and safe passage. Therefore it should be able to turn 90 degrees and provide sufficient space to allow for the passing of boats. It is not necessary that the aircraft has any forward speed at this point. Furthermore a u-turn must be possible to change the taxi direction.

Docking must be very gentle. The aircraft has a very lightweight structure which will be vulnerable to hard impacts. A very slow approach with much manoeuvrability is needed to achieve this.

Next to these mission situation, the ability to slow the aircraft down is essential to ensure safety. As the engines will not have a reverse gear a solution for this must be found.

Summing up the previous paragraph it is concluded the aircraft needs no additional control options at speed to ensure proper take-off. small corrections in direction at this phase will be done by the regular control devices. High and precise manoeuvrability is required when lying still to allow for proper operations as well as braking opportunity. In the following sections a few common control options for boats are evaluated and the most optimal is selected.

11.6.2 Water Rudder

Rudders are a very effective and common used control mechanism for floatplanes and boats. An example of a rudder attached to a float is shown in Figure 11.10. The water rudder can be linked to the control system of the air rudders so they deflect simultaneously. This is making it easy for the pilot since he has the same control stick for manoeuvring the aircraft on water and in the air. A disadvantage is though that a rudder is a control surface and for control surfaces to be effective the particular vehicle must have a speed. Given that a high manoeuvrability is required at low speeds there is a risk the rudder will not be effective enough.

Figure 11.10: Water rudder of a float to provide control when floating on the water

The rudder will be attached at the rear of the hull. When the aircraft starts plaining the rudder will still be in the water and create a lot of hydrodynamic drag. The rudder must be retracted to solve this which ads complexity to the design.

Not to forget docking of boats with a rudder requires extensive training and yet for experienced sailors can still be very hard. Given the circumstances a control rudder will not be optimal for the *AerGo*.

11.6.3 Paddle

Another common steering method for boats are paddles. Paddles are lightweight and easy to use. They have been used ever since the first boats have been build and are proven to be very effective. An advantages of the paddle is

they can control the aircraft even when lying still and prevent the aircraft from drifting off. This is exactly what is desired when boats are passing or when docking. Another advantage of the paddle is that it can be used to slow the aircraft down as well. By just holding the paddle in the water the aircraft slows and sharp 90 degree turns can be made.

The aircraft is very wide and has a large moment of inertia that may require a lot of paddling strength for the pilot to steer. When docking the steering can go very slow as long as it is precise, so here it will not form a problem. When moving forward during taxi the paddle can be hold still in the water at one side causing drag to break as well a turning moment to manoeuvre. Just holding the paddle still instead of paddle costs significantly less force. To overcome the required force at low speeds the engines can be used to create a similar situation. It is expected that the pilot will have sufficient manoeuvrability with the combination of the regular control forces and a paddle for safe operations on water.

Using a paddle introduces the risk of damaging the aircraft when paddling. The skin and rips are very fragile so hitting them will damage the structure. This risk will be further examined in Chapter 16.

Keeping in mind design complexity the very simple solution of hand paddles and water gloves is considered as well. They are used a lot by long distance swimmers and beginner surfers to add a little extra efficiency to their strokes. However they do not provide sufficient area to create a large turning moment and it is expected that with only hand paddles control will be lost.

As the water engine was already discarded the best option left is using an ultralight paddle to control on the water and making use of the regular control mechanisms as soon as they are effective.

While thinking of what paddle to be used, operations should be taken into account. A paddle of 2m will be inconvenient to switch steering direction and to store the paddle on board. Considering all impact on the aircraft will be a risk as well it is desired that the paddle will be as small as possible, while the pilot will still be able to use it without problems. To be sure the paddle will fit the operations department a 1 m paddle is considered.

As it has been during the entire design of the *AerGo*, weight plays a huge role in the choice the paddle. This makes it easier for the pilot to control the paddle and has less effect on the performance of the aircraft. A 90 cm wooden paddle will cost less than €20 and weighs about 700 g [(4)]. Obviously, the lighter the paddle the more expensive. With the use of carbon fibre the weight can be reduced, but prices go up very rapidly. For €200 the 1.15 m paddle shown in Figure 11.11 is one of the lightest available and weighs only 350g[(5)]. The assumption has been made that designing a custom made paddle of 90 cm can therefore reduce the mass with about 400g. However this will probably still be more expensive than just buying a wooden one for €20. If the weight reduction is worth the custom design should be investigated during a future design phase and is highly dependant on the amount of aircraft that is expected to be produced.

Figure 11.11: Paddle to support manoeuvring on water at low speeds

11.7 Spray

Spray can cause a lot of hazards for the aircraft and influences its performance. The large rotating propellers can be damaged when hit by water spray. Pilot vision and comfort should also be considered. Due to the low pilot position in the hull excessive spray can decrease the vision and be very cold causing discomfort and maybe affecting his flight capability. Furthermore, more spray implies more hydrodynamic drag and thus affects the hydrodynamic performance. Considering this all, minimum spray is desired and spray characteristics must be investigated when designing a flying boat.

An initial spray estimation is performed to asses the significance of spray on the *AerGo* to see if correcting measures have to be taken. Based on the aircrafts water displacement, the forebody length, beam and the water density a initial estimation of the spray characteristic is found. The book design for flying by Thurston [31] states :

$$K = \frac{\Delta_0}{\rho B L_f^2} \tag{11.19}$$

(4) urlhttp://www.cavinesspaddles.net/ProductDetails.asp?ProductCode=BP, Retrieved: 22-01-2018

(5) `https://sanborncanoe.com/products/nessmuk`, Retrieved: 18-01-2017

Where a K value of 0.0525 indicates light spray, 0.0675 indicates satisfactory spray and 0.0825 is acceptable for overload as defined by Gudmundsson[14]. A K value of 0.052 was found for the *AerGo*. Given this the aircraft will have light spray and it is assumed that spray will not cause any problems for the propellers due to its high position at the top wing as for the pilot.

Since this estimation method is very preliminary it is advised that during the tow tank test, which will be explained in more detail in Section 18.1.2 an investigation of the spray characteristics is performed.

If after testing the spray level appears to be to high spray can be reduced by using spray strips. Spraystrips redirect the water away from the aircraft, just like the chine. Figure 11.12 shows the effect of a spraystrip on the water flow. For now the spray is assumed to be satisfactory and no spray strips are used.

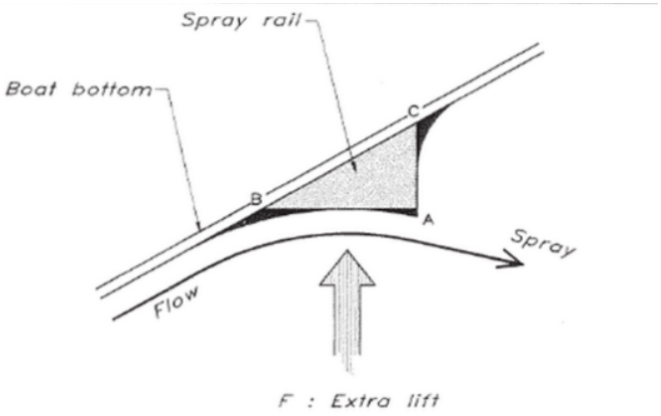

Figure 11.12: Water flow redirected by a spray strip

11.8 Verification and Validation

11.8.1 Hull drag model

In order to check if the chosen method is correctly implemented in the script, its results are compared to hand calculated values forfivesample points. Each of the samples consists of a different hull geometry and Froude number. These results show errors well below 0.01 %, from which can be concluded that no implementation errors have been made (the small differences are likely to be caused by rounding errors).

In order to check whether the chosen method accurately represents the physical system, the results of the script are compared to experimental data. This data comes from the DSDS database, where 6 random samples are taken. The results of this comparison can be found Appendix C, where the Hull ID corresponds to the model number of the hull in the DSDS database. Please note that in these experimental results, the displacement is constant, therefore the code corresponding to Equation (11.5) is removed for this comparison. As this is a very simple formula that has been validated time and time again, this will not significantly influence the validity of the script.

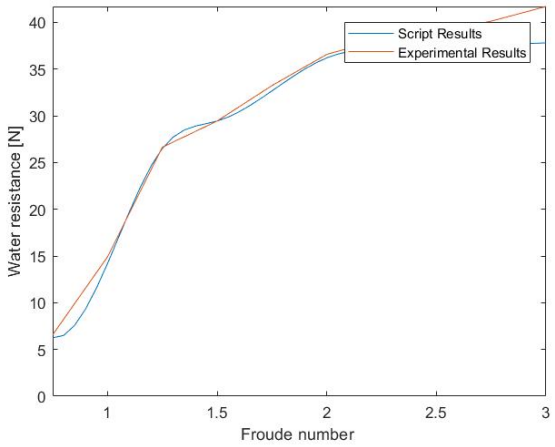

Figure 11.13: Example of comparison between script and experimental results for Model 251 from the DSDS.

From these results it can be seen that the model fairly accurately represents the actual physics of the system. As this is a method based on statistical data and several interpolations and fitted polynomials are used and several assumptions are made, this is not an extremely accurate method, however it provides a reliable rough estimation.

11.8.2 Lateral stability model

The stability model is verified by comparing the calculations to hand calculated values. For this purpose, the model is split up into three units. The first unit consists of the code that calculates the draft by iteration. This unit is checked by inputting simple prismatic shapes and letting the model calculate the draft. This draft is then used to calculate the volume of the underwater part by hand. This verification showed that the draft calculations had errors of less than 0.01% on the volume, which is the accuracy at which the model stops iterating. Therefore it is safe to assume that no errors are made in this unit. This unit is then validated using the hull shapes, volumes and draft values available in the DSDS database. Here the differences are larger, up to 5%. This is however not likely to be caused by calculation mistakes in the model. As only the major parameters of the hulls are imported, the shape of the hull in the model is not exactly the same as the actual shape. This is however not the case for the hull of the *AerGo*, as the script is written to exactly represent its shape.

The second unit encompasses the code calculating the righting and heeling moments. Once again, simple prismatic shapes are inputted to the program and the result are checked against hand calculated values. Please not that the draft is kept constant in these calculations, in order to verify this unit independently from the first. This check also gave results with an error percentage of less than 0.01 %, meaning that this unit can safely be assumed to be error-free.

The last unit calculates the actual heeling behaviour of the hull. In order to calculate this unit independently, simple linear R_m vs θ relations are used. The angular acceleration is then compared for several random heeling angles, which once again only gave minimal errors. It is however more difficult to calculate the heeling angle and angular velocity by hand. The formulae relating these to the acceleration are however fairly simple and can therefore be visually inspected. As there are no typing errors or differences between the formulae and their MATLAB equivalent, it is assumed that if the angular acceleration is modelled correctly, the angle and angular velocity is also modelled correctly.

11.9 Conclusion and Recommendations

In this chapter, the design choices and sizing of the hull, pontoons and hydrodynamic control systems are explained. Since the length and width of the hull are limited due to operational, mass and stability concerns, only limited improvements in hydrodynamic resistance can be made. However, a reduction of 20 % was still achieved, which results in lower take-off power required and a better take-off performance. Due to relatively high aerodynamical drag at take-off, further reductions in the resistance would not affect the size of the engines, nor will it lower the battery mass, meaning that further optimisation in hydrodynamic resistance is not required. However the hull shape might still be optimised to reduce aerodynamic drag and structural weight.

The final hydrodynamic configuration consists of a simple hull with a pontoon on each tip of the lower wing.

As can be seen in section 11.8, the model for the resistance estimations does not take into account the effects of the step. For this reason, it is proposed do to several towtank tests (explained further in section 18.1.2) with scale models of this hull and varying step locations and heights. This will help to optimise the hydrodynamic resistance even further, and determine how far the pilot will have to shift in order to reach α_{TO}.

Further recommendations include the construction of a detailed dynamical stability model, according to the methods taught in MT3408 Scheepsbewegingen at TU Delft. As this model will have more accurate, and less conservative, estimations of the heeling motion, it is expected that this will lead to a lower limit for the hull width, which would reduce drag (both aero- and hydrodynamic) and structural weight of the hull. Next to that, the model will help determine the size of the steering mechanisms.

12 Operations

The *AerGo* needs to be an easy operated aircraft to fulfil the customer requirements and lower the threshold of recreational flying. To do this not only the flight phase has to be tailored for this, but all operating aspects. This chapter discusses what design choices are made with this in mind. First all ground operations will be assessed before moving on to flight operations. Finally other operational aspects are discussed in the 'Reliability, Availability, Maintenance and Safety' section.

12.1 Ground Operations

Ground operations are definitely important, even more because the *AerGo* is a water aircraft so an additional transition phase between ground and water exists which will also be discussed in this section.

12.1.1 Storage

Requirements state that it should be possible to store the the *AerGo* in a garage. The mayor difficulty is that the wing span is far exceeding the required dimensions. For this reason the wings should be sectioned and stored parallel to each other. The wings are segmented at the side of the hull and at 2 meters from the wing tip for structural reasons. This will give 4 wing sections of 2.2 meter and 4 of 4 meter due to the sweep angle. The parts have to be positioned carefully since the structure is quite fragile and therefore a special support frame that holds all *AerGo* parts is used. This frame is made from aluminium to give enough rigidity and because it is lightweight as well as cheap. The frame visualised in Figure 12.1 consists of three supports, front, rear and middle. The longer wing sections are stored in between the struts of the centre hull section and supported on the front and rear by hanging the spars in the jig. The shorter wing sections will be placed on a slight angle outside the struts between the rear and middle support. Additionally the support frame consists of some members and wheels that will allow assembly, transport and docking operations as explained in the next section.

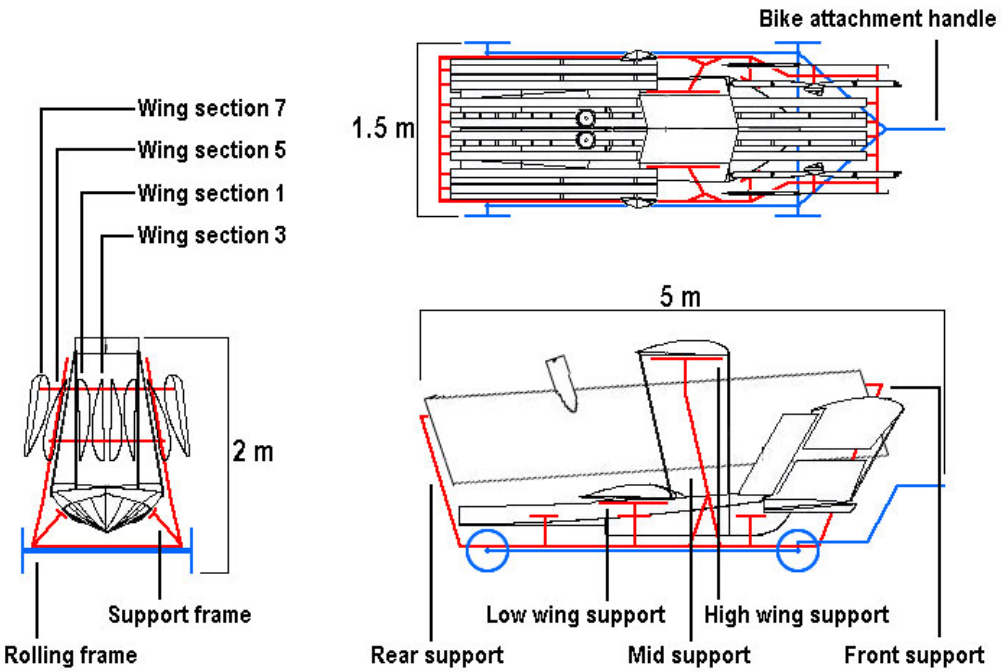

Figure 12.1: Three view bike trailer

12.1.2 Transport

To transport the *AerGo* by bike, a special bike trailer is designed that consist of 2 frames. The first is the support frame as explain in the previous subsection. To make this part move, a rolling frame is added. The supporting frame is placed on the axles of the rolling frame so it can still slide. For transport however this sliding can be blocked. The rolling frame has to carry the OEW of 44.6 kg so 2 axles are chosen to distribute the load. The wheelbase is set to three meter, where the front axle can rotate about z axis to make manoeuvring easier.

12.1.3 Assembly

Assembly of the *AerGo* is designed so that a single person can get it done in as little time as possible. The bike trailer helps the customer by giving a stable platform from which assembly is done. The main section with the hull is already in its correct position and the assembly is done by attaching all parts to this centre part. The frame also helps attaching the wings because it provides a surface to support the long wing sections on before sliding them into position. The assembly plan consists of the following 21 steps. Figure 12.2 is used as a reference for the parts referred to.

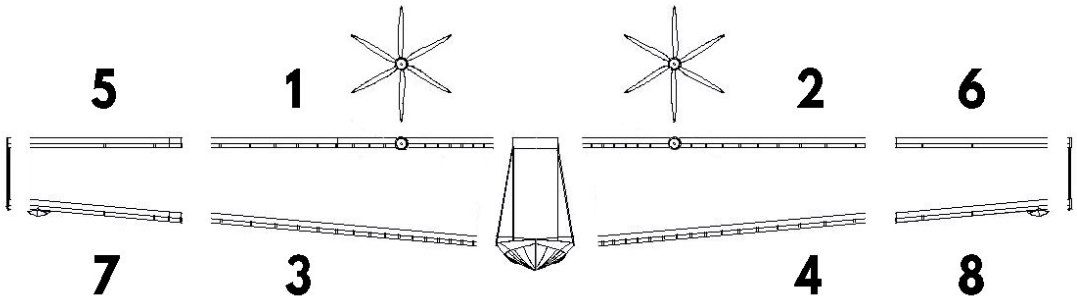

Figure 12.2: Wing section numbering

Step 1 Disconnect wing section 1 from the frame.
Step 2 Place it on the top support and slide into position.
Step 3 Connect the spars to the centre section.
Step 4 Connect the electrical cable to the engine.
Step 5 Connect the top roll wire.
Step 6 Repeat steps 1 to 5 for wing section 2.
Step 7 Disconnect wing sections 3 from the frame.
Step 8 Place it on the lower support and slide into position.
Step 9 Connect the spars to the centre section.
Step 10 Connect the roll control wire and yaw wire.
Step 11 Repeat steps 7 to 10 for wing section 4.
Step 12 Disconnect wing sections 5 from the frame.
Step 13 Slide section 5 into wing section 1.
Step 14 Connect the spars.
Step 15 Connect roll wire.
Step 16 Attach the skin over the connection.
Step 17 Repeat steps 12 to 16 for wing section 6 7 and 8. While also connecting the yaw wire for the later two.
Step 18 Attach the side plates and connect all control wires taking out any slack.
Step 19 Attach the propellers.
Step 20 Check if roll and yaw controls work by moving the control sticks.
Step 21 Remove rear support from frame assembly.

12.1.4 Water deployment

The *AerGo* trailer can deploy the aircraft from a ramp or stepped water bank. If there is a boat ramp available, the trailer can be backed up till the hull starts to float and the aircraft can then be released by lengthening the holding line. The hull will then travel backward over the rollers, similar to any conventional boat trailer. For a stepped water edge the frame can be slid along its wheels and then tilted to also reach the water as shown in Figure 12.3. This will

be especially useful for both deploying and retrieving the aircraft from canals. Retrieving of the aircraft is done with exactly the same steps, but reversing the order.

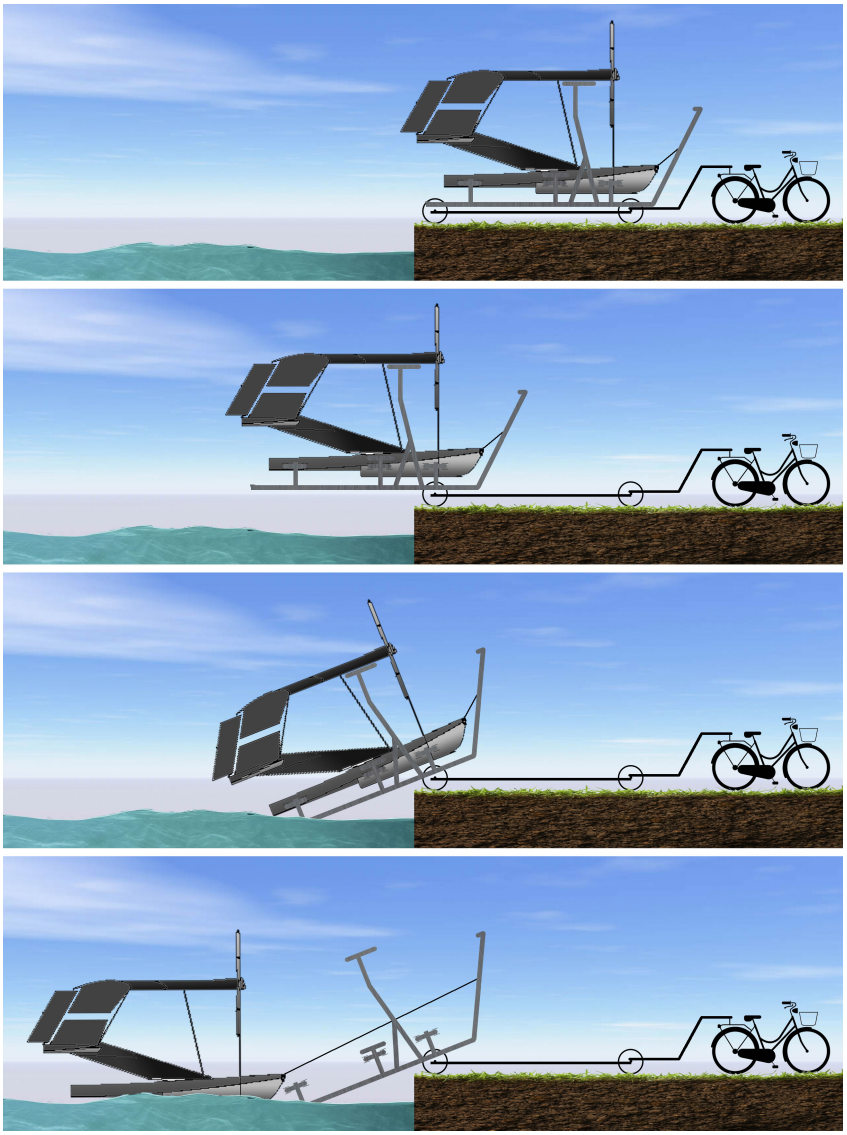

Figure 12.3: Stepped water deployment

12.1.5 Boarding

When the aircraft is facing the shore after deployment it will be very hard to change this orientation because of the large wingspan. Therefore the hull is designed to take the loads of the pilot boarding the *AerGo* from the nose. The front section of the hull is closed and the pilot can hold on at the struts connecting the upper wing. Then he or she steps over the lower wing to lower into the seat. After this taxiing can commence as explained in Section 11.6.1.

12.2 Flight Operations

Since the *AerGo* is a recreational aircraft very little operations apply to the flying phase. The pilot will be free to do whatever he or she wants while keeping the aircraft in its designed flight envelope. To assist the pilot to do so, information about its current flight parameters would be preferred. Therefore the instrumentation will be discussed in the next section.

12.2.1 Instrumentation

In order to fly the *AerGo* safe and efficiently some flight parameters would be very useful to know. First of all, a battery charge indicator which gives a readout of how long power can be provided makes deciding when to land very clear. This indicator will be implemented in the power system. Secondly to be able to achieve steady flight, the rate of climb would be very useful. If the pilot wants to fly as efficiently as possible, he or she can find this corresponding attitude by setting cruise power and than shifting weight so that the rate of climb is zero. This is, assuming there are no thermals. A rate of climb indicator is called a variometer and very often comes in combination with an altitude meter, because it uses change in pressure to give rate of climb and this can also be used to calculate the height relative to mean sea level or any other relative pressure. In para- and normal gliding devices like this are very common and therefore it is simple to just purchase this instrument. There various options, but very basic alt-variometers cost around 140€ [(1)]. There are also models which include GPS to make navigating easier starting at 350€. This instrument can be attached to the low wing spar section where it would be right in front of the pilot but still providing overview for flight.

12.3 RAMS

Reliability, Availability, Maintenance and Safety are important aspects that will influence the operating effectiveness and ease of use of any product. Since the *AerGo* is trying to set a new standard especially in ease of use, some design choices have been made to facilitate this to the highest level possible.

12.3.1 Reliability

The reliability is measured in the period of time a product operates in a satisfactory manner. Any malfunctions that would compromise this would therefore obviously be avoided. The system that is identified to be the most sensitive to malfunction is the structure and more accurately the skin and connection points. While assembling the *AerGo*, parts of the wing can be damaged which would need to be mended, creating downtime. This is however minimalised by having an short and easy repair procedure as explained in Section 12.3.3. Also the probability of such a malfunction is lowered by the having specialised assembly jig with clear instructions. Besides the fragile structure the power system is usually most susceptible to failure. However because the *AerGo* has a fairly simple power architecture any malfunctions can quickly be addressed. The access to all subsystems is easy so any downtime will be as short as possible.

12.3.2 Availability

The customer wants to be able to fly the *AerGo* as often as possible. The main limiting factor will be the weather. The requirements state that the aircraft needs to be designed for operation between March and October. To find the exact meaning of this requirement, Dutch weather data from the KNMI is analysed [(2)]. Hourly measurements of 46 weather stations is statistically plotted in Figure 12.4 to find the percentage of time with average winds of under certain speed. For 8 m/s this is 80.81 % of the time.

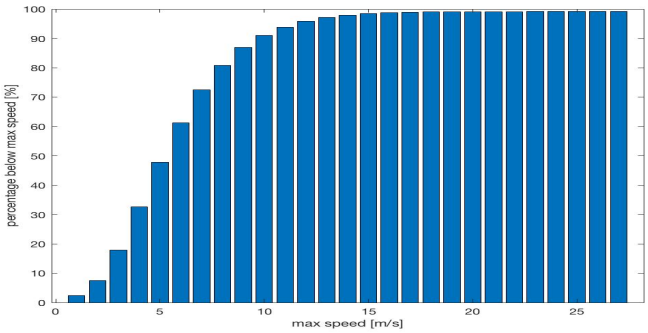

Figure 12.4: Percentage of hourly average wind speeds in the Netherlands below the indicated maximum

To accurately give the availability the gust speeds have to be taken into account. This is already evaluated in Section 5.2 and when multiplying the gust availability with the average wind speed this gives a value of 76.9%.

[(1)] `https://flybubble.com/shop/flight-instruments/alti-varios`, Retrieved: 22-01-2018
[(2)] `https://projects.knmi.nl/klimatologie/uurgegevens/selectie.cgi`, Retrieved: 07-12-2017

12.3.3 Maintenance

The subsystems of the *AerGo* are chosen such that customers can service its aircraft themselves. The wing skin is made from rip stop nylon and if punctured can be patched easily. The spars and ribs will be less likely to damage but would also require more material knowledge to repair. Electrical engines and gearboxes are normally not considered to be self serviced. However the *AerGo* is made with store bought engines which means replacements can be sourced easily. The replacing itself requires some more work, since the engines are located inside the wing, but they are made to be removed. The customer will need to open the skin before reaching the motor assembly, however with adequate information this is assumed to be possible for everyone.

12.3.4 Safety

The safety is defined to be the protection to danger, risk and injury. Risk is evaluated in Chapter 16, all mitigation that is done also helps with the safety of the aircraft. Protection to danger is harder since the intended customers are sporty thrill seekers and selling the product will not benefit when lots of warnings and limitations are set. The strategy here is to provide adequate training to future customers to teach them the constraints of the *AerGo*, like for instance, when not to fly. Pilots should have a basic understanding in aircraft physics so they do not put themselves in dangerous situations.

Redundancy is usually used in the aerospace industry to increase safety. In the *AerGo* design few systems are redundant because the extreme weight requirements do not allow for this. The malfunction that is considered though is an engine failure. When the *AerGo* is in a one engine out situation the control surfaces can still keep the aircraft in level flight as explained in Section 8.5.3

The pilot is located behind the spars of the lower wing. This causes a severe hazard, would the aircraft ever crash. Most crashes will occur with some forward speed so the deceleration would cause the pilot to be thrown forward. Unfortunately this hazard can not be mitigated with acceptable changes to the design. The low stall speed however will minimise the impact energy, as well as damage. Also because the *AerGo* lands on water, lots of possible landing sites exist. The footboard will be designed so that in the event of a crash, the feet of the pilot can be easely released. Also pilot will be required to wear a crash helmet, this will help for the survivebility of a crash.

12.4 Conclusion and Recommendations

In order to fulfil the operational requirements, the *AerGo* has a specialised bike trailer. This is a multipurpose system which will make storage, transportation and deploying the aircraft as easy as possible. The leading design factor is that it allows the *AerGo* to be operated by a single person. Simple flight instrumentation provides the battery charge indicator and a store bought vario-altimeter the pitch rates. The easy structural layout provides excellent maintenance possibilities which will also increase the availability. Safety measures will mostly entail proper training and a crash helmet will also be required.

For future more detailed design, the loads on the supporting and rolling frame have to be calculated so an accurate estimation can be made of the material thickness and therefore also for weight and cost. Also it is recommended that the following areas are reevaluated. First of all, to increase the reliability of the *AerGo*, actual values of the reliability of subsystems have to be found. Also the availability can be more elaborated, considering more weather aspects like rain, hail and extreme temperatures. Finally it is recommended to do a more extensive evaluation of the crash worthiness of the *AerGo*. The nose of the aircraft could be designed to be a crumple zone to better protect the pilot in a crash by absorbing more impact energy.

13 Mass Budget

The final mass budgets of all subdivisions are compiled in table 13.1 together with the initial estimates derived in the midterm report.

13.1 Changes in mass budgets

Overall, there was a significant drop in weight, going from an initial 57.8 kg to a final operational empty weight of 44.66 kg. The biggest reduction in mass occurred in the structures and hydrodynamics department, which is likely due to the use of carbon fibre as well as relatively conservative initial estimates. The structures department really tried to save as much weight as possible, even using a soft skin for the hull. Because of the radical approach it is likely that the structure will become heavier after more detailed design. Stability and control is the only department that experienced a small gain of 170 g.

Table 13.1: Initial and final mass budget of each subdivision[5]

Department	Initial budget [kg]	Final budget [kg]
Propulsion & power	26.9	26.2
Structures & materials	19.9	11.3
Stability & control	3.0	3.2
Hydrodynamics	8.0	4.0
Total	57.8	44.7

13.2 Mass budget breakdown

Figure 13.1 shows the percentage of mass for each technical discipline. Power and propulsion now make up the biggest fraction of the weight by far, suggesting it is the area with most room for optimisation. Replacing the heavy batteries with a combustion engine for example might reduce the total mass by up to 10 kg. Also, improvements in battery technology, as are to be expected in the next few years, will allow for lighter batteries to be used.

Overall, it shows that the initial estimates of the midterm report were quite accurate, apart from the very conservative budget of the structures department.

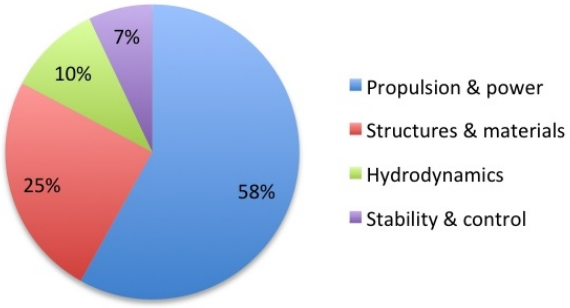

Figure 13.1: Mass percentages of each technical discipline

14 Cost Breakdown

Estimating the cost of producing one aircraft is essential in determining whether designing will be worth it from a business point of view. There is no correct way to give an exact prediction of the aircraft costs, but there are several prediction methods based on empirical data to estimate the development and production costs of an aircraft. Most methods focus on large and heavy air- and spacecraft. In general, the bigger the aircraft the higher the costs and thus the more important an accurate cost estimation is. However since the *AerGo* has such an extremely low structural weight it does not fall into the parameter range of any of these existing models.

The DAPCA cost estimation method as stated in the book *General aviation aircraft design* written by Snorri Gudmundsson [14]. The DAPCA cost estimation method was originally developed by the company RAND in order to estimate the cost of development of military aircraft. It has been optimised for general aviation aircraft on the basis of the *Cessna 172*. This method is found to have the most resemblance with the *AerGo* and is therefore used to make a cost estimation.

14.1 Assumptions

Since the DAPCA model is still based on aircraft in another parameter range than the *AerGo*, a number of assumptions are made in order to produce a better fit of the cost budget. These assumptions are listed below including those needed for the model.

- As found feasible in Chapter 3, 100 aircraft will be produced every 5 years.
- Each produced aircraft will be sold instantly.
- Research costs are made in the development phase only and will not be made after.
- The design phase take up to 2 years as defined in Chapter 18.
- The following aspects are considered for research costs: Engineering Hours, Tooling hours, Flight testing and development support[14].
- Costs of labour for manufacturing, tooling and engineering are assumed to be €53, €61 and €91 per hour respectively [14].
- An inflation rate of 3% has been implemented in the model for correction to produce accurate numbers for the year 2018.
- Material is bought at the beginning of each 5 year production cycle.

14.2 Labour Hours

Determining the labour hours spend on designing, tooling and manufacturing is essential in determining the cost of labour for a design. In industries in general, this cost estimation is based on statistical data and will be determined based on old designs. However there is little information available on the ultralight aircraft industry. With the DAPCA method, an estimate of the labour hours is made. The statistical relation for engineering hours is:

$$H_{eng} = 0.0396 \cdot W_{airframe} \cdot V \cdot F_{cert} \cdot F_{comp} \tag{14.1}$$

Where $W_{airframe}$ is the weight of the aircraft structural components, V the cruise speed, F_{cert} is the certification factor and F_{comp} the complexity factor based on airframe materials. Equations for manufacturing and tooling are similar but have different constants.

Figure 14.1a shows the relative increase in manufacturing hours compared to tooling and engineering hours. As production increases, the manufacturing cost increase the fastest and easily become the largest expense in the production process.

14.3 Unit Cost

The total cost is based on the costs of engineering, tooling, manufacturing, testing, development support, material and quality control. The full unit cost breakdown can be referred to Appendix D. The DAPCA model estimates all these values based on the aircraft frame weight, airspeed and aircraft complexity. In order to increase model accuracy, the material costs are computed by adding all component costs together. These cost were derived from the previous subgroups. The material cost breakdown is shown in Table 14.1. The cost of the wing and hull section are based on raw material cost of the frames[34].

Table 14.1: Distribution of the material cost for one aircraft

Component	**Costs** [€]
Wing	1,000
Hull	200
Populsion system	1,200
Battery	1,040
Paddle	20
Flight instruments	350
Control mechanisms	200
Total	4,010

If materials are bought in large quantities a discount on the material cost can be expected. This discount rate is determined through

$$F_{dis}^{1,4427\ln(N)} \tag{14.2}$$

Where N is the number of units produced and F_{dis} is the discount factor and assumed to be 0.95 which is considered to be common in the aerospace industry [14]. The final cost per unit as a function of the production rate per 5 years can be found in figure Figure 14.1b.

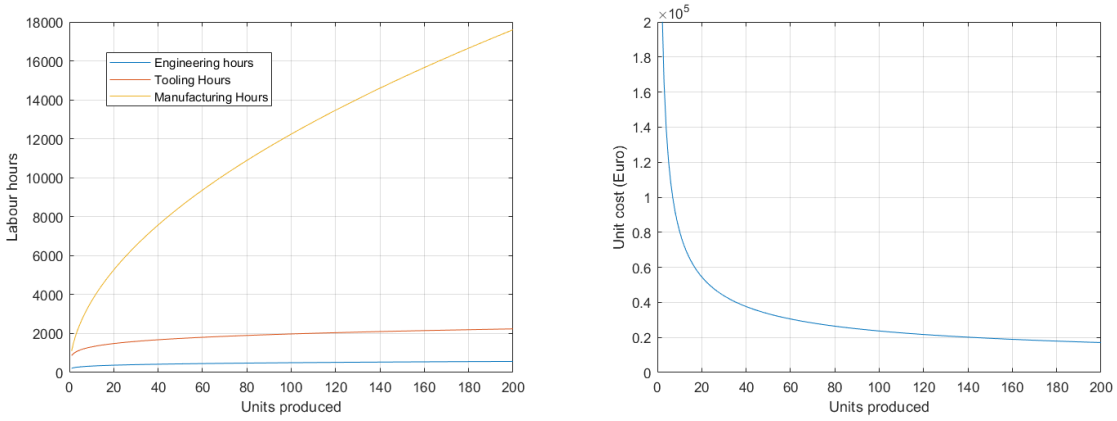

(a) Engineering, Tooling and Manufactoring hours dependant on the production.

(b) Cost per unit as a function of the units produced per 5 years.

Figure 14.1: Graphs displaying the relationship between labour hour, units produced and and unit cost.

It can be noted that trailer costs are not included in this cost estimation. Little research has been done on prices of these trailers and a rough estimation of this price is that it will be, because of the complexity of this trailer, between 2,000 and €3,000 [(1)]. It is chosen to add the trailer to an additional package. In this way someone who would not need the trailer is not forced into unnecessary costs. This is a business model that is very common (eg. boats).

[(1)] `https://maloneautoracks.com`, Retrieved: 22-01-2017

14.4 Return on Investment

This section gives insight on the methods of determining the return on interest. Figure 14.2a and Figure 14.2b show the cash flow as a function of the units sold and throughout the years respectively assuming a sale of 100 units per 5 years and a start of production after 2 years of development. The position where the lines cross the x axis represent the break-even point. It is found that with a sales price of €20,000, at least 148 units must be sold to break even. This will be 7.5 years after first production which is 9.5 years after start of the design phase. If the price is increased to €30,000, a profit will be made after the sale of 67 units and after 5.5 years the break even point is reached.

The kink in these figures at 5 years is due to the new material batch that is bought. The increasing incline of the graph is due to the fact that manufacturing and quality control processes have a learning curve based on the number produced. Note that this curve is not considering change in personnel, which will temporarily decrease the efficiency of these processes.

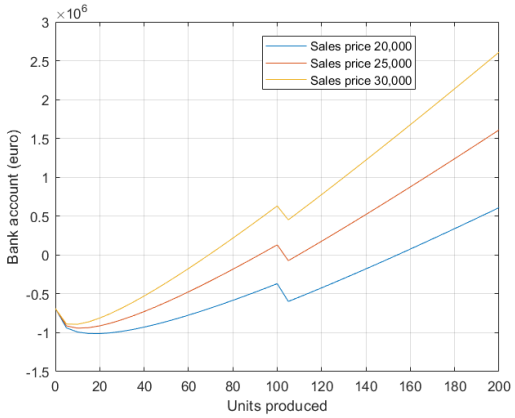

(a) The Cashflow of the *AerGo* company limited expressed in number of units sold. With the production rate of 100 units per 5 years

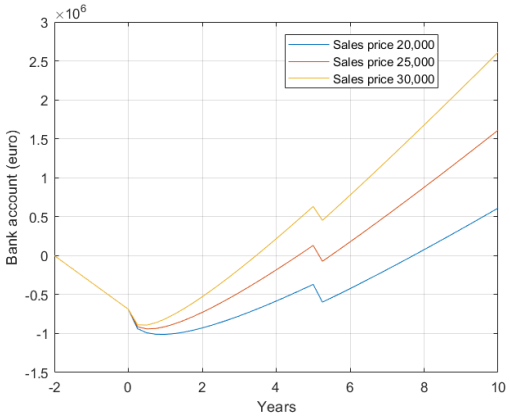

(b) The Cashflow of the *AerGo* company limited expressed in years. With the production rate of 100 units per 5 years

Figure 14.2: Graphs displaying the relationship between the bank account, units produced and the years needed to break even

Another note to make with this estimation is that no promotional costs are taken into account. The product will not sell without the world knowing about it therefore if it is decided to continue with the design, marketing costs will reduce the total profit and delay the break-even time. At this point it is decided that marketing will only be done by building and promoting a website. The average cost of building this is estimated to be around 5,000 [(2)].

Furthermore an investment or a loan of at least €1 million is needed to cover for the start-up costs. An investor giving a loan they would expect to get an interest over his dept or receive part of the profit, delaying the break-even time even further. Table 14.2 shows the estimated return on investment after 12 years in this project assuming exactly 200 units will be sold over time.

Table 14.2: Return on investment after 15 years with a sales price of €20,000

Revenue	€4,000,000
Development	€400,000
Material	€495,000
Manufactoring & Quality Control	€2,400,000
Marketing	€5,000
Return on investment	**€700,000**

[(2)] `https://www.webton.nl/webdiensten/website-bouwen-kosten/`, Retrieved: 22-01-2018

14.5 Operational Cost

Operational cost of the AerGo are very low. These cost are determined only by the energy consumption and the maintenance of the aircraft. If the maintenance is done by the owners themselves, which is falls in line with the philosophy of the product, the maintenance costs will be determined by the frequency in which all sub components must be replaced. To have an estimation of the costs at this stage of the design the maintenance cost estimation of the DAPCA method is used. The maintenance costs are computed by:

$$C_M = R_{mech} * F_{MF} \tag{14.3}$$

Where R_{mech} is the hourly cost of a mechanic which is estimated to be the same as that of the tooling engineer.F_{MF} is the maintenance to flight ratio which is determined to be 0.05 based on the complexity of the aircraft and mechanic type (hired engineer or self service) according to Gudmundsson [14].

Given that the maximum energy consumed during 1 hour flight is 3.55 kWh and the cost of 1 kWh is only 20 cents[(3)], the cost of energy consumption will not be of any significance. The operational cost per flight hour is at this stage estimated by adding the maintenance and energy cost and is assumed to be €3.75 per flight.

14.6 Conclusion

A sanity check of the labour hours of engineering says that one engineer should be able to design this aircraft within 10 weeks. Given the fact that this project is already running for 10 weeks and 10 engineering students have been working on it full-time, this is not a reasonable estimation. Having a closer look at the total hours does give better results. The total hours spent to produce one single aircraft is 2,184 hours. This corresponds to around 1 year of work by a dedicated hobby engineer, designing and building the entire aircraft on their own. Given the *Aeriane Swift* design situation was similar to this project and this was after collegiate phase build in 4 months time by 5 engineers [(4)] the estimated time seems to be on the low end.

Furthermore, at a production rate of 100 units per 5 years the average manufacturing time is 125 hours per aircraft. Even though the *AerGo* structure will be very simple and will be much lower than general aviation aircraft this estimation is very likely to be overshot. A sensitivity analysis has been done on the cost budget. The results of a change in parameter of 10% is shown in Table 14.3

Table 14.3: Percentage changes in the break-even point for a 10% parameter increase

Changed parameter	Break-even point units	Break-even point years
$\mathbf{W_{airframe}}$	10 %	14 %
$\mathbf{V_{cruise}}$	9.0 %	14%
Units produced	3.1%	9.2%
Material costs	2.9%	6.8 %

Given the sensitivity analysis it can be concluded that fairly small changes to the aircraft, like the cruise speed have a large impact on the cost model. This means the business model is very susceptive to change in the design. It is highly recommended that in future design phases an attempt will be made at creating a more accurate cost model. At this point of the design this rough estimation is deemed sufficient to estimate the order of costs, but it is adviced to increase the sale price from 20,000 to €25,000 in order to make sure chances in budget which are doomed to happen are accounted for. At this sales price the break-even point for this model will be at 9.75 years after the start of the design and after the sale of 93 units, which is a more safe investment. The reason all numbers in this chapter are rounded of is due to this sensitivity analysis. If small chances cause such a large chance in the outcome, having precise number does not make sense.

[(3)] `https://www.pricewise.nl/energieprijzen/kwh-prijs/`, Retrieved: 22-01-2017

[(4)] urlhttp://aero.stanford.edu/Reports/SWIFTArticle1991.html, Retrieved: 22-01-2018

15 Sustainability

This chapter merges the considerations and results for the purpose of sustainability that have played a role in the design of this aircraft. At the beginning of this project a strategy was devised to ensure the application of sustainable engineering in the design of the AerGo. The approach and execution of this strategy will be discussed in Section 15.1. Sections 15.2, 15.3 and 15.4 will cover the grading of the design with respect to noise, carbon footprint and recyclability of the aircraft. Finally, Section 15.5 will elaborate on the conclusions and will provide recommendations for the future.

15.1 Approach

Previous reports on this project have already elaborated on the approach with respect to Sustainable Development [6] and the setup of a Sustainable Design Strategy [4]. A brief summary of the strategy was that for each sustainability requirement, an appropriate reference frame should be setup to be able to put the sustainability characteristics of the aircraft in a reliable perspective.

WFH-Sys-SU01 The aircraft shall be recyclable up to 90% of its weight

WFH-Sys-SU02 End-of-Life Plans shall be specified for the aircraft

WFH-Sys-SU03 The noise of the aircraft shall not exceed 40 dB at 100m distance (=80dB @ 1m)

WFH-Sys-SU04 The aircraft shall be designed in such a way that the CO_2 footprint is maximum 100 g/km per passenger

The Midterm Report [5] elaborates on the influence of sustainability considerations in the trade-off process. During the concept generation and the trade-off process, sustainability has played a significant role. The initial concepts contained a lot of innovative aspects such as solar panels, electric propulsion and human powered propulsion. Sustainability has also been represented as a trade-off criterion in both of the trade-offs conducted in the converging phase during this project.
Since the final design was chosen, the focus has deviated from the initially stated strategy. It was concluded that the most effective way to make the aircraft sustainable in any way was to reduce the mass as much as possible. Lower mass generally means lower power, lower energy and lower carbon footprint. Lower power eventually also leads to lower noise. This mindset has had a major influence on the resulting final design. The grading of the design with respect to the requirements will be discussed in the next sections.

15.2 Noise

The aircraft produces several sources of noise. Most noise is expected to be produced by the propulsion system. As mentioned in Chapter 10, the propeller noise has been taken into account in the propulsion system trade-off. Other noise sources are for example aerodynamic noise, hydrodynamic noise, gear noise and engine noise. These other noise sources have been harder to properly estimate. Aerodynamic and hydrodynamic noise have been neglected in this analysis. Based on common sense, these sources are expected to be negligibly small compared to the noise from the propulsion system. Also, lack of resources has been standing in the way of a proper analysis. Lack of resources was also a major threshold to analyse the engine noise and the gear noise. Therefore the engine noise and the gear noise are assumed. The engine noise is expected to be less than the propeller noise. To be conservative, it is set to be equal to the maximum noise produced by the propellers, so 69 dB. The gear noise is assumed to be equal to 76 dB, which is a theoretical average according to a research performed by Dalian University Of Technology. [(1)]. To actually get to know the proper value, a thorough test should be performed as this noise depends on many variables. The total noise is investigated at three different critical points. At the very beginning of the takeoff run (1), during the climb phase to the screen height (2) and at cruise at an altitude of 100 m (3). The results of the total noise are listed in Table 15.1.

[(1)] `https://www.geartechnology.com/articles/0390/Gear_Noise_and_the_Making_of_Silent_Gears/`, Retrieved: 22-01-2018

Table 15.1: Noise breakdown

Noise source	1	2	3
Propeller (2x) [dB]	66	65	60
Engine (2x) [dB]	66	66	66
Gear (2x) [dB]	76	76	76
Total @ 1m [dB]	79.8	79.7	79.5
Total @ 100m [dB]	39.8	39.7	39.5

The addition of noise levels was performed with the following equation [(2)]:

$$N_{tot} = \log(\sum 10^{N_1} + 10^{N_2} + ... + 10^{N_i}) \tag{15.1}$$

N_{tot} is the total amount of noise, while N_1, N_2 up to N_i are separate noise sources in dB. It is clear from this analysis that the noise requirement of a maximum of 40 dB at 100 m distance is met.

15.3 Carbon Footprint

In the original strategy, the carbon footprint was only taken into account for the emission of the aircraft while in operation. If only emission is looked into, it is not considered to be a legitimate reflection of a carbon footprint. The emission caused during operation is for now assumed to be minimal due to the fact that electrical propulsion is used for all concepts. To achieve the carbon footprint per passenger-kilometer, the total produced CO_2 mass can be divided by the total expected kilometres that the aircraft will travel during it's life cycle. To make an estimation of the carbon footprint, the biggest components of the aircraft have been looked into; batteries, carbon fibre structures, glass fibre structures, Nylon and Dacron skin and the bonding material. Table 15.2 contains the carbon footprint rates for the different materials and the weight of the materials that have to be manufactured for the production of this aircraft.

Table 15.2: Carbon Footprint of different materials

Material	CO2 Footprint [kg/kg]	Mass [kg]	Total Footprint [kg]
Carbon Fibre	8.5	28.0	238.3
Adhesive	4.5	0.5	2.2
Glass Fibre	5.1	10.4	52.9
Dacron	6.3	1.0	6.4
Nylon	6.3	1.3	8.4
LiPo Batteries	65.0 kg/kWh	3.6 kWh	230.9

Diffferent carbon footprint values were obtained from various literature. For carbon fibre, the mean value found was used in this analysis. The adhesive was found have a footprint rate of 13.6 [(3)]. Entropy resins claim to be able to reduce this value by 33 %, so this value is used as resulting value for the adhesive [(4)]. The values for Dacron and Nylon[(5)] were used and the value for the LiPo Batteries was found in [21]. Note that the weights of the carbon fibre and the glass fibre have been increased by a factor 20 % four times. This is to account for the scrap losses in every manufacturing stage for these materials; cutting, mixing resin, trimming and assembly. The breakdowns of the masses and carbon footprints can be seen in Figure 15.1a and Figure 15.1b.

[(2)] `https://www.naa.nl/kennis-geluid/geluidsniveaus-optellen-aftrekken/`

[(3)] `http://www.welshcomposites.co.uk/downloads/environmental%20webinar.pdf`, Retrieved: 19-01-2018

[(4)] `https://europe.entropyresins.eu/store/supersap-oneonf/`, Retrieved: 19-01-2018

[(5)] `https://oecotextiles.wordpress.com/tag/nylon/`, Retrieved: 22-01-2018

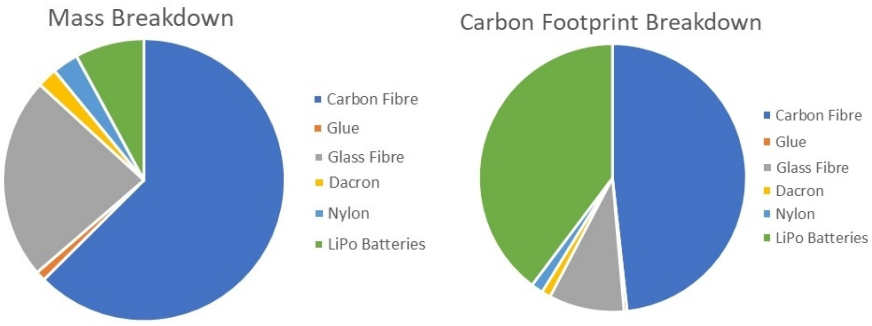

(a) Mass breakdown (b) Carbon footprint breakdown

Figure 15.1: Carbon footprint and mass breakdown of the main components

It is evident that the batteries and the carbon fibre contribution to the carbon footprint is rather large. Adding up the carbon footprints of the different materials results in a total carbon footprint of 581 kg. This is however when not taking into account the carbon footprint of the remaining materials used in engines, gears, cabling etc. These additional materials account for about 8 kg. For these materials, an average of 27 kg CO_2 was taken into account. The end footprint then comes down to 797 kg.

When taking the requirement of 100 grams per passenger-kilometer, this would impose roughly 100 cycles of use of the aircraft to make this requirement. This seams to be a rather fair value. On average, bicycles produce about 240 kg of CO_2, so this end result seems to be in the right direction [6].

15.4 Recyclability

The portion of the OEW that can be recycled is determined by looking at the same materials as for the carbon footprint in the previous section. For these materials, the most realistic recycling rates are compared to the respective weights. As the battery amounts to about 40 % of the total empty mass, recycling end-of-life solutions for the batteries are considered separately.

Battery Solutions from the US claims to be able to recycle 100 % of Lithium Ion batteries [7]. This seems rather overrated, but if this rate is actually true, it would mean that already 40 % of recyclability could be achieved with batteries alone.

The structural materials; Nylon, Dacron, Carbon Fibre and Glass Fibre have also been investigated. Nylon is a material that performs well in the sense of recycling. Many facilities and secondary manufacturers make use of recycled nylon in their products, such as outdoor clothing manufacturer Patagonia [8]. Dacron is a brand name for Polyethylene Terephthalate (PET) which has many recycling facilities worldwide [9]. Glass fibre recycling can be performed at many facilities and Carbon Fibre recycling is improving. However, unfortunately only the resin of the Carbon Fibre and Glass Fibre composites can be recycled, which only take up 33% on average. [10].

The materials and their respective recycling rates are listed in Table 15.3.

Table 15.3: Recycling rates of different materials

Material	Mass [g]	Recycling Rate [%]
Nylon Skin	1116.5	100
Glue	250	0
Glass Fibre Resin	5000	33
Carbon Fibre Wing	13520	33
Dacron Skin	850	60
Batteries	19200	100

[6] `http://www.slate.com/articles/health_and_science/the_green_lantern/2011/08/two_wheels_vs_four.html`, Retrieved: 22-01-2018

[7] `https://www.batterysolutions.com/recycling-information/how-are-batteries-recycled/`, Retrieved: 22-01-2018

[8] `http://www.patagonia.com/recycled-nylon.html`, Retrieved: 22-01-2018

[9] `http://www.epbp.org/`, Retrieved: 22-01-2018

[10] `http://www.jeccomposites.com/knowledge/international-composites-news/recycling-fibre-reinforced-plastics`, Retrieved: 22-01-2018

The total recycled portion for these materials is equal to 28 kg, 70 % of the total weight of these materials. This is of course when not taking into account the 8 kg of additional weights caused by the components not included in this analysis. To make the requirement of 90 % recyclability, a minimum of 43.2 kg needs to be able to be recycled. Even if the remaining 8 kg is fully recyclable, the 90 % would still unfortunately not be achieved. For now it is therefor stated that the recyclability of the OEW will lie between 65–83 %.

15.5 Conclusions and Recommendations

Unfortunately, not all requirements regarding sustainability are met. The aircraft produces an acceptably low amount of noise and an acceptable carbon footprint. End-of-Life plans for the design have good potential, but not sufficient to be able to recycle 90 % of the weight. The fact that carbon fibre and glass fibre perform relatively poor in the sense of recyclability causes the majority of this deficit. If the recyclable amount of these materials increases rapidly in the next 5 years, this requirement might be met. This is however not expected. Otherwise, a replacement material with better recyclability would be recommended. At the moment, a potential replacement material for carbon fibre has not yet been found and may not be on the market yet.

Another option for better recycling performance is to reuse the CFRP into lower grade material applications. Assembling used carbon fibres and transforming them into bulk materials can provide convenient materials for applications such as jigs and similar wood- and metalworking tools.

The noise requirement is met according to the performed analysis. However, due to limited resources, many assumptions had to be made in order to get these results. It is expected that a detailed analysis on gear noise will need to be conducted in order to get to a more reliable result. This detailed analysis has not been performed because it was considered beyond the scope of the project.

Another notable feature of the aircraft is that it actually performs at remarkably low power. This feature may provide a sanguine future if solar cells are considered as an energy source. The average solar power per square meter in the Netherlands on a yearly basis is around 120 W/m^2 during daylight hours (see Figure 15.2b). If the top wing and half of the bottom wing (half of the bottom wing is assumed to mostly be in the shadow of the top wing) would be installed with flexible solar panels such as manufactured by Flisom (efficiency of 20.4 % [11]) , then the aircraft would have a power generation of an estimated 347 W. Adding solar panels however also adds weight to the wing structure. Current solar panels use a minimum of 2 kg per square meter of weight. Following this assumption, the total weight would increase by almost 19 kg. However, most of the weight of solar panels comes from the reinforcement material on the back of the panels. If further investigation could blend the solar panels into the skin of the wing structure, then a massive weight reduction may arise. If this optimisation is performed, up to 4.8 kg of batteries could be removed from the design. This would not only be beneficial performance-wise, but also reduces the designs carbon footprint.

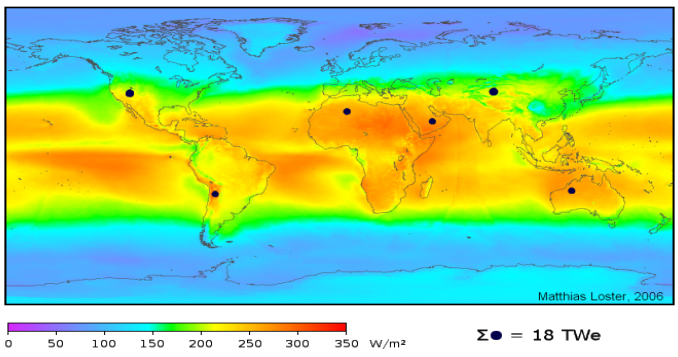

(a) Solar Intensity Chart [12]

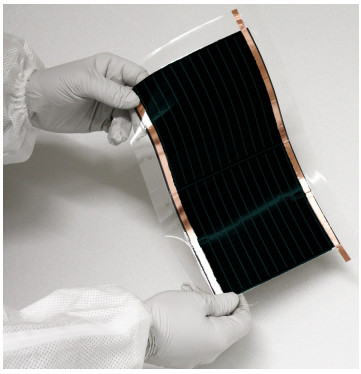

(b) Solar film [13]

Figure 15.2: The solar intensity distributed over Earth and new existing solar cells

[11] `https://flisom.com/products/`, Retrieved: 22-01-2018

16 Risk Analysis

During the technical analysis several product risks have been determined. In this chapter these risks will be summarised and an investigation on other not yet identified risks has been done. All risks are examined and mitigation methods are considered. When high risks cannot be mitigated, they must be addressed in future development of the *AerGo*.

16.1 Risk Identification

The risk identification methods used through the entire design phase will be used for the mission risk assessment too. At this point during the design it is still not possible to give accurate values for the likelihood of a risk. Therefore Table 16.1 is used to categorise all risk on their likelihood. A probability value range is given as an indication but risks given a probability rating can not be supported by calculations. Table 16.2 is used to determine the impact category.

Table 16.1: The probability of mission risk

Category	Probability description	Estimated Probability
5. Highly probable	The event will most likely happen during the lifespan of the aircraft. If severe, risk mitigation is a necessity.	0.7 <P <1.0
4. Probable	The event is likely to happen during the lifespan. If severe, risk mitigation is strongly advised.	0.4 <P <0.7
3. Improbable	There is a small chance the event happens during the lifespan. Risk mitigation should be considered.	0.1 <P <0.4
2. Highly improbable	The chance of this event is very small and will most probably not occur during the lifespan.	0 <P <0.1
1. Impossible	The event will never happen.	P = 0.0

Table 16.2: The impact of mission risk

Category	Impact description
5. Catastrophic	Crash is inevitable.
4. Critical	Proper control of the aircraft impossible. Emergency landing needed take-off must be aborted.
3. Severe	Noticable damage is done to the aircraft. Performance is not directly affected but maintenance should be performed to fix and prevent escalation.
2. Marginal	Deficiency correctable in flight. Emergency landing might be needed or take-off may be aborted but the aircraft will not be damaged.
1. Negligible	Small impact on performance of the aircraft. Does not do any harm to the aircraft.

16.2 Risk Evaluation

During the design phase several risks have been identified. Table 16.3 shows a summary of all risk found and where they are originated. Some new risk assessed during the risk assessment are included. Table 16.3 uses a numbering and shows a severity assessment which is used in the risk map shown in Figure 16.1a.

Table 16.3: Assessment of the mission risk due to the final design features

	Risk	Identification Origin	Probability	Severity
1.	Damaging wing during paddling	Chapter 11	5	3
2.	Inaccurate cost breakdown	Chapter 14	4	3
3.	Structural damage during operations	Chapter 16	4	3
4.	Pilot Tiring	Chapter 8	4	2
5.	Customer assembly failure	Chapter 16	3	5
6.	Pontoons hitting the water during take-off	Chapter 11	2	4
7.	Stall due to gusts	Chapter 5	2	4
8.	Engine failure	Chapter 8	2	4
9.	Water damage to systems	Chapter 16	2	4
10.	Trailer theft	Chapter 16	2	2

Damaging wing during paddling: The pilot position in the aircraft is not the most convenient to paddle without hitting the trailing edge of the wing. The sensitivity of the aircraft to impact makes the aircraft vulnerable to impact damage when paddling. Local impact strips on the trailing edge of the wing and hull must be considered in order to mitigate this risk.

Inaccurate cost breakdown: The cost estimation method used is optimised for general aviation aircraft. There is a large uncertainty to this estimation and the model is very sensitive to chance. Since cost is one of the most important requirements set by the customer, going over the cost budget influences the business feasibility of the *AerGo* severely.

Structural damage during operations: The ultralight and fragile pieces of the aircraft can get damaged easily when for example dropped during assembly. When assembling the aircraft the pilot should take extra care in handling all parts. When damaged reparation or substitution of parts is necessary.

Pilot tiring: With a required control force between 5 to 10 kg per arm for roll control and pushing twice your body weight with your legs at take-off the pilot must be in shape. When manoeuvring a lot and flying for one hour, controlling the aircraft becomes quite an exercise. If the pilot suffers cramps he will be unable to steer the aircraft. Fortunately the aircraft will level out if no forces are exerted and the pilot sits at the neutral point.

Customer assembly failure: Before every flight the customers assembles the aircraft from storage configuration to ready before flight configuration. This assembly does not include high level manufacturing, but is nevertheless sensitive to mistakes. By for example, forgetting the safety pin on the attachment of one wingtip the owner wouldn't notice anything at first because the aircraft can still fulfil its mission. In extreme load cases, the aircraft would be at risk of the connection pins detaching, resulting in losing a part of a wing in the air.

Pontoons hitting the water during take-off: If the pontoons hit the water during take-off they cause a lot of drag and with that a turning moment. Aborting take-off and restarting the take-off process will fix this risk. If this would occur during landing, worst case the aircraft crashes into the wall of the river it lands on. Given the low landing speeds, this would not cause major injury to the pilot, which cannot be said for the aircraft. Section 11.5 however found that this yawing moment will only be significant at speeds higher then 5 m/s and at this speed the aircraft is very stable. With sidegusts of 10 m/s it would take more than one minute to roll from the neutral point to the point where pontoons hit the water, at which the aircraft is long past take-off.

Stall due to ear gusts: The difference between the cruise speed and stall speed is much lower than in conventional aircraft. This makes the aircraft more susceptible to gusts. However an analysis of the weather in Section 5.2 finds that the probability of stalling due to a rear gust is negligible if the pilot checks weather conditions beforehand and avoid flying when gusts are expected to exceed the safety limit.

Engine failure: If one engine or propeller fails, there is a serious risk for the *AerGo* to crash. The aircraft cruises at low altitude which means there is not much time searching for an emergency landing spot. An analysis has been started to check the feasibility of increasing the engine power of the remaining engine to maintain levelled flight which can mitigate this risk but at this point there are no results yet.

Water damage: Electronics never go well with water. Even though the batteries are positioned in watertight sections there always remains a possibility of it being damaged. Spray can have a huge impact on the propellers but with the positioning on the top wing in combination with the estimated spray characteristics this will be highly improbable.

Trailer theft: Transporting the aircraft and launching it in the water from a trailer is very convenient operations wise and although the trailer will be custom made for the use of the *AerGo* only, there is always a chance of people stealing it. A wheel clamp can be used to mitigate this risk.

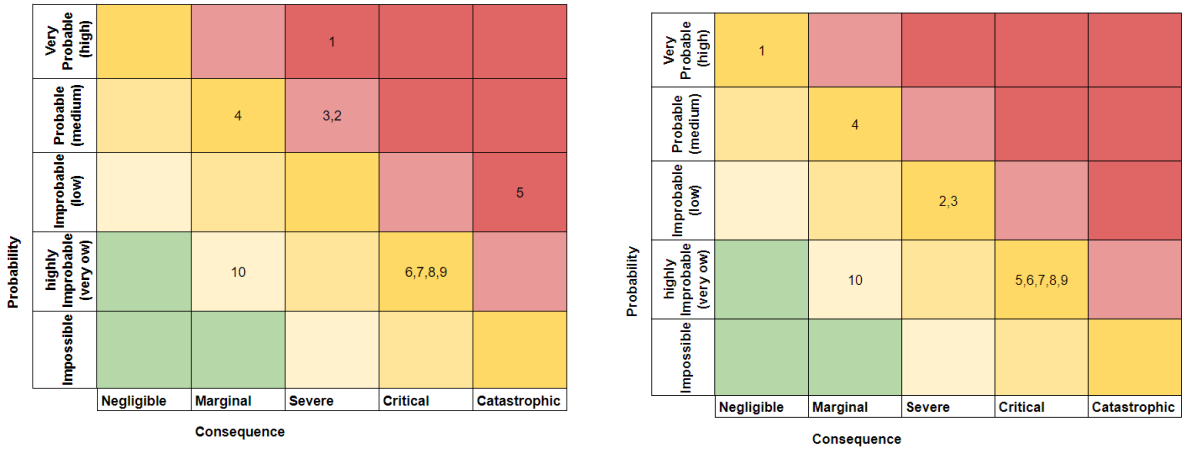

(a) Mission risk map

(b) Mission risk map after mitigation

Figure 16.1: Two pictures of the biplane *Moodywing*

16.3 Risk Mitigation

When looking at the risk map there are 2 risks endangering the future design and feasibility of the *AerGo* that need to be mitigated. One of which is fairly easy to solve. Adding structural reinforcements to the hull and trailing edge of the wing as stated before reduces the severity of hitting the wing. When boating in a canoe there is a high chance of hitting the edges however the impact will be negligible due to impact resistance of the hull. The *AerGo* should locally have the same impact resistance. The effects on the performance and especially weight of the aircraft must be investigated in future design plans, but are expected to be fairly low.

The risk of customer assembly failure will unfortunately always remain. It is one of the drawbacks of designing a product built to be taken apart by the customer for transportation. Pilots will however have an intensive instruction before first flight and there will be an elaborate manual focused on the on-spot assembly, reducing the probability. To reduce the consequence extra safety measures must be taken into account that will alarm the pilot if assembly is done wrong so it can be fixed before taking off and safety gear should be considered like a helmet, lifevest and a back protector.

Furthermore mitigation is desired for the the Risk of inaccurate cost breakdown and structural damage during operations. Adding extra structural strength would decrease the probability of structural damage during operations. The structure will become less brittle and more resistant to impact reducing the risk level. This will however automatically imply that the structure will become more heavy and therefore negatively influencing the aircraft performance. Finding the optimal balance between risk and structural weight must be further investigated on during the detailed design phase.

As stated before in chapter 14, the cost breakdown is sensitive to small parameter changes introducing a risk for the business feasibility. A more elaborate cost breakdown optimised for ultralight aircraft must be performed in a future design phase. Furthermore, if the detailed design phase continues aircraft parameters will be less susceptible to change so more accurate assumptions can be made concerning the costs making the cost breakdown less sensitive. The probability of overshooting the cost breakdown will then decrease and can go to improbable during the detailed design phase or even highly improbable during the manufacturing phase.

The Final risk map after mitigation is found in Figure 16.1b.

17 Sensitivity Analysis

In this chapter a sensitivity analysis is conducted for several subsystems. The stability of subsystem parameters is analysed when there is a change in a major system parameter. The sensitivity analysis is conducted for performance, aerodynamics, structures and hydrodynamics respectively. These technical disciplines are considered to be most sensitive to changes in the design. The sensitivity analysis for stability is covered in Chapter 8.

17.1 Performance

For performance, the sensitivity is analysed by looking at different wing spans. Table 17.1 shows the change in aspect ratio, A, induced drag coefficient, Cd_i, Power required, P_r, and battery mass, Δm. As the wing span increases the aircraft becomes more efficient, which results in the drag going down as well as the power required. This change in power required is also visible in Figure 17.1. If the power changes by a large enough amount, a battery can be added or removed, resulting in a change in mass.

Table 17.1: Change in performance parameters due to wing span change

b [m]	**A [-]**	**Cd_i [-]**	**P_r [10^3W]**	**Δ m [kg]**
9.0	11.9	0.045	1.75	0.00
12	7.62	0.050	1.91	0.00
15	4.29	0.059	2.25	-2.41

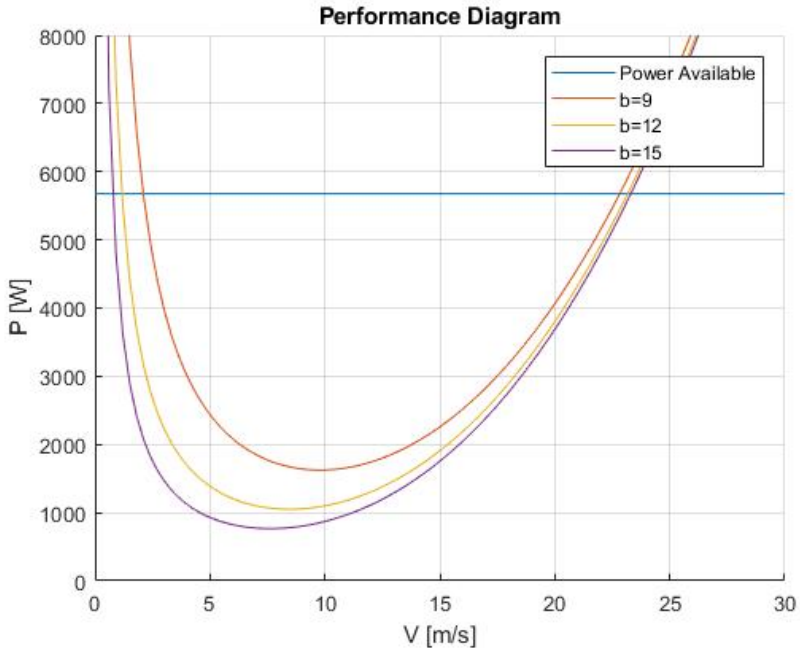

Figure 17.1: Performance sensitivity analysis

17.2 Aerodynamics

For aerodynamics, the sensitivity is analysed by changing the sweep angle[28]. In theory, if there is an increase in sweep angle , it will cause the C_{L_α} and C_{L_0} to decrease. A test was done by using sweep angles of 0°, 15° and 30°. Figure 17.2 and Table 17.2 depict the changes in C_{L_α} and C_{L_0}. It can be seen that the values do indeed decrease with an increase of sweep.

Table 17.2: Change in lift coefficient due to change in sweep angle

Λ[°]	$\mathbf{C_{L_\alpha}}$ [**1/rad**]	$\mathbf{C_{L_0}}$ [−]
0	5.43	0.605
15	5.25	0.587
30	4.77	0.533

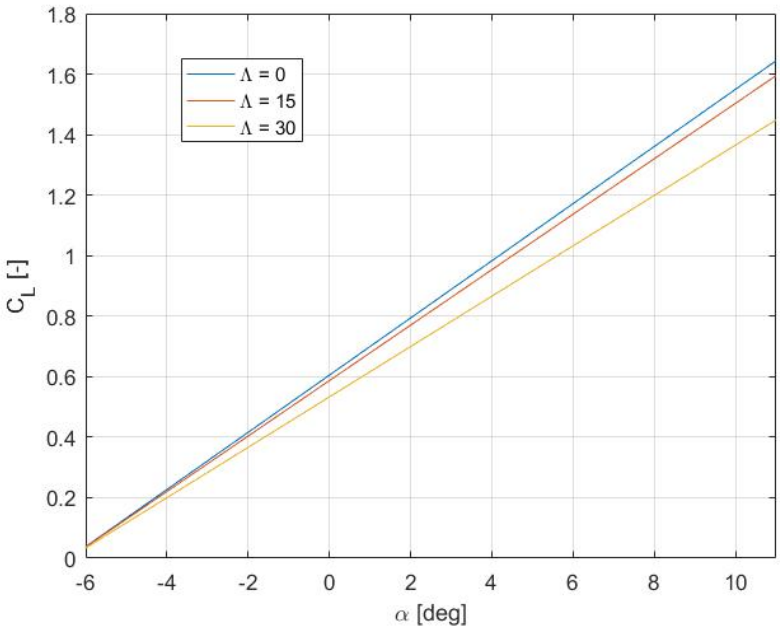

Figure 17.2: Sensitivity of C_L

17.3 Structures

Similar to the sensitivity analysis in performance, there is a change in the wing span. This leads to a change in the spar length which affects the moment and deflection of the wing. Table 17.3 shows that when the spar length increases the moment and deflection increase significantly. This is visualised in Figure 17.3. It is interesting to note that the shear force remains the same, which makes sense because the total lift does not change.

Table 17.3: Change in moment and deflection due to change in spar length

$\mathbf{L_{sp}}$[**m**]	**M**[$\mathbf{10^3}$**Nm**]	**EIv**[$\mathbf{10^4}$**Nm**$^\mathbf{3}$]
5.0	4.59	2.54
6.2	5.67	4.82
7.4	6.75	8.16

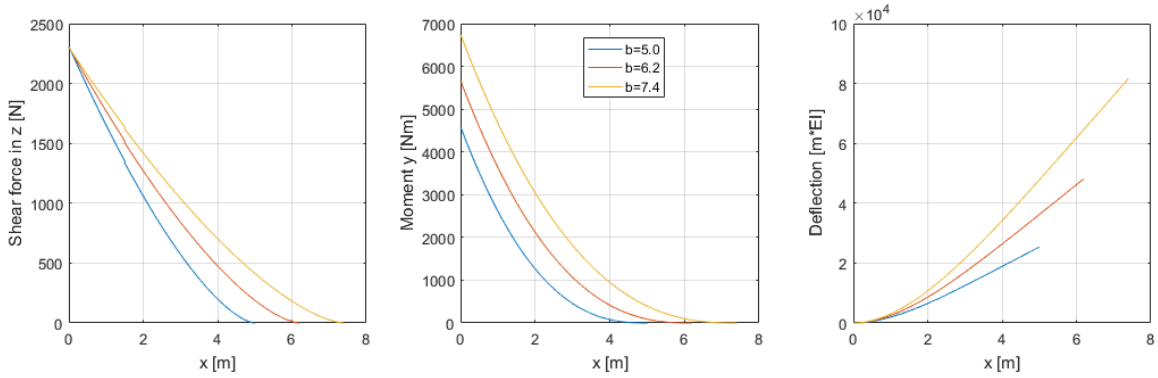

Figure 17.3: Sensitivity of shear (left) moment (middle) and deflection (right)

17.4 Hydrodynamics

For hydrodynamics the drag force is analysed for different values of the lift coefficient at zero angle of attack, C_{L_0}. In Figure 17.4 one can see that for a C_{L_0} of 0.90 the drag goes down again after a velocity of about 7 m/s. This is because once the aircraft starts lifting from the water, the hull starts to plane and the drag decreases significantly. As C_{L_0} decreases, the planing of the hull is postponed and the maximum drag increases. The increase in maximum drag can be found in Table 17.4.

Table 17.4: Change maximum drag force due to change in C_{L_0}

$\mathbf{C_{L_0}}$ [−]	$\mathbf{D_{max}}$ [N]
0.00	190
0.30	150
0.59	130
0.90	111

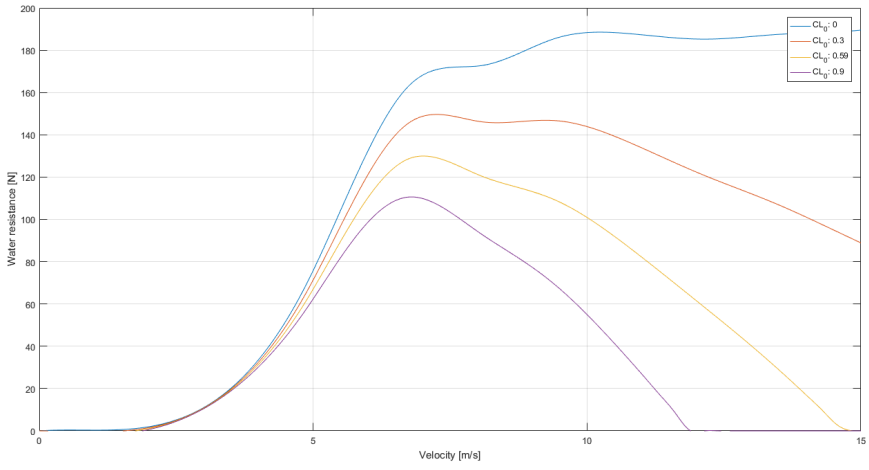

Figure 17.4: Hydrodynamics drag analysis

18 Post DSE

In this chapter, the development phase after the DSE project is discussed. A global overview is given from the detailed design phase up to the production. Section 18.1 describes the development phase of the AerGo and section 18.2 describes the production and sales phase.

18.1 Design and Development

18.1.1 Optimisation phase

During the the optimisation phase, every subsystem group will continue further with designing. This entails thorough reiterations as well as implementing of all the recommendations given in each chapter. This will ensure that the most accurate results will be used to begin building the prototype that will be used for the first flight test.

18.1.2 Testing phase

A lot of analysis have been performed with analytical models. In order to be sure all models are correct and the aircraft can be certified and sold on the market a number of tests must be performed.

Structures and material tests

The material testing phase will consist several different forms of testing. First, it will start with simulation testing which mainly used for aerodynamics/hydrodynamics and structures. This will consist of CFD test and FEM test respectively. No wind tunnel tests will be performed because they fall outside of the budget therefore is is opted to use CFD tests. Once, these tests have been performed, experimental testing will begin. A pyramid of the levels of these test is depicted in figure 18.1.

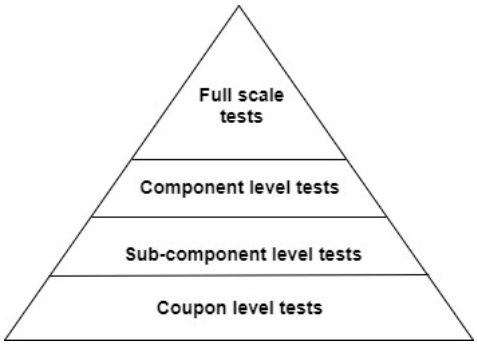

Figure 18.1: Different levels for experimental testing

It shall start with coupon level testing which is conducting tests on all the different materials such as dacron, CFRP, etc. They will mainly go under tensile and bending tests. After this, the sub-component level testing will take place. This will be the testing of the ribs, the spars and the skin of the structure. The ribs and spars will be tested on compression as well as buckling. Also the control systems will be tested to check if the control behave as wanted. The skin will be tested on tearing. When these test are complete then it is time to move on to the component level tests. At this point the structure for the wing and hull are put together and they will be be put under load tests individually. This can be done with bending tests and by compressing the structures to find the key stress points. Finally one this is complete the 1st prototype can be built. This prototype will then undergo a full scale load test and once given the OK, flight tests commence.

Towtank Test

The total resistance of a hull is determined by adding the resistance due to waves, called residual drag and the skin friction drag together [(1)]. The resistance due to waves is based on the Froude number and the resistance due to

[(1)] `http://www.engr.mun.ca/~bveitch/courses/r-p/Assignments/ITTC-calculation-procedures-Lab1.pdf`, Retrieved: 23-1-2018

friction is a function off the Reynolds number. Unfortunately it is not possible to keep both coefficients the same for the model and the hull. In the test the Froude number will be held the same for both the model and the design and the Reynolds number will be corrected for. So the $C_r(Fn)$ will be equal for both of them. The smaller the difference, the less the Reynolds number correction will influence the results and thus of course the more correct they will be.

Due to the limitations of the speed and size of the towtank however a smaller model is required. The towtank is 142 m long, 4.22 m wide and 2.5 m deep. The maximum speed that can be reached is 7m/s.The froude number as a function of displacement is used to scale the model speed to the design speed and is computed according to

$$F_{n_\nabla} = \frac{v}{\sqrt{g\nabla^3}} \tag{18.1}$$

It might be logical to test the model only until take-off speed, however at zero angle of attack the aircraft will lift of at a speed of 13 m/s which is slightly higher than the take-off. So if the test is conducted up until 13 m/s the hydrodynamic drag will be tested until the maximum speed achieved while on water. using Equation (18.1) for the aircraft speed of 13 m/s and 7 m/s while keeping the froude number the same results in a displacement volume of 0.0037 m^2 for the model. This is ... as small as the *AerGo*. Now the total resistance can be expressed by

$$R_{total} = R_f(Re) + R_r(Fn) \tag{18.2}$$

Where all friction forces are based on the same equation with only a different friction coefficient this can be rephrased as follows

$$C_{Total} = C_f + C_r \tag{18.3}$$

One of the results of the towtank test is the total model resistance. With this total drag, the speed, wetted area and water density the total friction coëfficient of the model can be computed according to:

$$C_{total_m} = \frac{R_{total_m}}{0.5 * \rho * v_m^2 * A_m} \tag{18.4}$$

Using the ITTC-57 Model-Ship correlation line the skin friction coefficient of both the model and the hull can be computed

$$C_f = \frac{0.075}{(log(Re) - 2)^2} \tag{18.5}$$

Equation (18.4) and Equation (18.5) implemented in Equation (18.3) can be used to find the residual drag coefficient. However, if the Froude number is kept the same so is the residual drag coefficient so there is no need in doing this. By adding Equation (18.3) for the model and for the aircraft hull together the total friction coefficient of the hull can be found.

$$C_{total_H} = C_{total_m} - C_{f_m}(Re) + C_{f_H}(Re) \tag{18.6}$$

Rewriting Equation (18.4) the total resistance for the hull can be found. Repeating this for every test speed results in the hull resistance curve which can be compared with the modelled .

A spray analysis of the model should be done visually to have an indication of the effect on the pilots vision during take-off.

18.1.3 Redesign phase

The redesign phase will go on for a long time. Once the test are all complete and new optimisations must be made, a redesign is done. Basically the same steps taken as in the previous two phases will occur. This redesign phase can go on for a while until the desired performance is achieved. If the initial prototype is really good, this phase can be skipped as well.

18.2 Production Phase

The production phase consists of two parts. The manufacturing and the sale of the aircraft. Both basically are taking place at the same time and are described in the sections below.

18.2.1 Manufacturing

The manufacturing phase starts after all testing of the final design is complete. At this point the aircraft is completely ready to be produced. This phase can be a lengthy process since it was decided to produce about 100 of them. A simplified layout of the production plan is shown in Figure 18.2 with arrows indicating the direction in which the production flows. Inputs are coloured blue whereas the final assembly, which is to be completed by the customer, is green. Before the production plan can be implemented moulds, tools and production facilities have to be organised.

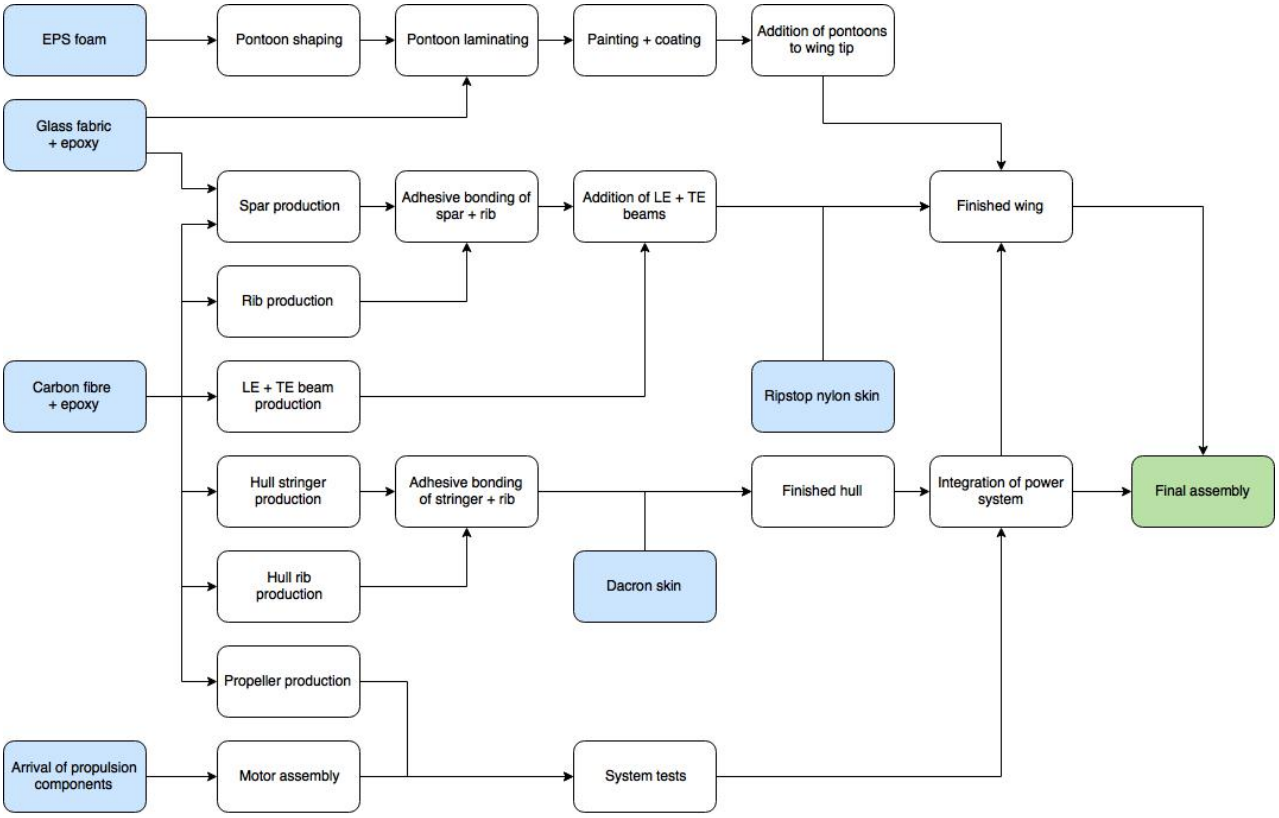

Figure 18.2: Production plan of the *AerGo*

18.2.2 Sales phase

The sales phase consists of the steps taken upto the point when the *AerGo* is ready to be sold. The first step is to establish a sales plan. After the plan is made then advertising can be done such as making websites and networking with companies, letting the name of *AerGo* be heard to the population, create awareness. Simultaneously, more marketing will happen getting more details about competitor and opportunities. After it is decided that the proper amount of advertising and marketing is made then let the sales begin!

18.2.3 Conclusion

The goal of this chapter was to give an understanding of which steps will be taken after this DSE project is finished. The *AerGo* design will continue with further optimisation then under go several testing. After that, redesigns will occur with further testing. When the testing and redesign are complete then manufacturing of the product takes place and finally the aircraft is ready to be sold. Appendix E contains figures of the Gantt chart and the flow diagram that give another perspective of the phases.

19 Conclusions & Recommendations

Ten students have been working for ten weeks to provide a recreational hydroplane that is transportable by bike, costs less than €20,000 and can operate from a 20 meter wide body of water. The aim of this report was to present the procedure of the entire design phase and focus on the final preliminary design of the *AerGo*. This section explains to which extent the mission need statement is satisfied with the final design of the *AerGo*. Decisive challenges and trade-offs that led to the final design are discussed and future challenges and recommendations are given. From a technical point of view, the most driving factor was to design for the lowest possible operational empty weight. Low weight leads to the benefit of not requiring a pilot license, but it also implies low power and therefore low energy. A lightweight and energy-efficient design contributes to the unique features of the *AerGo* compared to current competitors on the market. These unique features are the ease of use, transportability, affordability and low noise.

In performance, the crucial decision was to select a cruise speed that optimised the mass of the batteries, while staying within the safety margins with respect to wind gusts and maintaining the required range. A propulsion system was designed to match the performance requirements while aiming for the highest efficiency and the lowest amount of noise. Also, the charging features were decided to discard in favour of having additional batteries. The structures and materials used in strengthening the design were optimised for minimum weight with the given structural requirements. The aerodynamic and hydrodynamic properties of the design of the *AerGo* have been optimised for minimum drag, while remaining within the stability limits. It was pursued to design the stability and control systems as simple and cheap as possible. Finally, a customised bike trailer has been designed to ensure the ease of operation before and after flight.

The resulting design configuration can be narrowed down to a biwing structure attached to a monohull with a silent electrical twin propeller pull propulsion system and two pontoons at the lower wing tips, controlled by weight shifting and wing warping. With a wing area of 18.9 m^2 and a span of 12 m, the *AerGO* is designed for a cruise speed of 15 m/s and a stall speed of 9 m/s. The total operational empty mass of the aircraft is 44.7 kg, which enabled minimisation of the carbon footprint.

Obviously, in this stage of the design, the *AerGo* still contains some deficiencies. Regarding the key requirements as specified in Chapter 5, one of these is for the moment not entirely satisfied. A selling price of €20,000 is achievable, but with small changes in the model and design the expected break even point will be far into the future, which will not make a good impression on external investors. Either the design will have to be redesigned to become cheaper to manufacture, the business model will have to be analysed in more detail or the sale price must be increased to €25,000.

During the analysis and design phase of the different subsystems, a number of recommendations popped up to attenuate or eliminate the occurring deficiencies. The range of the *AerGo* is expected to increase when considering an even lower operational empty weight and payload weight. The propulsion system provides a redundant amount of power, which can be used to design for the case of failure of one of the propellers or engines. The rudder is already designed to provide sufficient controllability in this case, but it is recommended to investigate this flight case in more depth. For the propulsion system, it is recommended to investigate the probability of adding solar cells to the wing. The wing area is relatively large, which could enable the feasibility of flying the aircraft while recharging the batteries, or to replace part of the batteries as a whole. In terms of stability, it is advised to perform actual experiments to determine the feasibility of the current efforts required by the pilot to perform weight shifting. Furthermore, due to the fact that the resulting mass of the structures is surprisingly low, it is plausible that reinforcements need to be considered in future redesign of the aircraft. The structure needs to be assembled and disassembled many times by a pilot who probably does not have a structural engineering background, so extra resources are recommended to investigate this subsystem further.

All the same, the design is considered to be a worthy homage to the *Wright Flyer*. The engineering spirit of this iconic and groundbreaking aircraft have been combined with modern cutting edge technologies, resulting in a silent, lightweight, compact, sustainable hydroplane at minimal cost that adheres to FAR 103, by 10 students in 10 weeks.

Appendix A Trade-off Table

Here, the final trade off, performed before the midterm, is included. Table A.1 shows the weights of all criteria, while Table A.2 shows the final score for each of the tree concepts. The full trade-off is given in Table A.3.

Table A.1: Criterion weights for the final trade-off

Criterion	Customer weights	Engineering weights	Total weights
Mass	2.25	4	21
Cost	2.5	2	16
User Friendliness	2.5	2	21
Sustainability	1.5	2	12
Development Risk	1.75	3	16
Flight Experience	3.25	2	19

Table A.2: Final results of the Trade-off

Concept	Weighted Score
Flying Biwing	300
Surf-Glider	295
X-Machine	270

	Mass	Cost	User Friendliness	Sustainability	Development Risk	Flight Experience
Surf Glider	3. Estimated at 53 kg, significant mass reductions are improbable	4. Estimated at €10,500.	2. Canopy collapse is a safety issue and water operations will be difficult	2. Noise requirements can be met with some changes	4. TRL 9, full scale versions exist and have been used for years	2. Completely uncontrollable after stall, pilot noise will be uncomfortable
X-Machine	2. Estimated at 65 kg, when using mostly CFRP it is possible to meet the requirements	2. Estimated at €16,000. No major cost reductions can be made in production or materials, due to material restriction	3. Docking might pose problems due to the long and wide shape	1. Noise requirements can be met with some changes, however materials and production have a high environmental impact	3. TRL 7, concept is used and proven in RC aircraft, no seaplane versions exist	3. Stable and agile, pilot noise can be mitigated.
Flying Biwing	3. Estimated at 58 kg, significant weight reductions are still possible (eg. box wing)	3. Estimated at €13,500. Cost can still be decreased by using slightly heavier but cheaper materials.	3. Docking might pose problems due to the wide shape	2. Has high probability to meet noise requirements, materials with a medium to low environmental impact can be used.	4. TRL 9, full scale models exist and have been used for over a century.	2. Not intrinsically stable, but can be made stable. Pilot noise can be mitigated

Table A.3: Trade-off table for the final trade-off.

Appendix B Detailed FFD

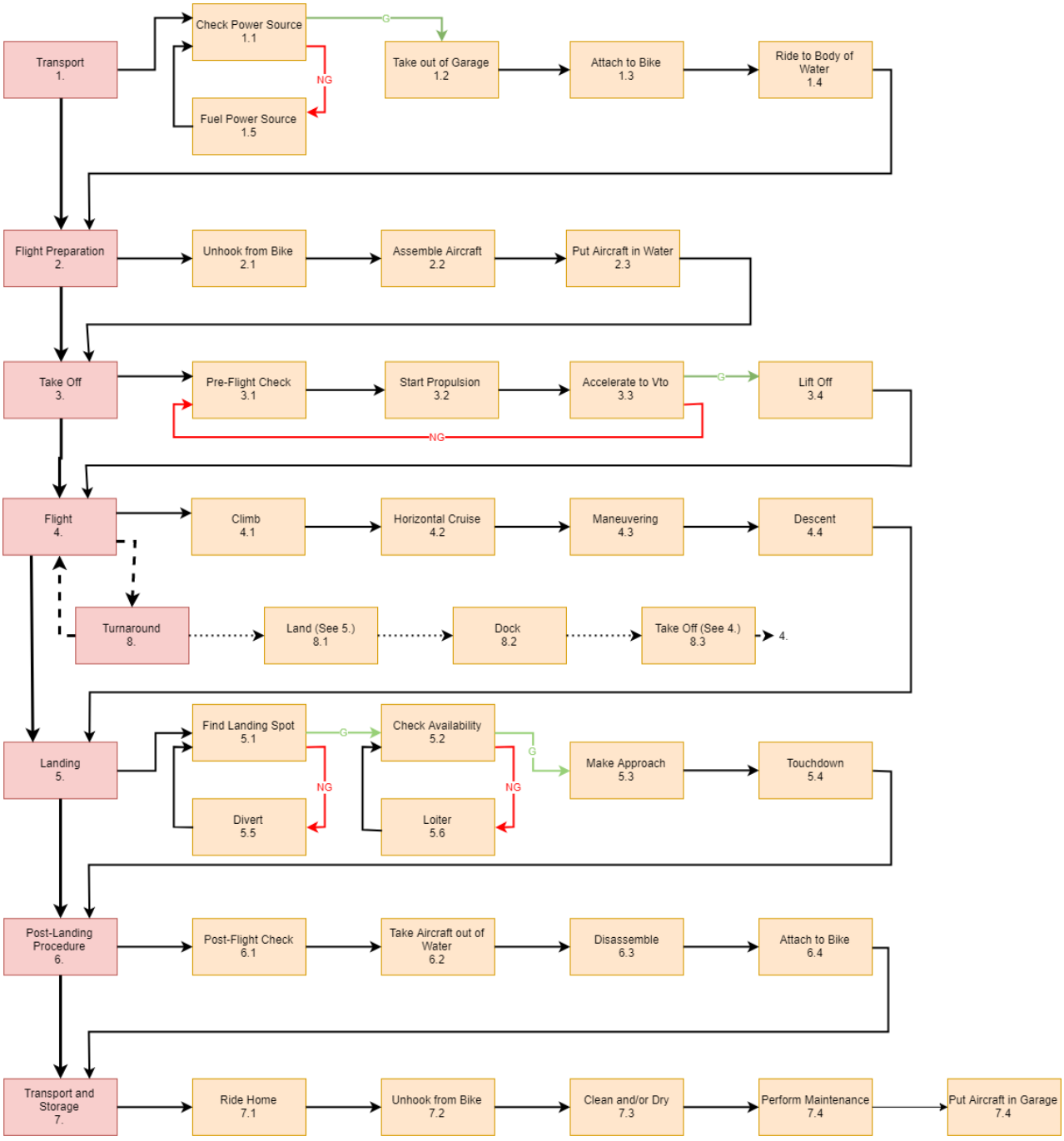

Figure B.1: The detailed Functional Flow Diagram for the *AerGo*.

Appendix C Graphs accompanying V&V of the hydrodynamical analysis

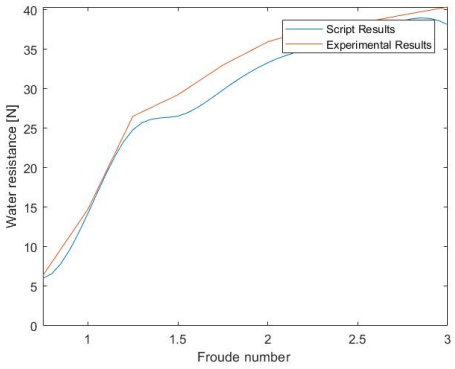

(a) Comparison between script and experimental results for Model 188 from the DSDS.

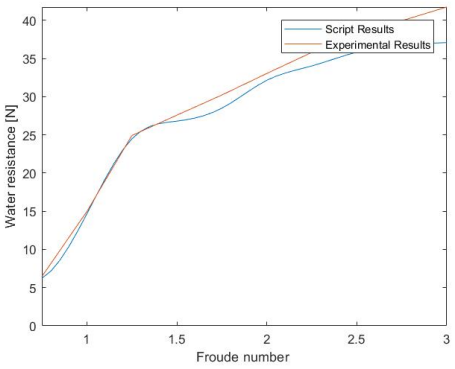

(b) Comparison between script and experimental results for Model 2332 from the DSDS.

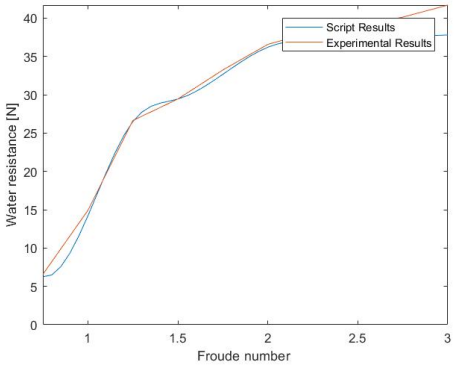

(c) Comparison between script and experimental results for Model 251 from the DSDS.

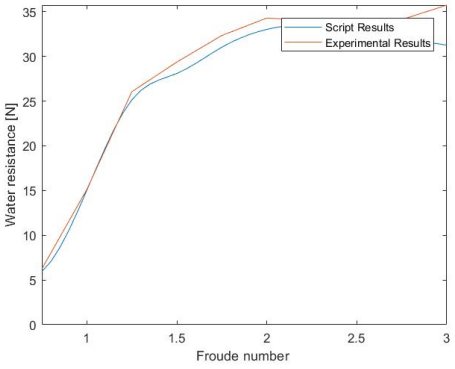

(d) Comparison between script and experimental results for Model 362 from the DSDS.

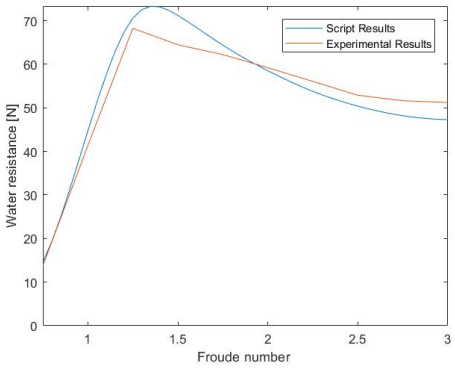

(e) Comparison between script and experimental results for Model 4665 from the DSDS.

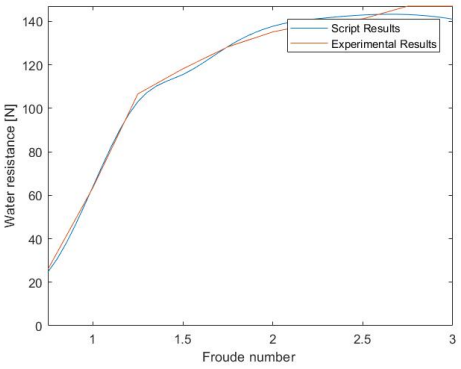

(f) Comparison between script and experimental results for Model 56671 from the DSDS.

Figure C.1: Graphical comparison between the results of the Matlab script for hydrodynamical drag and experimental results taken from the DSDS database.

Appendix D Cost Breakdown

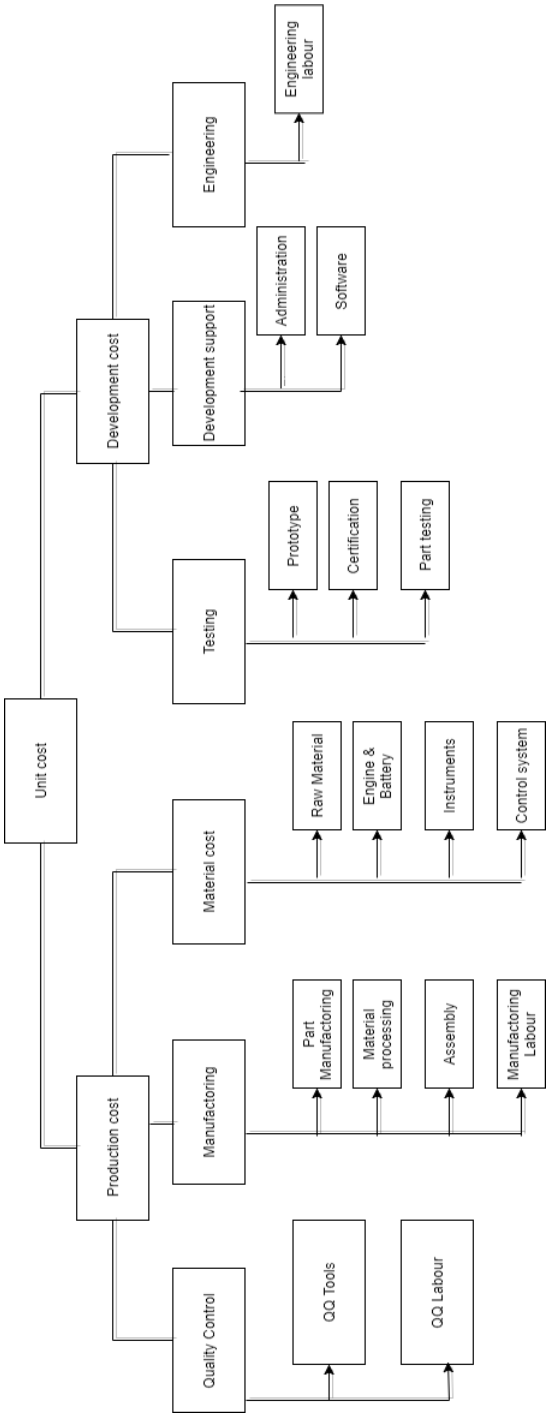

Figure D.1: Cost breakdown of the unit cost

Appendix E Design and Development

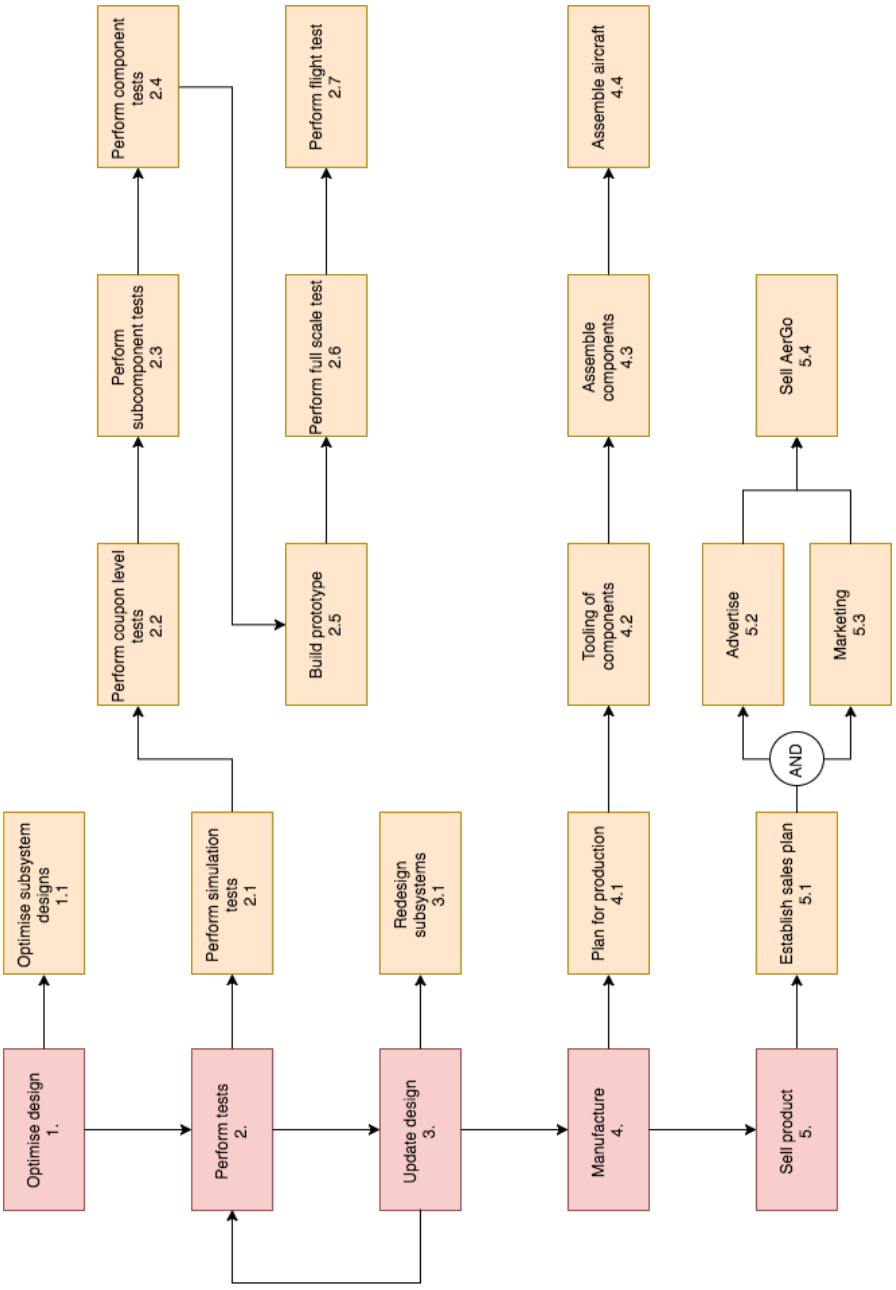

Figure E.1: Flow chart of the post development phase

ID	WBS	Task Name	Duration	Start	Finish
1	**1**	**Design optimization**	**6 mons**	**Mon 12-2-18**	**Fri 27-7-18**
2	1.1	Aerodynamic iterations	6 mons	Mon 12-2-18	Fri 27-7-18
3	1.2	Hydrodynamic iterations	6 mons	Mon 12-2-18	Fri 27-7-18
4	1.3	Stability and control iterations	6 mons	Mon 12-2-18	Fri 27-7-18
5	1.4	Structures and materials iterations	6 mons	Mon 12-2-18	Fri 27-7-18
6	1.5	Performance and propulsion iterations	6 mons	Mon 12-2-18	Fri 27-7-18
7	**2**	**Testing**	**3 mons**	**Mon 30-7-18**	**Fri 19-10-18**
8	**2.1**	**Simulation testing**	**5 days**	**Mon 30-7-18**	**Fri 3-8-18**
9	2.1.1	Conduct CFD test for aerodynamics	2,5 days	Mon 30-7-18	Wed 1-8-18
10	2.1.2	Conduct CFD test for hydrodynamics	2,5 days	Wed 1-8-18	Fri 3-8-18
11	2.1.3	Conduct FEM test for structure			
12	**2.2**	**Coupon level testing**	**5 days**	**Mon 20-8-18**	**Fri 24-8-18**
13	2.2.1	Test materials on tension	2,5 days	Mon 20-8-18	Wed 22-8-18
14	2.2.2	Test materials on bending	2,5 days	Wed 22-8-18	Fri 24-8-18
15	**2.3**	**Subcomponent testing**	**10 days**	**Mon 27-8-18**	**Fri 7-9-18**
16	2.3.1	Test ribs for compression	2 days	Mon 27-8-18	Tue 28-8-18
17	2.3.2	Test spars for bending	2 days	Wed 29-8-18	Thu 30-8-18
18	2.3.3	Test spars for buckling	2 days	Fri 31-8-18	Mon 3-9-18
19	2.3.4	Test skin for tearing	2 days	Tue 4-9-18	Wed 5-9-18
20	2.3.5	Test control systems	2 days	Thu 6-9-18	Fri 7-9-18
21	**2.4**	**Component testing**	**5 days**	**Mon 10-9-18**	**Fri 14-9-18**
22	2.4.1	Perform load tests on wing	2,5 days	Mon 10-9-18	Wed 12-9-18
23	2.4.2	Perform load tests on hull	2,5 days	Wed 12-9-18	Fri 14-9-18
24	**2.5**	**Full scale test**	**5 wks**	**Mon 17-9-18**	**Fri 19-10-18**
25	2.5.1	Build prototype	2 wks	Mon 17-9-18	Fri 28-9-18
26	2.5.2	Conduct load test on aircraft	1 wk	Mon 1-10-18	Fri 5-10-18
27	2.5.3	Perform flight test	2 wks	Mon 8-10-18	Fri 19-10-18
28	**3**	**Redesign of subsystem**	**6 mons**	**Mon 22-10-18**	**Fri 5-4-19**
29	3.1	Repeat testing	3 mons	**Mon 14-1-19**	**Fri 5-4-19**
30	**4**	**Manufacturing**	**4 mons**	**Mon 8-4-19**	**Fri 26-7-19**
31	4.1	Plan for production	1 mon	Mon 8-4-19	Fri 3-5-19
32	4.2	Tooling of components	1 mon	Mon 6-5-19	Fri 31-5-19
33	4.1	Assemble components	1 mon	Mon 3-6-19	Fri 28-6-19
34	4.2	Assemble aircraft	1 mon	Mon 1-7-19	**Fri 26-7-19**
35	**5**	**Sales**	**3 mons**	**Mon 29-7-19**	**Fri 18-10-19**
36	5.1	Establish sales plan	1 mon	Mon 29-7-19	Fri 23-8-19
37	5.2	Advertise product	1 mon	Mon 26-8-19	Fri 20-9-19
38	5.3	Marketing	1 mon	Mon 23-9-19	Fri 18-10-19
39	5.4	**Sell product**			

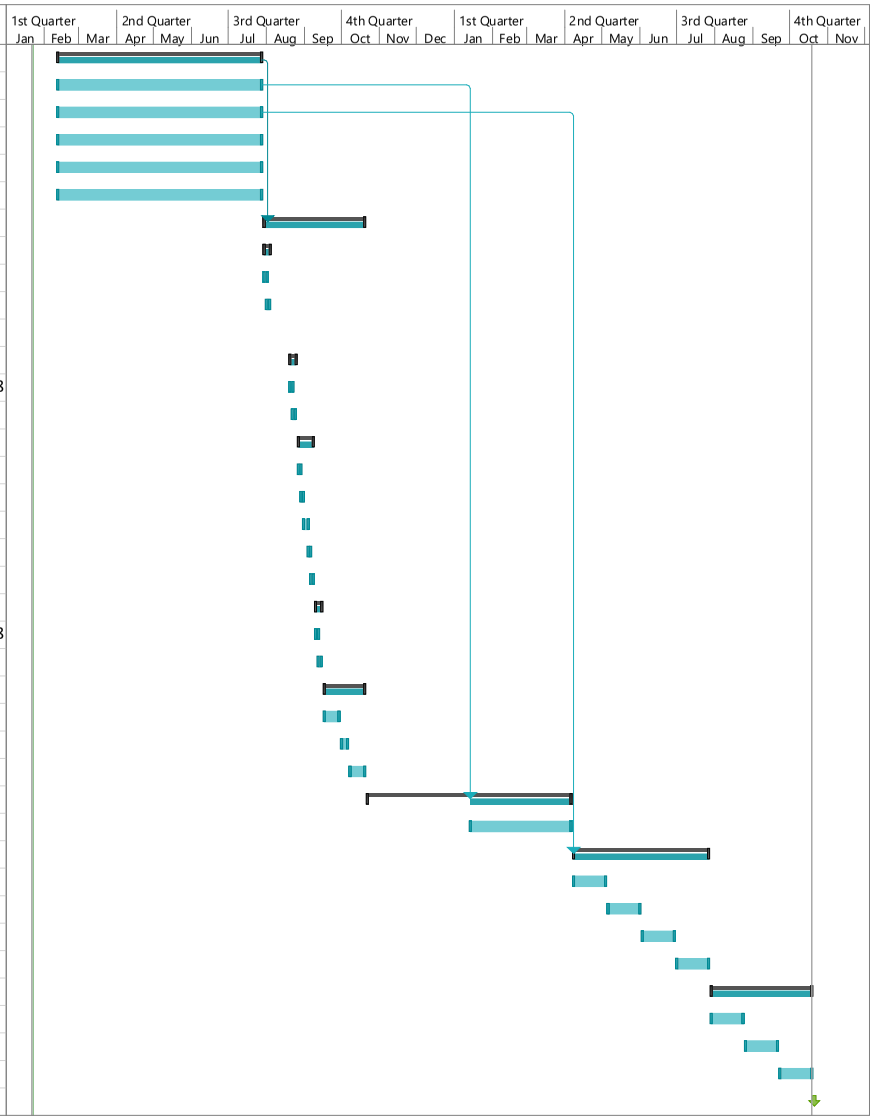

Page 1

Figure E.2: Gantt chart of the post development phase

Appendix F Task Division

Table F.1: Task division for the Final Report

Name	Contributed to	Proofread
A. van den Bergh	Project scope: Team organisation. Performance: Cruise, Descent. Propulsion: Power system design, electrical system design, V&V, Conclusions & recommendations. Post DSE.	Aerodynamics, Sensitivity analysis, Post DSE.
L. Callens	Project Scope: Background. Configuration. Hydrodynamics: analysis, stability and V&V. Catia, Structures & Materials: Hull design. Introduction	Stability & Control, Cost Breakdown, Sensitivity analysis, Sustainability, Risk Analysis, Market Analysis
M. Garber	Stability analysis, Pitch control, Yaw Control, V&V, Summary, Editing, Report layout	Operations, Introduction, Conclusion
J. Jördens	Mass Budget, Post DSE: Production plan, Structures & Materials: Wingbox problem statement, Material selection, Spar design, Spar web design, Connecting mechanisms, Pontoons, Other relevant structures, Results, Validation, Conclusion and recommendations,	Configuration, Propulsion
S. de Kok	Organisation, Aerodynamics, Design&Development, Post DSE, Market Analysis, V&V, Gantt chart, Stability derivatives, Editing	Cost breakdown, Hydrodynamics, Summary
R. Palings	Cost breakdown, Risk, Hydrodynamics:Hydrodynamic control, Floats, Hydro trade-off, Hydro initial sizing. Summary, Market analysis, Post DSE:Towtank testing	Performance, Requirement compliance, Conclusion, Operations, Aerodynamics
M. Reekers	Performance: Approach, Dragdiagram, Pr-Pa Diagram, Takeoff, Climb, Landing, V&V. Conclusion. Propulsion: Approach, Propeller Design, V&V. Sustainability. Conclusion.	Organisation, Risk Management, Structures & Materials
N. Smith	Structures & Materials: Rib problem statement, Load distribution, Rib design. Hull design: ribs. Design Configuration: Functional flow. Detailed FFD. N2-Chart	Sensitivity analysis
M. Taams	Structures & Materials; Wing problem statement, Hull problem statement, load distributions. Stringer design, spar web deisgn, Hull design; stringers. V&V, Sensitivity Analysis, Quality Control	Introduction, Market Analysis, Risk analysis, Hydrodynamics, Sustainability.
K. Beukers	Configuration, Control, Operations, weather data and flight envelope plots	Performance, Aerodynamics, Propulsion Sustainability

Bibliography

[1] *VERORDENING (EG) Nr. 216/2008 VAN HET EUROPEES PARLEMENT EN DE RAAD*. European Parliament, 2008. Retrieved from: http://eur-lex.europa.eu/legal-content/NL/TXT/HTML/?uri=CELEX%3A32008R0216&from=EN.

[2] A.Elham. Aerospace design & systems engineering elements ii, lecture notes, 2013. Delft University of Technology.

[3] John D. Anderson. *Fundamentals of Aerodynamics, 4th Edition*. McGraw-Hill, 2004.

[4] The Wleft Brothers. Hydro biplane baseline report. Technical report, 2017.

[5] The Wleft Brothers. Hydro biplane midterm report. Technical report, 2017.

[6] The Wleft Brothers. Hydro biplane project plan. Technical report, 2017.

[7] J. Carrier. Design standards for advanced ultralight aeroplanes, 2004. Light aircraft manufacturers association of Canada.

[8] Walter S. Diehl. Relative loading on biplane wings. *Report No. 458*.

[9] D.Scholz D.Schiktanz. Box wing fundamentals-anaircraft design perspective. 2011.

[10] Xavier Ortiz et al. Forces and moments on flat plates of small aspect ratio with application to pv wind loads and small wind turbine blades.

[11] Fabio Fossati. *Aero-hydrodynamics of sailing yachts*. Bloomsbury, 2009.

[12] David H. Munro George P. Succi and Jeffrey A. Zimmer. Experimental verification of propeller noise prediction. *AIAA Journal*, 20(11), 1982.

[13] William Gracey. Measured moment of inertia of 32 airplanes. Technical report, National Advisory Commitee for Aeronautics. October 1940.

[14] Snorri Gudmundsson. *General aviation aircraft design*. Butterworth-Heinemann, 2014.

[15] Russell C. Hibbeler. *Mechanics of Materials*. Pearson Education Centre, 2014.

[16] S.F. Hoerner. *Fluid-Dynamic Drag*. S.F. Hoerner, 1965.

[17] C.C. de Visser A.C. in t Veld E. Mooij J.A. Mulder W.H.J.J. van Staveren J.C. van der Vaart, E. de Weert. *Lecture Notes Flight Dynamics*. TU Delft, March 2013.

[18] J.A. Keuning and L. Hillege. he results of the delft systematic deadrise series, 2017. Delft University of Technology.

[19] S. C. Lakkad. Mechanical properties of bamboo, a natural composite. *Fibre Science and Technology*, 14(4): 319–322, 1981. http://www.sciencedirect.com/science/article/pii/0015056881900233.

[20] Marcus Langley. *Seaplane Float & Hull Design*. Sir Isaac Pitman & Sons, LTD., 1935.

[21] Peng Zhou Liexun Yang and Ning Zhang. Ghg emissions from the production of lithium-ion batteries for electric vehicles in china. 2017.

[22] T.H.G. Megson. *Aircraft Structures*. Elsevier, 2007.

[23] Abdulkareem Sh. Mahdi Al-Obaidi Mun Hon Koo. Calculation of aerodynamic drag of human being in various positions. *EURECA*, 2013.

[24] Volker Nolte. Introduction to the biomechanics of rowing. 2014.

[25] G. D. Padfield and B. Lawrence. The birth of flight control: An engineering analysis of the wright brothers' 1902 glider. *The Aeronautical Journal*, 107(1078):697–718, 2003. `http://pcwww.liv.ac.uk/eweb/fst/publications/2854.pdf`.

[26] L. Prandtl. Induced drag of multiplanes. *Technical Notes National Advisory Committee for Aeronautics*, 1924.

[27] J.A. Melkert R. Vos and B.T.C. Zandbergen. Aerospace design & systems engineering elements i, lecture notes, 2017. Delft University of Technology.

[28] Daniel P. Raymer. *Aircraft Design, A Conceptual Approach.* American Institute of Aeronautics and Astronautics, 1992.

[29] Jan Roskam. *Airplane Design.* DARcorporation, 1985.

[30] P. D. Soden. Variables affecting the strength of balsa wood. *The Journal of Strain Analysis for Engineering Design*, 11(4):225–234, 1976. `http://journals.sagepub.com.tudelft.idm.oclc.org/doi/pdf/10.1243/03093247V114225`.

[31] David B. Thurston. *Design for Flying.* TAB Books, 1995.

[32] L.L.M. Veldhuis. Review of propeller-wing aerodynamic interference. *24TH INTERNATIONAL CONGRESS OF THE AERONAUTICAL SCIENCES*, 2004.

[33] Theodore Wildi. *Electrical Machines, Drives and Power Systems, 6th Edition.* Pearson, 2006.

[34] Jr. William D. Callister. *Materials Science and Engineering, An Introduction.* John Wiley & Sons, Inc., 2007.